NISTIR 6949

Infrared Thermography for Nondestructive Evaluation of Fiber Reinforced Polymer Composites Bonded to Concrete

Monica A. Starnes
Nicholas J. Carino

NIST
National Institute of Standards and Technology
Technology Administration, U.S. Department of Commerce

NISTIR 6949

Infrared Thermography for Nondestructive Evaluation of Fiber Reinforced Polymer Composites Bonded to Concrete

Monica A. Starnes
Nicholas J. Carino
Materials and Construction Research Division
Building and Fire Research Laboratory

January 2003

U.S. Department of Commerce
Donald L. Evans, Secretary

Technology Administration
Phillip J. Bond, Under Secretary for Technology

National Institute of Standards and Technology
Arden L. Bement, Jr., Director

ABSTRACT

Fiber-reinforced polymer (FRP) composites, in the form of pultruded laminates or built-up woven fabrics, are being used widely to strengthen existing concrete and masonry structures. The success of these materials in performing their intended functions depends, to a large extent, on how well they are bonded to themselves and to the substrate. There is a need for an efficient and reliable method to detect and characterize defects at the substrate interface and within multi-ply systems. Infrared thermography is well suited for this purpose because it is inherently sensitive to the presence of near-surface defects and can interrogate large areas efficiently. Before infrared thermography can be developed into a standard methodology, however, an understanding is needed of the effects of testing parameters and different types of defects. This report focuses on establishing the potential for quantitative infrared thermography, that is, not only detecting but also characterizing subsurface flaws. Numerical and experimental methods are used to investigate the effectiveness of infrared thermography to estimate the width of subsurface flaws in fiber-reinforced polymer laminates bonded to concrete.

First, a dimensional analysis of a simplified case of one-dimensional heat diffusion in an infinite half space is performed to establish the parameters that affect the thermal response of the test object. The results from the dimensional analysis identified the factors that had to be investigated in the parametric study.

Next, the finite-element method is used to carry out parametric analyses of the thermal response of simulated defects in fiber-reinforced polymer laminates applied to a concrete substrate. In this study, a "defect" is an air gap between laminates, at the laminate/substrate interface, or in the substrate. The aim is to assess the potential for quantitative infrared thermography in not only detecting a flaw but also being able to describe its physical characteristics. Six parametric studies are presented, namely: 1) relationships between the thermal input, the maximum signal, and the maximum surface temperature; 2) effect of thermal material properties of FRP composites and concrete; 3) effects of flaw depth and the number of FRP layers; 4) effect of flaw thickness; 5) effect of flaw width and estimation of flaw width; and 6) a multi-parameter screening study to determine relevant factors. From these simulations, procedures are established for selecting the thermal input and estimating the flaw depth and width.

The third component of the investigation focuses on laboratory studies. Controlled-flaw experiments are performed to evaluate the potential of infrared thermography testing to quantitatively assess subsurface flaw in FRP bonded to concrete. First, a qualitative test is successfully performed to evaluate the potential for detection of each simulated flaw embedded in the test object. The next two experiments involve quantitative thermography testing of an air void embedded at the interface between a pultruded FRP laminate and the concrete substrate. A comparison between the quantitative infrared thermography test and finite-element simulations of the same test is also performed. Good agreement between experimental thermal response parameters and those calculated from finite-element models provides assurance of the validity of parametric studies based on numerical simulations. Controlled-flaw experiments are also performed to verify the procedure for estimating the width of subsurface flaws. Good agreement is found between the estimated and actual flaw dimensions. Data smoothing is shown to be effective in removing "noise" from measured temperature profiles. An experimental screening experiment is carried out to determine the relevant factors affecting the thermal response of the

controlled-flaw specimens. The results indicate that the depth of the flaw is the only relevant factor affecting the time to maximum signal. Finally, an experiment is performed to determine the degree of repeatability of infrared thermography testing and the assessment of adequate sampling rate. It is concluded that sampling rates of 1 Hz are adequate for quantitative evaluation of FRP bonded to concrete.

The results of investigation provide demonstrable evidence of the potential of infrared thermography to characterize the depth and width of flaws (air voids) embedded in FRP composites bonded to concrete.

Keywords: Building technology

Acknowledgements

The authors would like to express their gratitude to Professor Eduardo Kausel of the Massachusetts Institute of Technology for his contribution to the research project.

The authors would also like to thank Mr. Andre Witcher, of the Materials and Construction Research Division, for his help with the fabrication of the experimental apparatus, and to Dr. Daniel Flynn and Dr. William Healy, of the Building Environment Division, for their help in the field of heat transfer.

TABLE OF CONTENTS

Chapter 1

Introduction

1.1 Background

The trend in civil engineering is toward the development of high-performance structures that incorporate advanced materials. Moreover, the up front application of advanced materials in civil engineering structures incorporates the use of fiber composites. Fiber-reinforced polymer (FRP) composites are two-phase engineered materials that combine high performance fibers within a polymer matrix. These advanced materials are characterized by their high strength, high stiffness, low density, and durability. Consequently, wide application of advanced composites may allow engineers to design innovative structures.

Most FRP materials are generally used as thin elements or structural subsystems. In civil engineering applications, FRP composites are undertaking a major role in the rehabilitation of existing civil infrastructure. Rehabilitation involves the repair and strengthening of functional or structural deficiencies of structural components. For this purpose, composite layers or laminates are primarily bonded to existing reinforced concrete and masonry structures using adhesives such as epoxy resins. The primary purpose of bonded FRP composites is to enhance the structural capacity of the rehabilitated structure.

However, the major factor that contributes to the optimum performance of the composite system is the quality of bond between the FRP and the concrete or masonry substrate. For example, in beam and wall applications, fabricators must be able to guarantee bond and sufficient development length and anchorage of the FRP laminates. Yet, standard quality control procedures to assess the integrity of FRP composite systems still need to be developed for civil engineering applications. Ultimately, quality control of the final product is a requirement for the successful implementation of any new material in structural engineering systems.

Furthermore, the final mechanical properties of FRP composites are affected by environmental aspects such as temperature, moisture, and contaminants. As such, the quality of a FRP composite is influenced by the manufacturing process and where (factory vs. *in situ*) the composite is fabricated. For civil structures, installation and curing of FRP composites occur typically in the field rather than in a controlled environment. Generally, installation involves manual application of fabric and resins. Thus, there is potential for high variability of the final product unless appropriate quality control procedures are used. Composite thickness,

interlaminar adhesion, and substrate bonding must be carefully monitored. Additional defects intrinsic to this process are air voids and contaminants, which may accelerate the formation of in-service delaminations and debonds in the FRP composite.

A variety of techniques exist for installation of external FRP composite systems. The most common techniques in civil engineering applications are wet lay-up, prepreg, precured shells, resins infusion, and pultruded sheet. Figure 1.1 illustrates some of the applications of FRP composites for rehabilitation of civil engineering structures.

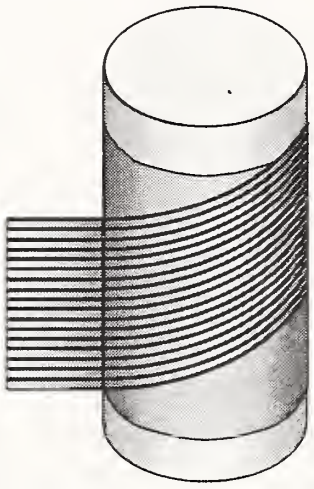

Column wrapping using wet lay-up

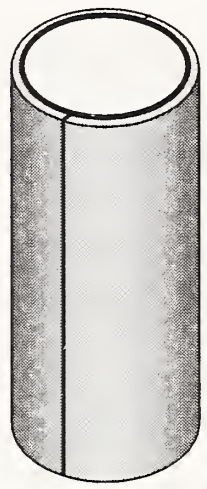

Column wrapping using precured shell

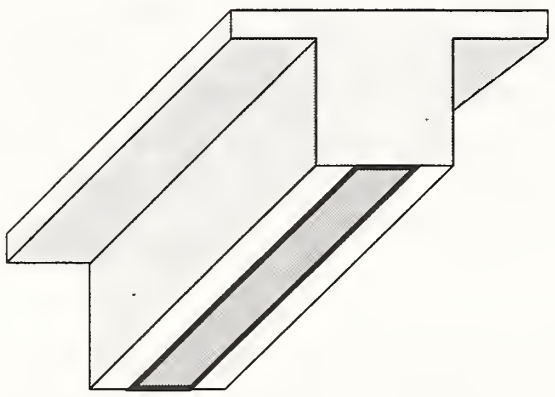

Beam reinforcement using pultruded sheet

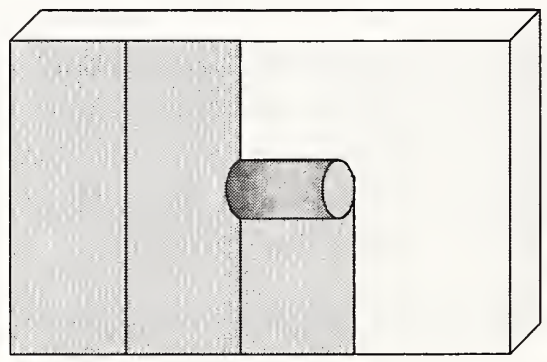

Wall reinforcement using prepregs

Fig. 1.1 Examples of applications of FRP composites for rehabilitation purposes

Lay-up using fabric, tape, or tow is probably the most used technique (Karbhari et al., 1998). The installation process is simple: fiber fabric or tow is wrapped or wound around the structural member; resin is then impregnated using a wet bath. The primary advantages of this technique are that it provides the maximum flexibility for installation and is economical. Because installation involves manual application of fabric and resins, variability of the final product is to be expected. Air voids and contaminants are defects intrinsic to this process.

Prepreg laminates are sheets of resin-preimpregnated fibers. Prepreg lay-up is similar in installation procedure to wet lay-up. These laminates are also manually placed on the structural element. Although, generally more expensive than wet lay-up systems, prepreg systems are more consistent and have fewer defects. Additionally, prepregs need high curing temperatures, which produce higher glass transition temperature of their matrices. Despite the benefits of using prepregs, researchers claim that the application of these composites to masonry walls may be difficult due to the inherent stiffness of the plies (Christensen et al., 1996).

Precured shells are manufactured in a factory and then bonded in the field. The primary application of these jackets is for retrofitting of columns. The controlled fabrication process assures the quality of the FRP shell. However, adequate bonding of the shell to itself and to the concrete structure is critical.

The resin infusion process is a recently developed installation method. Dry fibers are first applied to the structure (primarily columns) and then followed by infusion of resin using a vacuum. Resin infusion systems are cured at ambient temperatures. Low glass transition temperature is a disadvantage. This technique achieves higher uniformity in the composite than wet lay-up.

Finally, the pultrusion manufacturing method allows fabrication of continuous cross sectional components (rods, laminates, channels, etc.). Pultruded FRP composites are manufactured at the factory and externally bonded to the concrete structure in the field. Pultruded composites are mostly used in beam applications where thin strips are bonded to the tensile faces. Due to the high quality control at the factory, these FRP systems posses high uniformity and a minimum amount of defects within the composite but they must still be bonded to the structure in situ.

1.2 Motivation

FRP composites bonded to concrete are, by their nature and installation method, prone to high variability of thickness and other internal anomalies. Effective quality control methods for these composite systems must provide quantitative information regarding the thickness and fiber content of the applied composite and amount, location, and size of defects at any given time through the life of the structure. In addition, FRP composites are starting to be widely used without a complete understanding of the structural mechanics and durability properties of these materials. The inherent danger of erroneous expectations about the capabilities of FRP composites is an incentive for the development of reliable nondestructive testing techniques. Nondestructive testing (NDT) methods together with mechanics and durability studies should be able to predict structural reliability and material integrity and thus allow for prioritization of the maintenance of civil infrastructure.

Nondestructive testing techniques for FRP composites are widely researched and used in the aerospace industry for both manufacturing quality control and routine maintenance inspection. Yet, the quality of the manufacturing process, sizes of the structures, boundary and environmental conditions, and available budget for inspection of aerospace structures are quite different from those of civil structures. Thus quality control of composite materials used in civil engineering applications requires the development of reliable and economical NDT techniques and standard test methods for this particular application.

Nondestructive testing techniques can be categorized into two major groups: electromagnetic methods and mechanical vibration methods. Likewise, electromagnetic methods are subdivided into nuclear, radar, thermographic, magnetic, and electrical. Mechanical vibration methods include ultrasonics, acoustic emissions, acousto-ultrasonics, vibration methods, and coin tap testing.

Nuclear NDT methods such as radiography (X-rays) are of limited use in the inspection of fiber reinforced polymers. The method has been tried for the determination of structure composition, density, permeability, thickness, fiber volume ratio, and moisture content, among others. The method does not detect interlaminar defects such as voids, debonds, and delaminations. The primary reason why interlaminar defects are not detected is that such flaws are perpendicular to the X-ray beam making detection nearly impossible. Debonds can not be detected because the absorption of the adherent is generally very high. The only solution for optimum inspection is the introduction of radio-opaque penetrants (Bar-Cohen, 1986). However, penetrants require surface breaking and are highly toxic.

The bases for radar testing are very simple. A beam of electromagnetic energy is transmitted to the structure. Portions of the energy are transmitted through the structure, and the remaining energy is reflected back from each boundary (surface, layer, or flaw) encountered (Malhotra et al., 1991). An example of radar methodology is short-pulse radar, which uses microwave energy. This method is used for the evaluation of delaminations and water content in concrete. Additionally, thickness, density, fiber orientation, volume ratio, material degradation, and flaws of FRP composites can be inspected using short-pulse radar. However, radar technology needs further improvements in antenna resolution for its application to FRP composites bonded to concrete structures.

Thermographic techniques (infrared thermography, liquid crystal thermography, etc.) consist of applying heat to the structure and observing the temperature gradients on the surface of the specimen. Infrared thermography is best suited for detection of anomalies near the surface of the specimen. Thus, detection of internal anomalies in thin FRP composites bonded to concrete is possible. In civil applications, current infrared thermography testing of FRP composites is focused on qualitative assessment of the state of the structure. The reason for the qualitative nature of the results is the complex relationship between the variables affecting the thermal response of the bonded assemblies.

Three examples of magnetic testing are magnetic induction, flux-leakage method, and nuclear magnetic resonance or magnetic resonance imaging (MRI). Both magnetic induction and flux-leakage testing are only effective for ferrous materials. Thus, testing of FRP composites is not feasible. Nuclear magnetic resonance is widely used in other fields such as medicine. Only small specimens can be tested in a lab environment, hence making this method irrelevant for civil engineering applications.

Eddy-current is the most popular electrical technique for testing FRP composites. Two basic methods are used to determine the stacking sequence, or direction of the fiber: resistive eddy-current path and resistive capacitive eddy-current path. In the resistive eddy-current path technique, electric current passes from one fiber to another at the points of contact. On the other hand, the resistive capacitive eddy-current path method allows for an interfiber capacitive path in

addition to the resistive path. Since the method requires a conductive material, glass fiber reinforced polymers cannot be tested. This method can determine the stacking sequence in carbon fiber reinforced polymers (CFRP). Eddy-current testing is also limited to composites with high fiber-volume ratio. An additional disadvantage is that eddy-current methods are insensitive to porosity, delaminations, and other nonconductive inclusions in the material.

Ultrasound techniques such as pulse echo, impact echo, impulse response, surface waves, and plate wave method are widely used in civil engineering inspections. In this technique, a stress pulse is introduced to the surface using a transmitter. After the introduction of the pulse, a series of compression waves travel through the depth of the specimen. Waves are reflected to the surface by cracks or ply interfaces giving quantifiable data about the state of the material. Currently pulse echo is the most successful ultrasonics methods for testing composite materials in aerospace applications. Pulse echo techniques can determine the thickness of FRP composites and their elastic modulus. However, due to the high attenuation of FRP composites, only low frequencies can be used to test these materials.

Acoustic emission testing records elastic stress waves generated by localized cracking in the structure. Analysis of the wave propagation gives the location of damage in the structural member. Although the method is widely used in lab and factory settings, field use is limited. Acousto-ultrasonic methods are similar to ultrasonic techniques.

Dynamic or vibration methods include techniques such as resonant frequency, pulse velocity, and lamb-wave methods. The resonant frequency method evaluates the dynamic elastic modulus of the structure using its fundamental frequency. This technique requires a transducer to be acoustically coupled to the test object using a liquid couplant. The geometry of the structure or test object directly affects the resonant frequency. The transducer produces a standing wave in the test object. The presence of an internal flaw changes the pattern of the standing wave in the material. Although successful in aerospace structures, this method is limited to laboratory size specimens. The primary reason for the small specimen size is that small defects have little effect on the natural frequency of a large structure. Therefore, resonant testing is usually conducted on individual structural components to detect localized damage.

The coin tap test is widely used for the detection of flaws in FRP such as delaminations and debonds. This method is simple, inexpensive, and requires minimum instrumentation. However, the test is a point test method and qualitative in nature. Quantitative techniques are currently being investigated and developed at the Center for NDE at Iowa State University (CNDE, 1999). An example of a potential quantitative technique is the Computer-Aided Tap Tester (CATT).

Two optical techniques show potential for testing FRP composites: laser doppler vibrometer and shearography. The laser doppler vibrometer technique is based on the local-membrane vibration of the composite laminates at the location of an internal flaw. The vibration is produced by exciting the FRP composite using piezoelectric actuators. The surface of the test object is then scanned with a laser. The method is able to detect debonds between the substrate and the FRP composite. However, the surface of the test object needs to be covered with reflecting tape in order to produce the required doppler effect.

Shearography is based on the principles of laser interferometry. As such, it requires the superposition, or in this case the subtraction, of two speckle patterns of the test object under different strain conditions. This technique employs a single laser beam, which is expanded and projected onto the surface of the test object. An image of the surface of the test object is taken with the shearography camera before the loading is applied. This camera incorporates a bifringent lens that shifts the recorded image. The specimen is then loaded to produce the needed strain. The strain condition may be produced using various techniques such as vacuum stressing, thermal stressing, and vibrational excitation. A second image of the loaded specimen is recorded and subtracted from the before-loading image. The image processing produces a series of fringes that quantify the amount of strain in the test object. Research has shown that internal flaws are detectable using shearography (der Hovanesian et al., 1995). The technique also allows for the estimation of the depth of the anomaly. The primary inconvenience of this technique is the high cost of the equipment.

The final nondestructive testing technique is infrared thermography. This method is based on the measurement of the radiation emitted by the object under transient heat flow. This radiation is related to the fourth power of the surface temperature of the test object. Internal flaws produce significant changes in the thermal diffusion pattern of the object. These changes affect the surface temperature above the flaw compared with the temperature above sound material. By measuring the surface temperature, the presence of a subsurface flaw is revealed.

All of these NDT methods have advantages and disadvantages. The best technique to detect and characterize a defect depends on critical flaw size, the size of the structure being tested, and the environment in which the inspection is carried out. Successful implementation of any NDT method requires the technique to be accurate, cost efficient, and easy to use. The technique should be able to detect the size, type, and location of expected flaws. In addition, for civil engineering applications, the ideal inspection technique must allow for *in situ* and preferably global testing. Global testing refers to the ability to measure the characteristic of the complete structural element from a single measurement.

Nondestructive testing of FRP composites presents a variety of difficulties due to material characteristics such as anisotropy, high electrical resistance, variable ultrasonic attenuation, and non-magnetic properties. Thus, uncommonly used methods like infrared thermography may be more suitable for testing FRP composites than most traditional testing methods based on sonic and electromagnetic wave propagation techniques.

The simplicity and global testing nature of infrared thermography makes it an ideal method for civil engineering inspections. Infrared thermography has already been used to assess the integrity of structural systems. Present inspection of bonded FRP composites using infrared thermography is focused on qualitative rather than quantitative estimates of the state of the structure. Current inspection data are not being exploited fully because of the lack of knowledge about the relationship between variables affecting the thermal response of the bonded laminates, lack of standard data collection protocols, and insufficient understanding of radiometric theory by thermography inspectors (Connolly, 1991).

In order to allow widespread use of thermography for quantitative assessment of FRP applied to concrete and masonry structures, a standard test method is needed. To develop such a standard,

it is necessary to develop a greater understanding of the factors affecting the thermal response of thin layers of FRP composites bonded to concrete or masonry.

1.3 Research Objectives

Infrared thermography (IR) is an inspection method currently used successfully to locate subsurface flaws in FRP laminates bonded to concrete (Hawkins et al., 1999). Trial case studies performed by the FHWA and New York DOT (Alampalli et al., 2001), among others, confirmed that infrared thermography is a promising NDE method considering testing speed and ability to detect flaws. Inspections using infrared thermography, however, are primarily focused on qualitative assessment of the state of the structure. The qualitative nature of the results is due to the complex relationships between the variables affecting the thermal response of the bonded laminates. Nevertheless, the need for defect characterization, not just defect detection, demands research in quantitative infrared thermography. Knowledge of the fundamental parameters affecting heat transfer and infrared thermography testing is needed to develop the foundation for quantitative thermographic inspection of civil structures. Therefore, experimental and analytical studies are needed to determine the capabilities and limitations of IR thermography for quantitative assessment of FRP bonded to concrete or masonry.

This doctoral report focuses on experimental and analytical studies to establish the scientific bases for the development of a standard methodology for using infrared thermography in nondestructive evaluation of concrete and masonry structures strengthened with FRP composites.

1.4 Research Approach

The research project had three phases. The investigation starts with a literature search, which includes an overview of civil engineering applications of FRP composites, various nondestructive evaluation methods, and a review of infrared thermography (its theoretical principles and recent research).

The second phase of the investigation focuses on analytical studies including non-dimensional analysis and extensive parametric studies involving numerical simulation of infrared thermography testing. The finite element method is used in the parametric studies.

The final phase of the research project was controlled-flaw laboratory studies, which involved the fabrication and testing of specimens with simulated flaws in FRP laminates bonded to concrete substrates.

1.5 Outline of Report

This report is composed of six chapters, including this introductory chapter.

Chapter 2 summarizes the theoretical principles of infrared thermography. Relevant studies are reviewed and outlined from an extensive literature survey. The literature review focuses on numerical modeling, using finite-element and finite-difference methods, of infrared thermography testing.

Chapters 3 and 4 present analytical studies of thermal evolutions typical of infrared thermography testing. Chapter 3 develops the dimensional analysis of the simplified heat transfer problem of a multi-layer semi-infinite space subjected to a heat flux pulse. The results from the dimensional analysis help to identify the relevant variables for the parametric study of Chapter 4.

Chapter 4 presents analytical studies of the main parameters affecting thermal evolution in infrared thermography testing by using finite-element modeling. Both single-parameter and multi-parameter investigations are carried out. The primary objective of the single-parameter study is to investigate the effect of each factor on the thermal response during thermography testing. The following investigations are performed for the single-parameter studies:

- Effect of thermal input;
- Effect of thermal material properties;
- Effect of flaw depth;
- Effect of flaw thickness; and,
- Effect of flaw width.

The multi-parameter study investigates which parameters that characterize subsurface flaws (depth, thickness, and width) have the greatest effect on the thermal responses.

Chapter 5 focuses on experimental research and validation of theoretical models. This chapter summarizes procedures involving construction of controlled-flaw test specimens, design and construction of test apparatus, determination of input heat flux, determination of material emissivity, and infrared thermography testing. Qualitative and quantitative thermography tests are described. Results from testing of a subsurface air void are compared with finite-element simulations to verify the validity of the numerical modeling from Chapter 3. Also, a simple procedure for flaw width estimation is validated. Next, a screening experiment is carried out to verify the results from the multi-parameter analytical investigation described in Chapter 3. The chapter concludes with the results of an investigation involving test repeatability and effect of sampling rate.

Chapter 6 summarizes the results of the analytical and experimental studies of the report. Conclusions are drawn and topics for future research are recommended.

Chapter 2

Literature Review

2.1 Introduction

Infrared thermography is being used successfully for defect detection in fiber-reinforced polymer (FRP) laminates bonded to concrete. Current inspections using infrared thermography are focused on qualitative assessment of the presence of flaws. This qualitative nature of the inspections stems from the complex relationships between the variables affecting the thermal response of the bonded laminates.

This chapter summarizes the theoretical principles behind infrared thermography nondestructive testing. Additionally, the state-of-the-art in quantitative infrared thermography is examined through a literature survey of previous research. The literature review focuses on numerical simulations of IR thermography. This survey concentrates on applications from the aerospace and manufacturing industries because of the lack of research on quantitative infrared thermography inspection of civil structures.

2.2 Theoretical Principles

Infrared thermography, as a tool for flaw detection, is based on the principle that heat transfer in any material is affected by the presence of flaws or any other change in material thermal properties. Figure 2.1 is a schematic of a concrete substrate with several FRP laminates applied to the surface. There is a flaw within the FRP layer and this flaw affects the flow of heat into and out of the FRP-concrete composite. The difference in heat flow through the flawed and unflawed regions causes localized energy differences on the surface of the test object, which can be measured using an infrared detector or radiometer. Through data processing, the measured infrared radiation is transformed into a surface temperature distribution and recorded in the form of thermograms (isotherm plots). Thermal anomalies in the thermogram indicate the presence of subsurface flaws in the test object.

The relation between surface temperature and emitted radiation is based on the Stefan-Boltzmann (Eq. 2.1) and Wien displacement (Eq. 2.2) principles (Ede, 1967), as follows

$$W = \varepsilon \sigma T^4 \tag{2.1}$$

$$\lambda_{max} = \frac{b}{T} \tag{2.2}$$

where,

W = radiant intensity (W/m^2);
ε = emissivity of the test object (dimensionless quantity);
σ = Stefan-Boltzmann constant (5.67×10^{-8} $W/(m^2 \cdot K^4)$);
T = absolute temperature (K);
λ_{max} = wavelength of the maximum radiation intensity (μm); and,
b = Wien displacement constant (2897 μm·K).

Equation 2.1 indicates that the emitted radiation is a nonlinear function of temperature, and Eq. 2.2 indicates that the wavelength of the peak intensity decreases with increasing temperature. At near room temperatures, the wavelength is in the infrared region of the electromagnetic spectrum. The emissivity is a property of the surface and has a value between zero and one. An emissivity value of one is found in perfect emitters such as a black body.

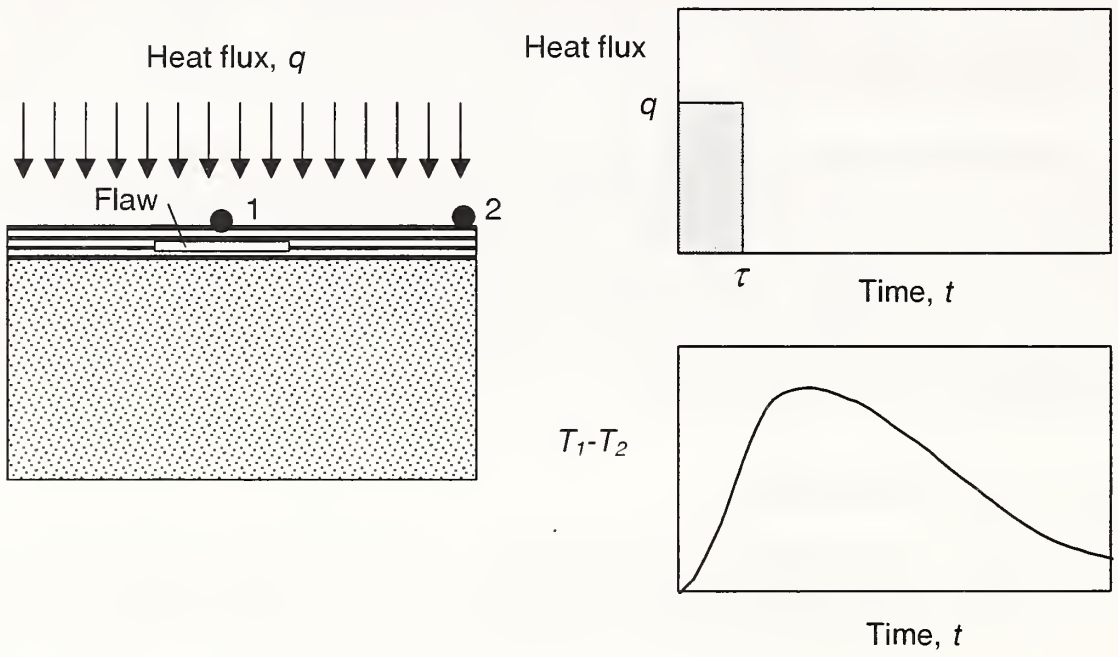

Fig. 2.1 Schematic of the infrared thermography method to detect presence of a flaw based on surface temperature differences

Infrared thermography is subdivided into two major testing approaches: *passive* IR thermography and *active* IR thermography. The difference between the two approaches is that an external thermal stimulus is required for active thermography, while in passive thermography the specimen itself is the source of the thermal stimulus. Passive thermography usually involves steady state thermal conditions and active thermography generally involves transient heat transfer conditions. Flaw detection and characterization in civil engineering structures require active thermography. In addition, defect characterization requires the use of time-resolved IR

thermography. Using this technique, the surface temperature of the test object is monitored and analyzed as a function of time, instead of being monitored statically at only one particular point in time.

Infrared thermography is currently used for defect detection in FRP laminates bonded to concrete (Hawkins et al., 1999). Inspections using infrared thermography are mostly qualitative in nature because of the complex relationships among the variables affecting the thermal response of the bonded laminates. Defect characterization, however, requires quantitative or time-resolved thermography.

Quantitative characterization of internal anomalies requires the study of the transient heat transfer phenomenon. Starting with the general case, the thermal evolution in a material is governed by the theory of diffusion (Lienhard, 1981) as follows:

$$\vec{\nabla} \cdot K \vec{\nabla} T + Q = \rho c \frac{\partial T}{\partial t} \tag{2.3}$$

where,

$\vec{\nabla} \cdot$ = divergence operator;
K = heat conductivity tensor;
$\vec{\nabla}$ = gradient operator;
T = temperature;
Q = internal heat generation;
ρ = density;
c = specific heat; and,
t = time.

The term "thermal evolution" refers to the spatial and temporal distribution of temperature within the test object. If the change in the conductivity tensor is relatively small with respect to the temperature of the material, Eq. 2.3 simplifies to

$$K\left(\nabla^2 T\right) + Q = \rho c \frac{\partial T}{\partial t} \tag{2.4}$$

where,

∇^2 = Laplacian operator.

For example, in the Cartesian coordinate system, the Laplacian is defined as

$$\nabla^2 T = \frac{\partial^2 T}{\partial x^2} + \frac{\partial^2 T}{\partial y^2} + \frac{\partial^2 T}{\partial z^2} \tag{2.5}$$

When heat is applied suddenly to the surface of an object, transient heat flow occurs until thermal equilibrium is reached. During transient heat flow, the temperature at any point in the object changes with time. If the object has large dimensions perpendicular to the direction of uniform heat input and the area of uniform heat input is large compared with the depth, heat flows parallel to the input, and the problem is reduced to one-dimensional heat flow. One-

dimensional transient heat flow theory states that the temperature within the object changes in a nonlinear manner upon a step change in surface temperature, as follows (Lienhard, 1981):

$$T_d = T_\infty + (T_i - T_\infty)\ erf\left(\frac{y}{2\sqrt{\alpha t}}\right) \tag{2.6}$$

where,

T_d = temperature at any depth y in the object;
T_∞ = applied constant temperature at the surface of the specimen;
T_i = initial temperature of the solid;
erf = the Gaussian error function for ( );
t = time; and,
α = thermal diffusivity of the material.

Thermal diffusivity is defined as

$$\alpha = \frac{k}{\rho\, c} \tag{2.7}$$

where,

k = thermal conductivity;
ρ = density; and,
c = specific heat.

Thermal diffusivity affects how fast a material changes temperature under transient conditions.

The nonlinear behavior described in Eq. 2.6 is illustrated in Fig. 2.2. Figure 2.2 shows the temperature history at various depths of a concrete slab initially at 0 °C after a constant temperature of 10 °C is applied at the surface.

In summary, during transient heat transfer through an object, surface temperature changes caused by internal anomalies in the material are time dependent. Surface temperatures depend on the thermal input, elapsed time, and the type, size, and depth of the defect. The surface temperature distribution is established by measuring the emitted radiation using an infrared camera. Accurate measurement of the surface temperature distribution depends on knowing the value of the emissivity of the surface and on environmental "noise" such as atmospheric attenuation and air movement.

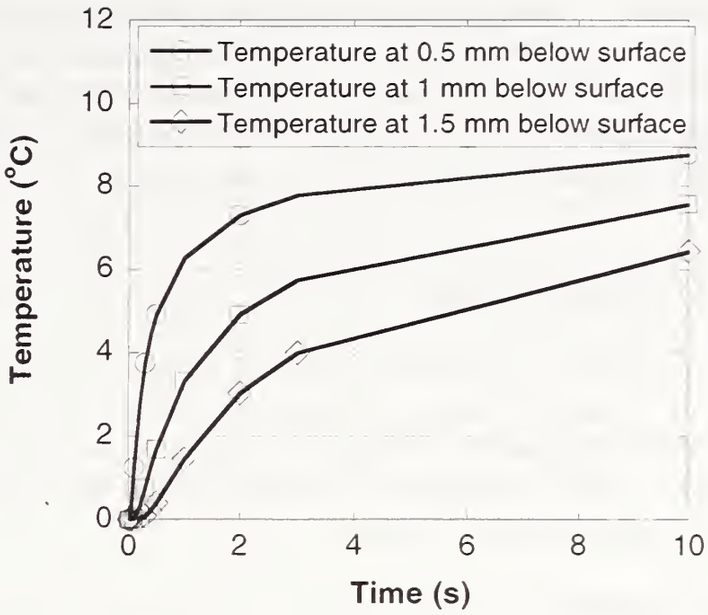

Fig. 2.2 Example of nonlinear behavior of thermal evolutions

2.3 Literature Review

This section presents a summary of a literature review of research involving infrared thermography testing. The review indicates that, from an analytical point of view, most researchers have investigated infrared thermography using numerical simulations. Since infrared thermography is a versatile testing technique, this section summarizes only investigations of interest, primarily those involving FRP composites or multi-layer systems.

2.3.1 Closed-Form Versus Numerical Analytical Studies

Looking back at the diffusion principle, Eq. 2.3, solution of the governing equation is simple, and of closed form, for linear one-dimensional heat flow. Most engineering situations, however, involve complex geometries and boundary conditions that must be considered in their analysis. Additionally, when the thermal flow encounters a buried flaw, heat begins to flow in other directions in addition to the original direction, which was normal to the surface of the object. Simple closed-form analytical solutions are unattainable once the thermal phenomenon involves two-dimensional and three-dimensional transient heat transfer. Numerical modeling is the only analytical method capable of simulating realistic heat transfer problems. Furthermore, numerical analysis provides approximate solutions to the complex model within a small percentage of the exact solution. Thus, high accuracy could be easily achieved if the analytical model is properly defined. In the past, the main disadvantage of numerical simulation, particularly for complex geometries, has been the large computation time and data storage space required to obtain the solution. These problems have become trivial, however, due to the advances in both computer processing power and data storage.

In the field of nondestructive testing, numerical modeling is used to simulate experimental data, confirm test results, evaluate potential testing procedures, and aid further developments in the field. Numerical methods are effective resources for gaining an understanding of test results and improvement of testing methods. Past research has focused on the evaluation of the various parameters that influence thermal evolution.

2.3.2 Summary of Investigations

Recent analytical investigations of heat transfer applied to infrared thermography have provided some general conclusions regarding diagnostic capabilities of this NDT method. The parameters investigated include material properties, attributes of anomalies, thermal stimulation, observation time, and testing mode. Brief descriptions of conclusions from parametric studies using numerical methods are discussed in this section.

2.3.2a Material Properties

Since active thermography is based on transient thermal evolution, the thermal response depends on the elapsed time and on the material properties of the materials tested. Thermal conductivity and diffusivity are the primary material properties that affect thermal response of an object.

Based on the thermal properties and the time dependency of thermal evolution, deeper anomalies in a material are detected later (Cielo et al., 1987) and with decreased contrast (Allport et al., 1988)

$$t \approx \frac{z^2}{\alpha} \tag{2.8}$$

$$dc \sim \frac{1}{z^3} \tag{2.9}$$

where,

t = detection time;
z = depth of the anomaly; and,
dc = detection contrast.

Based on this dependency of defect depth and detection time, time-resolved infrared thermography is required for quantitative measurement of anomalies in the object. Detection contrast is defined by Allport et al. (1988) as

$$dc = \frac{T_d - T_b}{T_b} \tag{2.10}$$

where,

T_d = surface temperature above the defect; and,
T_b = surface temperature in the background.

Thermal conductivity and diffusivity are the primary material properties linked to thermal diffusion and thus, to the thermal response of a particular material. These two material properties are particularly important for the detection of internal flaws using infrared thermography. For example, Vavilov et al. (1993) reported that a 10 % increase in thermal conductivity of the sound material tends to enhance the temperature contrast, and thus, detectability, by 10 %. Increases of thermal diffusivity by 10 %, however, may amplify the contrast only 5 %. Hence, thermal conductivity is the main property affecting temperature contrast between sound and flawed areas. Furthermore, considering the material properties of the flaw itself, thermal conductivity again proves to be far more important than diffusivity for defect detection.

Thermal diffusivity is the primary material property affecting detection time. Materials with high thermal diffusivity are difficult to inspect using infrared thermography due to the fast thermal response of the material. Looking at a particular engineering application, Connolly (1991) reported that low thermal diffusivity coatings bonded to high thermal conductivity substrate produce high defect detectability. On the other hand, defect detectability on specimens with high thermal diffusivity coatings and low diffusivity substrate was significantly lower. The primary reason for the low detectability was that the fast thermal response experienced at the surface of the specimen was difficult to capture.

Considering the temporal effects on thermography, Vavilov et al. (1993) stated that observation time is short for materials with high diffusivity because of their fast thermal response. In agreement with Connolly (1991) they noted that high diffusivity materials are difficult to inspect using infrared thermography. CFRP composites are materials with a medium value of diffusivity. Thus, capturing thermal evolutions of CFRP with infrared equipment may be a complex task.

Three-dimensional heat diffusion effects through the material tend to produce rounding or blurring effects on the thermograms of the anomaly. The amount of roundness depends on the material composition of the test object. Rounding effects observed in the temperature field of delaminated composites were investigated by Varis (1995). The rounding of the edges of the defect was primarily caused by the difference in thermal conductivities of the anisotropic material. In this particular case, the composite material tested included both glass and graphite fibers. The highest temperature differences were observed at the glass fiber location. The numerical simulation indicated that the temperature signal in the carbon fiber area was too small to be detected experimentally with the chosen infrared equipment. This indicates the need for specific test procedures for particular applications and materials.

Varis et al. (1995) also concluded that the effect of anisotropy was minimal when the defect was located at the interface of deeper layers.

2.3.2b Defect Characteristics

Defect characterization involves several parameters: type, size, shape, depth, and thickness of the defect.

Type of Defect

In IR thermography testing of FRP composites, the most typical anomalies investigated are delaminations, debonds, and inclusions parallel to the surface of the specimen. These types of flaws are easily detected using infrared thermography provided optimum testing conditions (i.e. thermal input, observation time, etc.) are used. Partially conductive anomalies such as resin rich/poor areas block only a portion of the heat flux through the material. This behavior produces a low thermal contrast making it difficult to detect the anomaly.

Cracks perpendicular to the surface of the sample are difficult to detect and nontraditional methods are required to detect them. Some of these techniques include the use of innovative heating techniques such as electric current and moving line heating (Satonaka et al., 1995).

Post-processing of temperature data, such as the calculation of the Laplacian of the temperature distribution, also allows for the detection of cracks (Cramer et al., 1992). Results show that it is possible to detect surface cracks and short and shallow cracks provided their depth is at least half the thickness of the sheet. However, cracks should have large thermal contrast resistance in order to be detected.

Size of Defect

Vavilov et al. (1993) point out the importance of size on detection. This dependence involves both diameter and thickness of the flaw.

The flaw has to be larger in diameter than its depth under the surface in order to be detectable (Rantala et al., 1991). Additionally, a decrease of flaw size produces a rounder image as well as a decrease in thermal contrast.

For defect size characterization, it is necessary to determine the relationship between the actual defect size and the estimated defect size observed in the thermograms. Results based on numerical simulations, such as finite element analysis, tend to overestimate the size compared with experimental results. One of the reasons for the overestimation is the ideal testing conditions used in the numerical model. An additional source of size inaccuracies may arise from the selected signal measuring technique. Simple signal measuring techniques, such as the use of a temperature signal threshold above noise levels, lack precision. This technique also depends highly on noise and time (Vavilov, 2000). Another simple method is the full-width at half-maximum (FWHM) technique, which consists of determining where the signal is half the maximum value. The FWHM method provides size predictions with estimation errors on the order of 15%, and it tends to underestimate the true size of the defect. The method is, however, simple enough for practical use. Introducing methods that are more complex may solve the lack of accuracy. For example, a successful method is the computation of the Laplacian or second derivatives of the temperature profile. The technique involves the determination of where the inflection point ($d^2T/dx^2 = 0$) of the temperature profile occurs (Vavilov, 2000).

Connolly et al. (1990) presented analytical and experimental techniques to examine carbon-carbon composite materials. For their application, the size of the estimated flaw was larger than

the actual flaw size. Thus, as further research, the authors stated that it is necessary to determine the relationship between the actual and the estimated defect size.

Depth of Defect

Detection of delaminations decreases as depth increases. Increasing the depth of the flaw also increases the time for maximum thermal signal and maximum thermal contrast. Additionally, partially conductive anomalies located deep in the material may be difficult to detect and quantify (Allport et al., 1988).

The depth of the flaw affects the rounding behavior of the surface temperature above the defect due to diffusivity. Deeper flaws develop more rounded or diffused edges than flaws located near the surface. For optimum detection, testing of CFRP should be restricted to objects containing flaws between 1.5 mm and 2 mm deep (Vavilov, 1993).

Vavilov (2000) also investigated the effect of multiple and overlapped flaws on temperature data. For the case of multiple flaws, he observed that average surface temperatures were higher than for cases with a single flaw. The problem of overlapped flaws was more complex, since near-the-surface flaws may eclipse deeper anomalies. This situation tended to produce an increase in the surface temperature signal, which could be misinterpreted as a single flaw having higher thermal resistance.

Thickness of Defect

The final factor for characterization of internal defects involves the thickness of the flaw or, in general, the thermal resistance of the flaw. The thermal resistance is directly proportional to the thickness of the flaw (Özişik, 1985)

$$R = \frac{\Delta z}{k} \tag{2.11}$$

where,

R = thermal resistance;
Δz = thickness; and,
k = thermal conductivity of the flaw.

Increasing the thermal resistance of the flaw improves the thermal signal at the surface of the specimen.

2.3.2c Thermal Input

Active infrared thermography involves the application of an external thermal impulse to the object under test. As such, the type, amplitude, and duration of the thermal stimulus affect the detection of subsurface flaws.

Several types of thermal stimuli have been used for active thermography. Traditional methods include uniform heating, moving line heating, and spot heating. Uniform heating usually involves heating the surface of the specimen with high power lamps, but it is difficult to obtain

substantially uniform heating. Line heating typically involves moving a thermal line source along the surface of the specimen. Moving gas flame and laser sources are commonly used for this procedure. Spot heating is the least productive mode of heating; thus, it is seldom used.

From the simulation perspective, moving line heating is the most complex method since it involves transverse diffusion effects in the material. Nonetheless, the effect of transverse diffusion on the line heating method allows for the detection of cracks perpendicular to the surface, which are undetectable with traditional static heat sources.

The Joule-effect-heating technique (Satonaka et al., 1995) is among the nontraditional methods that may be used to detect perpendicular-to-the-surface defects. The procedure consists of clamping the specimen with electrodes and applying an electric current, which flows parallel to the tested surface. Within the flawed specimen, the electrical flow creates a distinctive distribution of electric current density. By the Joule effect, this current density is converted into heat, thus, producing transient thermal effects. Currents of 2000 A to 3000 A applied for a few milliseconds are sufficient to detect open-to-the-surface cracks. This technique is only applicable to materials able to conduct electricity.

Most researchers agree that thermal pulses with high intensity and short duration produce the highest temperature gradients and thus, better flaw detection (Lulay et al., 1994). Generally, pulse duration must be as short as possible in order to attain the highest thermal signal. For example, Vavilov et al. (1993) concluded that carbon composites benefited from heat intervals of less than 0.5 s. Also, defects close to the heated surface require shorter heating pulses. A potential practical problem is that short pulses may not be capable of delivering enough heat to raise the temperature of the surface sufficiently (Connolly, 1991). The greater the quantity of heat supplied, the greater the temperature signal.

2.3.2d Optimum Observation Time

The optimum observation time is defined as the moment of maximum thermal signal or contrast. At this instant, the image of the buried flaw emerges well defined and the edges are as sharp as possible. As the time increases beyond the optimum the image becomes increasingly rounded due to the diffusion effect (Rantala et al., 1991). Additionally, increasing the depth of the flaw lengthens the time to maximum contrast.

The optimum observation time depends highly on the material properties of the test object. As previously stated, thermal diffusivity has a major effect on observation time. Hence, due to their fast thermal response, high diffusivity materials are difficult to inspect using infrared thermography. Most FRP composites used in civil infrastructure have low to medium diffusivity values; thus, they are good candidates for this testing technique.

2.3.2e Testing Mode

There are two methods of observation for active infrared thermography: reflection (one-sided) and transmission (two-sided). Figure 2.3 illustrates the configurations for one-sided and two-sided testing. Each method has its advantages and disadvantages. For example, observation by

reflection provides greater resolution but the thickness of the tested layer must be small. Thick objects are tested better by transmission, but this method does not provide depth information and has low resolution. Two-sided IR thermography is inappropriate for quantitative nondestructive evaluation of FRP composites bonded to concrete or masonry substrates.

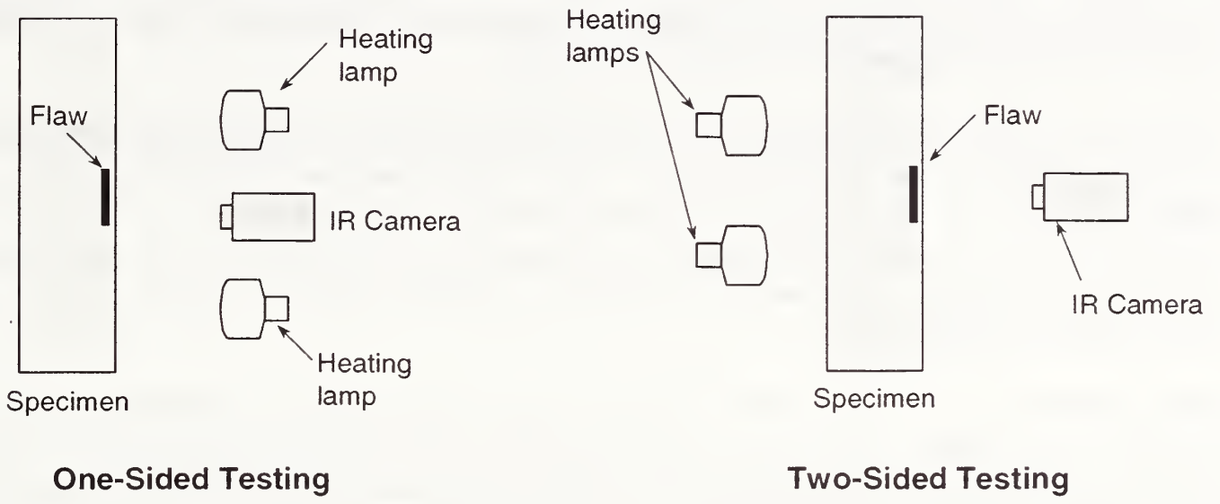

Fig. 2.3 Schematic of one-sided and two-sided testing modes

The thermographic configuration is also relevant to the observation time. In general, reflection thermography is more time dependent than transmission thermography (Vavilov et al., 1993).

2.3.2f Additional Considerations

Additional considerations involve ambient conditions during *in situ* inspection. The accuracy of thermography measurements depends highly on environmental conditions such as solar radiation, cloud cover, ambient temperature, wind speed, and surface moisture. For example, over long distances (meters) absorption of the IR signal by the atmosphere must be taken into account (Maldague, 1993).

Most of the uncertainty in simulation solutions arises from the simplification of the testing conditions. To better simulate *in situ* testing conditions, most numerical algorithms allow for the incorporation of convection heat losses and, with some software packages, ambient noise into the model. The incorporation of ambient conditions in the numerical model notably increases the amount of calculation time and computer memory required for the simulation. Hence, one must assess and balance the benefits of accurate modeling with the amount of computation time and data storage available.

2.3.3 Simulation Outputs Versus Experimental Data

Cowell and Burleigh (1990) assessed the potential detection of defects in carbon composites. The researchers used computer simulations and experimental trials to determine the types, sizes, and depths of detectable defects. Two-sided active infrared thermography using uniform heating over the surface of the specimen was selected. Comparison of numerical and experimental data showed consistent disagreement among the results.

Cowell clarified that the disagreements between experimental and theoretical results were due to assumptions made in the modeling process. For example, uniform heating was assumed over the entire top surface of the laminate. Uniform heating is hardly achieved in real testing. As an additional source of error, the material properties of the composite were not measured for comparison with those of the numerical simulation. Hard to predict convective losses could have caused additional differences.

Other researchers have successfully compared results from experimental and theoretical studies. Hamzah et al. (1996), for example, investigated the potential size estimation of back-drilled holes in bakelite plates. The agreement between experimental and numerical results confirmed the potential of infrared thermography as a quantitative NDT method.

2.4 Summary

Infrared thermography is still an immature nondestructive inspection method. Inspection hardware and techniques are rapidly evolving without complete understanding of the parameters affecting the thermal responses of test objects.

This literature review provided a summary of recent investigations in the field of quantitative infrared thermography. Most investigations focused on evaluation of various parameters involved in heat transfer phenomena. The parametric studies were performed on problems representing different engineering applications, which illustrate the versatility of infrared thermography. All the reviewed investigations, however, have focused on the aerospace and manufacturing industries. The lack of studies involving civil engineering applications and materials indicates that further research is required to establish the effect of relevant parameters on the thermal response. The resulting knowledge will provided the bases for standards for quantitative testing of FRP composites bonded to concrete structures using infrared thermography.

Chapter 3

Dimensional Analysis

3.1 Introduction

This chapter focuses on preliminary analytical studies of the heat diffusion problem involved in thermography testing. The objective of the analytical study summarized in this chapter was the determination of relevant parameters that describe transient heat transfer in a solid. This was done through dimensional analysis of a simplified model.

3.2 Dimensional Analysis

In general, dimensional analysis is used to isolate the relevant parameters that need to be examined for a specific physical phenomenon. The results from the dimensional analysis summarized in this chapter will help identify the variables that need to be investigated in subsequent parametric studies.

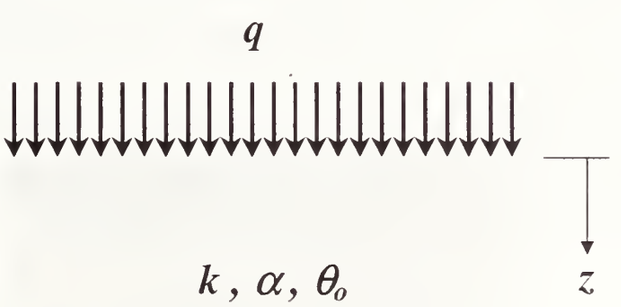

Fig. 3.1 Semi-infinite half-space studied on dimensional analysis

For simplicity, a homogeneous semi-infinite half-space was investigated (Fig. 3.1). The top surface of the model was heated with a uniform heat flux q. The semi-infinite half-space had a thermal conductivity k, thermal diffusivity α, and initial temperature θ_o. One-dimensional transient heat transfer in the z-direction was assumed.

The equation that governs the heat transfer problem is the following partial differential equation, which represents a one-dimensional, linear, and purely diffusive phenomenon:

$$\frac{\partial^2 \theta}{\partial z^2} = \frac{1}{\alpha}\frac{\partial \theta}{\partial t} \tag{3.1}$$

where

θ = temperature;
z = depth;
t = time; and,
α = thermal diffusivity of the material.

Initially, the test object is at a temperature θ_o, thus the initial conditions of the problem are:

$$at\ t = 0; \quad \theta = \theta_o;\ \theta - \theta_o = 0 \tag{3.2}$$

The top surface is heated with a uniform heat flux, thus the boundary conditions are the following:

$$at\ z = 0; \quad -k\frac{\partial \theta}{\partial z} = q \tag{3.3}$$

$$at\ z = \infty; \quad \theta = \theta_o; \quad \theta - \theta_o = 0 \tag{3.4}$$

Observation of the governing equation and its initial and boundary conditions indicates that the dependent variable is the change in temperature $\theta(z,t)$-θ_o. As previously mentioned, one of the fundamental principles of infrared thermography inspection is the change in surface temperature. The change in temperature is a function of the spatial and temporal parameters, the thermal diffusivity, the thermal conductivity, and the prescribed heat flux:

$$\theta - \theta_0 = f(z, t, \alpha, k, q) \tag{3.5}$$

thus, there are 5 parameters that influence the temperature behavior (N=5). The five parameters on the right hand side of Eq. 3.5 are the independent arguments. The change in surface temperature θ-θ_o is the dependent variable. Thus, equation 3.5 describes the relationship between N+1 physical parameters that characterizes the heat transfer problem.

Next, the system of units is selected. The Length-Mass-Time-Temperature (L-M-T-Θ) system is used for this particular analysis. Each independent parameter could be expressed as a product of the units involved in its definition, for example

$$[A] = L^a M^b T^c \Theta^d \tag{3.6}$$

where the exponents are dimensionless numbers that follow from the quantity definition. Following the L-M-T-Θ system, the five independent quantities expressed in Eq. 3.5 could be expressed as follows:

$$[z] = L^1 M^0 T^0 \Theta^0 \tag{3.7}$$

$$[t] = L^0 M^0 T^1 \Theta^0 \tag{3.8}$$

$$[\alpha] = L^2 M^0 T^{-1} \Theta^0 \tag{3.9}$$

$$[k] = L^1 M^1 T^{-3} \Theta^{-1} \tag{3.10}$$

$$[q] = L^0 M^1 T^{-3} \Theta^0 \tag{3.11}$$

Observation of the dimensions of the independent variables indicate that four of the variables, z, t, q, and k, have independent dimensions, while α has dependent dimensions. The thermal diffusivity α has dependent dimensions because it can be expressed as a function of z and t

$$[\alpha] = [z]^2 [t]^{-1} \tag{3.12}$$

Thus, there is a subset of k=4 dimensionally independent physical quantities. Observation of the independent and dependent physical quantities indicate that there should be N-k+1=2 dimensionless numbers. The following step involves defining the two invariants.

For the purpose of constructing the two required dimensionless variables, the following linear transformations of the 6 physical quantities were performed:

$$z = Z\, z^* \tag{3.13}$$

$$t = T\, t^* \tag{3.14}$$

$$\alpha = A\, \alpha^* \tag{3.15}$$

$$k = K\, k^* \tag{3.16}$$

$$q = Q\, q^* \tag{3.17}$$

$$\theta - \theta_o = \Theta\, \theta^* \tag{3.18}$$

where z^*, t^*, α^*, k^*, q^*, and θ^* are dimensionless counterparts of the physical quantities z, t, α, k, q, and θ-θ_o of dimensions Z, T, A, K, and Θ. Substituting the linear transformations into the governing diffusion equation, Eq. 3.1 transforms into:

$$\left(\frac{Z^2}{AT}\right)\frac{\partial\theta^*}{\partial t^*} = \alpha^* \frac{\partial^2\theta^*}{\partial z^{*2}} \tag{3.19}$$

Additionally, the initial and boundary conditions, Eqs. 3.2, 3.3, and 3.4, transform into the following:

$$at\ t = 0; \quad \theta - \theta_o = \Theta\theta^* = 0 \tag{3.20}$$

$$at\ z = 0; \quad -\left(\frac{K\Theta}{ZQ}\right)k^* \frac{\partial\theta^*}{\partial z^*} = q^* \tag{3.21}$$

$$at\ z = \infty; \quad \theta - \theta_o = \Theta\theta^* = 0 \tag{3.22}$$

In order for the transformed set to satisfy the same equation as those in the original diffusion problem, the following should be true:

$$\left(\frac{Z^2}{AT}\right) = 1 \tag{3.23}$$

and

$$\left(\frac{K\Theta}{ZQ}\right) = 1 \tag{3.24}$$

Equivalently, using the linear transformation, two dimensionless parameters, π and π_1 are obtained.

$$\pi = \frac{k(\theta - \theta_0)}{zq} = \frac{k^*\theta^*}{z^* q^*} \tag{3.25}$$

$$\pi_1 = \frac{z}{\sqrt{\alpha t}} = \frac{z^*}{\sqrt{\alpha^* t^*}} = (Fo)^{1/2} \tag{3.26}$$

where,

Fo = Fourier number.

The dimensionless parameter π indicates that the temperature θ can be solved in terms of the depth, the input thermal flux, and the thermal conductivity of the solid. The dimensionless parameter π_1 relates the distance and the diffusion length $\sqrt{\alpha t}$. The diffusion length is the distance over which the effects of a sudden, localized change in temperature can be felt after a time t. For cases in which $z >> \sqrt{\alpha t}$ the thermal effect is imperceptible.

3.3 Summary

The dimensional analysis demonstrates that in the case of a solid semi-infinite half-space solid the physical quantities that influence the thermal evolution are z, t, k, α, and q. In the case of a solid containing a subsurface flaw or inclusion, additional physical quantities, such as the thermal resistance of the flaw, should be taken into consideration. The results from the dimensional analysis helped identify the variables that needed to be investigated in the parametric study presented in Chapter 4.

Chapter 4

Parametric Studies

4.1 Introduction

The complexity of transient heat transfer through a finite heterogeneous object remains a key obstacle to the effective use of quantitative infrared thermography for flaw detection. The greatest contributor to the complexity is the dependency of thermal evolutions on space as well as time. Furthermore, the time dependency is nonlinear. From a theoretical perspective, solutions to heat transfer problems could be attained by direct solution of the governing thermal diffusion equation or by using numerical methods. Most heat transfer problems, however, can only be solved using numerical analysis. In addition to being the only analytical method to provide results, numerical modeling provides the most effective method for theoretical analysis of non-trivial heat transfer problems.

The flexibility of numerical analysis allows the engineer to simulate different testing scenarios such as, passive versus active thermography, steady state versus transient heat transfer, or linear versus nonlinear modeling (due to material properties). Because of its diverse simulation capability, computer modeling is a cost efficient alternative to experimental testing. Furthermore, in some engineering fields, the impressive performance of properly verified numerical modeling has caused the replacement of otherwise expensive and time consuming experimental testing with computer simulation. Computer simulation tends to reduce the overall cost of engineering research and design projects. In the field of nondestructive testing, numerical modeling is used to predict experimental results, conduct parametric studies, evaluate potential testing procedures, and aid further developments in the field.

The second component of the author's research program involved numerical modeling of infrared thermography testing of FRP layers bonded to concrete substrates. The study focused on the evaluation of the various parameters that influence thermal evolution (the spatial and temporal variations of surface temperature). Understanding how these diverse parameters affect heat transfer is the key to successful implementation of testing procedures, inversion algorithms, and ultimately, standard test methods. It was hoped that observation and evaluation of surface temperature variations as a function of time could be used to indicate the size, shape, orientation, and depth of internal anomalies.

4.2 Single-Factor Parametric Study

The finite element method (FEM) was the chosen analytical tool for this phase of the project. The first parametric study involved evaluation of single parameters that affect the thermal response.

The objectives of the single-factor parametric study were the following:

- Optimize heating time and intensity for maximum thermal signal;
- Determine the effects of material properties on the resulting thermal signal;
- Investigate the effect of flaw depth;
- Examine the effect of type of flaw (delamination versus debond);
- Study the effect of defect thickness on flaw detection and characterization; and
- Determine minimum detectable flaw size.

All analytical simulations were performed using ANSYS 5.6[†].

4.3 Parametric Study No. 1: Effect of Thermal Input

The first parametric study involved the evaluation of the effect of the amplitude (heat flux) and duration of the input thermal pulse. The input heat pulse was modeled as a rectangle or "hat" function of amplitude q and duration τ, as illustrated on Fig. 4.1.

The parametric study was designed to address several issues:

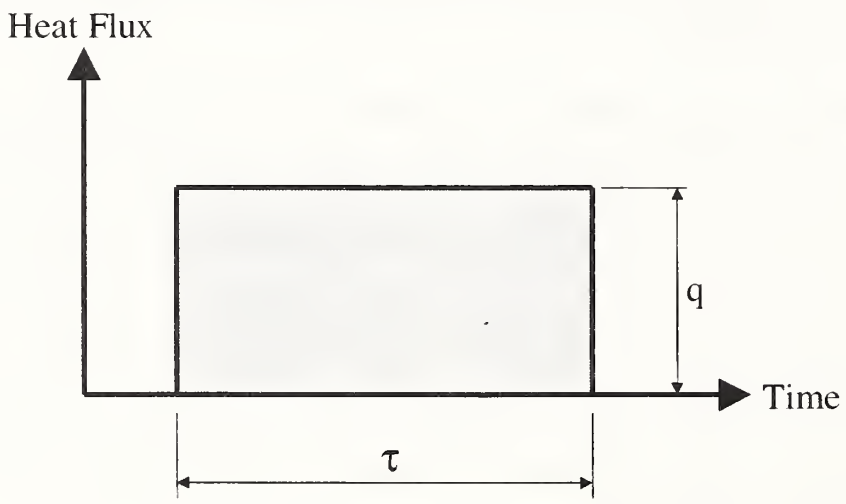

Fig. 4.1 Square thermal impulse

- Understand the effects of pulse duration and heat flux amplitude on the thermal response; and,

[†] Certain commercial equipment, instruments, or materials are identified in this report in order to specify the experimental procedure adequately. Such identification is not intended to imply recommendation or endorsement by the National Institute of Standards and Technology, nor it is intended to imply that the products are necessarily the best available for the purpose.

- Determine the optimal combination of input heat flux and pulse duration for FRP composites applied to concrete substrates.

The investigation was focused on estimating the optimal thermal energy for experimental configurations relevant to civil engineering applications. The study involved eighteen different simulations with pulse durations ranging from 0.05 s to 3 s, and applied heat flux ranging from 5000 W/m^2 to 100 000 W/m^2.

For the purpose of comparison, two-dimensional (2-D) and three-dimensional (3-D) models were used. Models that included free convection cooling of the surface were also compared with models that did not include such cooling.

4.3.1 2-D Models

The first set of simulations involved two-dimensional models. The simulation object consisted of a 100 mm long by 20 mm thick concrete slab covered with two layers of carbon FRP. Each layer of CFRP was 0.5 mm thick. The bonded FRP contained a flaw delamination at the interface with the concrete substrate. The debond had a length of 25 mm and a thickness of 0.2 mm, which corresponds to a thermal contact resistance of 8.33×10^{-3} m^2·K/W.

The thermal contact resistance of the flaw can be estimated using equation 4.1 (Özişik, 1985)

$$R = \frac{\Delta y}{k_y} \tag{4.1}$$

where,

R = contact resistance,
Δy = thickness of the flaw, and
k_y = thermal conductivity of air in the y-direction.

As a note, in this model the x-direction corresponds to the length of the specimen and the y-direction corresponds to the thickness. Since plane two-dimensional modeling was used, the slab is of infinite size in the z-direction.

The interface flaw was located at the center of the model. The model to be analyzed was simplified by using plane symmetry. Thus, only a half section was modeled (Fig. 4.2). The model was constructed using rectangular blocks with dimensions in meters shown (Fig. 4.3).

The material properties of the model were those of concrete for the substrate, air for the defect, and CFRP for the bonded composite. The CFRP layer in direct contact with the concrete had the fibers running in the x-direction, while the outer CFRP layer had the fibers running in the z-direction. The material properties are presented in Table 4.1. The material properties were gathered from Maldague (1993) and MatWeb (a material information resource in the World Wide Web).

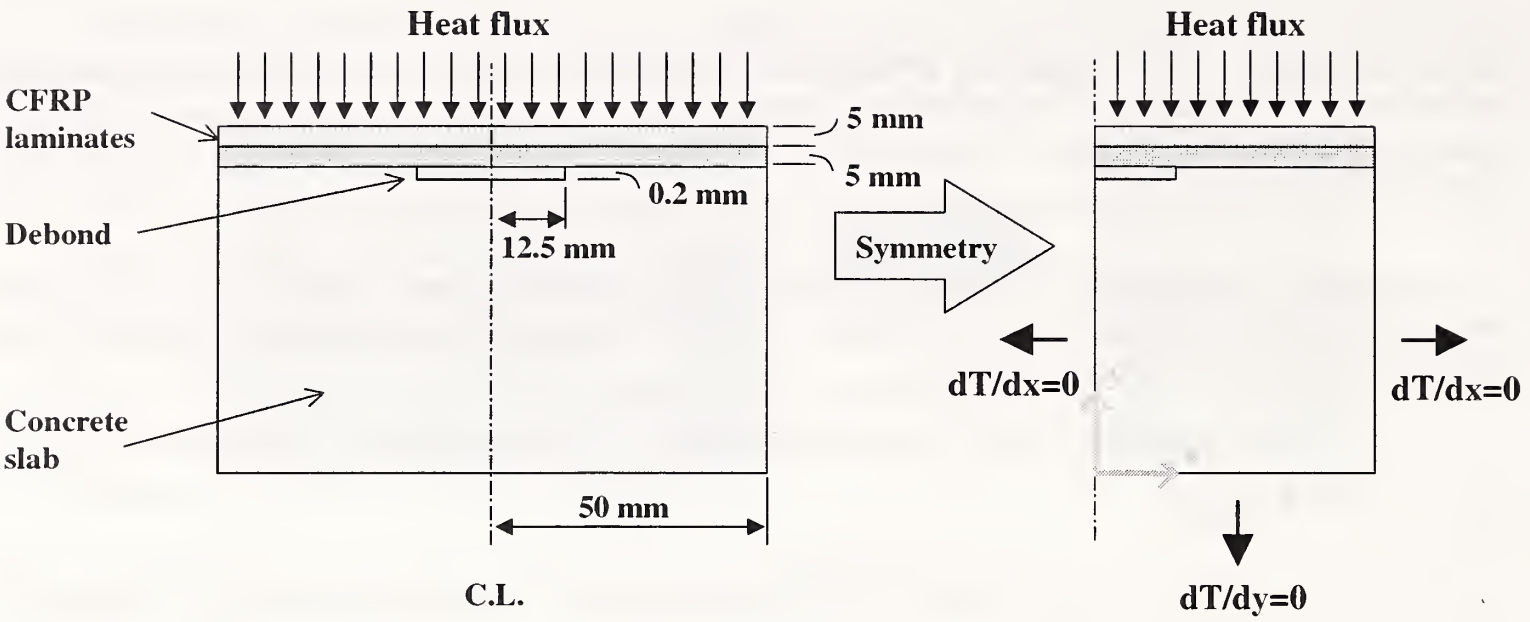

Fig. 4.2 Two-dimensional simulation test object

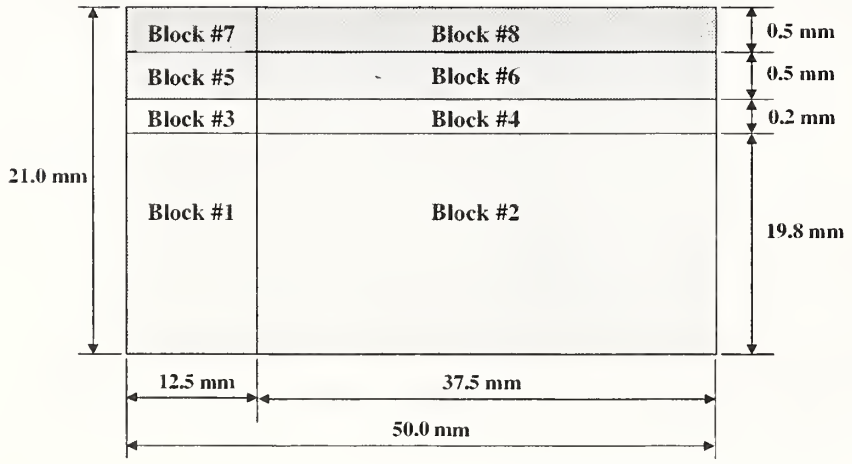

Block #1	x_1 =	0.0000	x_2 =	0.0125
	y_1 =	0.0000	y_2 =	0.0198
Block #2	x_1 =	0.0125	x_2 =	0.0500
	y_1 =	0.0000	y_2 =	0.0198
Block #3	x_1 =	0.0000	x_2 =	0.0125
	y_1 =	0.0198	y_2 =	0.0200
Block #4	x_1 =	0.0125	x_2 =	0.0500
	y_1 =	0.0198	y_2 =	0.0200
Block #5	x_1 =	0.0000	x_2 =	0.0125
	y_1 =	0.0200	y_2 =	0.0205
Block #6	x_1 =	0.0125	x_2 =	0.0500
	y_1 =	0.0200	y_2 =	0.0205
Block #7	x_1 =	0.0000	x_2 =	0.0125
	y_1 =	0.0205	y_2 =	0.0210
Block #8	x_1 =	0.0125	x_2 =	0.0500
	y_1 =	0.0205	y_2 =	0.0210

Fig. 4.3 Two-dimensional geometry of blocks used to generate finite-element mesh

Table 4.1 Material properties

	Material 1 Concrete	Material 2 CFRP (outer layer)	Material 3 CFRP (inner layer)	Material 4
ρ (kg/m^3)	2400	1600	1600	1.2
c (J/kg·K)	800	1200	1200	700
k_x (W/m·K)	1.5	7	0.8	0.024
k_y (W/m·K)	1.5	0.8	0.8	0.024
k_z (W/m·K)	1.5	0.8	7	0.024

The model was meshed using 2-D thermal solid elements. Four-noded quadrilateral elements were used. In particular, PLANE55 elements were selected from the ANSYS library. The test object was meshed using "mapped meshing" instead of "free meshing". Free meshing is simpler and faster, but, the mesh may contain some triangular elements in addition to quadrilaterals. In addition, element size is not as consistent as in mapped meshing. Mapped meshing allows the user to control directly the element size and type in the model. For this particular parametric study, the global element length in the x-direction was set to 1 mm. Mesh refinement, however, was applied to the thin composite layers and at the flaw location. The thickness of each composite ply was subdivided into four elements, while the thickness of the flaw and adjacent concrete was subdivided into two elements (Fig. 4.4). The rest of the concrete specimen was meshed using a graded mesh with finer mesh (in the y-direction) at the top and coarser mesh at the bottom of the specimen. Specifically, the average element size for the concrete was 0.00275 m with a "spacing ratio" of 10. The spacing ratio is the ratio of the dimension of the largest element to the dimension of the smallest element.

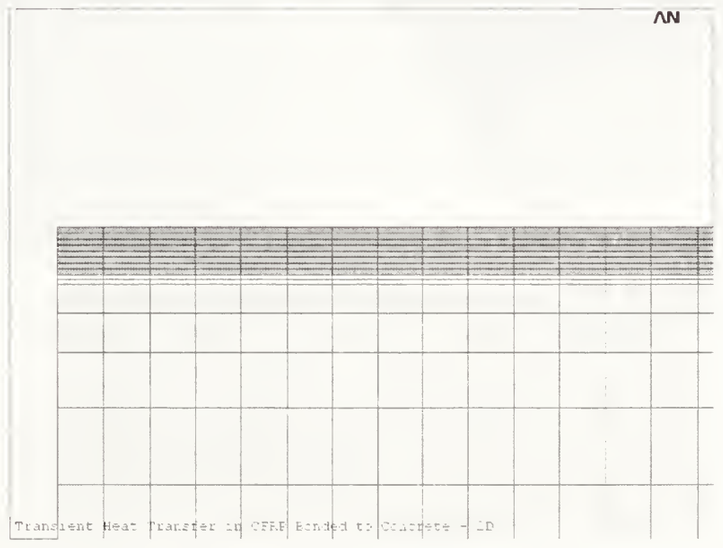

Fig. 4.4 Close up of two-dimensional meshing at the location of the flaw

4.3.2 3-D Model

The second set of simulations involved three-dimensional models for comparison with the results obtained with 2-D models. The simulation object consisted of a 100 mm long by 100 mm wide by 20 mm thick concrete slab. The slab was covered with two layers of carbon FRP. Each layer of CFRP was 0.5 mm thick. The specimen contained a flaw (debond) at the interface of the CFRP and the concrete substrate. The debond had an area of 25 mm $\times$ 25 mm and a thickness of 0.2 mm.

The delamination was located at the center of the model. The modeling of the test object was simplified by using planes of symmetry so that only one quarter of the model was simulated. The test object was created using 16 individual blocks. The individual blocks were "glued" together using boolean operations. Although this procedure may seem time-consuming and redundant, it facilitated the mapped meshing procedure.

Similar to the 2-D model, the material properties of the 3-D model were those of concrete for the substrate, air for the defect, and CFRP for the bonded composite. The CFRP layer in contact with the concrete had the fibers running in the x-direction, while the external CFRP had the fibers running in the z-direction.

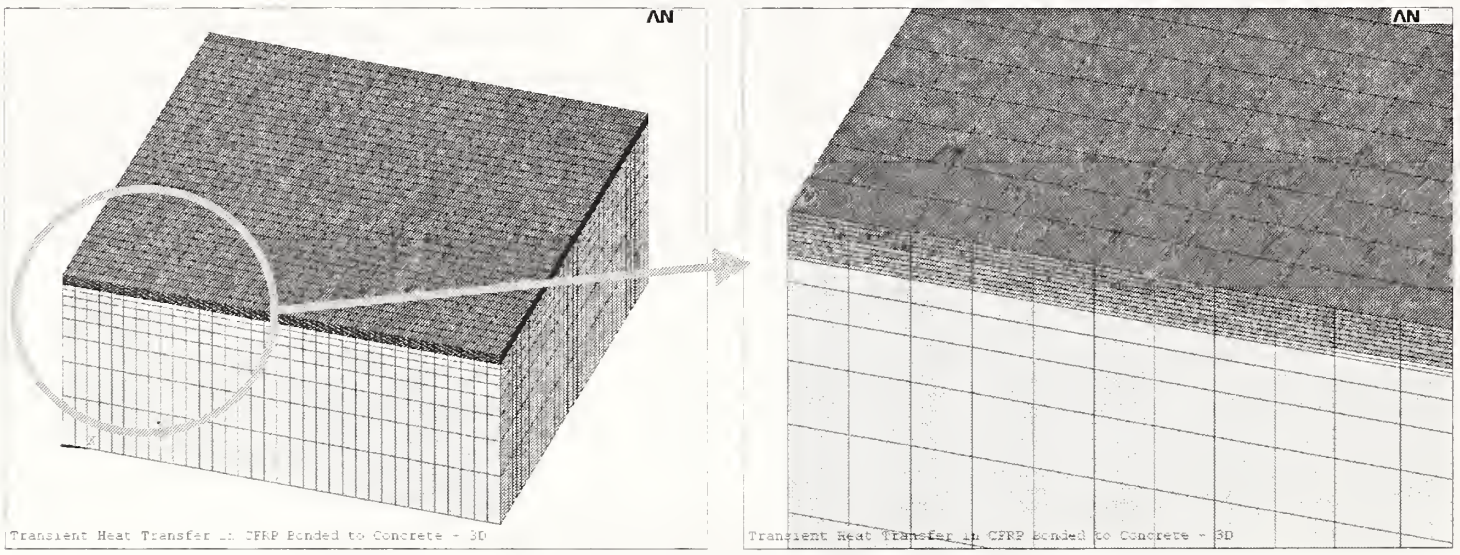

Fig. 4.5 Three-dimensional meshing of simulation object

The model was meshed using 3-D thermal solid elements. In particular, eight-noded quadrilateral SOLID70 elements were used. The general element size was set to 1.5 mm; however, mesh refinement was used for the thin composite layers and for the flaw. The thickness of each composite ply was subdivided into four elements, and the thickness of the flaw and adjacent concrete was subdivided into two elements (Fig. 4.5). The bulk of the concrete slab was meshed using a graded mesh with a finer grid at the top and a coarser grid at the bottom of the specimen. Specifically, the average element size for the concrete was 0.00275 m with a spacing ratio of 10 in the y-direction.

4.3.3 Thermal Loading and Boundary Conditions

The analysis was defined as a transient heat transfer problem. A rectangular pulse of intensity q and duration τ (Fig. 4.6) was applied to the top surface of the test object (Fig. 4.7). Adiabatic conditions ($dT/dx = 0$, $dT/dy = 0$, and $dT/dz = 0$) were assumed for the other surfaces. Adiabatic conditions on these surfaces implied no heat flux across those planes. These assumptions were realistic for the physical conditions during such an actual test. The initial temperature for all the cases was set to 23 °C. Eighteen different analyses were performed with pulse durations varying from 0.05 s to 3 s, and heat flux varying from 5000 W/m^2 to 100 000 W/m^2.

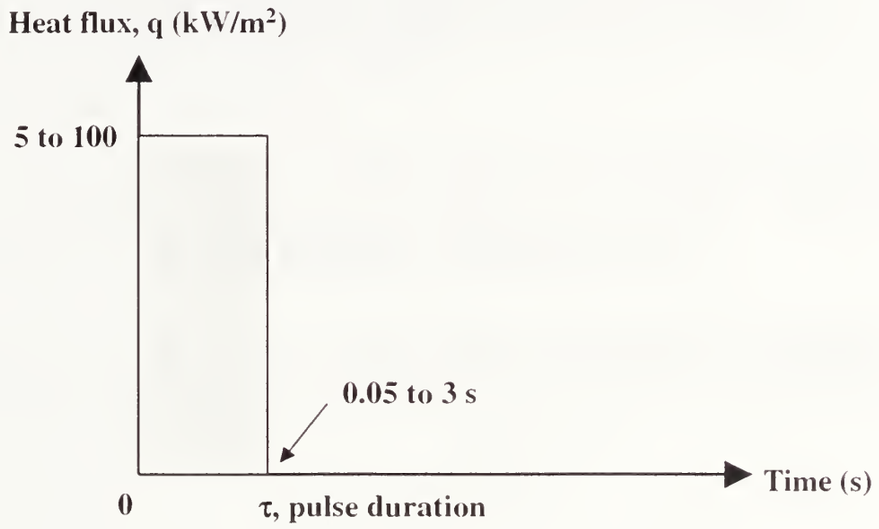

Fig. 4.6 Applied thermal pulse

For simplicity, uniform heating and no cooling losses were assumed for the eighteen analyses. One trial simulation, however, was performed to determine the effect of free convection cooling on the test object. Free convection cooling occurs naturally on any surface that is in contact with a fluid and is subject to a change in temperature. The trial simulation used the two-dimensional model with a thermal input of 100 000 W/m^2 for 0.5 s. To provide for the free convection effect, surface elements (SURF151) with a heat transfer coefficient of 2.0 W/(m^2·°C) and ambient temperature of 23 °C were added to the two-dimensional model. In ANSYS, SURF151 elements are thermal surface-effect elements, which are used to apply multiple loads to the surfaces of solid elements. For this particular model, the surface elements chosen were 2-noded (no thickness) elements. The heat transfer coefficient was applied to the surface elements and the ambient temperature was applied to an added node.

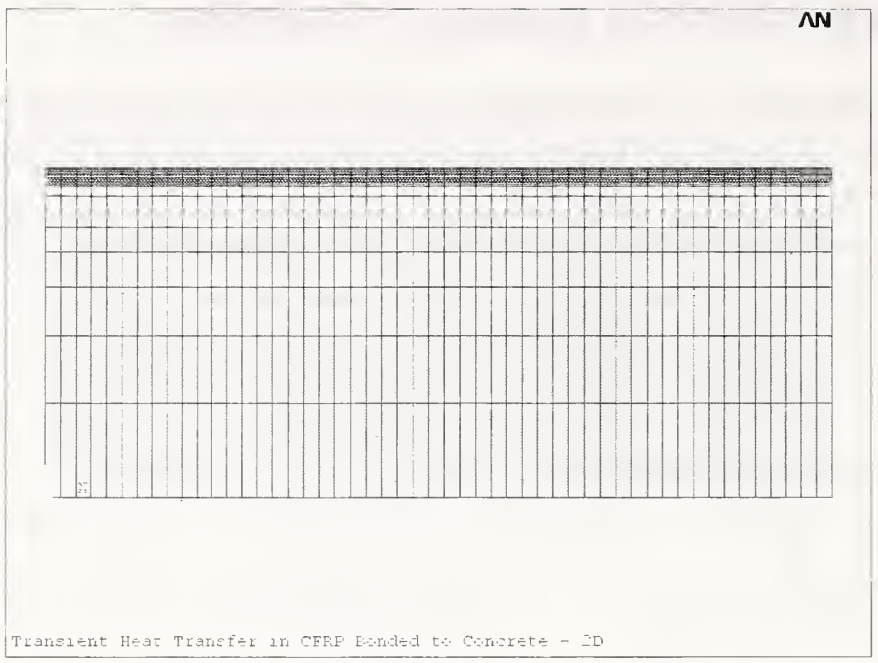

Fig. 4.7 Application of thermal load

The heat transfer coefficient h is defined as the following

$$h = \frac{k\,Nu}{L} \tag{4.2}$$

where,

Nu = Nusselt number;
k = thermal conductivity of the fluid; and,
L = length of the solid surface.

The Nusselt number is estimated using the expression for a horizontal wall with uniform heat flux applied to the top surface (Özişik, 1985)

$$Nu = 0.13(Gr\,Pr)^{1/3} \quad \text{for} \quad Gr\,Pr \leq 2x10^{8} \tag{4.3}$$

where,

Nu = Nusselt number,
Gr = Grashof number, and
Pr = Prandtl number.

The Nusselt number is a dimensionless value that represents the ratio of heat transfer by convection to that by conduction across a characteristic length

$$Nu = \frac{hL}{k} \tag{4.4}$$

where,

h = heat transfer coefficient;
L = length of the solid surface; and,
k = thermal conductivity of the fluid.

Similarly, the Grashof number represents the ratio of the buoyancy force to the viscous force acting on a fluid. Its value is defined as

$$Gr = \frac{g\beta(T_w - T_\infty)L^3}{\nu^2} \tag{4.5}$$

where,

g = acceleration due of gravity;
β = $1/T_f$, $T_f = (T_\infty + T_w)/2$;
T_∞ = ambient temperature;
T_w = temperature reached by the wall;
L = *length of the solid surface*, and,
ν = kinematic viscosity of air.

The Prandtl number is also a dimensionless parameter that represents the ratio of molecular diffusivity of momentum to molecular diffusivity due to heat. Values for Pr are usually tabulated for materials at specific temperatures (Özişik, 1985).

For this trial problem, T_∞ and T_w were specified as 296 K and 298 K, respectively. The Grashof number was computed as 9.67×10^5. The Prandtl number was 0.712. The average heat transfer coefficient was computed by combining equations 4.2 and 4.3, as expressed in equation 4.6

$$h = 0.13\frac{k}{L}(Gr\ Pr)^{1/3} \tag{4.6}$$

To investigate the effect of thermal cooling, the results of the analysis were presented in terms of thermal signal and thermal contrast. Thermal signal is defined as

$$\Delta T = T_{defect} - T_{backgr} \tag{4.7}$$

where,

T_{defect} = surface temperature above the internal flaw and
T_{backgr} = surface temperature in the background where no internal flaw is present.

The thermal contrast C is defined as

$$C = \frac{\Delta T}{\Delta T_{backgr}} \tag{4.8}$$

where,

ΔT = thermal signal; and
ΔT_{backgr} = surface temperature increase in the background or the difference between the background temperature and the initial temperature of the object.

The results indicated that free convection cooling produced a temperature difference of only 0.12 °C in the thermal signal, and 0.03 in the thermal contrast, with respect to the results of the same model without cooling. The small difference in results did not justify the high increment in

computation time for the more complex model. Therefore, free convection cooling was not considered in these parametric studies.

The thermal loading for the different analyses is indicated in Table 4.2. The information is tabulated in groups to better compare the results. Cases 1 through 4 had the same heat flux with varying pulse duration. On the other hand, cases 4 through 18 were grouped by a specific pulse duration with varying heat flux. Cases 1 through 4 included 2-D and 3-D analyses, while the rest of the cases involved only 2-D analyses.

Table 4.2 Description of thermal input for different analyses

Case No.	Pulse duration, τ (s)	Heat flux, q (W/m^2)
1	1	100 000
2	0.5	100 000
3	0.1	100 000
4	0.05	100 000
4	0.1	100 000
5	0.1	50 000
6	0.1	10 000
1	1	100 000
9	1	50 000
8	1	25 000
7	1	10 000
10	1	5000
11	2	25 000
12	2	20 000
13	2	10 000
14	2	5000
18	3	20 000
15	3	15 000
16	3	10 000
17	3	5000

The simulations involved transient analyses. ANSYS uses a time integration procedure to estimate the solution at discrete points in time (integration time steps, ITS). Selection of the appropriate time step is important to provide both accurate and stable results. For example, if the time step is too small, unstable oscillations may occur and result in thermal behavior that is physically incorrect. Large time steps, however, may not capture the temperature gradients adequately. To avoid problems with the integration time stepping, ANSYS suggests specifying a conservative initial time step and allow automatic time stepping to take place. In its automatic time stepping routine, ANSYS increases the time step as needed while checking for stability and convergence of the results at each time step.

For comparisons, all simulations used the same time step pattern (automatic stepping with same initial, maximum, and minimum time steps). The initial time step was estimated using the initial time step criterion (ANSYS Heat Transfer Manual, 2000), which is a function of the element size in the direction of the flow and the thermal diffusivity of the material

$$ITS = \frac{\Delta y^2}{4\alpha} \tag{4.9}$$

where,

ITS = recommended initial time step;
Δy = element size in the y-direction; and,
α = diffusivity of the material.

The Biot and Fourier numbers provide a rough estimate of the initial time step. The Biot number, Bi, expresses the ratio of convective and conductive thermal resistance (ANSYS Heat Transfer Manual, 2000)

$$Bi = \frac{h\Delta y}{k} \tag{4.10}$$

where,

h = heat transfer coefficient for convection losses;
Δy = mean element length in the direction of heat flow; and,
k = thermal conductivity of solid.

Likewise, the Fourier number, Fo, or dimensionless time, quantifies the relative rates of heat conduction and heat storage in the material (ANSYS Heat Transfer Manual, 2000)

$$Fo = \frac{k\Delta t}{\rho\, c\,(\Delta y)^2} \tag{4.11}$$

where,

k = thermal conductivity;
Δt = time step;
ρ = density of the material;
c = specific heat of the material; and,
Δy = mean element length in the direction of the heat flow.

As previously mentioned, convection cooling was not considered. Thus, the Biot number was zero. For the case $Bi<1$, a reasonable time step ,Δt, was estimated using the expression (ANSYS Heat Transfer Manual, 2000)

$$\Delta t = \varphi\frac{\rho c(\Delta y)^2}{k} \tag{4.12}$$

where,

φ = scaling factor with values ranging from $0.1 < \varphi < 0.5$.

Time steps are more or less conservative depending on the value of φ that is chosen.

Based on the properties of the composite layers and $\varphi = 0.25$, the estimated initial time step was 0.009 s. ANSYS requires that the minimum time step must be smaller than the initial time step. The selected minimum time step was 0.008 s. The maximum time step selected for the simulations was greater that the time step suggested by equation 4.12. The selected maximum time step for the simulations was 0.5 s. Automatic time stepping was carried out during the analysis. The simulation results were recorded at every time step.

4.3.4 Results

The simulations illustrated the dynamic thermal behavior of the test object due to the thermal impulse. Additionally, the 3-D model revealed the two-dimensional thermogram of the surface temperature. Surface temperature values were gathered at each node over the entire period of simulation.

Figure 4.8 shows the temperature distribution of the three-dimensional model for case number 1. The temperature values are in °C.

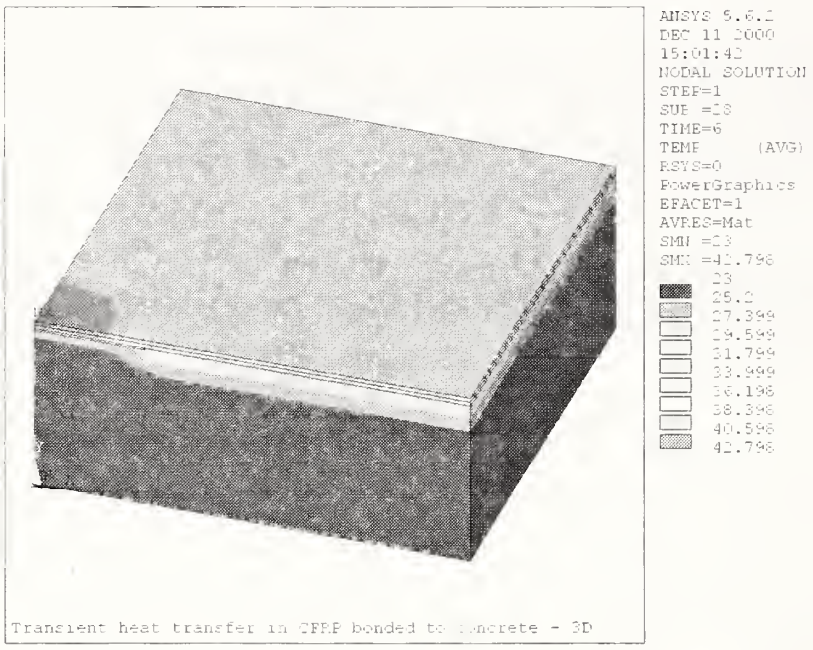

Fig. 4.8 Temperature distribution at 6 seconds (q = 100 000 W/m^2, $\tau = 0.5$ s)

As mentioned, two basic measurements are used to detect flaws: thermal signal and thermal contrast. Both the thermal signal and the thermal contrast were calculated for the entire duration of the test.

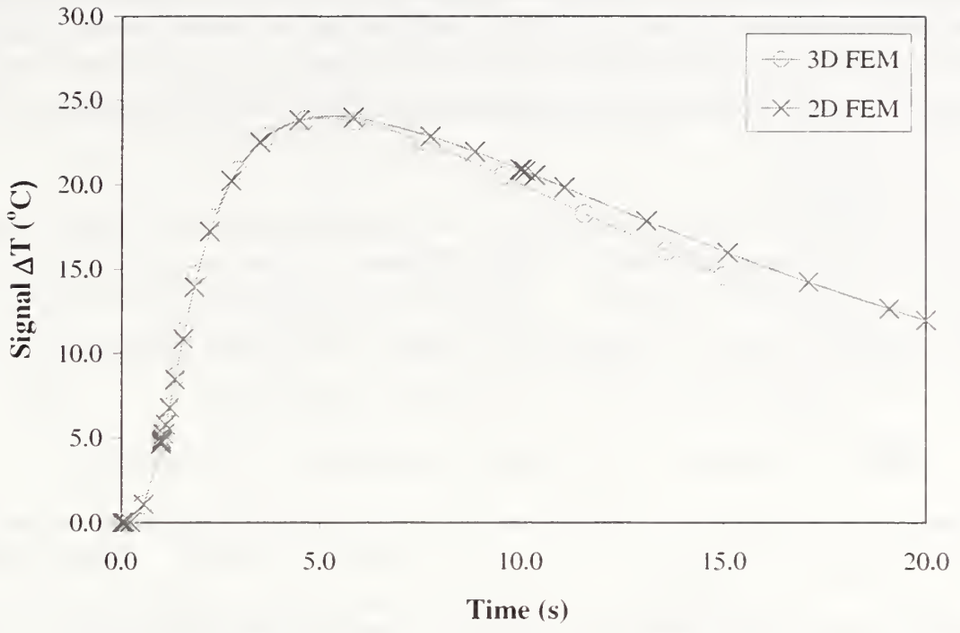

Fig. 4.9 Thermal signal for case 1 (q = 100 000 W/m^2, τ= 1 s)

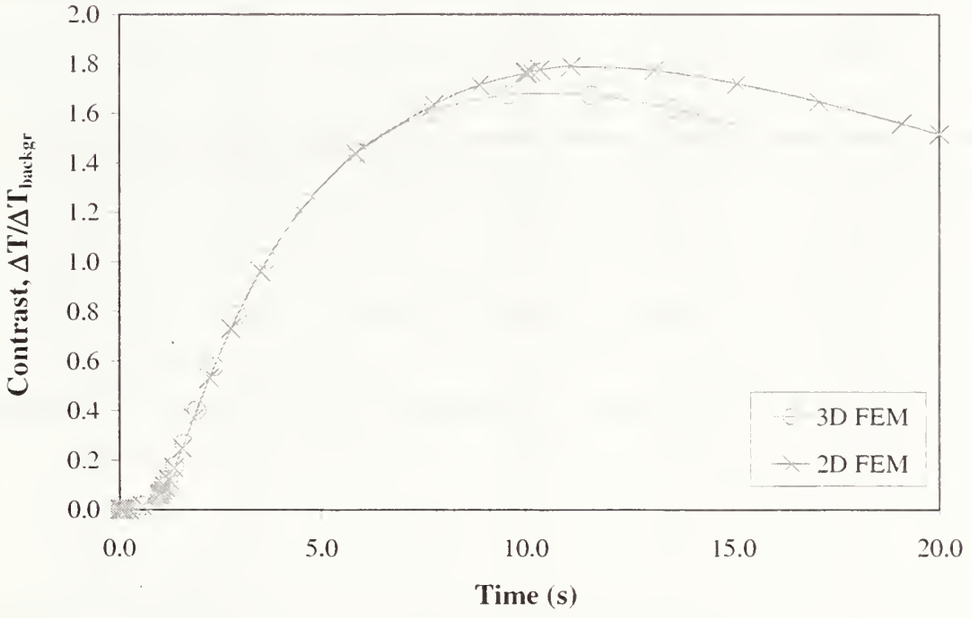

Fig. 4.10 Thermal contrast for case 1 (q = 100 000 W/m^2, τ= 1 s)

Cases 1 through 4 were analyzed using both two-dimensional and three-dimensional models. The results demonstrated that the value of the maximum signal differed slightly for the two models. Thermal contrast, however, differed to a greater degree. For example, for case number 1, the maximum thermal signal for the 2-D model was 24.4 °C and was reached at 5.24 s after the beginning of the simulation. Maximum thermal contrast occurred later than the maximum thermal signal. The maximum thermal contrast was observed 11 s after the start of the

simulation, and had a value of 1.83. The three-dimensional model provided similar results. For example, the maximum thermal signal of 23.8 °C was reached at 4.64 s after the beginning of the simulation. The maximum contrast occurred at 11.59 s and had a value of 1.67. Plots illustrating the development of thermal signal and thermal contrast behaviors are presented in Fig. 4.9 and 4.10.

The results indicated that the thermal signal for the three-dimensional model decayed slightly faster than for the two-dimensional model. This difference, however, occurred mostly after the maximum signal had been reached. Because three-dimensional models are more computationally intensive than two-dimensional models, the small difference in signal results justified the use of the simpler 2-D model for subsequent simulations.

Table 4.3 Results of simulations 1 through 18 (2-D models)

Case	τ (s)	q (W/m^2)	Energy ($q \cdot \tau$) (J/m^2)	T_{max} (°C)	Maximum Signal		Maximum Contrast	
					t_s (s)	ΔT_{max} (°C)	t_c (s)	$\Delta T_{max}/\Delta T_{backgr}$
1	1	100 000	100 000	114.25	5.24	24.41	11.24	1.83
2	0.5	100 000	50 000	84.85	5.17	12.24	10.67	1.83
4	0.1	100 000	10 000	50.18	5.23	2.46	10.73	1.83
3	0.05	100 000	5000	41.39	4.75	1.22	10.75	1.83
4	0.1	100 000	10 000	50.18	5.23	2.46	10.73	1.83
5	0.1	50 000	5000	36.59	5.23	1.23	10.73	1.83
6	0.1	10 000	1000	25.72	5.00	0.25	10.70	1.83
1	1	100 000	100 000	114.25	5.24	24.41	11.24	1.83
9	1	50 000	50 000	68.63	5.24	12.20	11.24	1.83
8	1	25 000	25 000	45.81	5.24	6.10	11.24	1.83
7	1	10 000	10 000	32.13	5.24	2.44	11.24	1.83
10	1	5000	5000	27.56	5.24	1.22	11.24	1.83
11	2	25 000	50 000	58.54	5.7	12.14	11.70	1.83
12	2	20 000	40 000	51.43	5.7	9.71	11.70	1.83
13	2	10 000	20 000	37.21	5.7	4.86	11.70	1.83
14	2	5000	10 000	30.11	5.7	2.43	11.70	1.83
18	3	20 000	60 000	60.83	6.41	14.49	11.91	1.83
15	3	15 000	45 000	51.37	6.41	10.86	11.91	1.83
16	3	10 000	30 000	41.91	6.41	7.24	11.91	1.83
17	3	5000	15 000	32.46	6.41	3.62	11.91	1.83

The results for cases 1 through 18 are presented in Table 4.3. Table 4.3 provides data regarding the pulse duration (τ), the input heat flux (q), input energy per unit area (product of q and τ),

maximum surface temperature (T_{max}), time and value of the maximum thermal signal, and time and value of maximum thermal contrast. The results are for two-dimensional models.

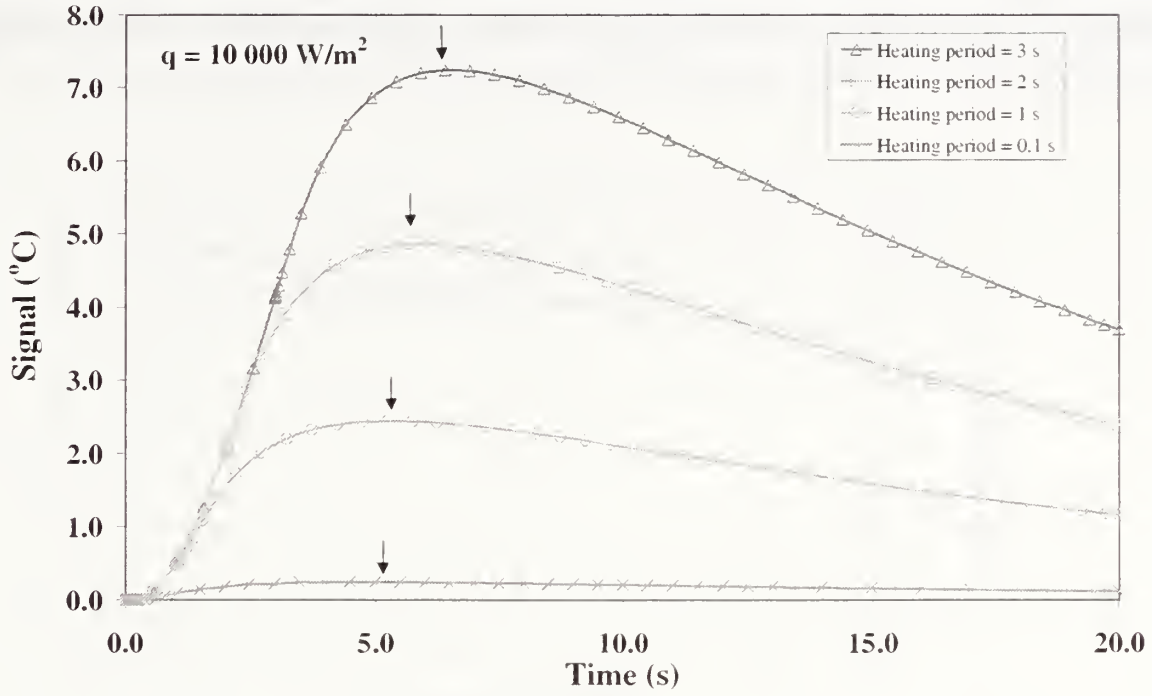

Fig. 4.11 Thermal signal for simulations with increasing pulse duration for q = 10 000 W/m^2

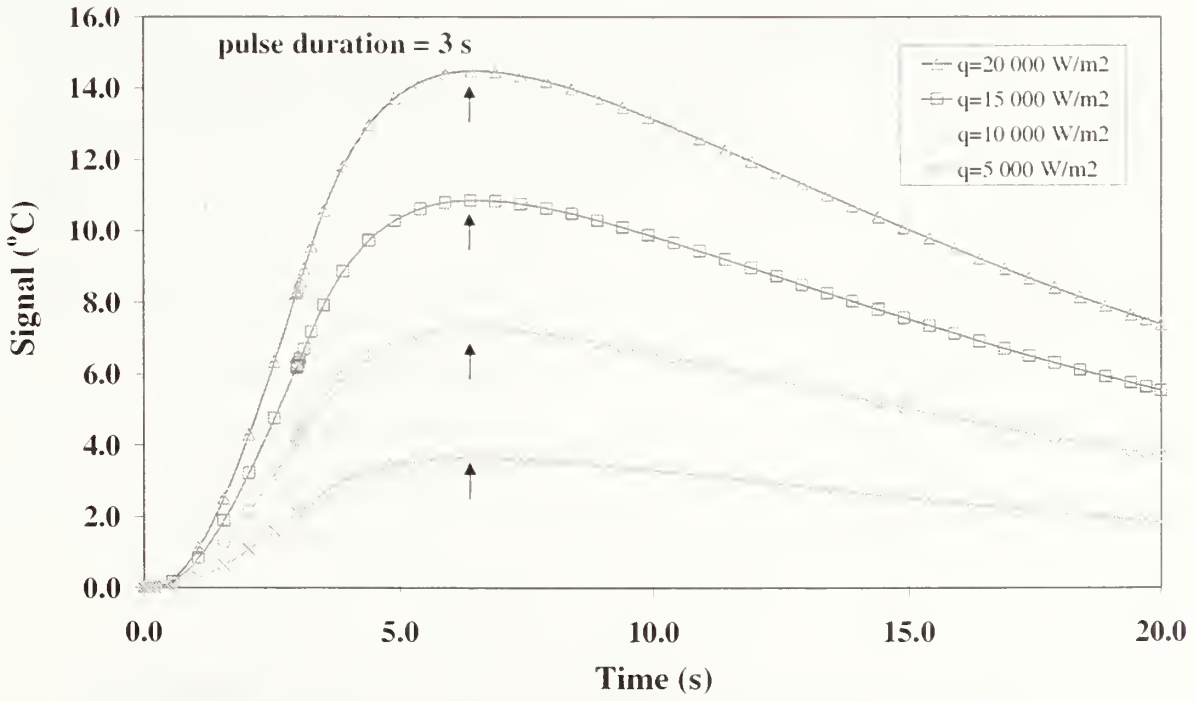

Fig. 4.12 Thermal signal for simulations with different heat flux input and same pulse duration τ = 3 s

A first look at the results indicated that for a given input thermal flux, the magnitude and time for maximum thermal signal increase with pulse duration (Fig. 4.11).

Comparison of the results for equal pulse duration shows that the time for maximum signal does not depend on the heat flux but depends on the heating period. As long as the pulse duration remained constant, the time for maximum signal did not change with added energy (Fig. 4.12). As expected, for a given pulse duration the maximum signal increases with increasing input heat flux (Fig. 4.12).

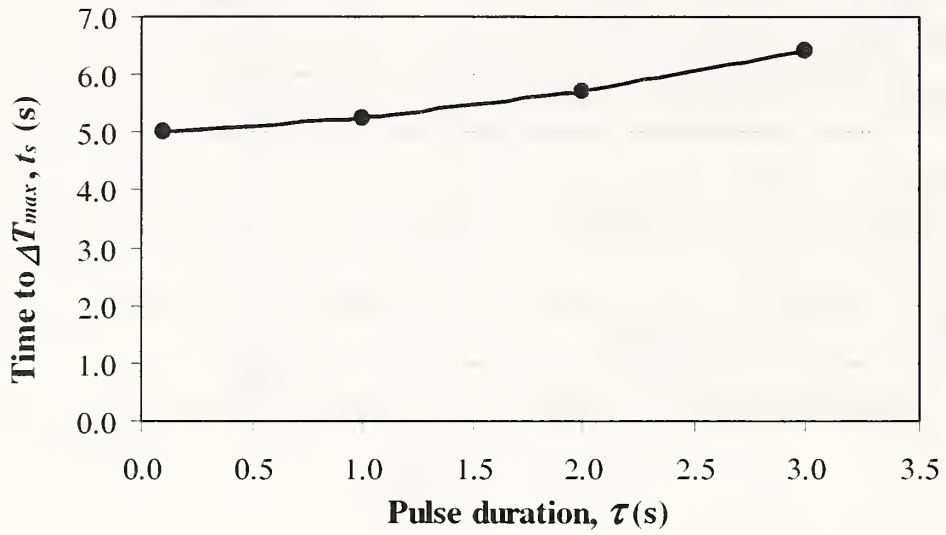

Fig. 4.13 Time for maximum signal as a function of pulse duration

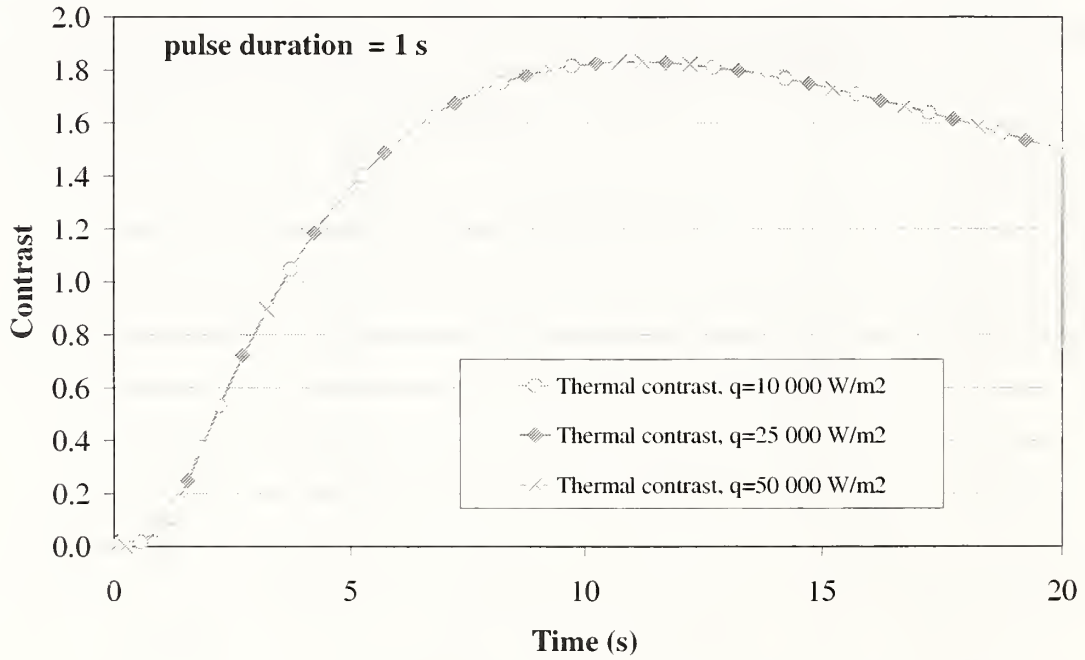

Fig. 4.14 Thermal contrast for cases 7, 8, and 9 with pulse duration of 1 s.

The time for maximum signal was found to increase in a nonlinear manner with increasing pulse duration, τ, as illustrated in Fig. 4.13. The variation in time for maximum signal, however, is only 1.4 s for heat pulse durations varying from 0.1 s to 3 s.

An additional observation is that the magnitude of the contrast is independent of the heat flux (Fig. 4.14). This behavior arises because of the normalized nature of the contrast variable and the fact that conduction is a linear problem. Thus, contrast is a function of the test object (e.g., material properties, flaw depth, thickness, etc.). This behavior may play an important role in solving the "inverse" problem, that is, determining flaw characteristics from measured thermal responses.

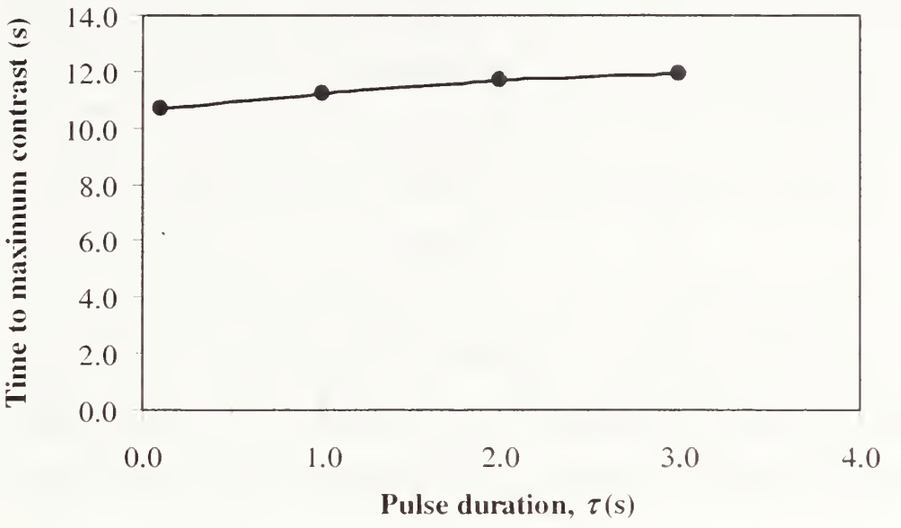

Fig. 4.15 Time for maximum contrast as a function of pulse duration

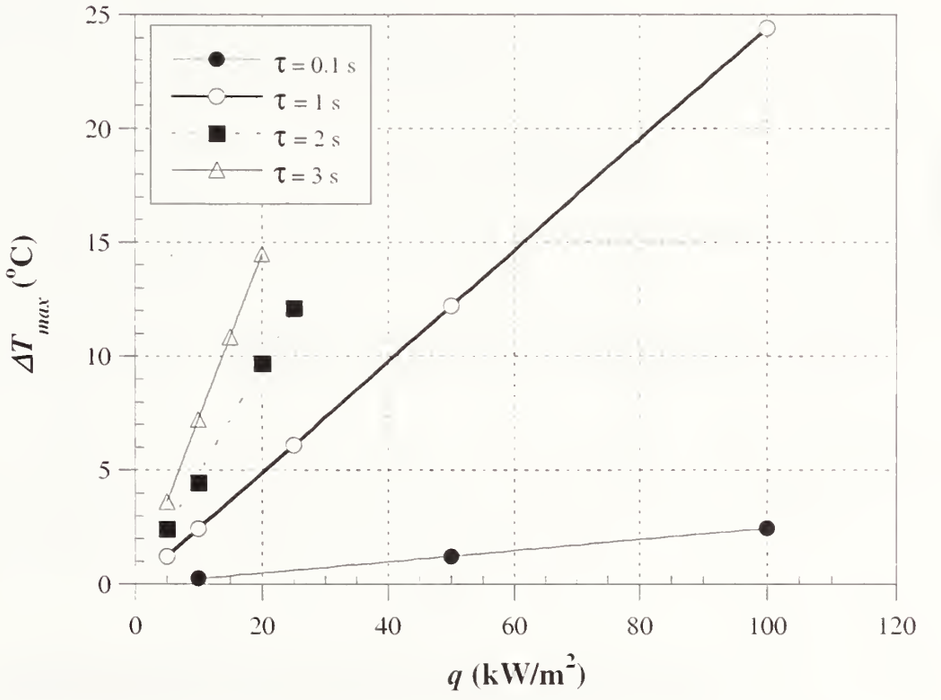

Fig. 4.16 Maximum signal as a function of thermal flux

The time for maximum contrast increases with the pulse duration. The rate of increase, however, decreases with longer heating periods as shown in Fig. 4.15. For a variation in pulse duration of 0.1 s to 3 s the time for maximum contrast only varied from 10.7 s to 11.9 s.

Table 4.4 Increase in maximum thermal signal as a function of heat flux for different pulse durations

Pulse duration, τ (s)	**Rate of increase, θ (°C/(W/m^2))**	**Equation**
0.1	0.000025	$\Delta T_{max} = 0.00002\ q$
1.0	0.000244	$\Delta T_{max} = 0.0002\ q$
2.0	0.000482	$\Delta T_{max} = 0.0005\ q$
3.0	0.000724	$\Delta T_{max} = 0.0007\ q$

Further comparisons indicated that for a given pulse duration, the maximum thermal signal increases linearly with heat flux, that is, $\Delta T_{max} = \theta \cdot q$ (Fig. 4.16). As an example, for a heating period of 2 seconds, the maximum thermal signal increases at a rate of 0.0005 °C/(W/m^2). The rate at which ΔT increases with q, increases with the pulse duration as indicated in Table 4.4.

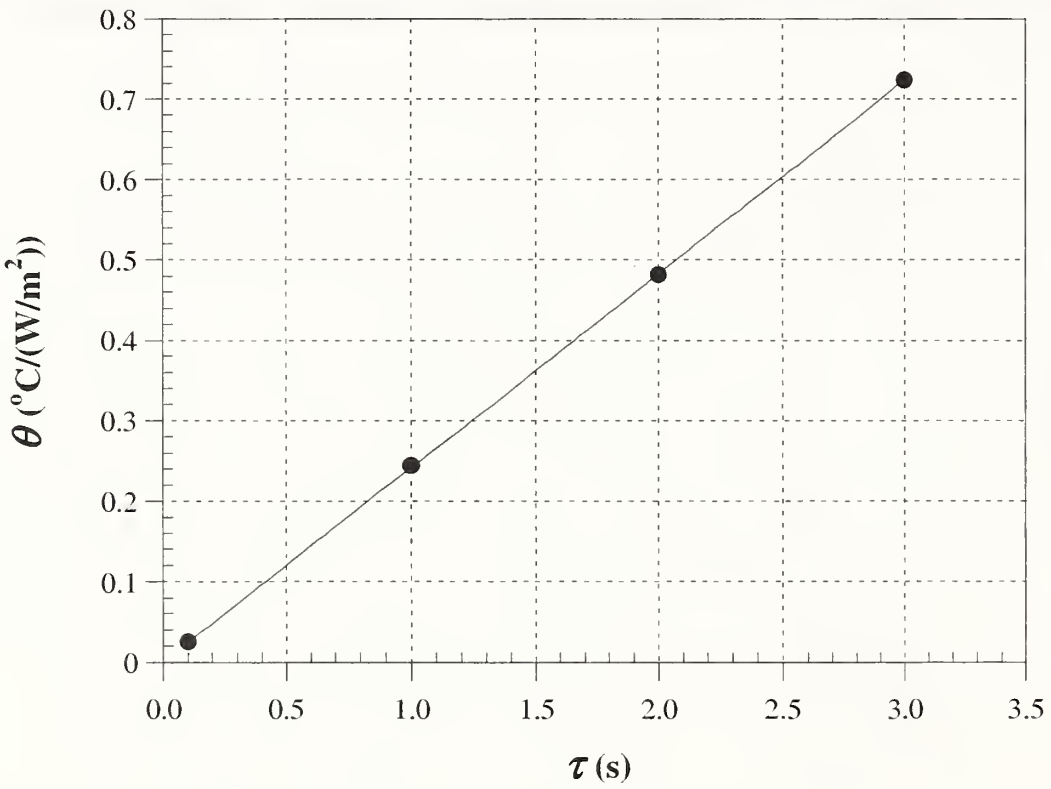

Fig. 4.17 Variation of the slope, θ, as a function of pulse duration

Figure 4.17 shows the variation of the slopes in Fig. 4.16 as a function of pulse duration. It is seen that the slopes are a linear function of pulse duration.

The straight-line relationship is $\theta = 0.00024 \cdot \tau$. Thus, the value of the maximum thermal signal is

$$\Delta T_{max} = 0.00024\,\tau\,q \tag{4.13}$$

This equation can be rewritten to express the input heat flux required to produce a desired maximum thermal signal as a function of the pulse duration

$$q = \frac{\Delta T_{max}}{0.00024\,\tau} \tag{4.14}$$

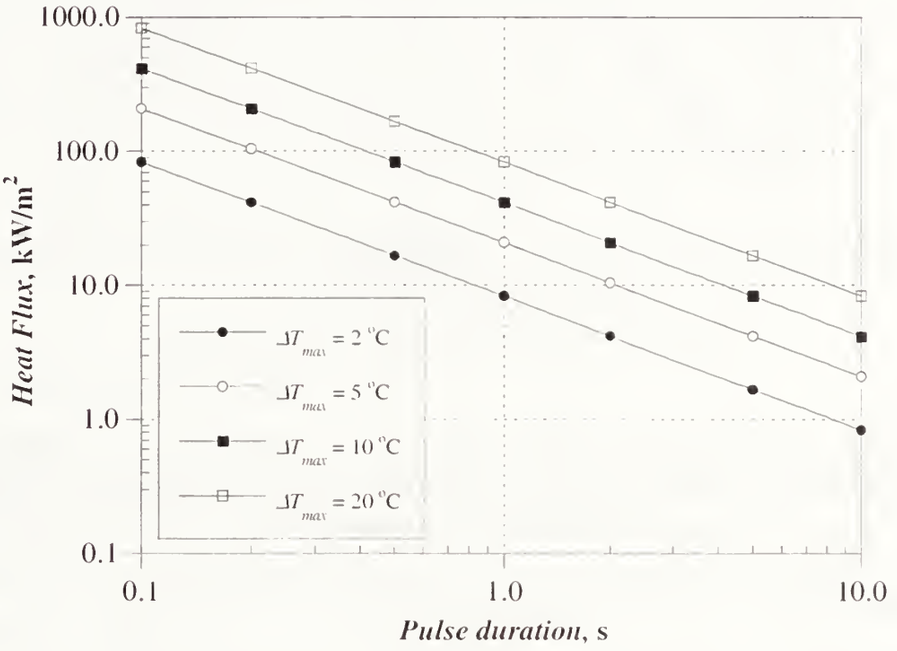

Fig. 4.18 Heat flux versus pulse duration for different maximum thermal signal

Equation 4.14 represents a family of curves corresponding to combinations of q and τ to produce a given ΔT_{max}. Figure 4.18 shows these curves when plotted using log scales.

Examination of Eq. 4.13 shows that there is an elegantly simple relationship between the maximum thermal signal and the thermal input. The product $\tau \cdot q$ is the area beneath the heating pulse and represents the input energy per unit area, that is,

$$E(J/m^2) = q(W/m^2) \cdot \tau(s) \tag{4.15}$$

Thus, the maximum signal is a linear function of the input energy

$$\Delta T_{max} = 0.00024E \tag{4.16}$$

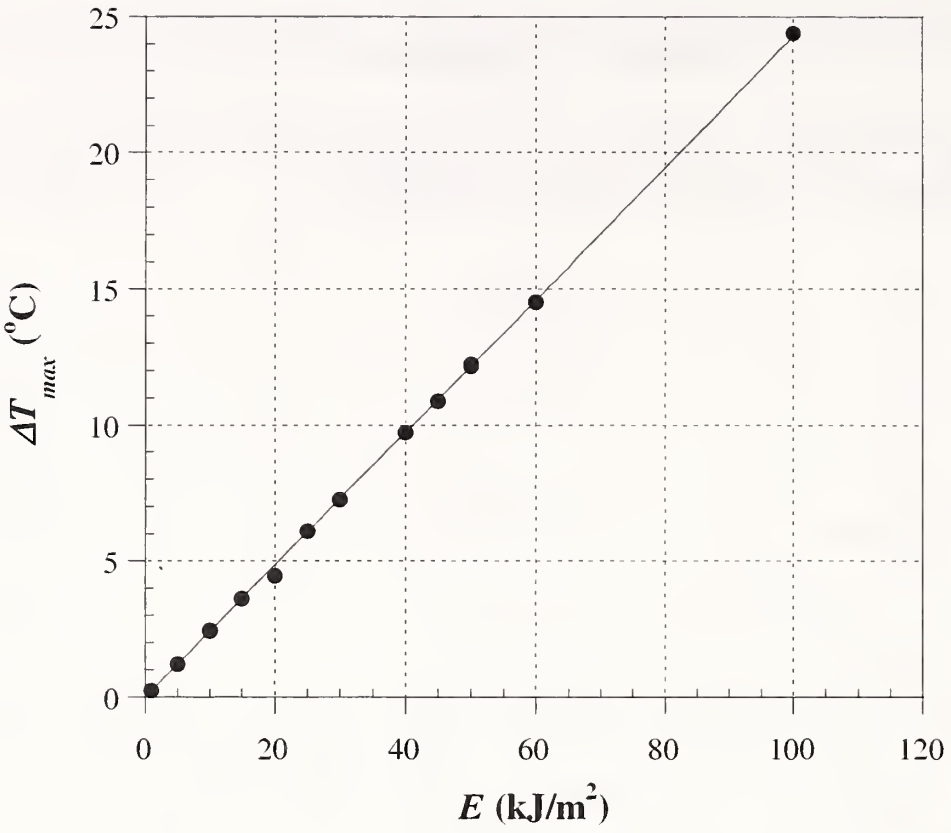

Fig. 4.19 Maximum signal versus energy

Figure 4.19 is a plot of the maximum signal versus energy values given in Table 4.3. The linear relationship is confirmed. This provides a powerful tool for selecting the thermal input to achieve a desired signal. Infinite combinations of input flux and pulse duration will result in the same maximum signal (Fig. 4.18). The only differences will be the time when the maximum signal is obtained and the maximum surface temperature that is attained.

The maximum surface temperature reached during thermographic testing is an important consideration for the successful application of this technique to FRP composites. The reason for the need to estimate the maximum temperature is the low glass transition temperature of these materials. When the temperature of the resin of the composite increases above the glass transition temperature, T_g, the mechanical properties of the matrix are degraded. Glass transition temperatures for CFRP used in civil engineering applications are on the order of 53 °C (Christensen et al., 1996).

Further analysis of the results in Table 4.3 indicated that, for a given pulse duration, the maximum surface temperature increases linearly with the heat flux. Thus, the maximum surface temperature is described by

$$T_{max} = 23 + \gamma(\tau)\, q \tag{4.17}$$

where,

$\gamma(\tau)$ = slope of the line for a given pulse duration.

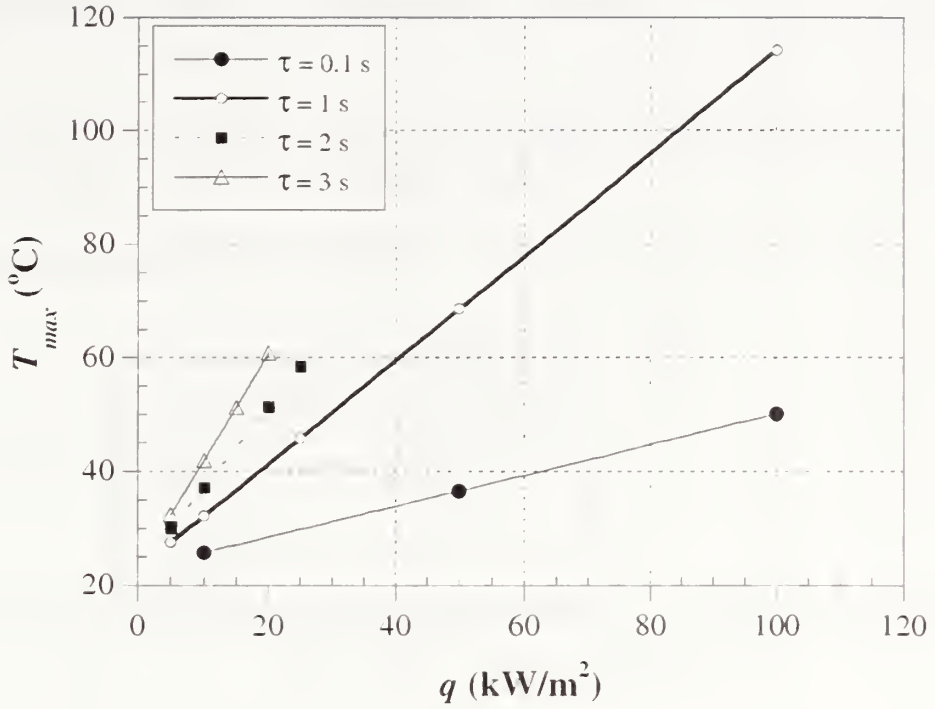

Fig. 4.20 Maximum surface temperature as a function of heat flux for different pulse durations

The linear behavior is illustrated in Fig. 4.20.

Table 4.5 Maximum surface temperature as a function of input heat flux for different pulse durations

Pulse duration, τ (s)	**Rate of increase, γ (°C/(W/m^2))**	**Equation $T_{max} = \gamma q + 23$**
0.1	0.0003	$T_{max} = 0.00027\ q + 23$
1.0	0.0009	$T_{max} = 0.00091\ q + 23$
2.0	0.0014	$T_{max} = 0.00142\ q + 23$
3.0	0.0019	$T_{max} = 0.00189\ q + 23$

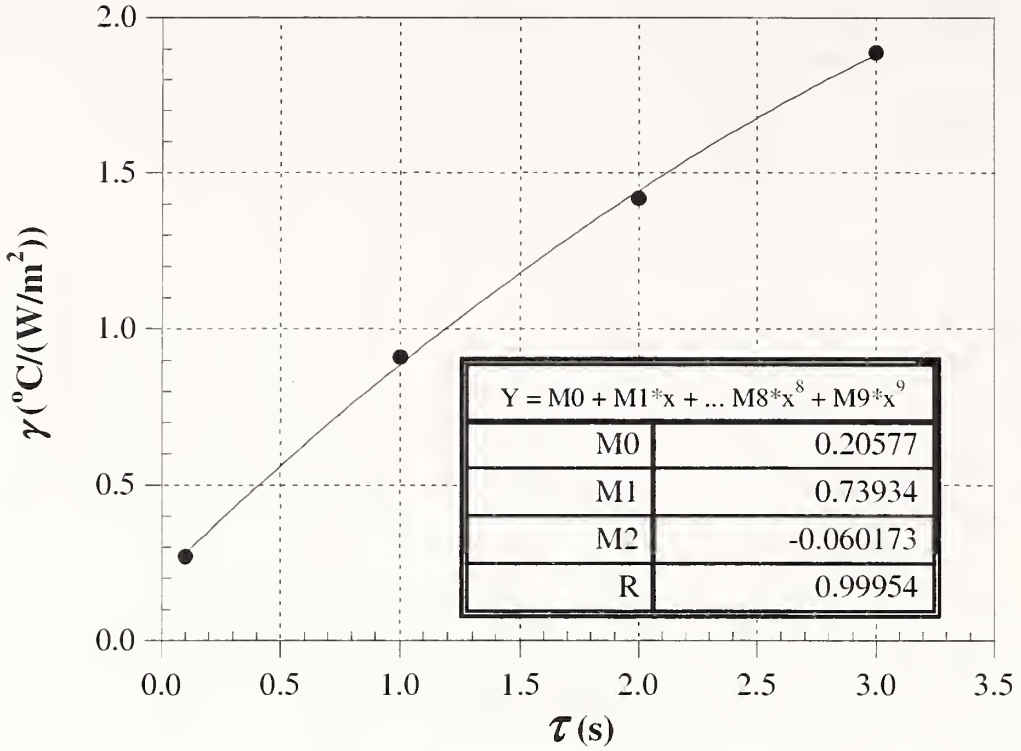

Fig. 4.21 γ as a function of pulse duration

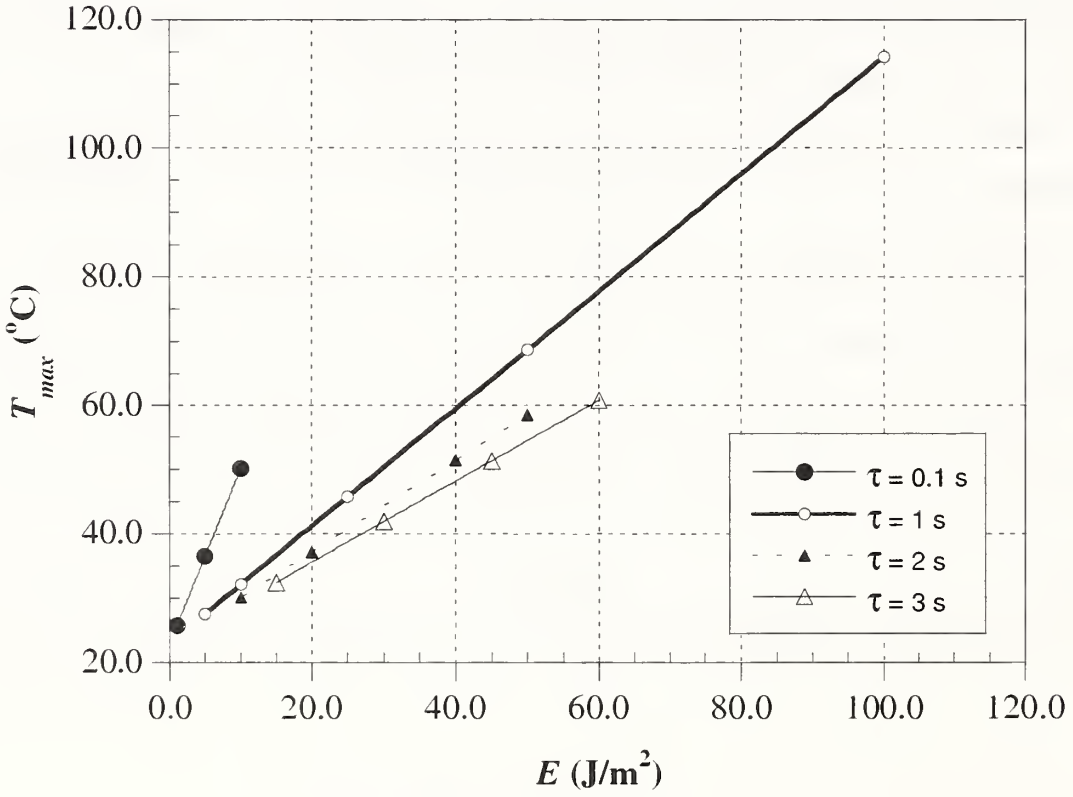

Fig. 4.22 Maximum surface temperature versus input energy

Table 4.5 lists the slopes (γ) of the lines in Fig. 4.20, and it is seen that the slopes increase with pulse duration. Figure 4.21 shows the values of γ as a function of pulse duration. It is clear that

the relationship between γ and τ is not linear. A quadratic function provided a good fit to the points in Fig. 4.21.

The maximum surface temperature attained for a given pulse duration was found to be a linear function of input energy. This is illustrated in Fig. 4.22.

Thus, the relationship between T_{max} and E is

$$T_{max} = \delta(\tau) E + 23 \tag{4.18}$$

where,

$\delta(\tau)$ = slope of the line for a given pulse duration.

Table 4.6 Maximum surface temperature as a function of input energy for different pulse durations

Pulse duration, τ (s)	**Rate of increase, δ (°C/(J/m^2))**	**Equation $T_{max} = \delta E + 23$**
0.1	0.0003	$T_{max} = 0.0027\ E + 23$
1.0	0.0009	$T_{max} = 0.00091\ E + 23$
2.0	0.0014	$T_{max} = 0.00071\ E + 23$
3.0	0.0019	$T_{max} = 0.00063\ E + 23$

Table 4.6 shows the value of δ for different pulse durations and these are plotted in Fig. 4.23. These results show that the value of δ is a highly nonlinear function of pulse duration. For short duration pulses, δ is large and surface temperature is more sensitive to the input energy than for longer duration pulses.

An approximate functional relationship for $\delta(\tau)$ was established as follows:

1. Assume that the relationship for $\gamma(\tau)$ is a quadratic function (see Fig. 4.21)

$$\gamma(\tau) = a + b\,\tau + c\,\tau^2 \tag{4.19}$$

2. Substitute into Eq. 4.17

$$T_{max} = \left(a + b\,\tau + c\,\tau^2\right) q + 23 \tag{4.20}$$

3. Use the definition E= τ·q

$$T_{max} = E\left(\frac{a}{\tau} + b + c\,\tau\right) q + 23 \tag{4.21}$$

4. Therefore,

$$\delta(\tau) = \frac{a}{\tau} + b + c\,\tau \tag{4.22}$$

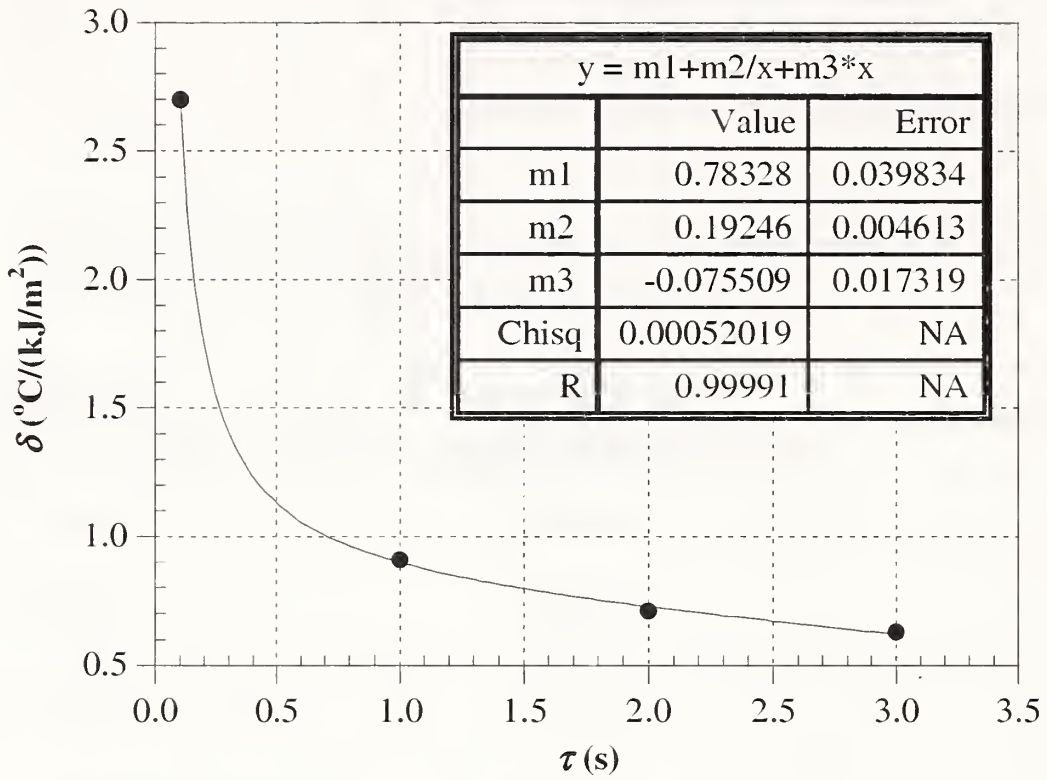

Fig. 4.23 Values of δ as a function of pulse duration

A least-squares fit of Eq. 4.22 to the points in Fig. 4.23 resulted in the following values for the constants a, b, and c:

$$a = 0.793 \quad (0.040)$$

$$b = 0.192 \quad (0.005)$$

$$c = -0.076 \quad (0.017)$$

where the numbers in parentheses are the standard errors of the coefficients.

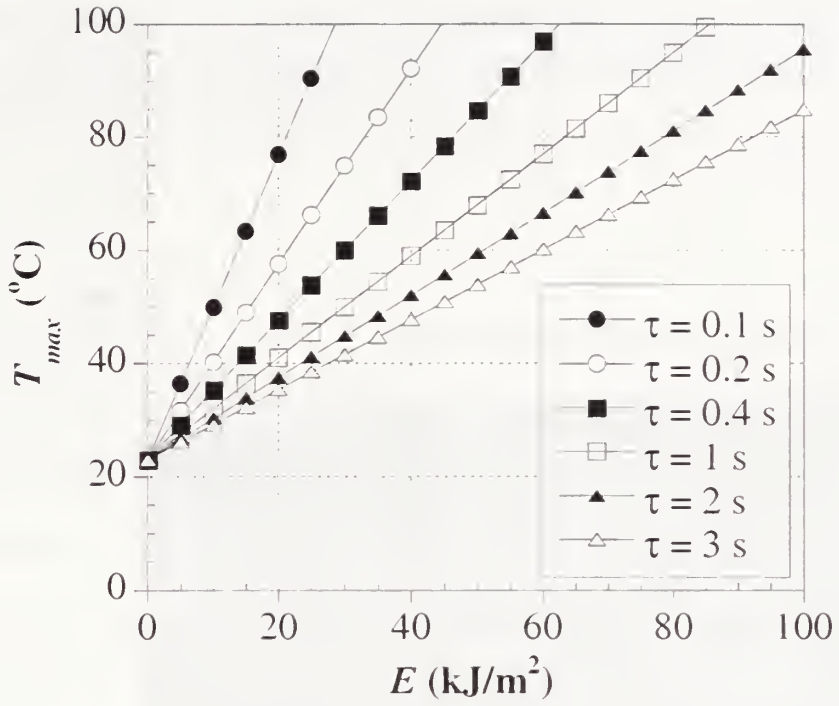

Fig. 4.24 Estimation of the maximum surface temperature as a function of the input energy for different pulse durations

Fig. 4.25 Illustration of thermal diffusion at time of maximum temperature for case 4 ($\tau = 0.1$ s, $q = 100{,}000$ W/m^2)

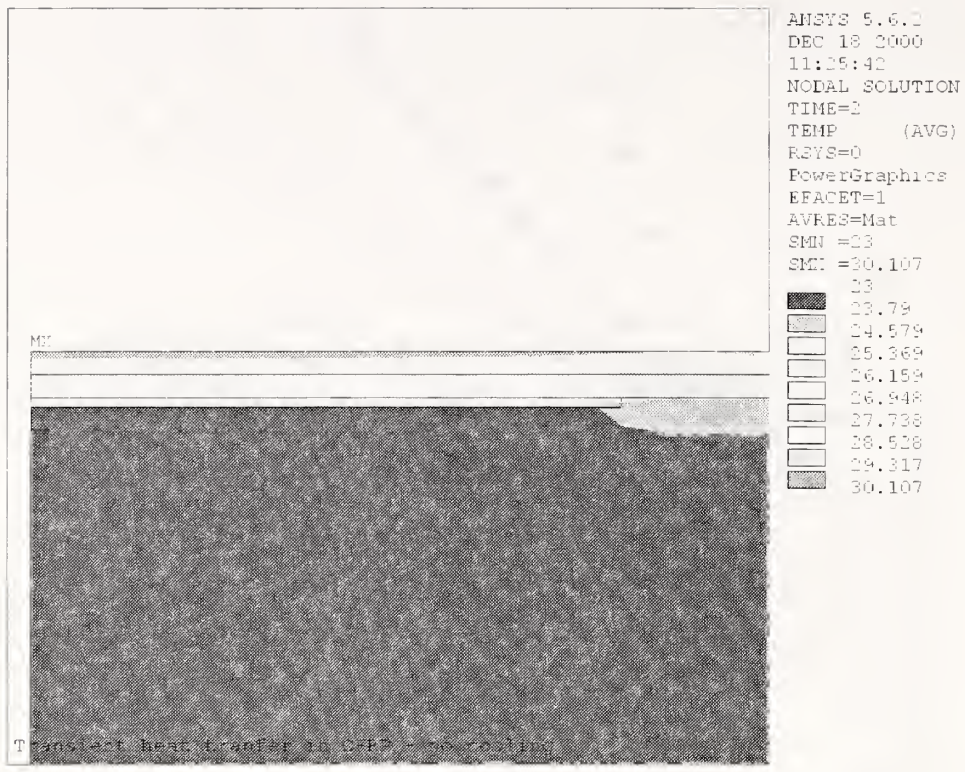

Fig. 4.26 Illustration of thermal diffusion at time of maximum temperature for case 14 ($\tau = 2$, q = 5,000 W/m^2)

Figure 4.23 shows that the function given by Eq. 4.22 provides a good fit to the results. It is now possible to estimate the relationships between T_{max} and E for any value of τ from 0.1 s to 3 s. Examples are show in Fig. 4.24.

Figures 4.22 or 4.24 show that for a given input energy the maximum surface temperature increases with decreasing pulse duration. This behavior is explained as follows. For equal input energy, a short pulse duration requires a large input heat flux, q. Since it takes time for the input energy to diffuse into the object, the higher the input flux the higher will be the surface temperature rise. This effect is illustrated in Figs. 4.25 and 4.26, which show temperature distributions at the time of maximum surface temperature for E values of 10 000 J/m^2 and pulse durations of 0.1 s and 2 s, respectively. For the short pulse, the maximum surface temperature is 50.2 °C, and for the longer pulse it is 30.1 °C.

The results of this parametric study have provided valuable insight into the interaction between thermal input and a given defect. The key to successful flaw detection using infrared thermography is to have a sufficiently large surface temperature gradient. For a given flaw geometry, Fig. 4.19 shows that the maximum surface temperature difference (signal) is a linear function of the input energy (expressed in J/m^2). Thus, a maximum value of input energy can be established for a given minimum signal. The selection of the pulse duration to produce the minimum input energy is governed by the maximum surface temperature that can be tolerated. For example, suppose we desire a thermal signal of ΔT_{max} = 10 °C. According to Fig. 4.19, the required input energy is about 40 kJ/m^2. Suppose it is desired to limit the surface temperature to 50 °C. Assuming that the initial temperature is 23 °C, Fig. 4.24 shows that the pulse duration should not be less than 2 s. The required input heat flux will be lower for a longer pulse duration. For a pulse duration of 2 s the required input flux is 20 kW/m^2, and for a 3 s duration it

is 13.3 kW/m^2. Of course, these relationships are applicable to the specific object that was used in these simulations. One of the objectives of subsequent simulations is to examine how these relationships are affected by changes in the test object.

4.3.5 Summary

The first parametric study addressed several issues regarding the effect of thermal input. The focus of the initial investigation was to

- understand diffusion behavior due to different heating and heat flux inputs,
- find appropriate thermal inputs for typical FRP composites bonded to concrete.

The test object presented a debond at the FRP/concrete interface and 2-D models were used to reduce computational efforts. Several conclusions were reached after analyzing the results due to varying thermal stimuli:

- For a given heating time (pulse duration), time for maximum signal is independent of the applied heat flux.
- Time for maximum signal increases nonlinearly with increasing pulse duration. The rate at which the time for maximum signal increases, rises with pulse duration.
- The time for maximum contrast increases with increasing pulse duration; however, the rate of increase decreases with τ.
- The magnitude of the thermal signal increases linearly with input energy (product of input heat flux and pulse length).
- The thermal contrast is independent of heat flux and pulse duration.
- For a given pulse duration, maximum surface temperature increases linearly with heat flux. The rate of increase rises with pulse duration, since more energy is applied to the specimen.
- For a given pulse duration, maximum surface temperature increases linearly with input energy. The rate of increase, however, decreases non-linearly with longer heating periods.

These results have led to a simple approach for selecting the thermal input so as to obtain a desired thermal signal while limiting the surface temperature due to heating. The next series of studies will examine the effects of thermal properties and geometry on the thermal response.

4.4 Parametric Study No. 2: Effect of Thermal Material Properties

Because it is expected that the thermal properties of installed FRP laminates may differ from nominal values, it is important to understand how thermal response is affected by thermal

properties. Hence, the second parametric study involved the evaluation of the effect of thermal material properties of FRP and concrete on the thermal response. The study had two objectives:

- Gain an understanding of thermal diffusion behavior due to different values of thermal conductivity and specific heat; and,

- Establish if accurate determination of material thermal properties is required for quantitative IR thermography of FRP laminates applied to concrete.

The parametric study focused on the analysis of the transient heat transfer behavior of CFRP bonded to concrete. Five different sets of analyses were performed involving a total of 28 finite element simulations. The first two sets of analyses involved changing thermal properties in the CFRP laminates. The next two sets of analyses corresponded to simulations in which the material properties of the concrete substrate varied. The final set of simulations involved different combinations of thermal conductivity and specific heat of FRP and concrete.

4.4.1 Geometry of Model

The geometry of the models was the same as in parametric study #1. The model consisted of a 10 cm long by 2 cm high concrete substrate covered with two layers of carbon FRP (Fig. 4.2). Each layer of CFRP was 0.5 mm thick. The bonded FRP contained a flaw (debond) at the interface with the concrete substrate. The debond had a length of 2.5 cm and a thickness of 0.1 mm, which corresponded to a thermal contact resistance of 4.17×10^{-3} m^2·K/W. As before, the interface flaw was located at the center of the analytical model. Plane two-dimensional modeling was used.

4.4.2 Material Properties

The variables in this parametric study were the thermal properties of the different constituents of the test object. The CFRP layer in direct contact with the concrete had the fibers running in the x-direction, while the external CFRP layer had the fibers running in the z-direction. Two material properties were varied: thermal conductivity and specific heat.

Table 4.7 Material properties of concrete and CFRP for "control" case.

Case	Material	ρ (kg/m^3)	c (J/(kg·°C))	$k_{parallel\ to\ fiber}$ (W/(m·°C))	$k_{perpendicular\ to\ fiber}$ (W/(m·°C))
19	Concrete	2400	800	1.5	1.5
	CFRP	1600	1200	7.0	0.8

Table 4.8 Material properties to investigate effects of thermal conductivity and specific heat of CFRP.

Case	Material	ρ (kg/m^3)	c (J/(kg·°C))	$k_{parallel}$ (W/(m·°C))	$k_{perpendicular}$ (W/(m·°C))	% change
20	CFRP	1600	1200	8.8	1.0	25
21	CFRP	1600	1200	10.5	1.2	50
22	CFRP	1600	1200	12.25	1.4	75
23	CFRP	1600	1200	14.0	1.6	100
24	CFRP	1600	1200	15.75	1.8	125
25	CFRP	1600	1200	17.5	2.0	150
26	CFRP	1600	1200	21	2.4	200
27	CFRP	1600	1020	7	0.8	-15
28	CFRP	1600	1080	7	0.8	-10
29	CFRP	1600	1140	7	0.8	-5

Table 4.9 Material properties to investigate effects of thermal conductivity and specific heat of concrete.

Case	Material	ρ (kg/m^3)	c (J/(kg·°C))	k (W/(m·°C))	% change
30	Concrete	2400	800	1.4	-5
31	Concrete	2400	800	1.6	10
32	Concrete	2400	800	1.8	20
33	Concrete	2400	880	1.5	10
34	Concrete	2400	960	1.5	20
35	Concrete	2400	1040	1.5	30

In general, the density and mechanical properties of most materials are well documented and provided by most manufacturers. The thermal properties of FRP composites, however, are usually not reported by the manufacturers. Thus, it is vital to determine how changes in thermal properties would affect the thermal diffusion behavior. The material properties are presented in Tables 4.7, 4.8, and 4.9. Case 19 incorporated the material properties of a "control" test object used for comparison purposes. Table 4.8 summarizes the material properties for the simulations in which the thermal conductivity (cases 19 through 26) and the specific heat (cases 19, 27, 28, and 29) of FRP were varied. It is important to note that thermal conductivity was varied in the direction parallel to the fiber as well as perpendicular to the fiber. Likewise, Table 4.9

summarizes the material properties for the models in which the thermal conductivity (cases 19, 30, 31, and 32) and the specific heat (cases 19, 33, 34, 35) of the concrete substrate were varied. The range of values for the thermal properties of CFRP and concrete were selected from available literature (ASHRAE Handbook; Maldague, 1993) and electronic databases (MatWeb Materials Property Database).

Table 4.10 Material properties for simulations 36 through 43

Combination	Case	k_{FRP} (W/(m·°C))		$k_{concrete}$ (W/(m·°C))	c_{FRP} (J/(kg·°C))	$c_{concrete}$ (J/(kg·°C))
		parallel	perpendicular			
low k_{FRP}-low k_{conc}	36	7	0.8	1.425	1200	800
low k_{FRP}-high	37	7	0.8	1.8	1200	800
high k_{FRP}-low	38	15.75	1.8	1.425	1200	800
high k_{FRP}-high	39	15.75	1.8	1.8	1200	800
low c_{FRP}-low c_{conc}	40	7	0.8	1.5	1020	800
low c_{FRP}-high	41	7	0.8	1.5	1020	1040
high c_{FRP}-low	42	7	0.8	1.5	1200	800
high c_{FRP}-high	43	7	0.8	1.5	1200	1040

Eight additional analyses were performed to explore the interaction of the material properties of FRP and concrete. The combinations of properties were based on a full factorial design with 3 factors and 2 levels per factor. Thus eight combinations of properties were used as shown in Table 4.10.

4.4.3 Thermal Loading, Boundary Conditions, and Time Stepping

The analysis was defined as a transient heat transfer problem. A square pulse of intensity 20,000 W/m^2 was applied at the top surface of the model. The duration of the pulse flux was 2 s. Adiabatic conditions ($dT/dx = 0$ and $dT/dy = 0$) were assumed for the additional surfaces. The initial temperature of the model and the ambient temperature was set to 23 °C.

The same time stepping was used for all the simulations. The initial time step was 0.009 seconds. The automatic time stepping capability of ANSYS was used with minimum and maximum time steps of 0.008 s and 0.1 s, respectively. A sensitivity analysis was performed to determine an appropriate maximum time step for this particular study. The first set of analyses (those involving changing thermal conductivity of the CFRP) were performed using three different maximum time steps, 0.009 s, 0.1 s, and 0.5 s. The maximum time step of 0.5 s was found to be too large to fully capture the thermal evolutions of these particular sets of simulations. Maximum time steps of 0.009 s and 0.1 s successfully captured the thermal behavior of the models. A maximum time of step of 0.1 s was selected as a balance between computational economy and accuracy.

The simulation output (nodal temperatures) was recorded at every time step.

4.4.4 Results

4.4.4a Effect of Thermal Conductivity of FRP

The finite element simulations illustrated the thermal behavior of the test object due to different material properties of the FRP composite laminates and the concrete substrate.

As previously mentioned, the first set of analyses examined the effects of changing the thermal conductivity of the CFRP, which was increased up to three times that in the "control" test object. The results indicated that changes in the thermal conductivity of the composite layers produce nonlinear changes in the thermal response of the test object. The parameters used to characterize the thermal response are:

- The maximum surface temperature, T_{max},
- The maximum difference in surface temperature, or the signal, ΔT_{max},
- The time when the maximum signal occurs, t_s,
- The maximum contrast, $\Delta T_{max}/\Delta T_{backgr}$, and
- The time for maximum contrast, t_c.

Table 4.11 Results for simulations involving changes in the thermal conductivity of CFRP.

Case	$k_{perpendicular\ to\ fiber}$ (W/(m·K))	T_{max} (°C)	Maximum Signal		Maximum Contrast	
			t_s (s)	ΔT_{max} (°C)	t_c (s)	$\Delta T_{max}/\Delta T_{backgr}$
19	0.8	51.6	5.75	9.92	11.25	1.86
20	1.0	49.9	5.24	10.09	10.14	1.84
21	1.2	48.7	4.94	10.18	9.34	1.82
22	1.4	47.8	4.64	10.24	8.74	1.79
23	1.6	47.2	4.36	10.27	8.24	1.76
24	1.8	46.7	4.23	10.28	7.83	1.73
25	2.0	46.3	4.13	10.27	7.43	1.70
26	2.4	45.6	3.83	10.24	6.83	1.65

A summary of the results for the first set of analyses is presented in Table 4.11.

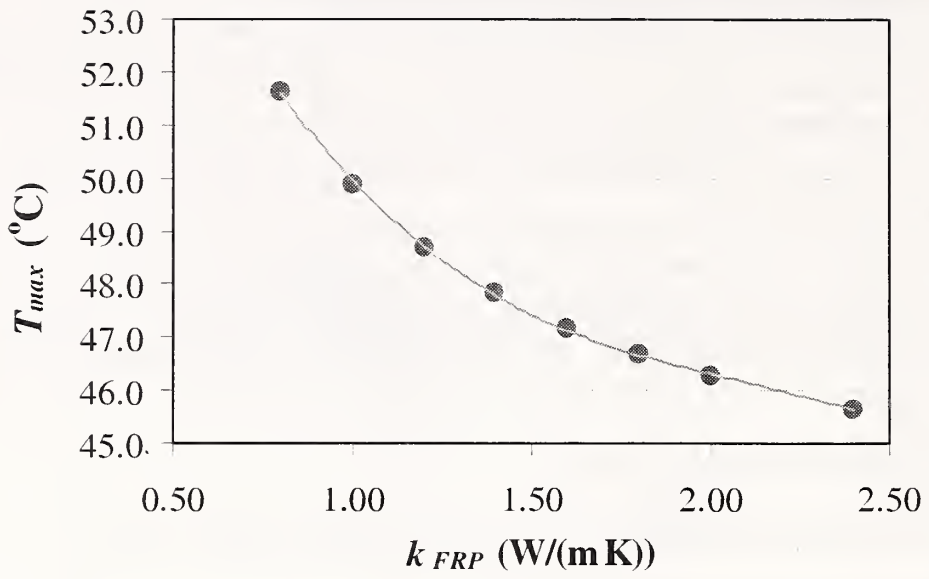

Fig. 4.27 Effect of thermal conductivity of CFRP on maximum surface temperature.

The results in Table 4.11 illustrate some interesting points regarding the effects of thermal conductivity of the FRP composite on the thermal evolutions. For example, as shown in Fig. 4.27, the maximum surface temperature decreases nonlinearly with increasing thermal conductivity of the FRP layers. As would be expected, the input thermal energy is transferred to the interior of the test object at a faster rate as the thermal conductivity increases and maximum surface temperature decreases.

In these analyses, the thermal conductivity of the FRP was increased by a factor of 3 but the maximum temperature decreased only 6 °C. Thus because of the limited thickness of the FRP; the maximum surface temperature does appear to be very sensitive to the conductivity of the FRP laminate for the case of a debond below two layers of FRP.

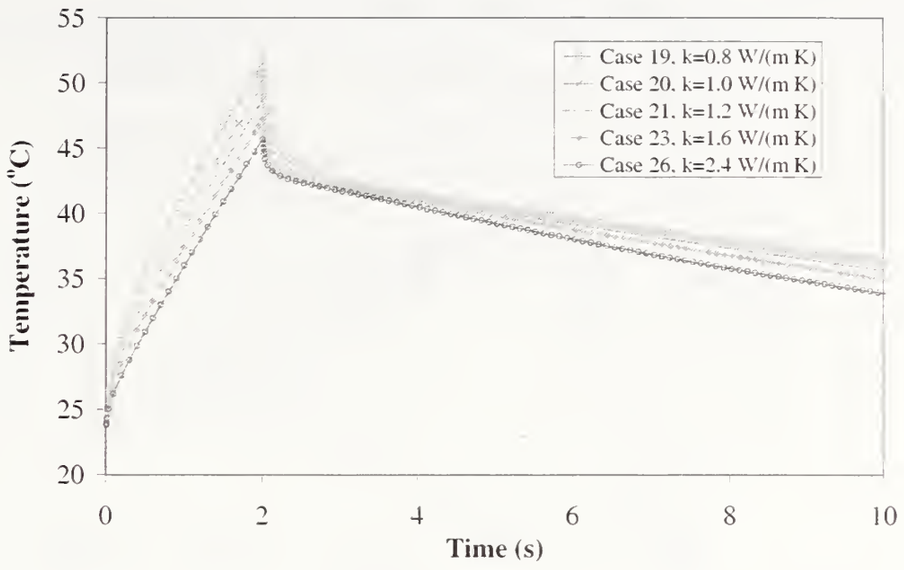

Fig. 4.28 Effect of thermal conductivity of CFRP on surface temperature above the flaw.

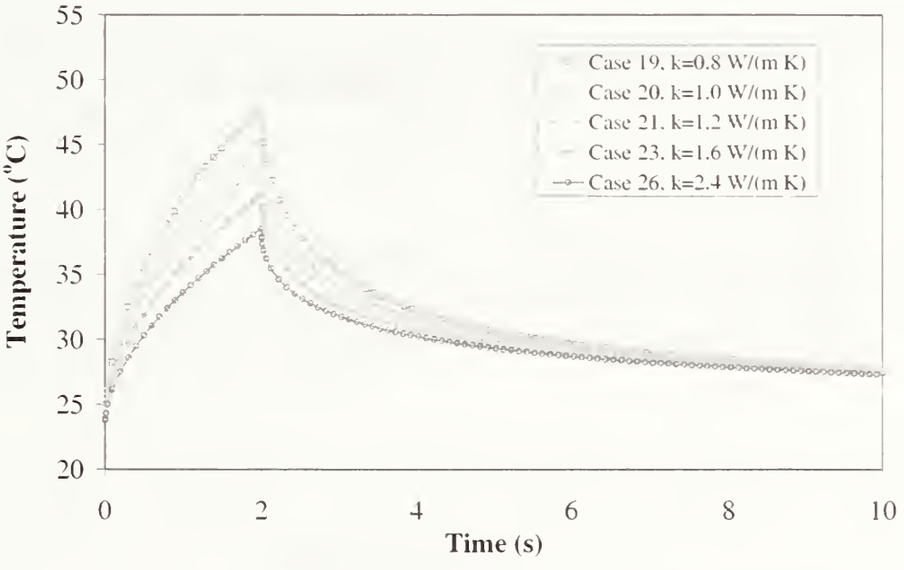

Fig. 4.29 Effect of the thermal conductivity of CFRP on the surface temperature of the background.

Figures 4.28 and 4.29 show the surface temperatures as a function of time for a point over the center of the flaw and a point in the background, respectively. The difference in the way the surface temperature rises and decays is due in part to the change in thermal properties; but, is also related to the specific geometry of the test object (e.g., depth of flaw, number and thickness of CFRP layers, etc.), which did not change.

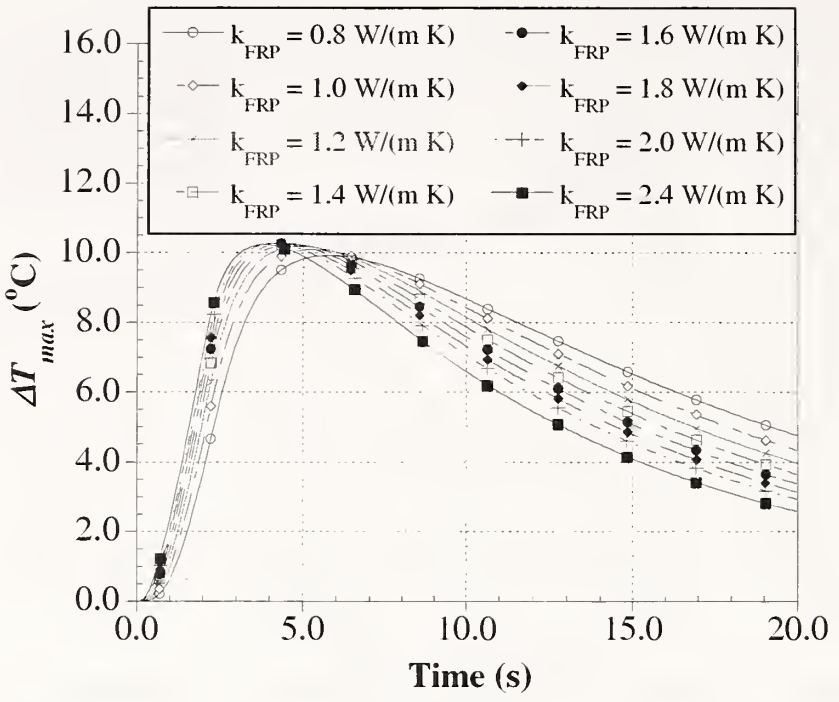

Fig. 4.30 Thermal signal for problems 19 through 26 (k_{FRP} = 0.8 W/(m·K) to 2.4 W/(m·K))

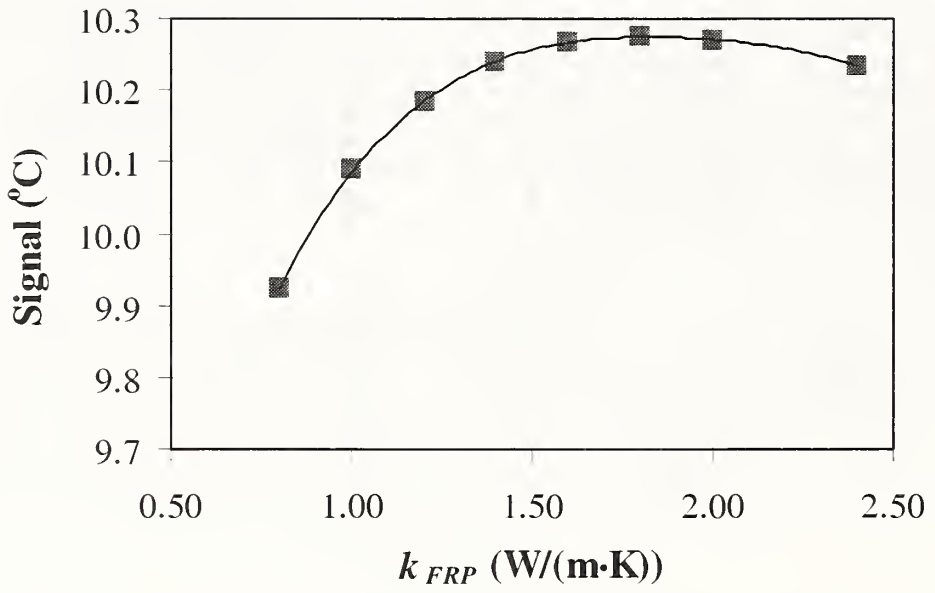

Fig. 4.31 Maximum thermal signal as a function of thermal conductivity of FRP

Figure 4.30 shows the thermal signal as a function of time for cases 19 through 26 and Fig. 4.31 shows the maximum signal as a function of the thermal conductivity of the FRP. It is seen that the maximum thermal signal varies nonlinearly with increasing thermal conductivity. The maximum thermal signal increases with increasing thermal conductivity until the thermal conductivity reaches 125 % of the initial value. Further increases in thermal conductivity of the FRP resulted in a slight decrease in the maximum thermal signal. It is noted that the maximum change in ΔT_{max} was 0.35 °C, which represents an increase in signal of only 3.6 %. Thus, for the

test object used in these analyses, the thermal signal is not very sensitive to the thermal conductivity of the FRP laminates.

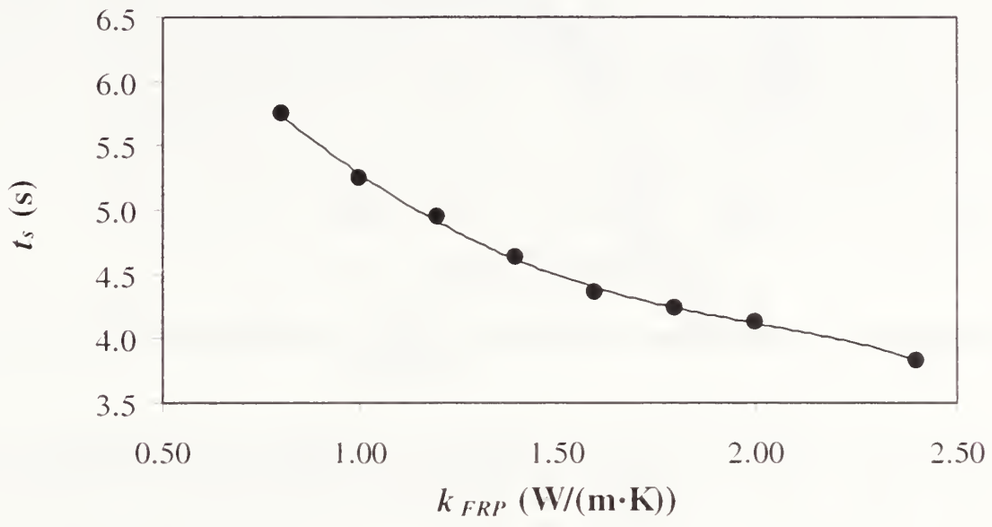

Fig. 4.32 Time for maximum signal as a function of the thermal conductivity of FRP

Figure 4.32 shows the time for maximum signal versus the thermal conductivity of the FRP. The time for maximum signal decreases nonlinearly with increasing thermal conductivity due to the increasing diffusivity of the FRP. The thermal front travels faster through the material, thus increasing the speed of cooling of the surface.

This behavior indicates that as the thermal conductivity of the FRP increases there will be less time from when the heat source is removed and when the maximum signal occurs. For a three-fold increase in thermal conductivity the time for maximum signal decreases from about 6 s to about 4 s. This decrease, however, would not have a detrimental effect on the ability to detect the debond.

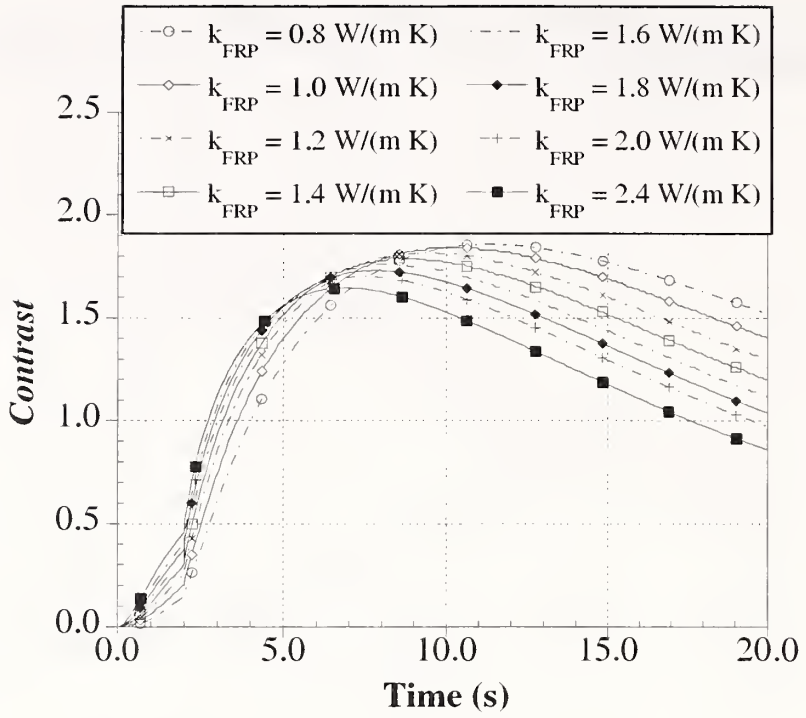

Fig. 4.33 Thermal contrast for problems 19 through 26 (k_{FRP} = 0.8 W/(m·K) to 2.4 W/(m·K))

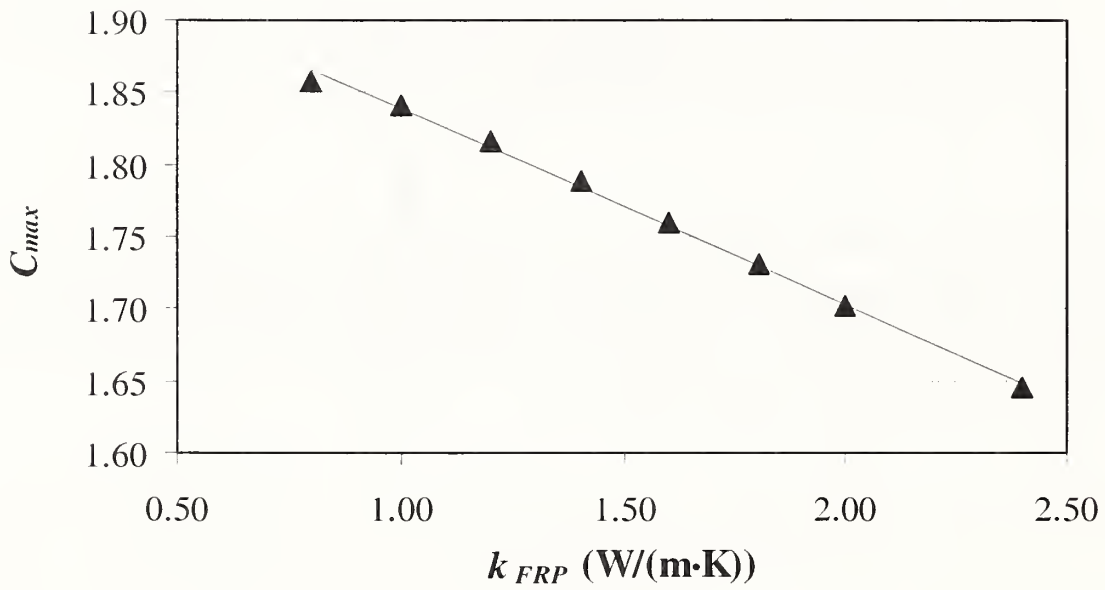

Fig. 4.34 Maximum thermal contrast as a function of thermal conductivity of FRP

Figure 4.33 shows the evolution of thermal contrast as a function of thermal conductivity of the FRP, and Fig. 4.34 show the variation of the maximum thermal contrast. The maximum thermal contrast decreased with increasing thermal conductivity of the FRP. Unlike the thermal signal, however, the thermal contrast decreased linearly with increasing thermal conductivity. The decrease in thermal contrast was on the order of 0.14 per W/m·K increase in thermal conductivity. Based on the "control", this represented a 1.5 % decrease in contrast per 25 % increase in thermal conductivity.

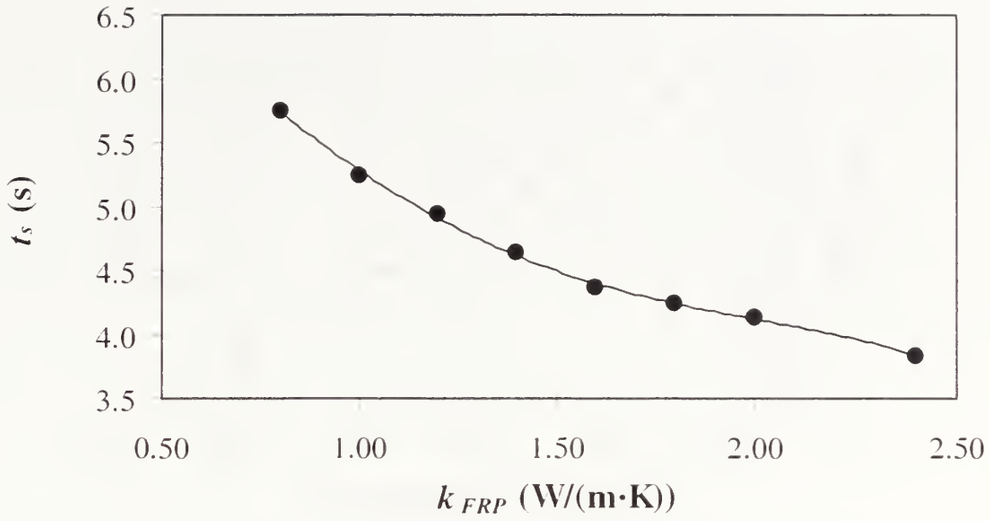

Fig. 4.35 Time to maximum contrast as a function of the thermal conductivity of FRP.

Figure 4.35 shows the time to maximum contrast as function of thermal conductivity of the FRP. Similarly to the time for maximum signal, the time for maximum contrast also decreased nonlinearly with increasing conductivity of the FRP. The time for maximum contrast decreased by 4.3 s with a three-fold increase in the thermal conductivity of FRP. Thus it appears that thermal contrast is affected by thermal conductivity more than the thermal signal.

4.4.4b Effect of Specific Heat of FRP

The next set of analyses (cases 19 and 27 through 29) investigated the effect of the specific heat of FRP on the thermal responses. As a reminder, the specific heat of a material is a measure of the amount of energy required to raise the temperature of a unit mass of the material by 1 K. The units are J/(kg·K).

Table 4.12 Results for simulations involving changes in the specific heat of FRP.

Case	c_{FRP} (J/(kg·K))	T_{max} (°C)	Maximum Signal		Maximum Contrast	
			t_s (s)	ΔT_{max} (°C)	t_c (s)	$\Delta T_{max}/\Delta T_{backg}$
27	1020	55.1	5.05	12.03	9.75	2.04
28	1080	53.8	5.25	11.25	10.25	1.95
29	1140	52.6	5.55	10.55	10.75	1.91
19	1200	51.6	5.75	9.92	11.25	1.86

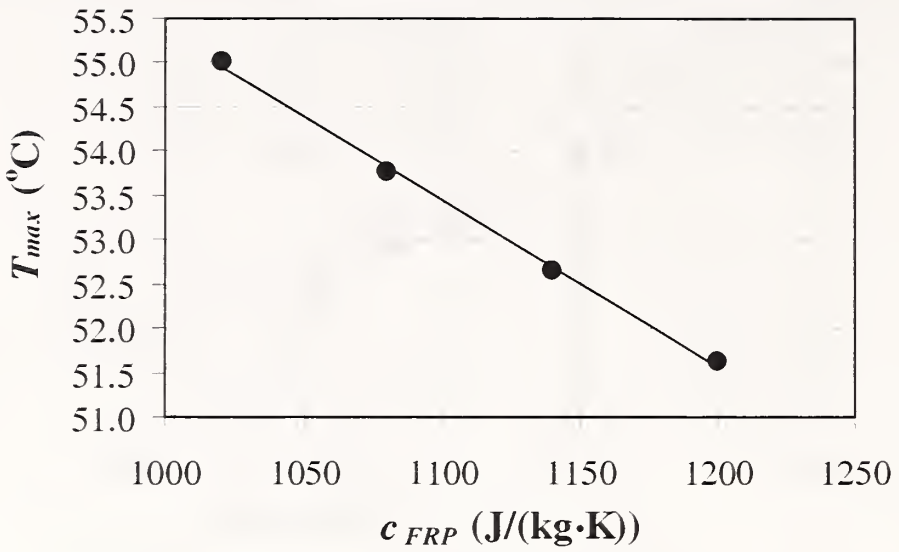

Fig. 4.36 Maximum surface temperature as a function of the specific heat of FRP

Table 4.12 summarizes the results as the specific heat of the FRP was decreased from 1200 J/kg·K to 1020 J/kg·K. Figure 4.36 shows that the maximum surface temperature decreased linearly with increasing specific heat. For this particular test object, the maximum surface temperature decreased at a rate of 0.019 K/(J/(kg·K)).

The behavior shown in Fig. 4.36 is not surprising. A material with higher specific heat requires a higher energy input to raise its temperature. Since the energy input was the same for all analyses, higher specific heat values of the FRP layers produced lower surface temperatures.

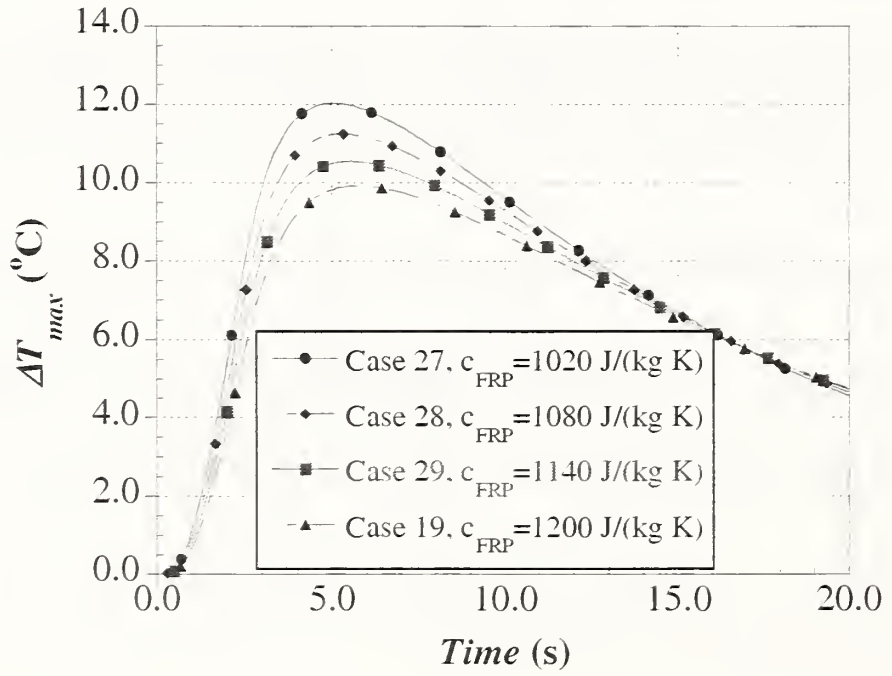

Fig. 4.37 Thermal signal for problems 19 and 27 through 29 (c_{FRP}=1020 J/(kg·K) through 1200 J/(kg·K))

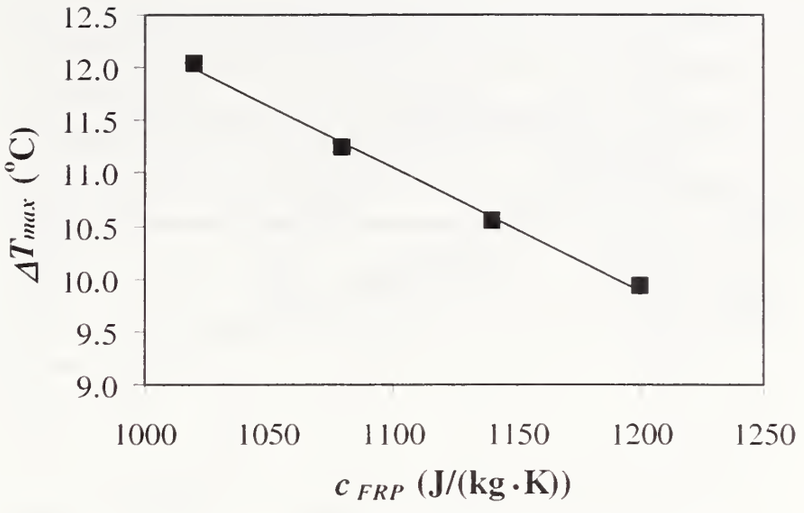

Fig. 4.38 Maximum thermal signal as a function of the specific heat of FRP.

Figure 4.37 shows the evolution of the thermal signal for the different values of specific heat and Fig. 4.38 shows the variation of the time for maximum signal. Both the maximum signal and the time for maximum signal varied linearly with specific heat. Figure 4.38 shows that the maximum signal decreased linearly with increasing specific heat at a rate of 0.012 K/(J/(kg·K)).

A comparison of Figs. 4.31 and 4.38 shows that, on a relative basis, changes in the specific heat of the FRP affected the maximum thermal signal more than the changes in the thermal conductivity. For example, while a change of 125 % in k_{FRP} produced only about a 4 % change in the maximum signal, a change of 15 % in the specific heat produced a change of 21 %.

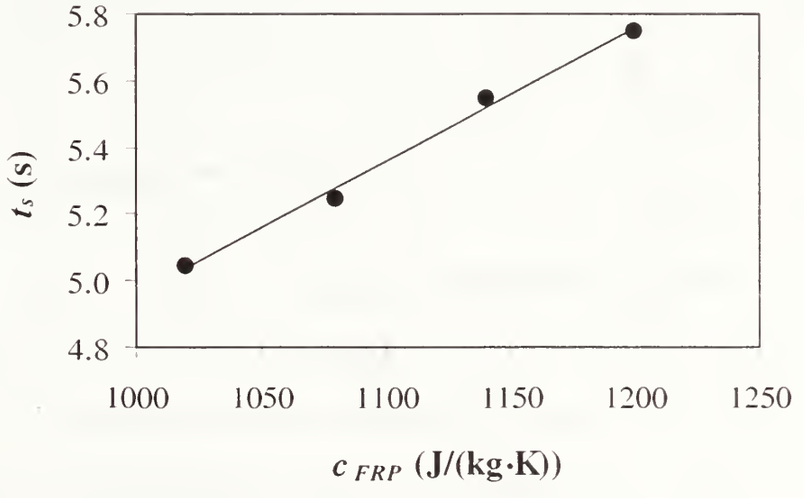

Fig. 4.39 Time for maximum signal as a function of the specific heat of CFRP.

Figure 4.39 shows that the time for maximum signal increased linearly with increasing specific heat. The increase, however, was small; for an increase in specific heat from 1020 J/(kg·K) to 1200 J/(kg·K), the time of maximum signal increased only 0.7 s.

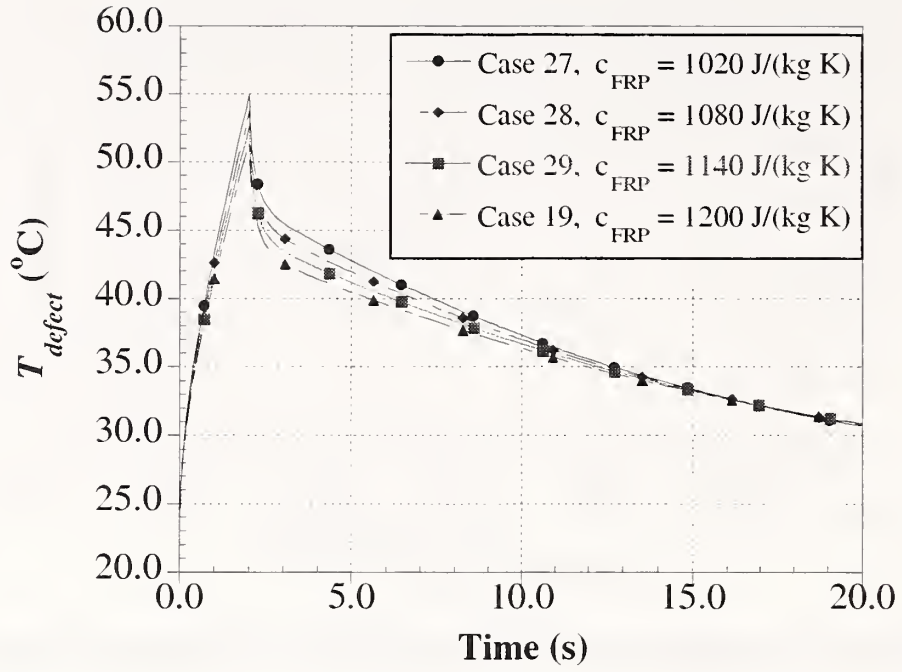

Fig. 4.40 Surface temperature above the defect

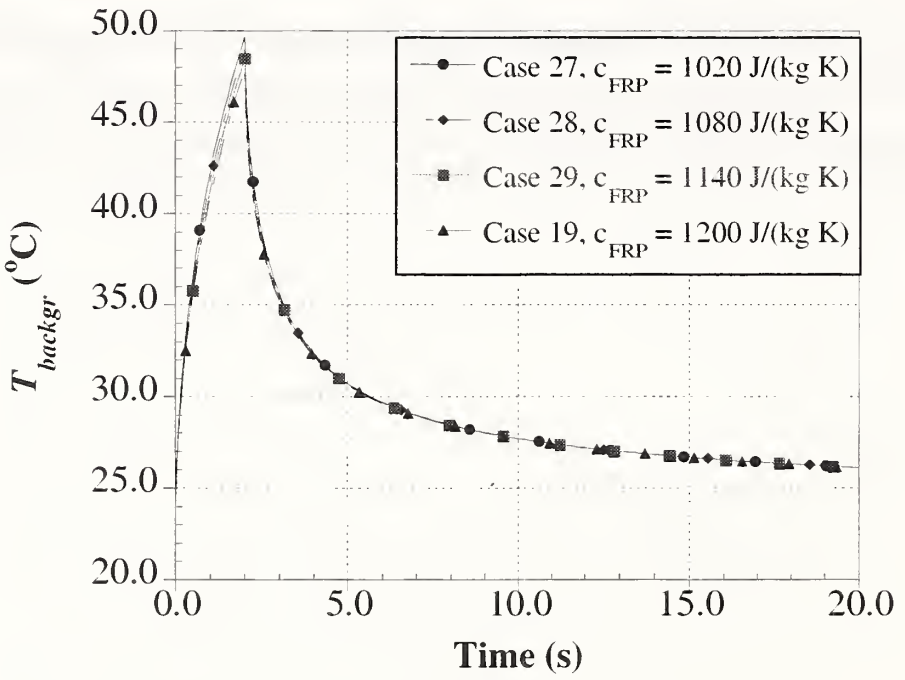

Fig. 4.41 Surface temperature in the background

Figures 4.40 and 4.41 show the evolution of surface temperature above the flaw and in the background respectively An interesting observation was that the changes in the thermal signal (Fig. 4.38) were driven primarily by changes in the surface temperature above the flaw. Surface temperatures above the defect were affected by the specific heat of the FRP (Fig. 4.40), whereas the background temperature was not affected (Fig. 4.41).

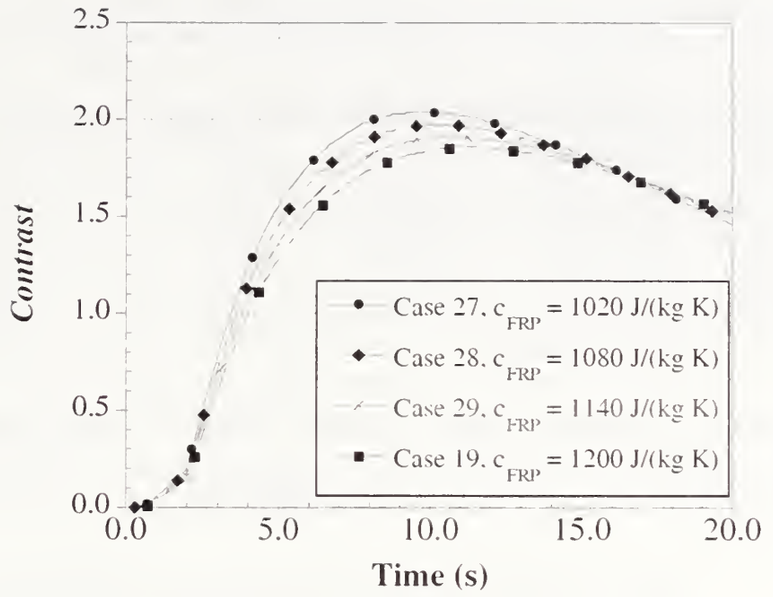

Fig. 4.42 Thermal contrast for problems 19 and 27 through 29 (c_{FRP}=1020 J/(kg·K) through 1200 J/(kg·K))

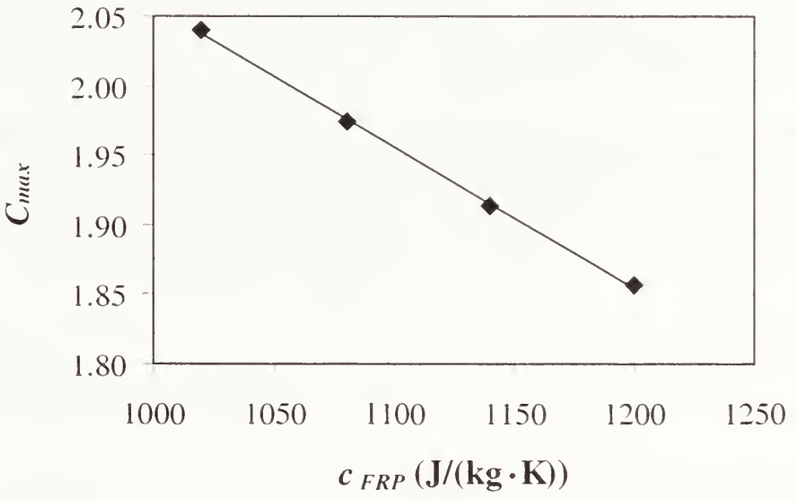

Fig. 4.43 Maximum thermal contrast as a function of the specific heat of FRP.

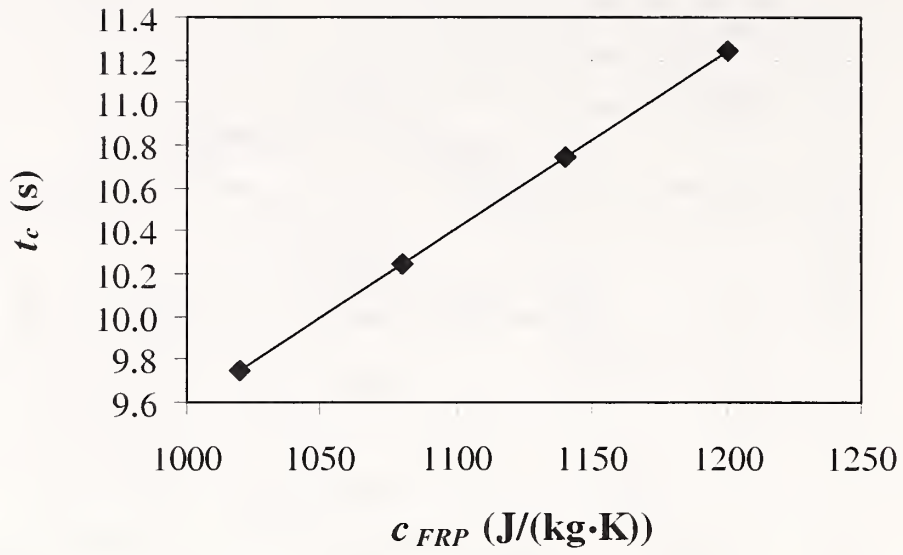

Fig. 4.44 Time for maximum thermal contrast as a function of the specific heat of CFRP

Figure 4.42 shows the evolution of the thermal contrast for the different specific heats of the FRP. The thermal contrast was affected in a way similar to the thermal signal. Figure 4.43 shows that the maximum thermal contrast decreased linearly with increasing specific heat, and Fig. 4.44 shows that the time of the maximum thermal contrast increased linearly with specific heat. For an increase of specific heat from 1020 J/(kg·K) to 1200 J/(kg·K), the time for maximum contrast increased by about 1.5 s.

The increase in time required for maximum signal and maximum contrast is the effect of the decreased diffusivity with increasing specific heat. As a reminder, thermal diffusivity is inversely proportional to the specific heat. Thus, the higher the value of the specific heat of the material, the lower the diffusivity and the slower the thermal evolutions.

In summary, changing the specific heat of the FRP layers from 1020 J/(kg·K) to 1200 J/(kg·K) reduced the maximum thermal signal and maximum contrast. The reductions, however, are not likely to have a significant impact on the ability to detect the presence of the debond.

4.4.4c Effects of the Thermal Conductivity of the Concrete

The next set of analyses (cases 19 and 30 through 32) involved changing the thermal conductivity of the concrete substrate. As shown in Table 4.9, the thermal conductivity was decreased by 5 % and increased up to 20 % from the value for the concrete in the "control" test object. Table 4.13 summarizes the results obtained in this set of simulations.

Table 4.13 Results for simulations involving changes in the thermal conductivity of concrete.

Case	k_{conc} (W/m·K)	T_{max} (°C)	Maximum Signal		Maximum Contrast	
			t_s (s)	ΔT_{max} (°C)	t_c (s)	$\Delta T_{max}/\Delta T_{backg}$
30	1.4	51.6	5.75	9.82	11.25	1.80
19	1.5	51.6	5.75	9.92	11.25	1.86
31	1.6	51.6	5.75	10.12	11.25	1.96
32	1.8	51.6	5.75	10.29	11.25	2.07

The maximum surface temperature above the flaw was not affected by the change in thermal conductivity of the substrate. This is because the flaw acts as an insulator, and only changes in the material above the flaw and/or in the flaw itself would affect the surface temperature above the flaw.

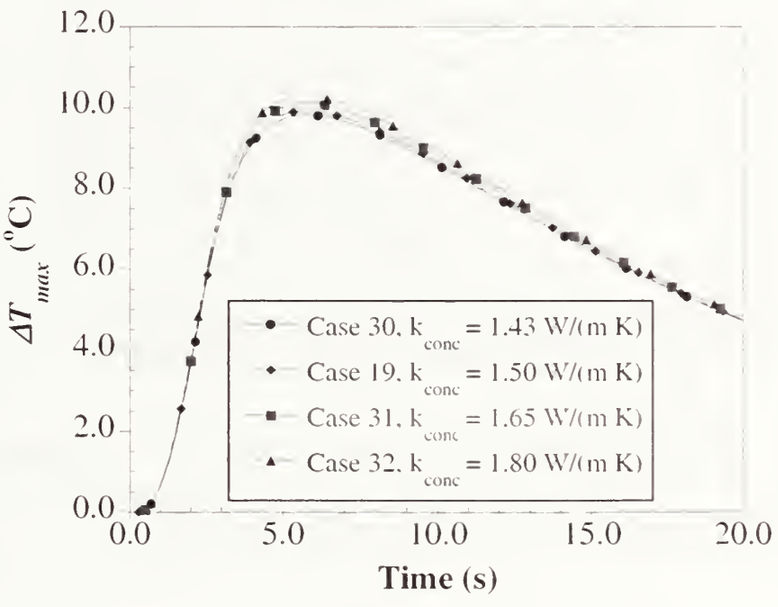

Fig. 4.45 Thermal signal for cases 19 and 30 through 32
(k_{conc}=1.43 W/(m·K) through 1.8 W/(m·K))

An increase in the thermal conductivity of the concrete, however, produced a decrease in the background surface temperature. Again, higher thermal conductivity means that there is less resistance to heat flow through the material. Thus, the thermal front travels faster and energy is transmitted to the interior of the object. As shown in Fig. 4.45 and Table 4.13, the decrease in the background surface temperature increased the maximum thermal signal.

The maximum thermal signal increased linearly with the thermal conductivity of the concrete according to the following equation:

$$\Delta T_{max} = 1.27 k_{conc} + 8.02 \tag{4.25}$$

where,

ΔT_{max} = maximum thermal signal and
k_{conc} = thermal conductivity of the concrete substrate.

Increases in the maximum thermal signal were on the order of 0.2 °C for a 10 % increase in the thermal conductivity of the substrate. The time for maximum thermal signal, however, remained constant at 5.75 s.

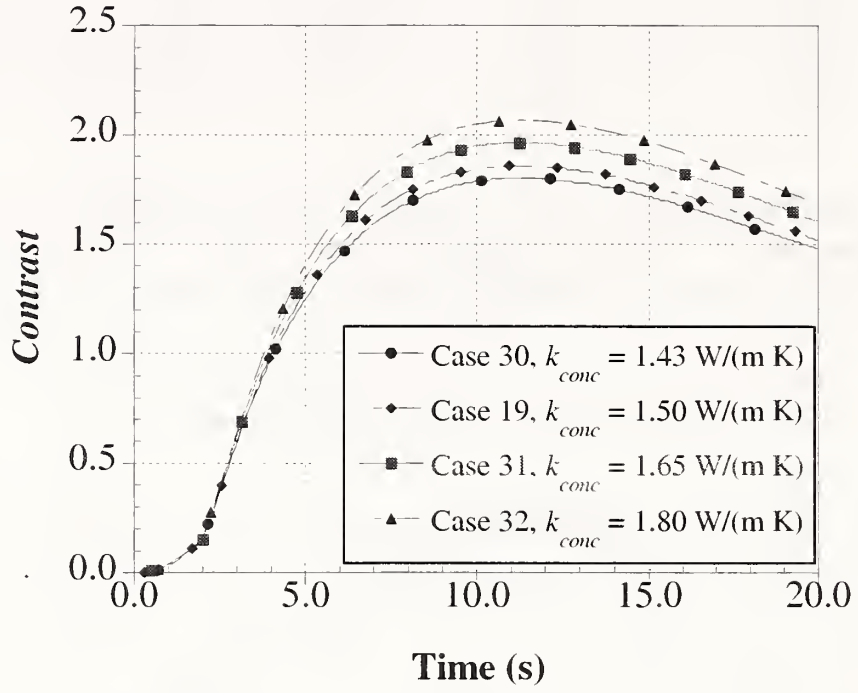

Fig. 4.46 Thermal contrast for cases 19 and 30 through 32
(k_{conc} = 1.43 W/(m·K) through 1.8 W/(m·K))

As shown in Fig. 4.46 and Table 4.13, the thermal contrast also increased with increasing thermal conductivity of the substrate. The increase in maximum thermal contrast was also a linear function of the thermal conductivity as expressed by the equation:

$$C_{max} = 0.705k_{conc} + 0.799 \tag{4.26}$$

The maximum thermal contrast increased about 0.1 per 10 % increase in thermal conductivity. The time for maximum contrast remained constant at t_c = 11.2 s.

4.4.4d Effects of the Specific Heat of Concrete

The next set of analyses involved the effects of the specific heat of the concrete substrate on the thermal responses. As shown in Table 4.14, the specific heat of the concrete was varied from 800 J/(kg·K) to 1040 J/(kg·K).

Similar to the case of changes in the thermal conductivity of concrete, the temperature above the flaw were not affected by changes in the specific heat of the substrate. Background surface temperatures, however, decreased with increasing specific heat. Physically, this behavior may be explained by the fact that a material with higher specific heat requires a larger amount of thermal energy to raise its temperature by the same amount. Since the input energy was maintained

constant in these simulations, lower temperatures were attained in the concrete and, hence, in the FRP.

Table 4.14 Results for simulations involving changes in the specific heat of concrete.

Case	c_{conc} (W/m·K)	T_{max} (°C)	Maximum Signal		Maximum Contrast	
			t_s (s)	ΔT_{max} (°C)	t_c (s)	$\Delta T_{max}/\Delta T_{backg}$
19	800	51.6	5.75	9.92	11.25	1.86
33	880	51.6	5.75	10.12	11.25	1.96
34	960	51.6	5.75	10.30	11.25	2.07
35	1040	51.6	5.65	10.46	11.25	2.17

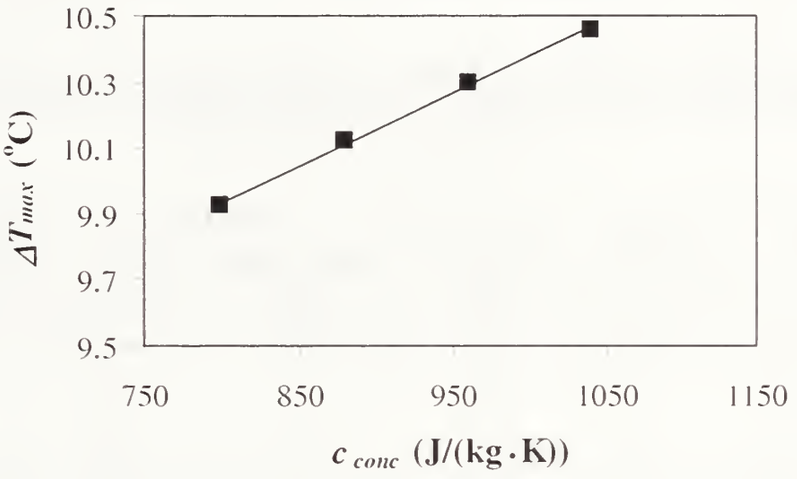

Fig. 4.47 Maximum signal as a function of the specific heat of concrete

As shown in Fig. 4.47, the reduction in background surface temperature produced an increase in the thermal signal as a function of specific heat. From the results shown in Table 4.14, it was found that the maximum thermal signal increased linearly with specific heat according to the equation:

$$\Delta T_{max} = 0.002 c_{conc} + 8.15 \tag{4.27}$$

where,

ΔT_{max} = maximum signal and
c_{conc} = specific heat of the concrete substrate.

The average increase in thermal signal was 0.2 °C per 10 % increase in specific heat. The time for maximum signal remained constant at 5.75 s.

The maximum thermal contrast also increased linearly with increasing specific heat according to the following equation:

$$C_{max} = 0.0013 c_{conc} + 0.834 \tag{4.28}$$

where,

c_{conc} = specific heat of concrete.

The thermal contrast increased by 0.1 for a 10 % increase in the specific heat of the concrete substrate.

4.4.4e Combined Effects of Changes in FRP and Concrete Properties

The final set of analyses involved different combinations of thermal conductivity and specific heat for FRP and concrete. These combinations are shown in Table 4.10 for simulations 36 to 43. The results, which are shown in Table 4.15, provide further insight into the thermal response of the test object due to simultaneous variations in the thermal properties of the FRP and concrete.

Table 4.15 Results for Cases 36 through 43 in which the thermal properties of FRP and concrete were varied simultaneously

Combination	Case	T_{max} (°C)	Signal		Contrast	
			ΔT_{max} (°C)	t_s (s)	$\Delta T_{max}/\Delta T_{backg}$	t_c (s)
low k_{FRP}-low k_{conc}	36	51.6	9.82	5.75	1.80	11.25
low k_{FRP}-high k_{conc}	37	51.6	10.29	5.75	2.06	11.25
high k_{FRP}-low k_{conc}	38	46.7	10.16	4.23	1.68	7.83
high k_{FRP}-high k_{conc}	39	46.7	10.68	4.24	1.92	7.84
low c_{FRP}-low c_{conc}	40	55.0	12.03	5.05	2.04	9.75
low c_{FRP}-high c_{conc}	41	55.0	12.64	4.95	2.37	9.75
high c_{FRP}-low c_{conc}	42	51.6	9.92	5.75	1.86	11.25
high c_{FRP}-high c_{conc}	43	51.6	10.46	5.75	2.16	11.25

The expected maximum signal and maximum contrast, due to the various combinations, were also estimated using the principle of superposition of the effects of k and c. This method resulted in estimations of the responses of test object that were within a 1 % of the simulations. For example, case 38 involved modifying the material properties of the "control" test object (case 19) in the two directions by increasing k_{FRP} (as in case 24) and reducing k_{conc} (as in case 30). The estimation was obtained using the signal results from problem 19 as a reference. The maximum signal difference ΔT_1 between the results of problem 24 and 19 was computed (see Table 4.11). The same procedure was applied to cases 30 and 10 (see Table 4.13) and ΔT_2 was obtained as 0.1 °C. Addition of these differences to the maximum thermal signal of 9.92 °C for case 19 resulted in an estimation of the maximum thermal signal of 10.18 °C for case 38.

$$\Delta T_{max}\big|_{new} = \Delta T_{max}\big|_{case\ 19} + \Delta T_1 + \Delta T_2 = 9.92 + 0.36 + 0.19 = 10.18 \tag{4.29}$$

The maximum signal from the finite element simulation for problem 38 is 10.16 °C. Thus, for this particular example, the error between the estimation and the FEM output was only 0.02 °C. Using the same approach, the maximum error occurred in the estimation of the ΔT_{max} of case 39, in which the error was 0.04 °C. The same procedure could be used in the estimation of the thermal contrast, with similar results. Thus it is concluded that there is no interaction effect due to thermal conductivity and specific heat.

4.4.5 Summary

Four different sets of analyses were performed to investigate the effect of material thermal properties on the thermal response of the flawed test object. The focus of the parametric study was two-fold:

- Gain an understanding of thermal diffusion behavior for different values of thermal conductivity and specific heat; and

- Establish if accurate determination of the material thermal properties of the structural components is required for quantitative IR thermography testing of FRP laminates applied to concrete.

The test object included a debond between the FRP composite and the concrete substrate. The thermal conductivity and specific heat of the composite and the concrete were varied to investigate the effect of these material properties on the thermal response. The models were subject to a square-wave thermal pulse of 2 s duration. The conclusions for this parametric study are as follows:

- The maximum surface temperature decreases nonlinearly with increasing k_{FRP} (Fig. 4.27), and linearly with increasing c_{FRP} (Fig. 4.36). The thermal properties of the concrete substrate do not affect the maximum surface temperature above the flaw (Tables 4.13 and 4.14).

- The maximum thermal signal varies nonlinearly with increasing thermal conductivity of the FRP (Fig. 4.37). The maximum signal reaches a peak value and decreases with further increase in k_{FRP}.

- The maximum thermal signal decreases linearly with increasing c_{FRP} (Fig. 4.38).

- The maximum thermal signal increases linearly with increasing $k_{concrete}$ (Eq. 4.25) or $c_{concrete}$ (Eq. 4.27).

- The maximum thermal contrast decays linearly with increasing k_{FRP} (Eq. 4.34) or c_{FRP} (Eq. 4.43).

- The maximum thermal contrast increases linearly with increasing $k_{concrete}$ (Eq. 4.26) or $c_{concrete}$ (Eq. 4.28).

- The time for maximum thermal signal is affected only by the thermal properties of the FRP layers. The time for maximum thermal signal decreases nonlinearly with increasing thermal

conductivity of the FRP (Fig. 4.32). The time for maximum thermal signal increases linearly with increasing c_{FRP} (Fig. 4.39).

- The time for maximum thermal contrast is only affected by the thermal properties of the FRP composite. The time for maximum thermal contrast decreases nonlinearly with increasing k_{FRP} (Fig. 4.35) and increases linearly with increasing c_{FRP} (Fig. 4.44).

- The effects of simultaneous changes in thermal conductivity and specific heat can be predicted by superposition of the effects resulting from the changes of each property. There is no interaction effect.

- The greatest change in maximum thermal signal was observed by changing the specific heat of the FRP. For the range of c_{FRP} investigated, this change was on the order of 2 °C. Most of the variations in maximum thermal signal due to changes in k_{FRP}, $k_{concrete}$, and $c_{concrete}$ were smaller than 0.6 °C.

In summary, while variations in the thermal properties of the FRP and concrete resulted in systematic variations in thermal response, none of the response parameters (maximum surface temperature, thermal signal, and contrast) were very sensitive to these variations. Thus, it would appear that the success of infrared thermography testing will not depend strongly on the specific values of the thermal properties of the FRP or concrete substrate.

The next series of studies will examine the effects of the depth of the flaw.

4.5 Parametric Study No. 3: Effect of the Depth of the Flaw

In the use of FRP layers to strengthen concrete or masonry structures, defects may arise between the FRP layers (delaminations) or at the FRP/concrete interface (debonds). In addition, failure planes may occur in the concrete if the shear stresses needed to transfer load to the FRP, exceed the capacity of the concrete (spalls). Thus, it is desirable to investigate how the location of a flaw affects the thermal response and to establish whether it may be feasible to determine the depth of the flaw from the characteristics of the thermal evolution. The third parametric study had the following objectives:

- Understand the effects of the depth of debonds on the thermal response;

- Understand the effects of the depth of delaminations on the thermal response;

- Understand the effects of the depth of concrete spalls on the thermal response; and,

- Investigate the feasibility of estimating flaw depth from the measured thermal response.

Seven different sets of analyses were performed which included 21 finite element models.

4.5.1 Geometry of Model

The basic geometry of the test object corresponded to that used in parametric studies No. 1 and No. 2, that is, a 100 mm long by 20 mm thick concrete slab covered with carbon FRP. Each ply of CFRP was 0.5 mm thick. The test object contained an internal flaw (air void) 25 mm long and 0.1 mm thick. The thermal contact resistance corresponded to 4.17×10^{-3} m^2/W. Plane two-dimensional modeling was used; thus, the test object is infinite in the z-direction. The internal flaw was located at the center of the model. The simulation was simplified using plane symmetry about the center of the specimen.

The test object was meshed using 2-D quadrilateral thermal solid elements containing 4 nodes. The model was meshed using mapped meshing with global element size of 0.5 mm. Similarly to the previous parametric studies, mesh refinement was applied in the thickness direction. The mesh refinement consisted of thin elements at the FRP layers, the defect, and at the concrete interface with the FRP. The element size was increased towards the bottom of the slab away from the heated surface. Thus, the meshing used in the current parametric study was the same as in parametric study No. 2.

For flaws located near the surface, the mesh configuration used in the previous parametric study showed some thermal gradient irregularities at the elements surrounding the edge of the flaw. To justify the use of the chosen mesh, a sensitivity analysis was performed to determine the accuracy of the results. The global element size was decreased to 0.25 mm, and this reduced the heat flux irregularities. The computational time, however, increased drastically and the differences in surface temperature changed only by 0.02 °C. The small difference in surface temperature results justified the use of the larger mesh size, regardless of the irregularities at the discontinuity.

Table 4.16 Geometry for simulations involving debond depth

Case	Number of plies	Depth of debond
44	1	0.5 mm
45	2	1.0 mm
46	3	1.5 mm
47	5	2.5 mm
48	6	3.0 mm
49	7	3.5 mm

The internal flaw (air void) was located at different depths and interfaces within the test object. The first set of simulations involved investigation of the effect of depth of debonds at the FRP/concrete interface and the number of FRP plies was increased from 1 to 7 as indicated in Table 4.16.

Table 4.17 Geometry for simulations involving delamination depth

Case	Number of plies	Location of flaw	Depth of delamination
47	5	Between 5th and concrete	2.5 mm
50	5	Between 4th and 5th layer	2.0 mm
51	5	Between 3rd and 4th layer	1.5 mm
52	5	Between 2nd and 3rd layer	1.0 mm
53	5	Between 1st and 2nd layer	0.5 mm

The second set of simulations involved investigation of the effect of delaminations between FRP layers. All the models in this set contained 5 layers of FRP. The depth of the flaw varied from 0.5 mm (delamination at top interface) to 2.5 mm (debond between FRP and concrete). Table 4.17 summarizes the geometrical characteristics.

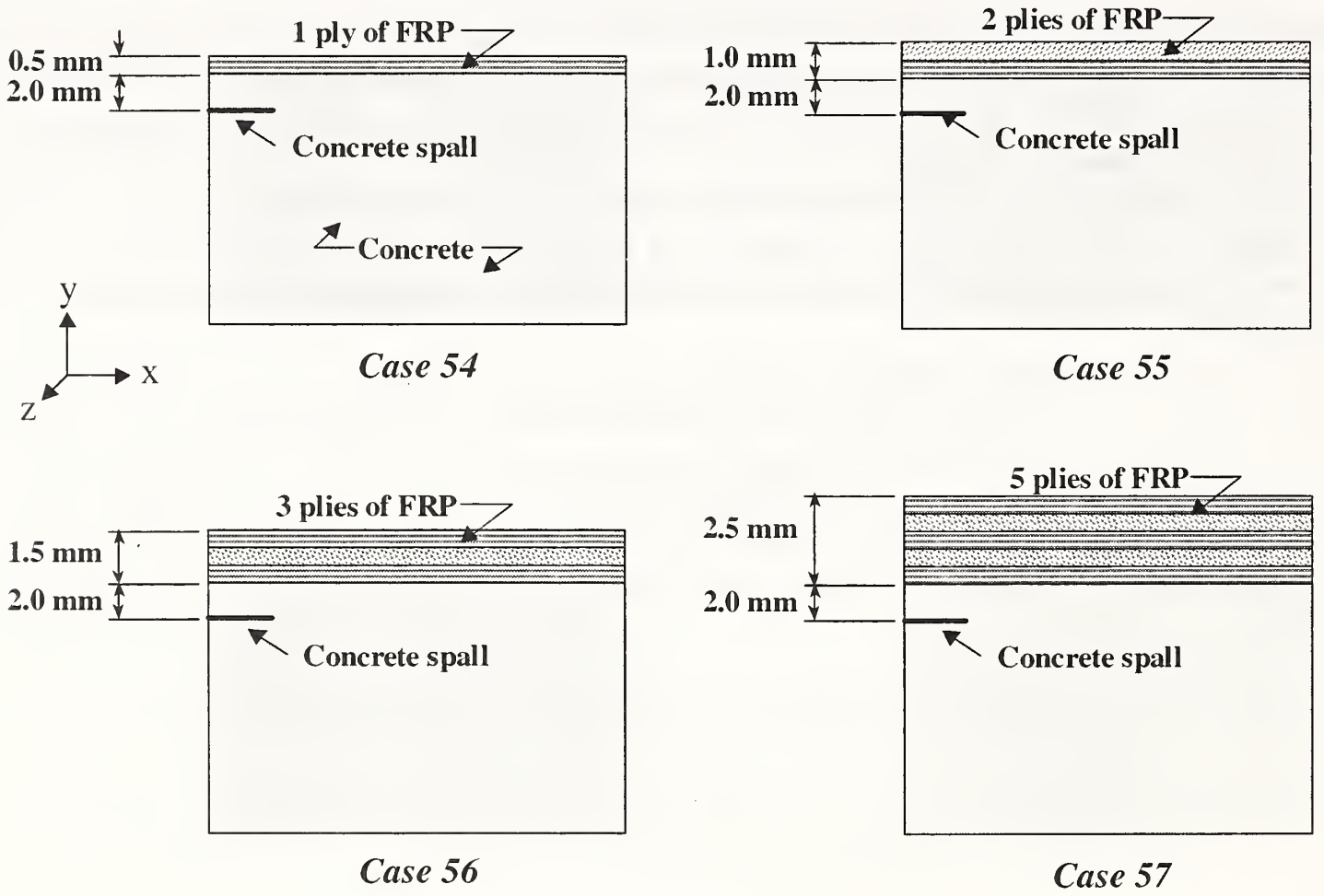

Fig. 4.48 Geometry of models for third set of simulations involving flaw in concrete with different numbers of FRP layers

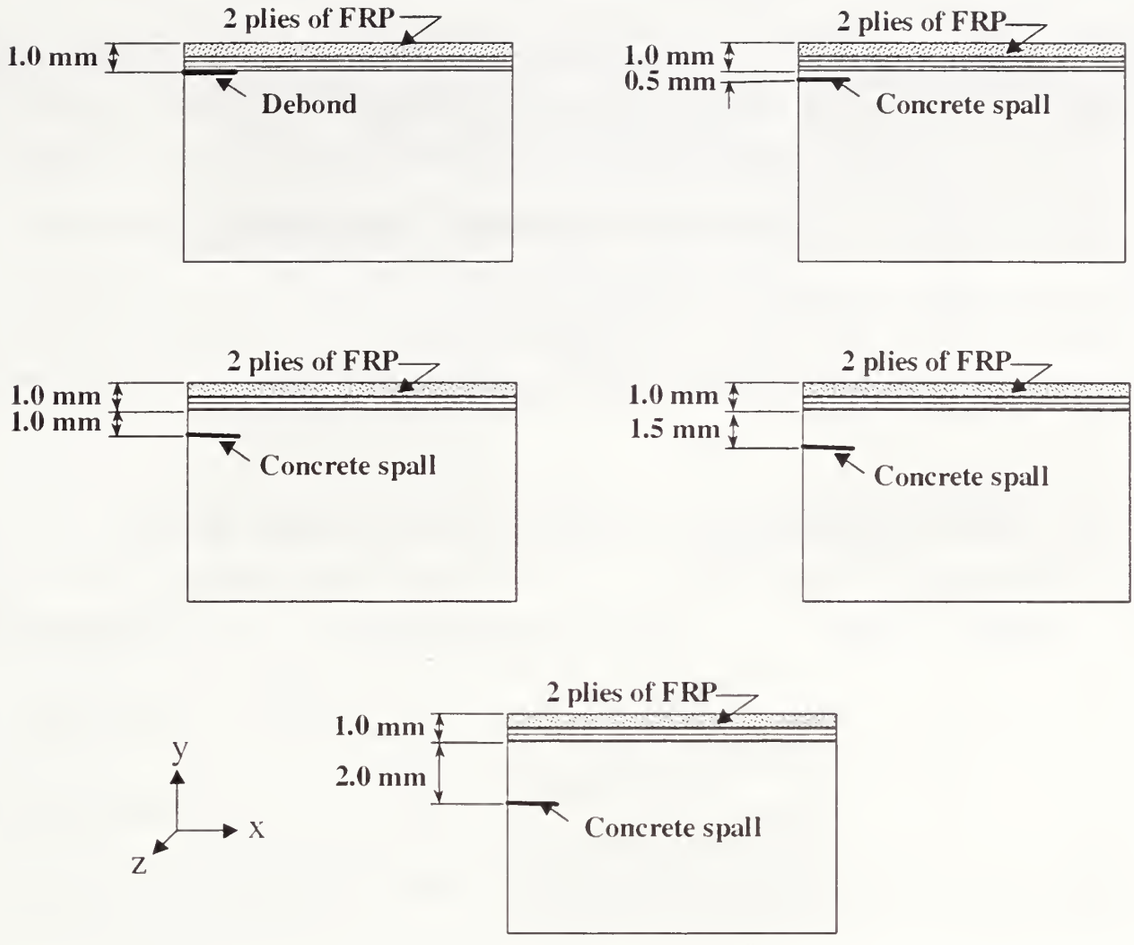

Fig. 4.49 Geometry of models for fourth set of simulations involving varying flaw depths in concrete with 2 layers of FRP

The third and fourth sets of simulations involved flaws or spalls in the concrete substrate. The third set of simulations examined the effect of the number of FRP plies on the thermal response. As shown in Fig. 4.48, the concrete spall was located 2 mm below the FRP/concrete interface and the number of FRP plies was varied from 1 to 5. The fourth set of simulations focused on the effect of concrete cover, and the number of FRP plies was kept constant at 2. As shown in Fig. 4.49, the depth of the flaw was increased from 0.0 mm (debond) to 2.0 mm from the FRP/concrete interface.

Table 4.18 Geometry for simulations involving 5 layers of FRP

Case	Number of plies	Type of flaw & location	Depth of flaw
53	5	Delamination between 1st and 2nd ply	0.5 mm
52	5	Delamination between 2nd and 3rd ply	1.0 mm
51	5	Delamination between 3rd and 4th ply	1.5 mm
50	5	Delamination between 4th and 5th ply	2.0 mm
47	5	Debond at interface	2.5 mm
57	5	Concrete spall 2 mm below interface	4.5 mm

Table 4.19 Geometry for simulations involving 3 layers of FRP

Case	Number of plies	Type of flaw & location	Depth of flaw
62	3	Delamination between 1st and 2nd ply	0.5 mm
63	3	Delamination between 2nd and 3rd ply	1.0 mm
46	3	Debond at interface	1.5 mm
64	3	Concrete spall at 1 mm below interface	2.5 mm
65	3	Concrete spall at 2 mm below interface	3.5 mm

Table 4.20 Geometry for simulations involving 2 layers of FRP

Case	Number of plies	Type of flaw & location	Depth of flaw
61	2	Delamination between 1st and 2nd ply	0.5 mm
45	2	Debond at interface	1.0 mm
58	2	Concrete spall at 0.5 mm below interface	1.5 mm
59	2	Concrete spall at 1.0 mm below interface	2.0 mm
60	2	Concrete spall at 1.5 mm below interface	2.5 mm
55	2	Concrete spall at 2.0 mm below interface	3.0 mm

The next three sets of simulations focused on the response due to flaws at any depth in three different FRP/concrete structures. As shown in Tables 4.18, 4.19, and 4.20, each set of simulations contained 5, 3, or 2 FRP plies. For each set, the depth of the flaw was varied to simulate delaminations, debonds, and concrete spalls. The purpose of these simulations was to examine whether there was a simple relationship for the thermal response due to a variation in the depth of any kind of flaw for a given test object

4.5.2 Material Properties

The material properties of the model were those of carbon FRP (CFRP) for the bonded composite, concrete for the substrate, and air for the defect (see Table 4.1). The CFRP layer in direct contact with the concrete had the fibers running in the x-direction. The direction of the fiber alternated between z- and x-direction for additional layers of FRP.

4.5.3 Thermal Loading and Boundary Conditions

Again, the analysis was defined as a transient heat transfer problem. A square pulse of intensity 20,000 W/m^2 and duration 2 seconds was applied at the top surface of the model. Adiabatic conditions ($dT/dx = 0$ and $dT/dy = 0$) were assumed for the remaining surfaces. The initial temperature of the test object was 23 °C.

The same time stepping was prescribed for all the problems of this parametric study. The initial time step was 0.009 s. The analysis was performed using ANSYS' automatic stepping with the maximum and minimum time steps set to 0.1 s and 0.008 s, respectively. The nodal temperatures were recorded at every time step.

4.5.4 Results

4.5.4a Debonds

The first set of simulations involved the study of debonds at the FRP/concrete interface. The number of plies was increased from 1 ply to 7 plies. Each ply of FRP had a thickness of 0.5 mm. Table 4.21 summarizes the results for this set of simulations.

Table 4.21 Results for simulations involving debonds (first set in parametric study #3)

Case	Depth, d (mm)	T_{max} (°C)	Maximum Signal		Maximum Contrast	
			t_s (s)	ΔT_{max} (°C)	t_c (s)	$\Delta T_{max}/\Delta T_{backg}$
44	0.5	64.6	2.44	20.85	3.94	2.02
45	1.0	51.7	4.45	8.16	8.05	1.23
46	1.5	49.1	7.35	4.41	12.05	0.84
47	2.5	48.6	14.65	1.86	22.55	0.48
48	3.0	48.6	19.55	1.36	29.53	0.40
49	3.5	48.6	23.93	0.97	35.55	0.32

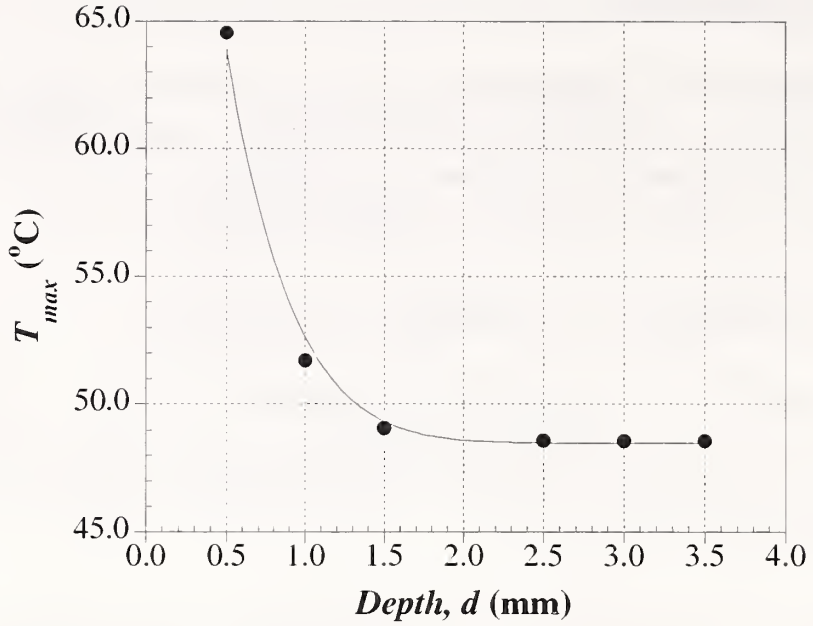

Fig. 4.50 Effect of debond depth on the maximum surface temperature

The results in Table 4.21 reveal some interesting relationships regarding the effect of debond depth on the thermal response. For example, as shown in Fig. 4.50, the maximum surface temperature decreases nonlinearly with flaw depth. For a depth of 2.5 mm or more, the maximum surface temperature is not affected by the depth of the debond of the size used in the models.

The relationship between maximum surface temperature and flaw depth can be approximated using Eq. 4.30:

$$T_{max} = \frac{2T_{\infty}}{1 + erf(d)} \tag{4.30}$$

where,

$erf(d)$ = error function for the depth of the flaw; and,
T_{∞} = asymptotic temperature reached when the flaw is deep in the material.

As a reminder, the error function for the depth of the flaw is

$$erf\,(d) = \frac{2}{\pi}\int_{0}^{d} e^{-t^2}\,dt \tag{4.31}$$

The best fit value of T_{∞} is found to be close to the theoretical surface temperature for a semi-infinite solid heated with a heat flux impulse (Carslaw et al., 1959)

$$T_{\infty} = \frac{2q}{k}\sqrt{\frac{\alpha\tau}{\pi}} + T_o \tag{4.32}$$

where,

q = magnitude of the input heat flux;

k = thermal conductivity of FRP;
α = thermal diffusivity of FRP;
τ = pulse duration; and,
T_o = initial temperature of the test object.

For this particular set of simulations the computed value of T_α was 48.8 °C.

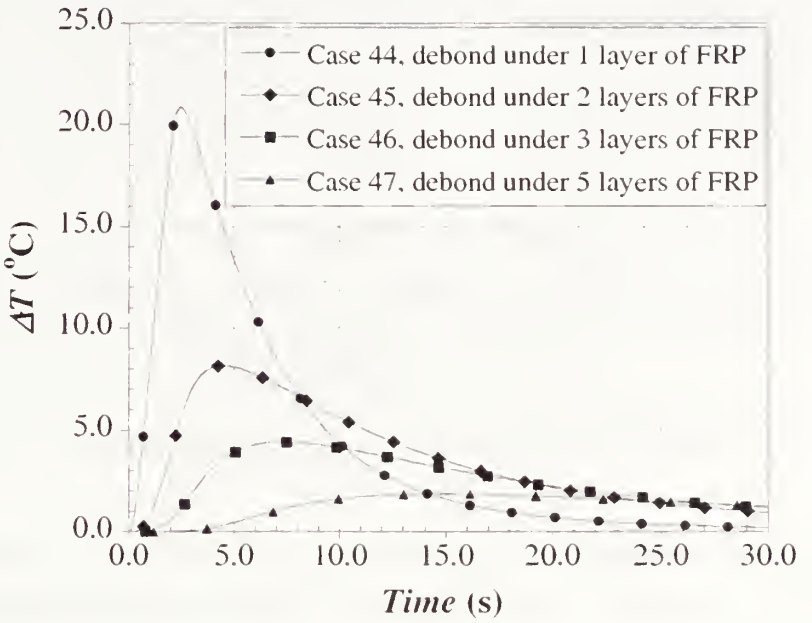

Fig. 4.51 Thermal signal as a function of debond depth

The results for the maximum thermal signal ΔT_{max} also showed a nonlinear relationship with flaw depth. Figure 4.51 illustrates the signal versus time behavior for the first set of simulations. It is seen that debonds located near the surface result in maximum thermal signal (ΔT_{max}) and short time for maximum signal (t_s), while deep debonds result in low ΔT_{max} and long t_s.

The variation of the maximum thermal signal with debond depth can be represented by the following power function:

$$\Delta T_{max} = 7.64\, d^{-1.57} \tag{4.33}$$

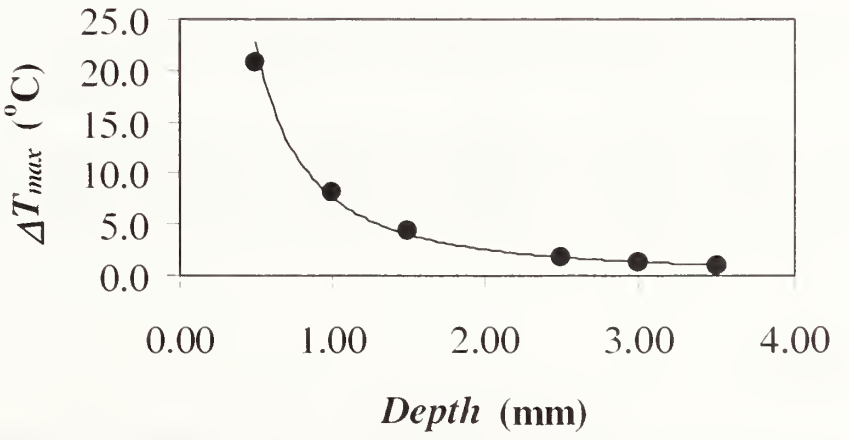

Fig. 4.52 Maximum thermal signal as a function of debond depth

Figure 4.52 illustrates the FEM output and curve fit for the maximum signal. Figure 4.52 shows that the maximum thermal signal drops off quickly with increasing depth. It may be difficult to discern the presence of debonds 25 mm wide with more than 3 mm of FRP.

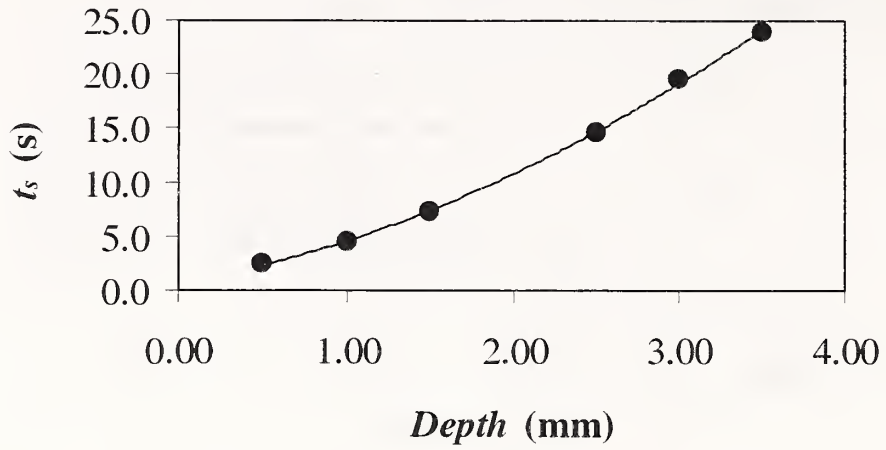

Fig. 4.53 Time for maximum signal as a function of debond depth

As shown in Fig. 4.53, the time for maximum signal increased with increasing depth of the debond and the variation could be approximated by the following quadratic function:

$$t_s = 1.08d^2 + 2.97d + 0.54 \tag{4.34}$$

An increase in depth from 1 mm to 3 mm resulted in a four-fold increase in time of maximum signal. This strong dependence between t_s and the depth of the debond indicates that the time for maximum signal may be a good indicator of relative flaw depth.

The maximum contrast also decreased nonlinearly with the depth of the debond. Again, the simulation output could be fitted by a power function, as follows:

$$C_{max} = 1.14d^{-0.95} \tag{4.35}$$

while the time for maximum contrast could be fitted with a quadratic equation, as follows:

$$t_c = 1.18d^2 + 5.89d + 0.76 \tag{4.36}$$

The time for maximum contrast also depended strongly on debond depth and varied from 3.94 s for the test object with only one layer of FRP to 35.55 s for the test object with 7 layers of fiber composite.

4.5.4b Delaminations

The next set of simulations focused on the effect of the depth of delaminations. All the simulations involved a test object containing 5 plies of FRP. The depth of the delamination was varied from 0.5 mm to 2.5 mm. Table 4.22 summarizes the results for this set of simulations.

Table 4.22 Results for simulations involving delaminations (second set in study #3)

Case	Depth, d (mm)	T_{max} (°C)	Maximum Signal		Maximum Contrast	
			t_s (s)	ΔT_{max} (°C)	t_c (s)	$\Delta T_{max}/\Delta T_{backg}$
47	2.5	48.6	14.65	1.86	22.55	0.48
50	2.0	48.6	11.55	2.60	18.85	0.59
51	1.5	49.1	7.90	3.86	13.75	0.70
52	1.0	51.8	4.64	6.95	9.24	0.91
53	0.5	64.9	2.53	18.35	3.93	1.41

The thermal response was similar to that produced by debonds. For example, the maximum temperature varied with depth in the same way as described for debonds. Thus, the maximum temperature can be estimated using Eqs. 4.30, 4.31, and 4.32. The maximum thermal signal as a function of depth could be described by following power function:

$$\Delta T_{max} = 6.89\, d^{-1.42} \tag{4.37}$$

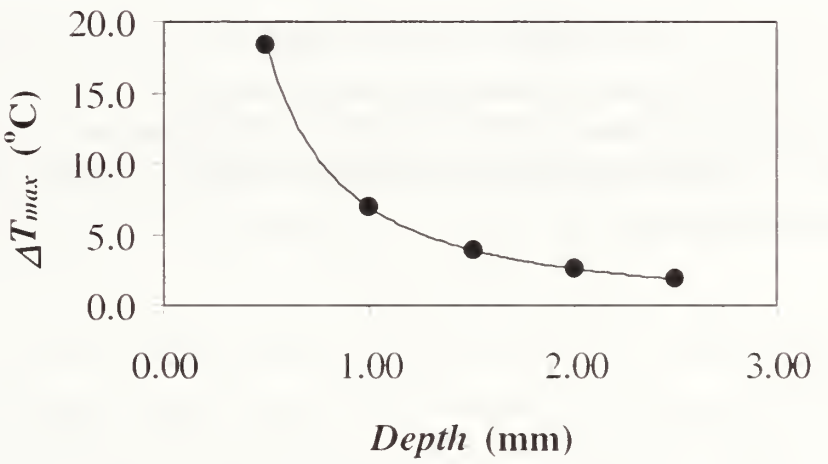

Fig. 4.54 Maximum thermal signal as a function of delamination depth

Figure 4.54 illustrates the FEM results and curve fit for the maximum signal resulting from delaminations at various depths.

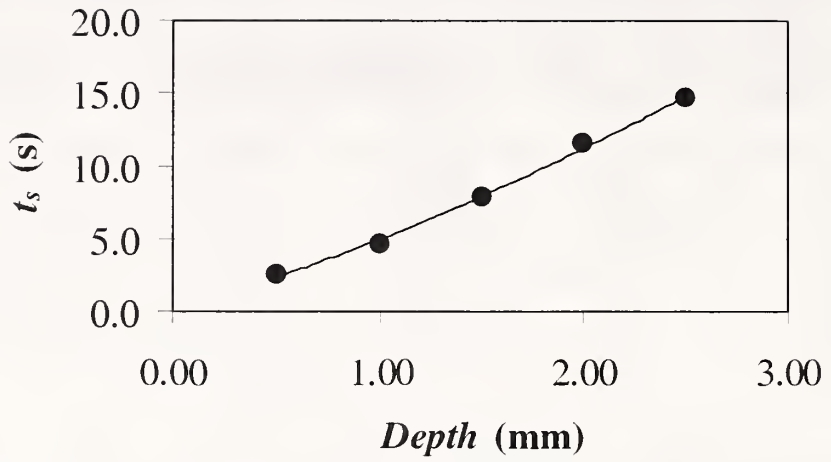

Fig. 4.55 Time for maximum signal as a function of delamination depth

Comparing the results in Table 4.21 and 4.22, it is seen that the time for maximum signal was slightly longer for delaminations than for debonds located at the same depth. The difference, however, was only on the order of 0.5 s. Figure 4.55 shows the time for maximum signal as a function of delamination depth. The time for maximum signal was a quadratic function of depth as follows:

$$t_s = 0.69d^2 + 4.19d + 0.10 \tag{4.38}$$

The difference in contrast varied from 1.41 to 0.48 for delaminations at depth between 0.5 and 2.5 mm, respectively. The maximum thermal contrast was also a power function of depth. The best fitting function was

$$C_{max} = 0.92d^{-0.56} \tag{4.39}$$

The maximum signal and maximum contrast values were lower than those values found for debonds at the same depth. The behavior can be explained by the fact that the background temperatures are higher for the delamination cases than for debonds. As a reminder, the thermal conductivity and diffusivity of concrete are higher than those of FRP. As a result, the background temperature of the simulations with debonds decreases at a higher rate than the background temperature of the delaminated test object.

The times for maximum signal and maximum contrast were longer for delaminations than for debonds located at the same depth. Some of these differences were on the order of 1 s to 1.5 s. The time for maximum contrast, although it is a quadratic function of depth, could be approximated as a linear function of depth without introducing a significant error; the linear function is as follows:

$$t_c = 9.37d - 0.39 \tag{4.40}$$

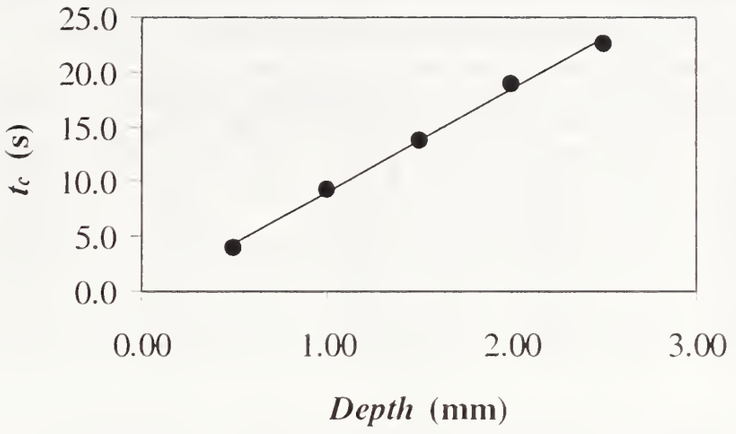

Fig. 4.56 Time for maximum contrast as a function of delamination depth

Figure 4.56 shows the FEM output and fitted linear function for the time for maximum contrast due to variations in delamination depth.

4.5.4c Concrete Spalls

The next set of simulations involved the study of concrete spalls. The study was divided into two different sets of models. First, the investigation focused on the case where the spall is located at 2 mm from the concrete/FRP interface, and the number of plies of FRP was increased from 1 to 5. For the second set of simulations, there were two FRP plies and the depth of the flaw in the concrete was varied. In presenting results, these simulations are called "set No. 3" and "set No. 4", respectively.

Tables 4.23 and 4.24 summarize the results for these two sets of simulations.

Table 4.23 Results for simulations involving concrete spalls with 1 to 5 plies of FRP (third set of simulations in parametric study #3)

Case	Depth, d (mm)	T_{max} (°C)	Maximum Signal		Maximum Contrast	
			t_s (s)	ΔT_{max} (°C)	t_c (s)	$\Delta T_{max}/\Delta T_{backg}$
54	2.5	46.2	11.76	2.22	19.06	0.62
55	3.0	48.0	15.90	1.66	24.95	0.53
56	3.5	48.5	19.85	1.22	29.55	0.42
57	4.5	48.6	30.50	0.72	43.15	0.29

Table 4.24 Results for simulations involving concrete spalls with 2 plies of FRP (fourth set of simulations in parametric study #3)

Case	Depth, d (mm)	T_{max} (°C)	Maximum Signal		Maximum Contrast	
			t_s (s)	ΔT_{max} (°C)	t_c (s)	$\Delta T_{max}/\Delta T_{backg}$
45	1.0	51.7	4.45	8.16	8.05	1.23
58	1.5	48.8	7.05	4.56	12.05	0.91
59	2.0	48.2	9.52	3.06	16.05	0.74
60	2.5	48.1	12.65	2.20	20.35	0.62
55	3.0	48.0	15.90	1.66	24.95	0.53

The first observation is that the maximum surface temperature increases with increasing flaw depth for set No. 3, while it decreases for set No. 4. For both cases, the behavior is easily explained in terms of the thermal properties of the materials. For the previous sets of simulations (debonds and delaminations), the maximum surface temperature was highly related to the depth of the flaw. For the cases involving concrete spalls, however, the depth of the defect has a lesser effect on the maximum surface temperatures. The reason is that the flaw is too deep in the test object to affect the thermal response at early times during the test. The thickness of the FRP and concrete cover has an important role on the development of maximum surface temperature. For example, the maximum surface temperature for set No. 3 increases as the thickness of FRP increases. The reason for this is that FRP has lower k and α than concrete, thus there is a lower rate of diffusion. With increasing number of plies, the heat tends to concentrate at the upper layers of the FRP instead of being diffused through the concrete. The opposite is true for set No. 4. As concrete cover over the spall increases, the thermal energy diffuses through the test object more readily and the maximum surface temperature decreases with flaw depth.

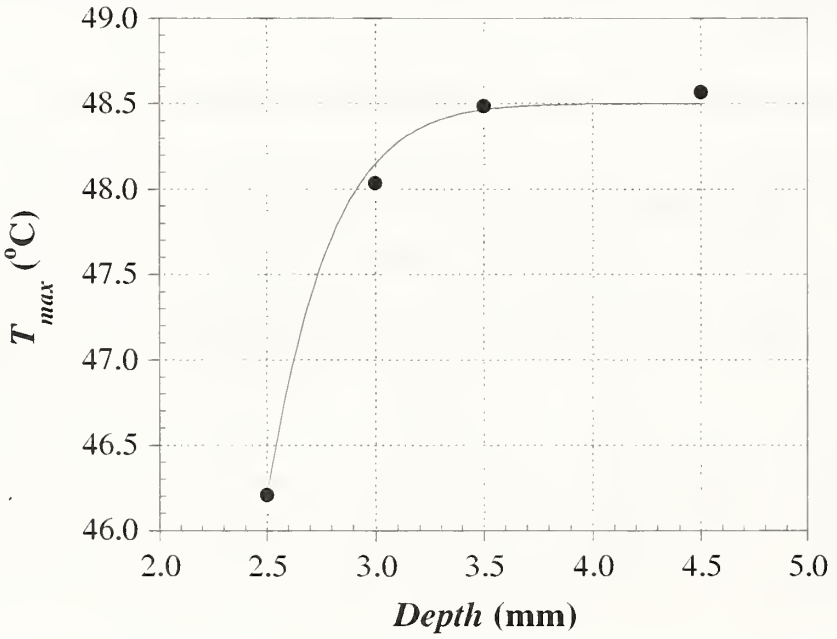

Fig. 4.57 Maximum surface temperature as a function of spall depth for set No. 3 (variable number of plies)

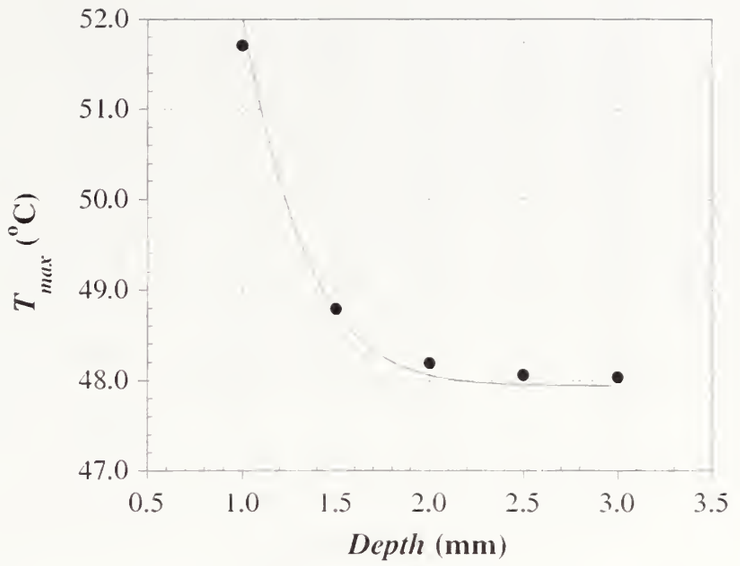

Fig. 4.58 Maximum surface temperature as a function of spall depth for No. 4 (2 plies)

As indicated in Tables 4.23 and 4.24, the maximum surface temperatures only varied by 2.4 °C for set No. 3 and 3.7 °C for set No. 4. Figure 4.57 shows the finite element output and the best-fit curve expressed for the set No. 3. Figure 4.58 illustrates the finite element output for the second set of concrete spall simulations (set No. 4).

The results for the maximum signal and maximum contrast displayed nonlinear behavior similar to that for debonds and delaminations. The change in magnitude, however, was smaller than for the previous type of flaws. For example, the change in maximum thermal signal for set No. 3 was only 1.5 °C for an increase in depth of 2 mm (from 2.5 mm to 4.5 mm). The change in maximum contrast was 0.33 for this case. The change in maximum signal and maximum contrast was slightly higher for the second set of concrete spalls problems. For this case, the decrease in maximum thermal signal and contrast was 6.5 °C and 0.70, respectively, for an increase in depth of 2 mm (from 1 mm to 3 mm).

The decrease of the maximum thermal signal and contrast could be described by power functions. For the first set of concrete spalls (set No. 3) the thermal signal and thermal contrast decreased as

$$\Delta T_{max} = 12.51\, d^{-1.86} \tag{4.56}$$

$$C_{max} = 1.95\, d^{-1.24} \tag{4.57}$$

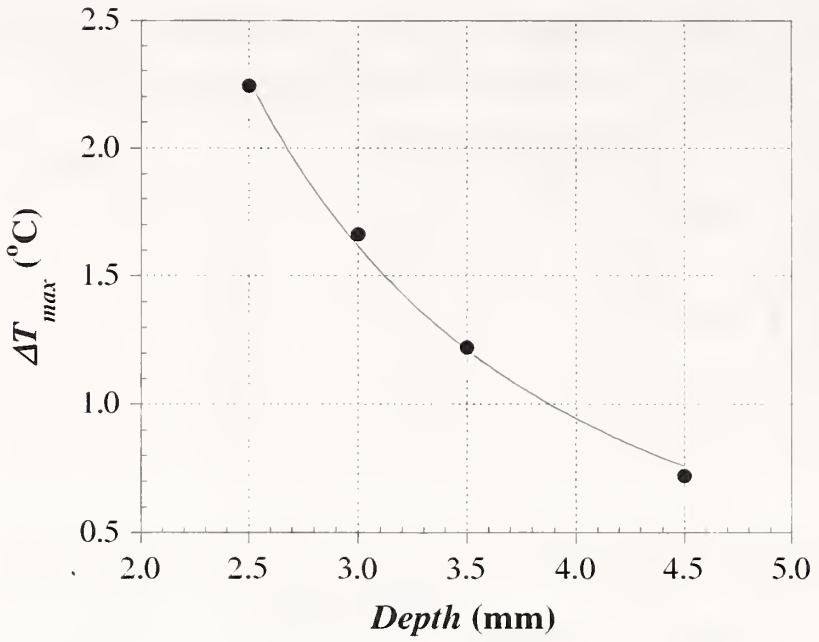

Fig. 4.59 Maximum signal as a function of spall depth for set No. 3 (variable number of plies)

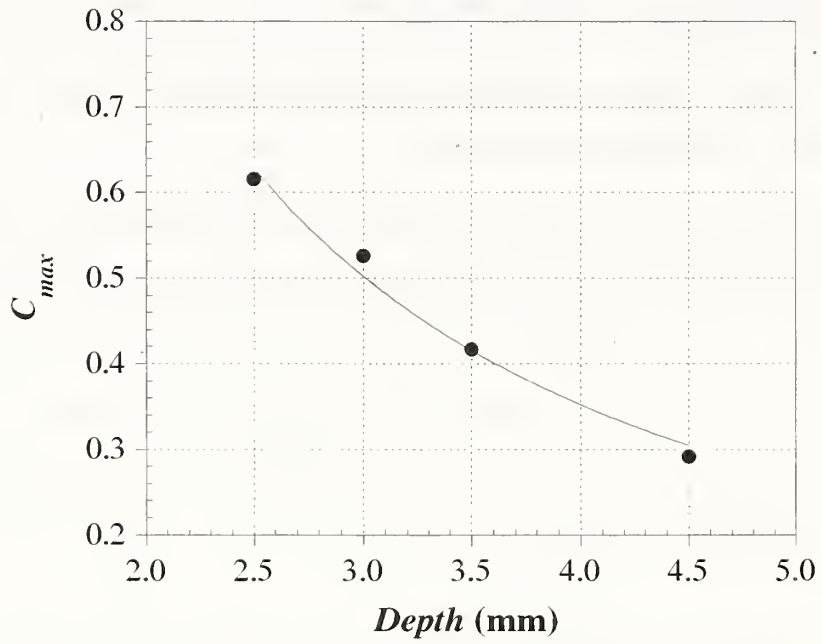

Fig. 4.60 Maximum contrast as a function of spall depth for set No. 3 (variable number of plies)

Figures 4.59 and 4.60 show the maximum signal and maximum contrast, respectively, as a function of the spall depth for set No. 3.

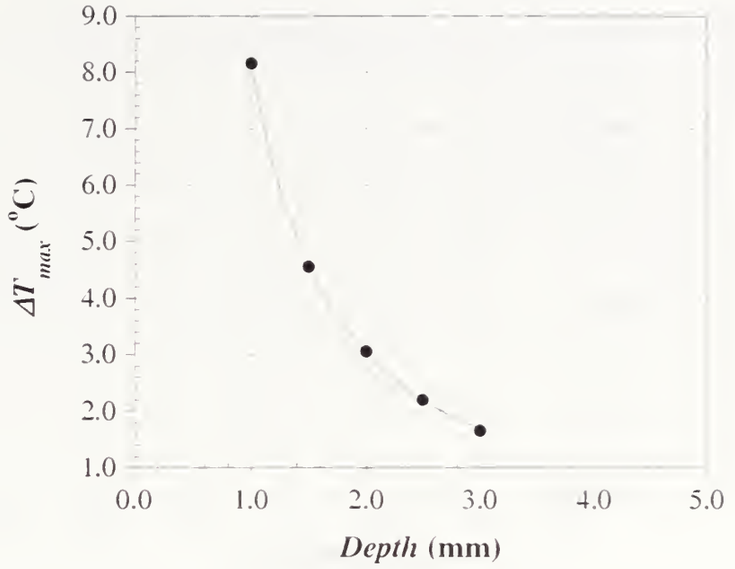

Fig. 4.61 Maximum signal as a function of spall depth for set of No. 4 (2 plies)

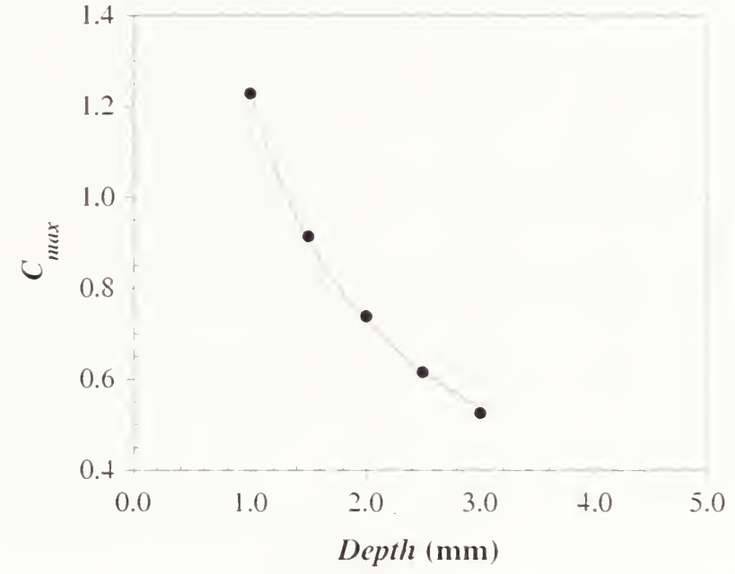

Fig. 4.62 Maximum contrast as a function of spall depth for set No. 4 (2 plies)

As shown in Figs. 4.61 and 4.62, the maximum signal and maximum contrast for the second set of concrete spalls (set No. 4) followed the following functions of depth:

$$\Delta T_{max} = 8.16\, d^{-1.43} \tag{4.58}$$

$$C_{max} = 1.23\, d^{-0.76} \tag{4.59}$$

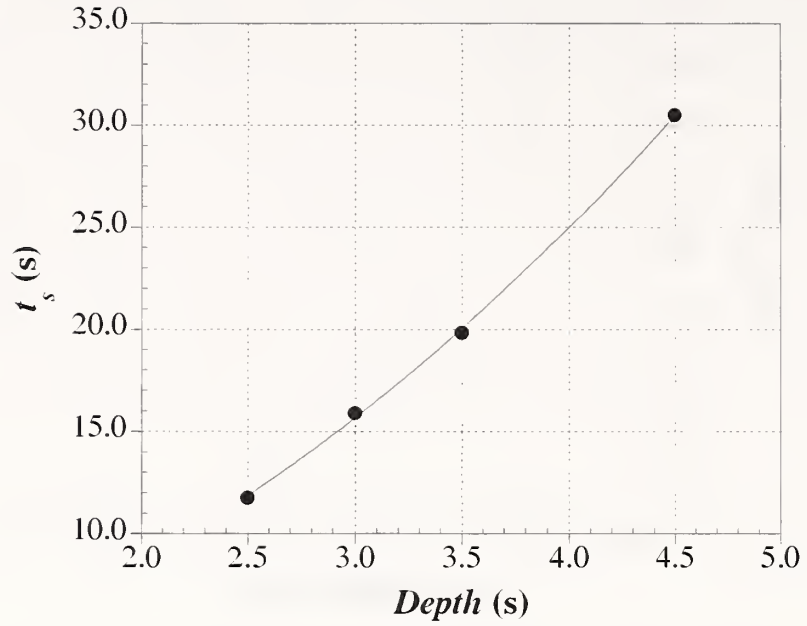

Fig. 4.63 Time for maximum signal for set No. 3 (spall at 2 mm with varying number of FRP layers)

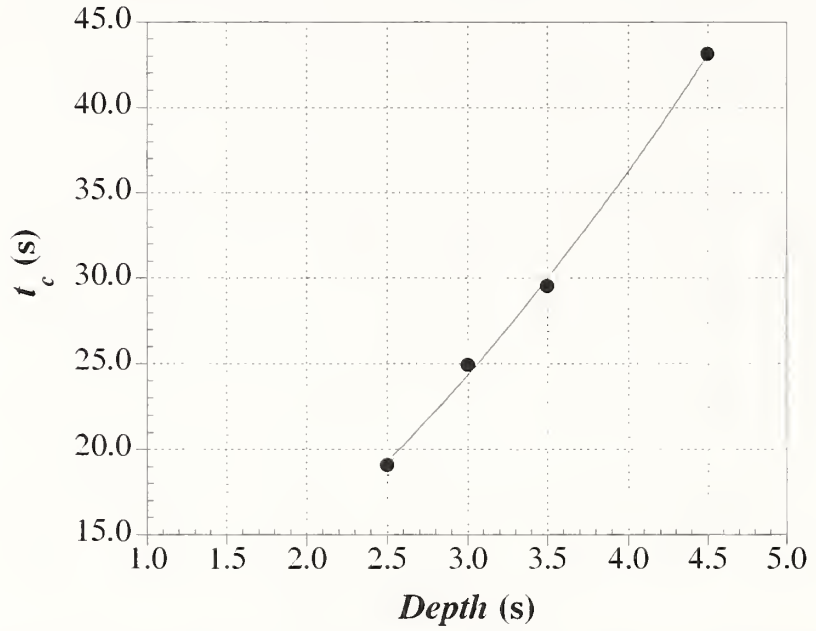

Fig. 4.64 Time for maximum contrast for problem set No. 3 (spall at 2 mm with varying number of FRP layers

As shown in Figs. 4.63 and 4.64, the time for maximum signal and maximum contrast for problem set No. 3 could be fitted by the following quadratic functions:

$$t_s = 1.129\,d^2 + 1.411\,d + 1.272 \tag{4.60}$$

$$t_c = 1.178\,d^2 + 3.646\,d + 2.807 \tag{4.61}$$

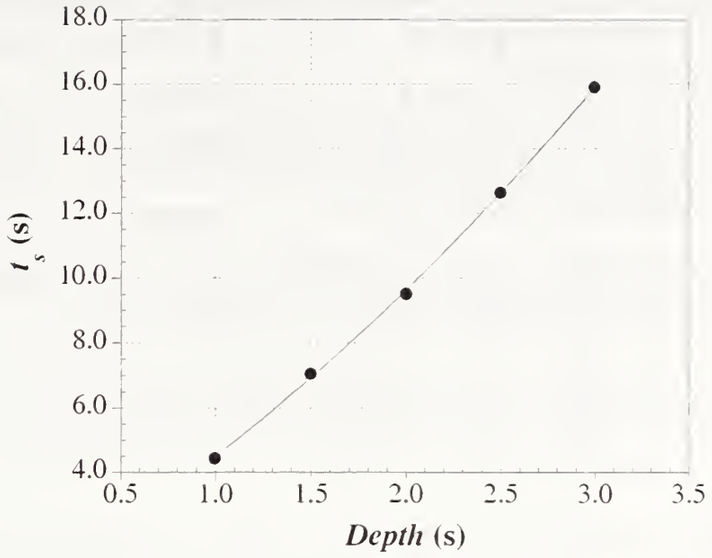

Fig. 4.65 Time for maximum signal for set No. 4 (2 layers of FRP and varying spall depth)

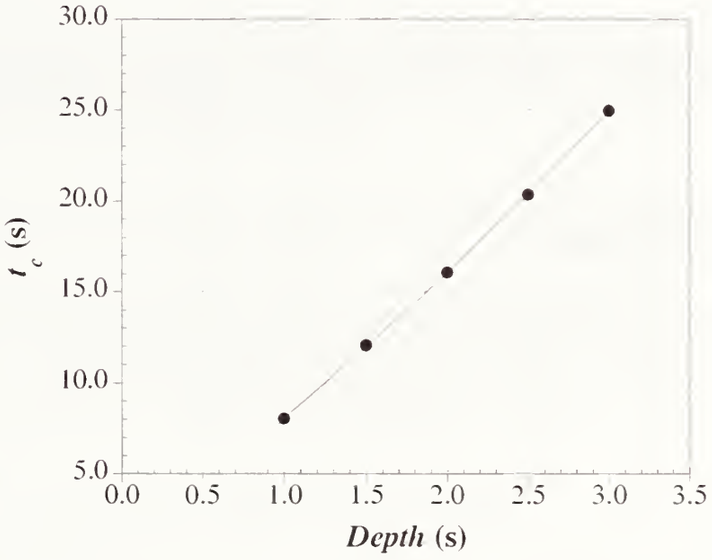

Fig. 4.66 Time to maximum contrast for set No. 4 (2 layers of FRP and varying spall depth)

As shown in Figs. 4.65 and 4.66, the time for maximum signal and maximum contrast could also be fitted using quadratic functions as follows:

Summarizing, this phase of the analysis provided some understanding of the effect of flaw depth on the thermal response:

- The maximum surface temperature is the same for delaminations and debonds located at the same depth (Tables 4.21 and 4.22).

- The maximum surface temperature decreases nonlinearly with increasing flaw depth. The variation of maximum surface temperature with flaw depth can be described using the error function (Figs. 4.50, 4.57, and 4.58).

- Debonds and delaminations located at the same depth result in approximately equivalent values of maximum signal (Figs. 4.52 and 4.54).

- Concrete spalls result in higher maximum thermal signals and contrasts than delaminations and debonds located at the same depth (Tables 4.21 through 4.24).

- The time for maximum signal increases with the depth of the flaw. The time for detection increases nonlinearly for debonds and delaminations and approximately linearly for concrete spalls (Figs. 4.53, 4.55, 4.63, and 4.65).

- Debonds are detected sooner than delaminations located at the same depth. For test objects with flaws at the same depth, the time for maximum contrast and signal increases with the number of FRP plies. The reason is that FRP has lower diffusivity than concrete. Hence, the higher the thickness of FRP the slower the rate of diffusion. For the investigated flaw size, however, the increase in time is less than one second (Tables 4.21 and 4.22).

- For the case of concrete spalls located at the same depth, the more layers of FRP the lower the maximum surface temperatures and the higher the maximum thermal signal (Tables 4.23 and 4.24).

4.5.4d Estimation of Depth

The FEM results reveal that the thermal response is a function of both the thickness of the FRP layer and the depth of the flaw. For the purpose of depth estimation, a simple procedure was developed based on the maximum thermal signal and contrast as a function of flaw depth.

Three sets of simulations were completed involving three different test objects with flaws at varying depths. Sets No. 5, No .6, and No .7 involved test objects with 5, 3, and 2 plies of FRP, respectively. For each set, the depth of the flaw was varied to include delaminations, debonds, and concrete spalls at different depths.

The results revealed thermal responses that followed the trends of power functions. Thus the basic form of the thermal response (ΔT_{max} or maximum contrast and corresponding times) is

$$Thermal\ response = \gamma\, d^{\varepsilon} \tag{4.62}$$

where,

d = depth of the flaw;
γ = coefficient; and
ε = exponent.

The best fitting power functions for simulation sets No. 5, No. 6, and No. 7 are presented in Table 4.25.

Table 4.25 Summary of relationships between thermal responses and flaw depth for simulations sets No. 5, 6, and 7.

No. of plies	Thickness of FRP, d_{FRP}	ΔT_{max} (°C)	C_{max}	t_s (s)	t_{ct} (s)
5	2.5 mm	$\frac{6.89}{d^{1.46}}$	$\frac{0.90}{d^{0.71}}$	$5.15d^{1.15}$	$8.72d^{1.08}$
3	1.5 mm	$\frac{7.34}{d^{1.39}}$	$\frac{1.03}{d^{0.67}}$	$5.03d^{1.06}$	$8.58d^{0.96}$
2	1.0 mm	$\frac{7.77}{d^{1.37}}$	$\frac{1.16}{d^{0.68}}$	$4.82d^{1.03}$	$8.42d^{0.95}$

The equations displayed in Table 4.25 indicate that the coefficients decrease with increasing number of FRP plies. The exponents, however, show increasing trends with increasing number of FRP plies.

Based on these results, an estimation procedure was developed. The steps are as follow:

- Estimate the depth of the FRP layer (in mm).
- Based on the thickness of the FRP, estimate the coefficient and exponents for the maximum signal, contrast, time for maximum signal, and time for maximum contrast.

  For the maximum thermal signal the coefficient and exponent are:

$$\gamma_{signal} = 7.76\, d_{FRP}^{-0.13} \tag{4.63}$$

$$\varepsilon_{signal} = -0.0648 d_{FRP} - 1.3004 \tag{4.64}$$

  For the maximum thermal contrast, the coefficient and exponent are:

$$\gamma_{contrast} = 1.1613\, d_{FRP}^{-0.275} \tag{4.65}$$

$$\varepsilon_{contrast} = -0.0537 d_{FRP} - 0.615 \tag{4.66}$$

  For the time for maximum signal, the coefficient and exponent are:

$$\gamma_{ts} = 4.8489 d_{FRP}^{0.0697} \tag{4.67}$$

$$\varepsilon_{ts} = 0.0816 d_{FRP} + 0.943 \tag{4.68}$$

  For the time for maximum thermal contrast, the coefficient and exponent are:

$$\gamma_{tc} = 8.4324 d_{FRP}^{0.037} \tag{4.69}$$

$$\varepsilon_{tc} = 0.867 d_{FRP} + 0.852 \tag{4.70}$$

where, d_{FRP} is the thickness of the FRP layer.

- The coefficients and exponents determined in the previous step provide the exponential equations for the thermal signal, contrast, time for maximum signal, and time for maximum contrast for flaws at any depth. These flaws include delaminations, debonds, and concrete spalls. Therefore,

$$\Delta T_{max} = \gamma_{signal}\, d^{\varepsilon_{signal}} \tag{4.71}$$

$$C_{max} = \gamma_{contrast}\, d^{\varepsilon_{contrast}} \tag{4.72}$$

$$t_s = \gamma_{ts}\, d^{\varepsilon_{ts}} \tag{4.73}$$

$$t_c = \gamma_{tc}\, d^{\varepsilon_{tc}} \tag{4.74}$$

where,

d = depth of the flaw;
ΔT_{max} = maximum thermal signal;
t_s = time to maximum signal; and,
t_c = time to maximum contrast.

- Inversion of Eqs. 4.71 through 4.74 allow the estimation of the depth of the flaw based on the thermal response of the test object.

$$d = exp\left[\frac{ln(\Delta T_{max}) - ln(\gamma_{signal})}{\varepsilon_{signal}}\right] \tag{4.75}$$

$$d = exp\left[\frac{ln(C_{max}) - ln(\gamma_{contrast})}{\varepsilon_{contrast}}\right] \tag{4.76}$$

$$d = exp\left[\frac{ln(t_s) - ln(\gamma_{ts})}{\varepsilon_{ts}}\right] \tag{4.77}$$

$$d = exp\left[\frac{ln(t_c) - ln(\gamma_{tc})}{\varepsilon_{tc}}\right] \tag{4.78}$$

It is important to note that these equations are appropriate for the test object under study.

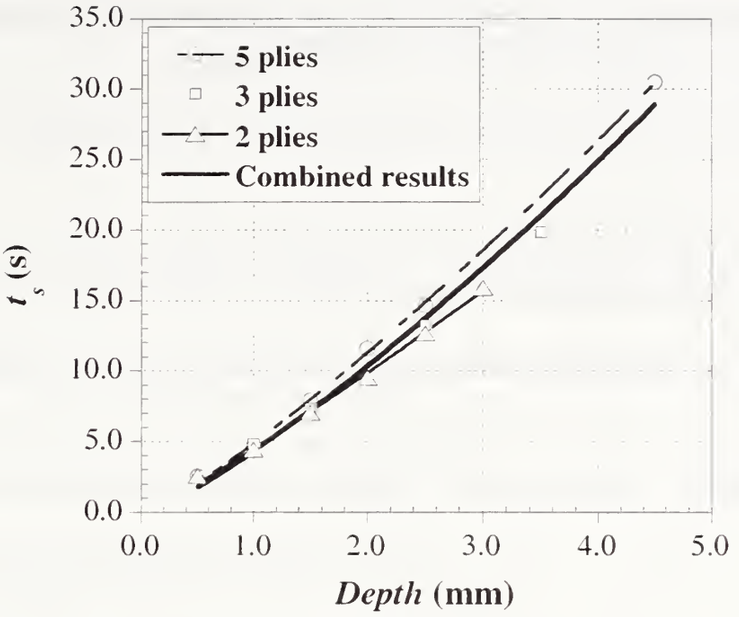

Fig. 4.67 Time for maximum signal as a function of flaw depth for test objects with 5, 3, and 2 layers of FRP

The flaw depth can also be estimated graphically. Figure 4.67 shows of the time for maximum signal as a function of flaw depth for test objects with 5, 3, and 2 plies of FRP. Based on the measured time to maximum signal, the flaw depth can be estimated. This procedure is simpler than the analytical approach and it provides an adequate estimate of the flaw depth.

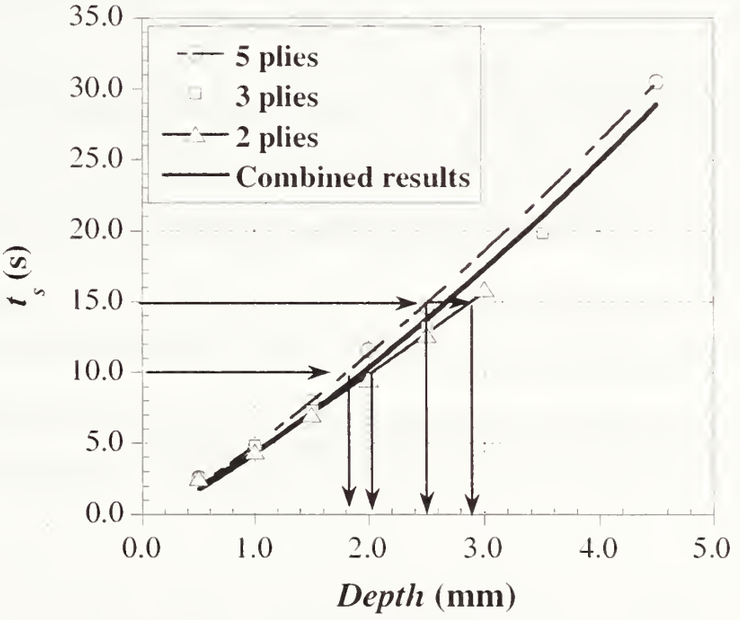

Fig. 4.68 Example of estimation of flaw depth

As illustrated in Fig. 4.68, for example, for a 10 s time for maximum signal, the estimated flaw depth is 1.8 mm for the case of a 5-ply test object, while it is 2.0 mm for a test object containing 2 layers of FRP. For this case, the estimation of flaw depth varies only by 0.2 mm. This value is less than the thickness of an FRP layer. For a long detection period, lets say 15 s for maximum signal, the estimated flaw depth is 2.5 mm for test objects containing 5 layers of FRP and 2.9

mm for test objects containing 2 layers of FRP. The estimation of the flaw depth varied slightly by only 0.4 mm, again, less than the thickness of an FRP layer.

4.5.5 Summary

The third parametric study focused on the effect of flaw depth on the thermal response. The parametric study had the following objectives:

- Understand the effect of delamination, debonds, and concrete spalls on the thermal response; and,

- Investigate the feasibility of estimating flaw depth from the measured thermal response.

Five sets of analyses, including 21 FEM simulations, were performed to evaluate the effect of flaw depth on the thermal response of the test object. Two different parameters were varied: the depth of the flaw and the number of FRP plies. These changes made possible the study of delaminations, debonds, and concrete spalls located at varying depths.

Several conclusions were reached from the results:

- The maximum surface temperature decreases nonlinearly with increasing depth. The relationships can be described using error functions.

- The maximum surface temperature is the same for debonds and delaminations located at the same depth.

- Debonds develop higher thermal signal and contrast than delaminations located at the same depth.

- Concrete spalls develop higher thermal signal and contrast than delaminations and debonds located at the same depth.

- For flaws at the same depth, the thermal signal decreases with increasing thickness of FRP.

- The time for maximum signal and maximum contrast increases with the depth of the flaw. The time for detection increases nonlinearly for debonds and delaminations and near-linearly for concrete spalls.

- Debonds are detected sooner than delaminations located at the same depth. For test objects with flaws at the same depth, the time for maximum contrast and signal increases with the number of FRP plies. For the case of concrete spalls located at the same depth, the more layers of FRP the lower the maximum surface temperatures and the higher the maximum thermal signal.

- Concrete spalls take a couple of seconds less to be detected compared with debonds.

The investigation has led to a simple procedure to estimate depth based on measured time to maximum signal.

The next series of studies involve the investigation of the effect of the thickness (resistance) of the internal flaw.

4.6 Parametric Study No. 4: Effect of the Thickness of the Flaw

The thermal resistance of subsurface flaws is an additional parameter that affects the thermal response of the test object and thus the response parameters at its surface. The thermal resistance of the flaw is directly proportional to the thickness of the air void. Thus, it is helpful to investigate the effect of the thickness of internal flaws on the thermal response.

The fourth parametric study had the following objectives:

- Understand the effects of flaw thickness on the thermal response; and
- Establish the minimum thickness of a detectable flaw.

Three different sets of analyses were performed, which included a total of 15 simulations.

4.6.1 Geometry of Model

The test object consisted of a 100 mm long by 20 mm thick concrete slab with 3 layers of FRP bonded to its surface. Each 0.5 mm thick layer of FRP was oriented at 90° with respect to the adjacent ply. A 25 mm long internal flaw was located at the center of the test object. The thickness of the flaw was varied from 0.4 mm to 1 μm. The depth of the flaw was varied as well to include delamination, debond, and concrete spall. The delamination was located at a depth of 0.5 mm, the debond at 1.5 mm and the concrete spall at 2.5 mm.

As in previous simulations, plane two-dimensional modeling was used. The meshing was similar to that of parametric study No. 2.

The simulations were divided into 3 sets. The first set involved the study of the effect of thickness of delaminations on the thermal response. The second set involved the study of the effect of thickness of debonds. The third set involved the study of the effect of the thickness of concrete spalls.

Table 4.26 Geometry for simulation set involving delaminations

Case	Flaw depth (mm)	Flaw thickness (mm)	Thermal resistance ($m^2 \cdot °C/W$)
66	0.5	0.4	16.67×10^{-3}
67	0.5	0.2	8.33×10^{-3}
68	0.5	0.1	4.17×10^{-3}
69	0.5	0.05	2.08×10^{-3}
70	0.5	0.025	1.04×10^{-3}
71	0.5	0.001	0.04×10^{-3}

For the first set of simulations, the thickness of the air void was varied from 0.4 mm to 1 μm, which represent a range of thermal resistance of 1.7×10^{-2} $m^2 \cdot °C/W$ to 4.0×10^{-5} $m^2 \cdot °C/W$, as indicated in Table 4.26.

Table 4.27 Geometry for simulation set involving debonds

Case	Flaw depth (mm)	Flaw thickness (mm)	Thermal resistance ($m^2 \cdot °C/W$)
72	1.5	0.4	16.67×10^{-3}
73	1.5	0.2	8.33×10^{-3}
74	1.5	0.1	4.17×10^{-3}
75	1.5	0.05	2.08×10^{-3}
76	1.5	0.001	0.04×10^{-3}

The second set of simulations involved debonds between the FRP and the concrete. Again, the thickness of the air void varied between 0.4 mm and 1 mm. Five models were analyzed as indicated in Table 4.27.

Table 4.28 Geometry for simulation set involving concrete spalls

Case	Flaw depth (mm)	Flaw thickness (mm)	Thermal resistance ($m^2 \cdot °C/W$)
77	2.5	0.4	16.67×10^{-3}
78	2.5	0.2	8.33×10^{-3}
79	2.5	0.1	4.17×10^{-3}
80	2.5	0.05	2.08×10^{-3}

The final set of simulations focused on concrete spalls located at a depth of 1.0 mm below the FRP/concrete interface. Due to the depth of the flaw, detection of thinner air voids was not expected. Thus, the thickness of the spalls was varied from 0.4 mm to 0.05 mm. Four models were analyzed as indicated in Table 4.28.

Figure 4.69 summarizes the geometry of the three different sets of simulations.

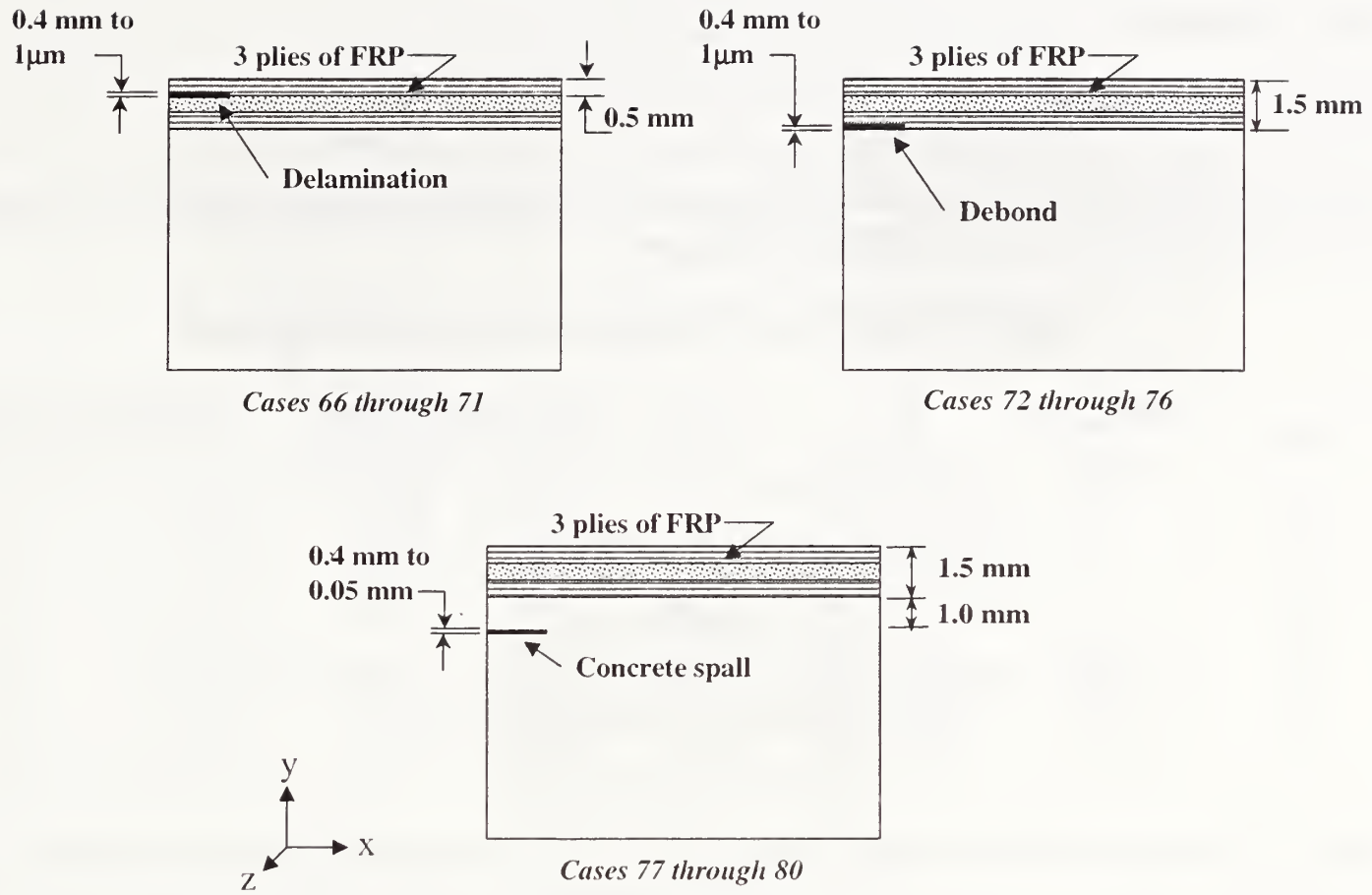

Fig. 4.69 Summary of models used to study effect of flaw thickness

4.6.2 Material Properties

The material properties of the model were those of concrete for the substrate, carbon FRP for the bonded composite, and air for the flaws (Table 4.7). As in previous parametric studies, the CFRP layer in direct contact with the substrate had fibers running in the x-direction. Each subsequent layer had its fiber direction rotated 90°.

4.6.3 Thermal Loading and Boundary Conditions

As in previous simulations, the analysis was defined as a transient heat transfer problem. A square pulse of intensity 20 000 W/m^2 with duration 2 s was applied to the top surface of the model. Adiabatic conditions ($dT/dx = 0$ and $dT/dz = 0$) were applied to the remaining free surfaces and at the axis of symmetry. The initial temperature of the model was 23 °C.

As in previous models, the simulations were performed using ANSYS automatic time stepping feature. The maximum and minimum time steps were 0.1 s and 0.008 s, respectively. The initial time step was 0.009 s. The FEM output was recorded at every time step.

4.6.4 Results

4.6.4a Delaminations

Table 4.29 summarizes the results of the first set of simulations, which focused on the study of 0.5 mm deep delaminations of different thickness.

Table 4.29 Results for simulations involving delaminations

Case	Thickness (mm)	R_{flaw} (m^2·°C/W)	T_{max} (°C)	Maximum Signal		Maximum Contrast	
				t_s (s)	ΔT_{max} (°C)	t_c (s)	$\Delta T_{max}/\Delta T_{backg}$
66	0.4	16.67×10^{-3}	88.6	2.73	44.4	6.63	4.71
67	0.2	8.33×10^{-3}	71.2	2.73	27.2	5.73	2.68
68	0.1	4.17×10^{-3}	64.9	2.53	18.5	4.43	1.54
69	0.05	2.08×10^{-3}	59.7	2.34	12.2	3.44	0.86
70	0.025	1.04×10^{-3}	55.5	2.24	7.4	2.84	0.46
71	0.001	0.04×10^{-3}	48.8	2.08	0.3	2.35	0.02

Table 4.29 indicates the thickness of the air void and its equivalent thermal resistance, R_{flaw}. Although the primary source of flaws in FRP composites bonded to concrete is air (e.g. bubbles entrapped in the epoxy matrix or cracks in the concrete), the results of the study can be generalized to any material by using the equivalent thermal resistance of the air void modeled in the study. Thermal resistance allows the representation of flaws of any thickness and any material, not just air voids. Thermal resistance of a flaw is defined as (Özişik, 1985)

$$R_{flaw} = \frac{\Delta z}{k_{flaw}} \tag{4.79}$$

where

Δz = thickness of the flaw; and
k_{flaw} = thermal conductivity of the flaw material.

The results summarized in Table 4.29 indicate some interesting aspects of the effect of flaw thickness or thermal resistance on the thermal response. The data reveal that the thermal response varies nonlinearly due to changes in the thermal resistance of the flaw. In general, thermal responses increase with increasing flaw thickness.

The maximum surface temperature, T_{max}, increases nonlinearly with increasing thermal resistance, and the relationship could be represented as a power function:

$$T_{max} = 47.2 + 266 R_{flaw}^{0.5} \tag{4.80}$$

where

R_{flaw} = thermal resistance of the flaw.

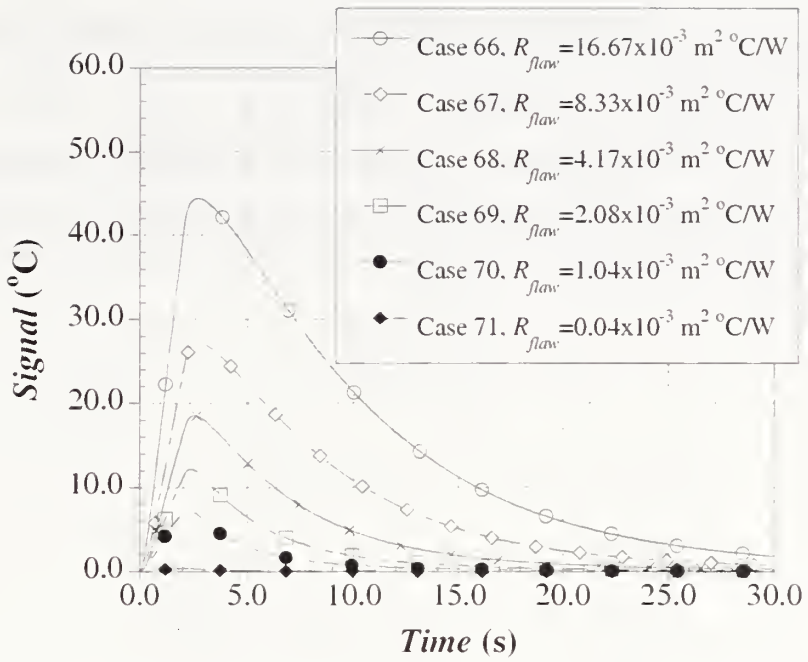

Fig. 4.70 Thermal signal for simulations involving delaminations of different thickness (Cases 66 through 71)

The results for the thermal signal as a function of time are presented in Fig. 4.70. Qualitatively, the results show that while the magnitude of the signal varies significantly with increasing resistance, changes in the time for maximum signal are negligible.

The maximum thermal signal as a function of thermal resistance could also be represented using a power function as follows:

$$\Delta T_{max} = 606\, R_{flaw}^{0.64} \tag{4.81}$$

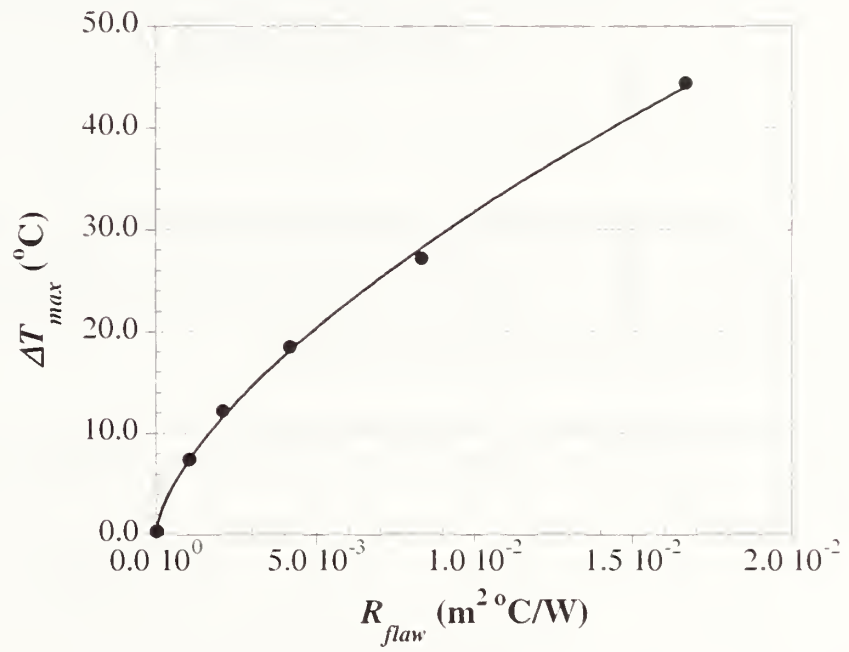

Fig. 4.71 Maximum thermal signal as a function of thermal resistance of the delamination

The FEM output and power fit function are presented in Fig. 4.71.

The time for maximum signal also increases nonlinearly with increasing thermal resistance of the flaw. As previously mentioned, changes in t_s are negligible since t_s only increases by a fraction of a second for changes in thermal resistance from 16.67×10^{-3} $m^2 \cdot °C/W$ to 0.04×10^{-3} $m^2 \cdot °C/W$. Once the thickness of the flaw becomes significant (i.e., thicker than 0.2 mm) the time for maximum signal does not vary for the case of a delamination in the upper layer of FRP. The increase in time for maximum signal can be represented as a power function:

$$t_s = 2.0 + 7.9 R_{flaw}^{0.5} \tag{4.82}$$

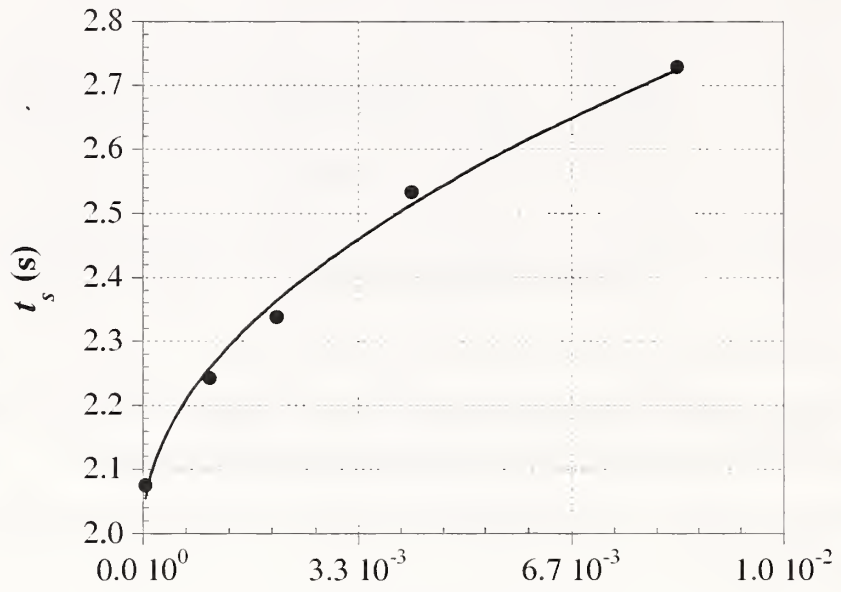

Fig. 4.72 Time for maximum signal as a function of flaw thermal resistance

It is important to note that equation 4.82 represents the increase in t_s for flaw thickness up to 0.02 mm. The case of a flaw thickness of 0.4 mm (case 66) is not considered since t_s becomes asymptotic for large values of R_{flaw}. Figure 4.72 presents the FEM output and the power fit of the time for maximum signal for cases 67 through 71.

The thermal contrast versus time curves for simulations 67 through 71 are presented in Fig. 4.73. The results show that the magnitude and the time to maximum contrast are both affected by the thermal resistance of the flaw.

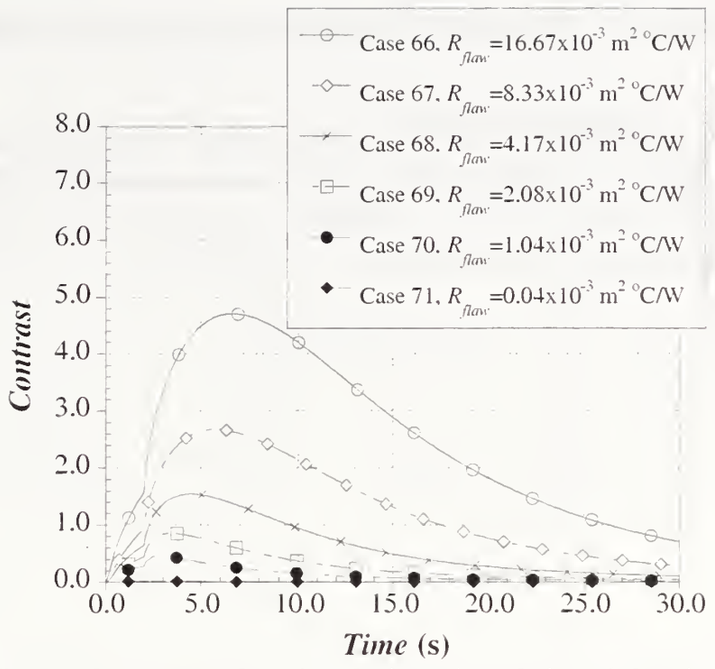

Fig. 4.73 Thermal contrast for simulations involving delaminations of different thickness (Cases 66 through 71)

Figure 4.73 reveals that the maximum thermal contrast increases with increasing thermal resistance of the flaw. The increase in maximum thermal contrast as a function of the thermal resistance of the flaw can be represented with the following equation:

$$C_{max} = 133 R_{flaw}^{0.82} \tag{4.83}$$

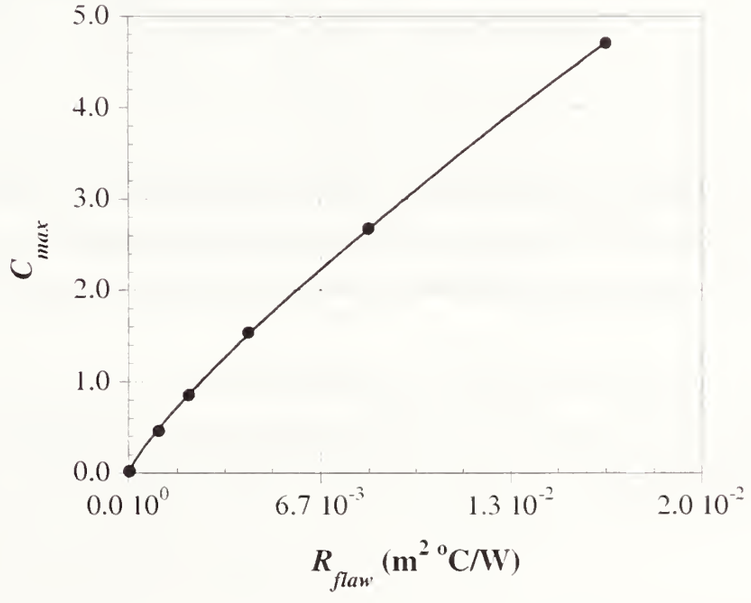

Fig. 4.74 Maximum contrast as a function of thermal resistance of delamination (Cases 66 through 71)

Figure 4.74 shows the maximum thermal contrast versus thermal resistance for the first set of simulations.

The time for maximum contrast, t_c, is more sensitive to changes in thermal resistance than the time for maximum signal. For example, the time for maximum contrast increases by 4.3 s for R_{flaw} ranging from 0.04×10^{-3} m^2·°C/W to 16.67×10^{-3} m^2·°C/W. The increase in t_c is nonlinear and could be represented using the following power function:

$$t_c = 2 + 36.8 R_{flaw}^{0.5} \tag{4.84}$$

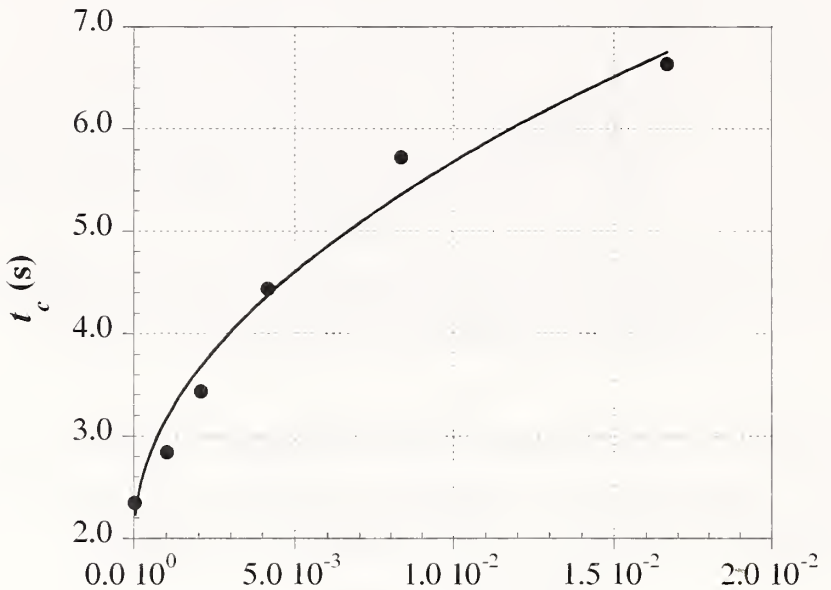

Fig. 4.75 Time for maximum contrast as a function of thermal resistance of delamination (Cases 66 through 71)

Figure 4.75 illustrates the output from the FEM simulations and the power fit for t_c versus R_{flaw}.

Comparison of Eqs. 4.82 and 4.84 indicates than changes in the time for maximum contrast as a function of flaw resistance are more pronounced than for the time to maximum signal.

4.6.4b Debonds

Table 4.30 summarizes the results of the second set of simulations, which focused on the study of debonds of different thickness.

Table 4.30 Results for simulations involving debonds

Case	Thickness (mm)	R_{flaw} ($m^2 \cdot °C/W$)	T_{max} (°C)	Maximum Signal		Maximum Contrast	
				t_s (s)	ΔT_{max} (°C)	t_c (s)	$\Delta T_{max}/\Delta T_{backg}$
72	0.4	16.67×10^{-3}	49.7	9.55	8.17	18.25	1.95
73	0.2	8.33×10^{-3}	49.3	8.55	6.10	14.32	1.31
74	0.1	4.17×10^{-3}	49.1	7.35	4.41	12.05	0.84
75	0.05	2.08×10^{-3}	48.9	6.45	2.91	9.85	0.49
76	0.001	0.04×10^{-3}	48.5	4.85	0.09	6.85	0.01

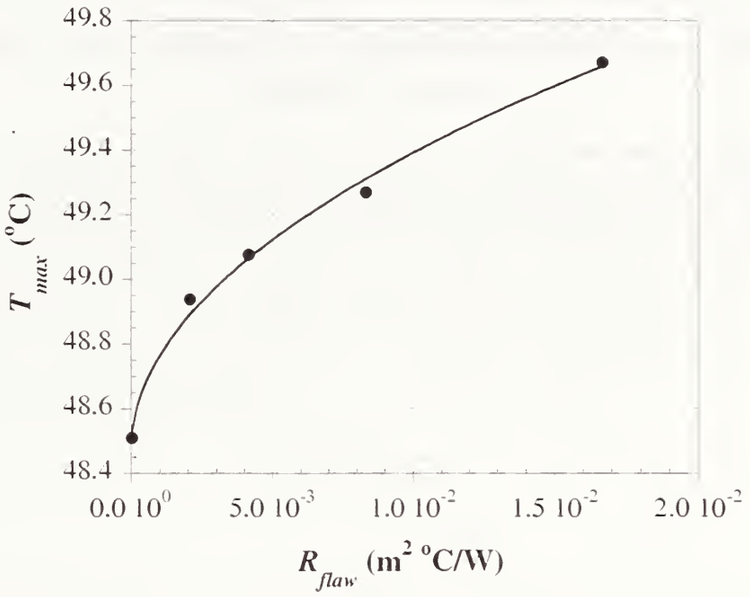

Fig. 4.76 Maximum surface temperature as a function of thermal resistance of debond (Cases 72 through 76)

The results show that similarly to delaminations, thermal responses vary nonlinearly with increasing thermal resistance. For example, Fig. 4.76 shows that the maximum surface temperature increases nonlinearly with increasing R_{flaw}. The change in maximum surface temperature, however, is only 1.2 °C for an increase from 0.04×10^{-3} $m^2 \cdot °C/W$ to 16.67×10^{-3} $m^2 \cdot °C/W$ in thermal resistance of the flaw.

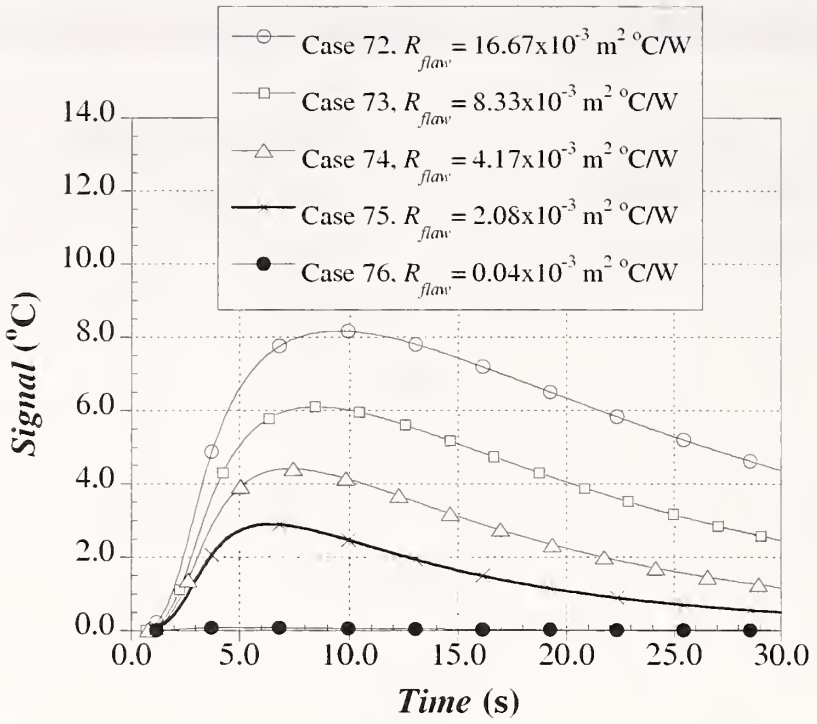

Fig. 4.77 Thermal signal for simulations involving debonds of different thickness (Cases 72 through 76)

The simulations suggest that the effect of R_{flaw} on the thermal signal is lower for the deeper debond than the shallower delamination. The thermal signal as a function of time is presented in Fig. 4.77.

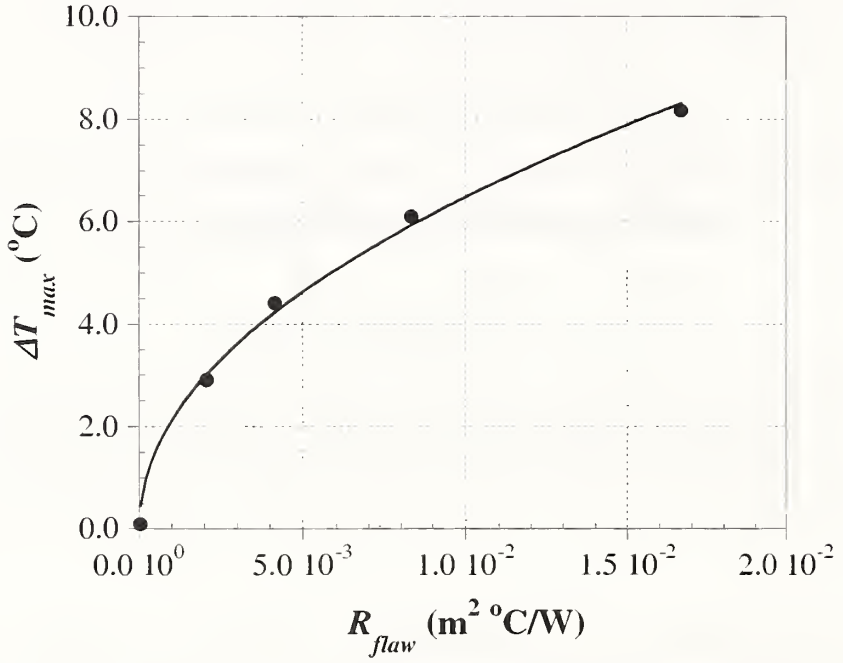

Fig. 4.78 Maximum signal as a function of thermal resistance of debonds (Cases 72 through 76)

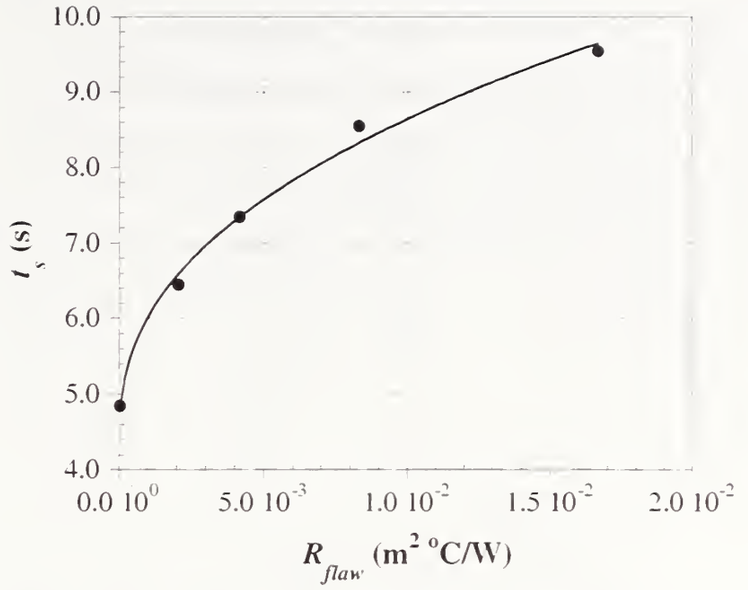

Fig. 4.79 Time for maximum signal as a function of thermal resistance of debonds (Cases 72 through 76)

The effect of thermal resistance of debonds on the maximum thermal signal follows similar trends to the case of delaminations. As shown in Fig. 4.78, the maximum signal increases nonlinearly with increasing R_{flaw}. The overall change in ΔT_{max} is about of 8.1 °C for increases of R_{flaw} from 0.04×10^{-3} m^2·°C/W to 16.67×10^{-3} m^2·°C/W. The results in Fig. 4.78 could be expressed as the following power function:

$$\Delta T_{max} = 60.9 R_{flaw}^{0.49} \tag{4.85}$$

As shown in Fig. 4.79, the time for maximum signal also increases nonlinearly with increasing flaw thermal resistance. Comparing Fig. 4.79 with Fig. 4.72 shows that the influence of R_{flaw}, however, is higher on the time to detect debonds than the time to detect delaminations. For example, an increase in R_{flaw} from 0.04×10^{-3} m^2·°C/W to 16.67×10^{-3} m^2·°C/W increases t_s by 4.7 s. The following power function could be used to represent the variation shown in Fig. 4.79:

$$t_s = 4.4 + 28.9 R_{flaw}^{0.4} \tag{4.86}$$

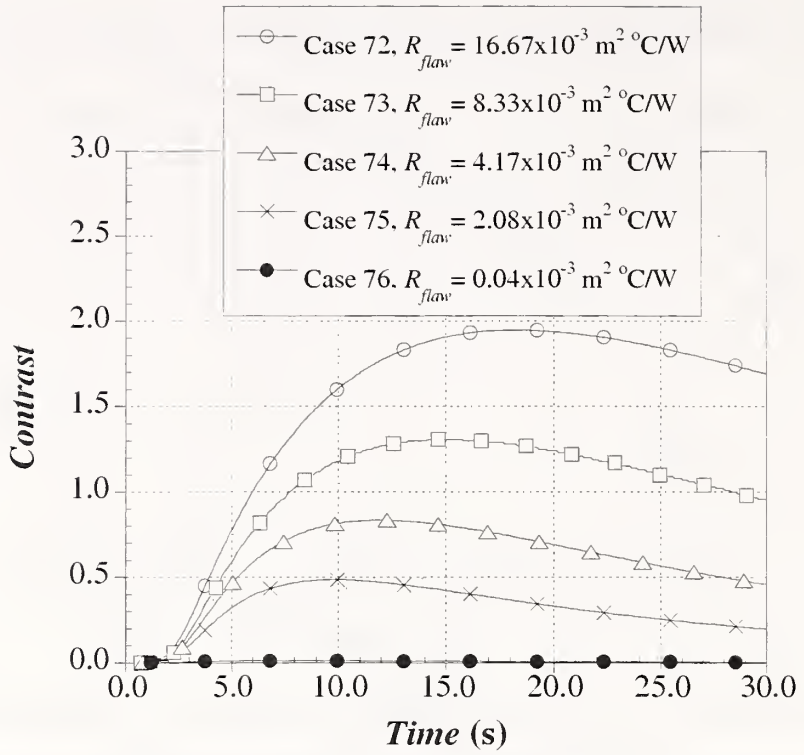

Fig. 4.80 Thermal contrast for simulations involving debonds of different thickness (Cases 72 through 76)

Comparison of Tables 4.27 and 4.26 indicates that variations in the thermal contrast are less pronounced for debonds than for delaminations. Figure 4.80 illustrates the thermal contrast as a function of time for the second set of simulations involving the effect of R_{flaw}.

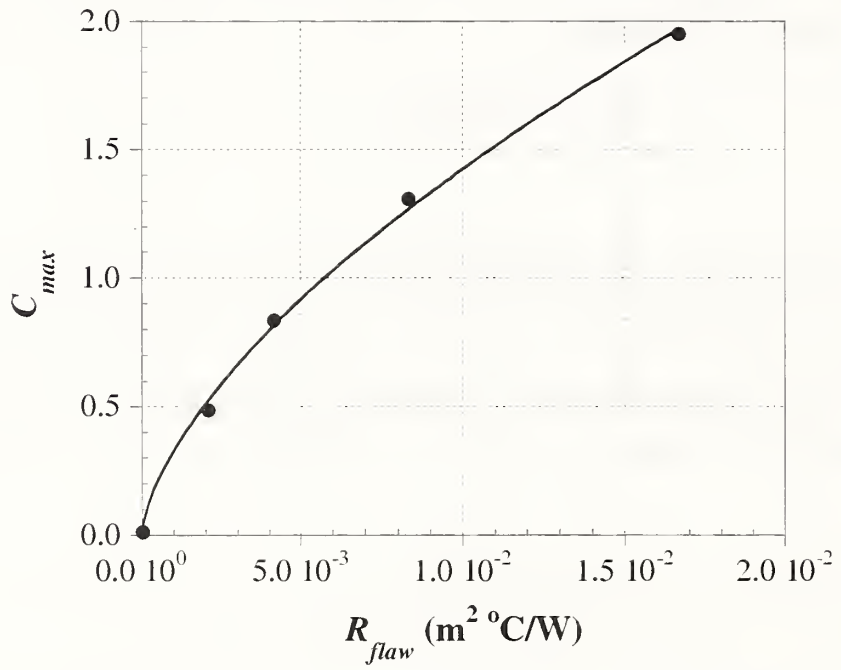

Fig. 4.81 Thermal contrast as a function of thermal resistance of debonds (Cases 72 through 76)

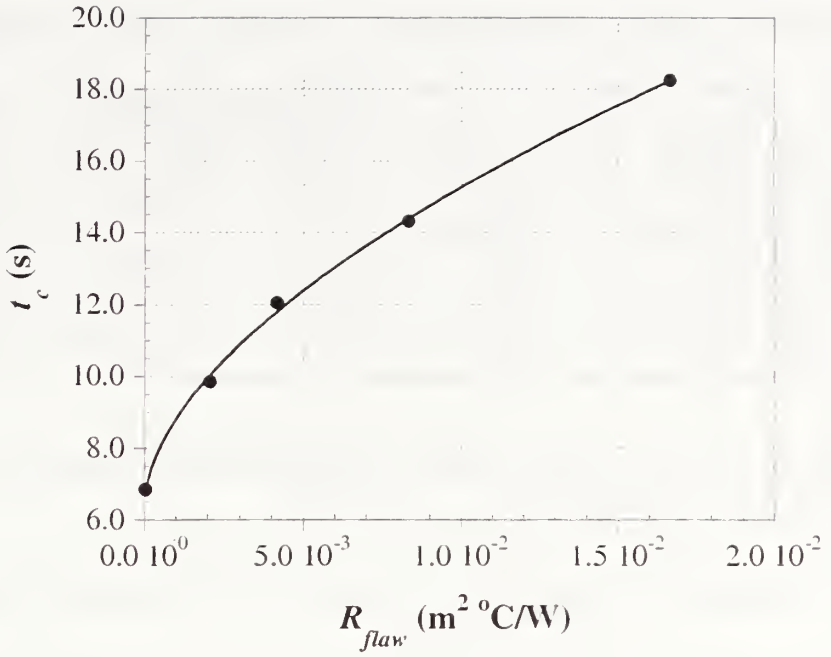

Fig. 4.82 Time for maximum contrast as a function of thermal resistance of debond (Cases 72 through 76)

The thermal contrast varies from 0.10 to 1.95 for values of thermal resistance from 0.04×10^{-3} m^2·°C/W to 16.67×10^{-3} m^2·°C/W. The effect of flaw thermal resistance on the maximum contrast is illustrated in Figure 4.81. The maximum contrast as a function of R_{flaw} could be expressed as the following power function:

$$C_{max} = 26.4 R_{flaw}^{0.63} \tag{4.87}$$

As expected, based on conclusions from parametric study No. 3, the time for maximum contrast was longer for debonds than for delaminations. The time for maximum contrast also increases nonlinearly with increasing R_{flaw}. The increase in time varies from 6.85 s to 18.25 s for debonds with thermal resistance ranging from 0.04×10^{-3} m^2·°C/W to 16.67×10^{-3} m^2·°C/W. The FEM output is presented in Figure 4.82.

Analysis of the FEM output suggests that the time for maximum contrast could be represented by the following power function:

$$t_c = 6.4 + 121.8 R_{flaw}^{0.6} \tag{4.88}$$

4.6.4c Concrete Spalls

The third set of simulations concentrated on the study of 2.5 mm deep concrete spalls and the effect that their thickness have on the thermal response. This set of studies involved test objects with flaw thickness between 0.4 mm and 0.05 mm. Thinner flaws were not considered since they were not expected to be detected. Results of the simulations are presented in Table 4.31.

Table 4.31 Results for simulations involving concrete spalls

Case	Thickness (mm)	R_{flaw} (m^2·°C/W)	T_{max} (°C)	Maximum Signal		Maximum Contrast	
				t_s (s)	ΔT_{max} (°C)	t_c (s)	$\Delta T_{max}/\Delta T_{backg}$
77	0.4	16.67×10^{-3}	48.5	16.5	3.89	29.3	1.26
78	0.2	8.33×10^{-3}	48.5	14.8	2.98	24.3	0.88
79	0.1	4.17×10^{-3}	48.5	12.9	2.14	19.8	0.57
80	0.05	2.08×10^{-3}	48.5	11.3	1.39	16.4	0.34

Observation of the simulation output indicates that variations in flaw thermal resistance have less effect for concrete spalls than for delaminations or debonds.

The maximum surface temperature varies insignificantly with increasing thermal resistance of concrete spalls.

The thermal signal as a function of time is presented in Fig. 4.83. Changes in the maximum signal as a function of thermal resistance of the 2.5 mm deep spall are quite small. For instance, the maximum signal increases only by 2.5 °C with increases in R_{flaw} from 2.08×10^{-3} m^2·°C/W to 16.67×10^{-3} m^2·°C/W. The variation in maximum signal is, again, nonlinear and could be represented as the following power function:

$$\Delta T_{max} = 26.2\, R_{flaw}^{0.46} \tag{4.89}$$

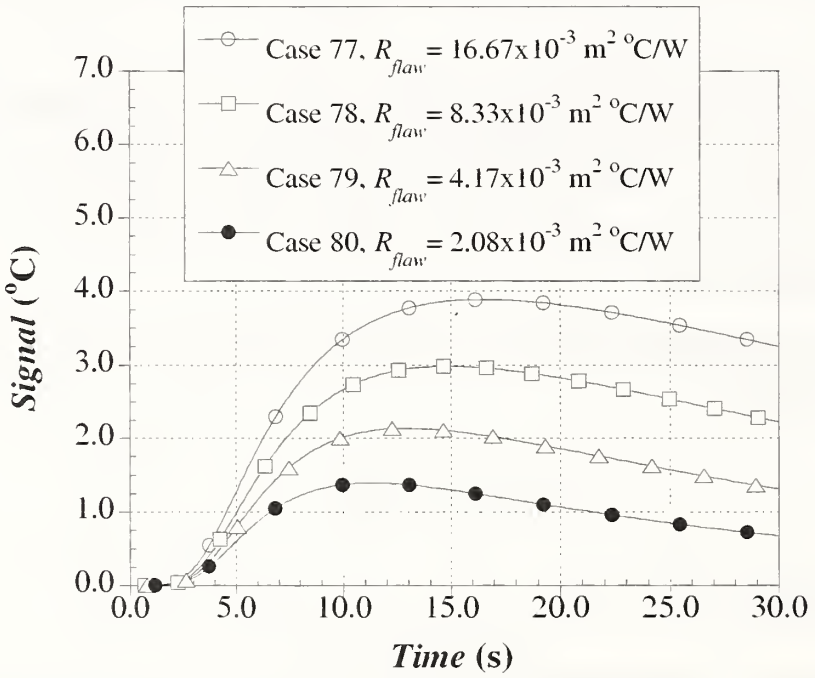

Fig. 4.83 Thermal signal for simulations involving concrete spalls of different thickness (Cases 77 through 80)

The FEM output and its power function fit are presented in Fig. 4.84.

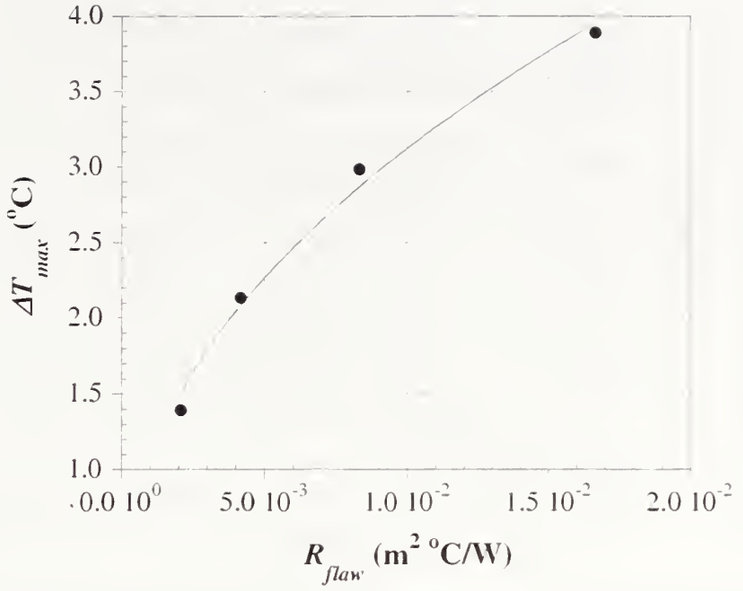

Fig. 4.84 Maximum thermal signal as a function of thermal resistance of spalls (Cases 77 through 80)

The time for maximum signal varies more significantly with R_{flaw} for concrete spalls than for delaminations and debonds. An increase of 5.2 s occurred for R_{flaw} ranging from 2.08×10^{-3} m^2·°C/W to 16.67×10^{-3} m^2·°C/W. Similarly to debonds and delaminations, the variation in t_s for concrete spalls varies as a power function. The equation that could be used to represent the time for maximum signal is

$$t_s = 35.0\, R_{flaw}^{0.2} \tag{4.90}$$

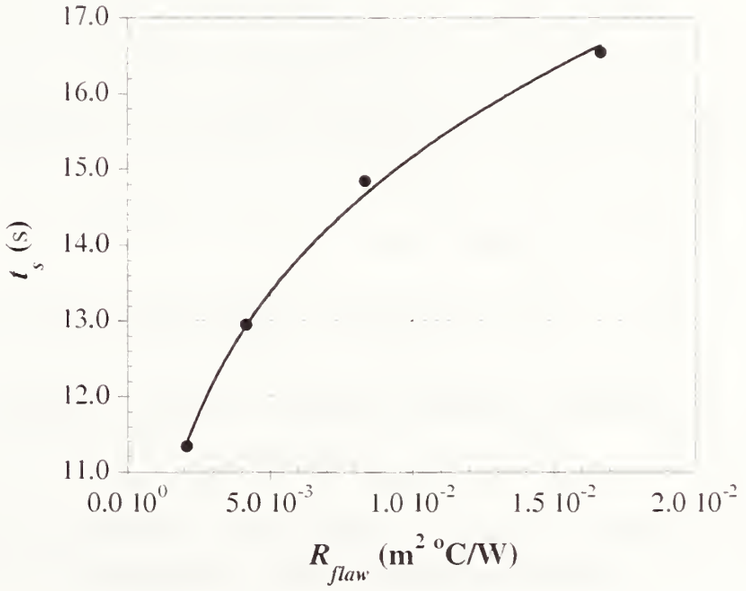

Fig. 4.85 Time for maximum signal as a function of thermal resistance of spalls (Cases 77 through 80)

Equation 4.90 and the results data are presented in Figure 4.85.

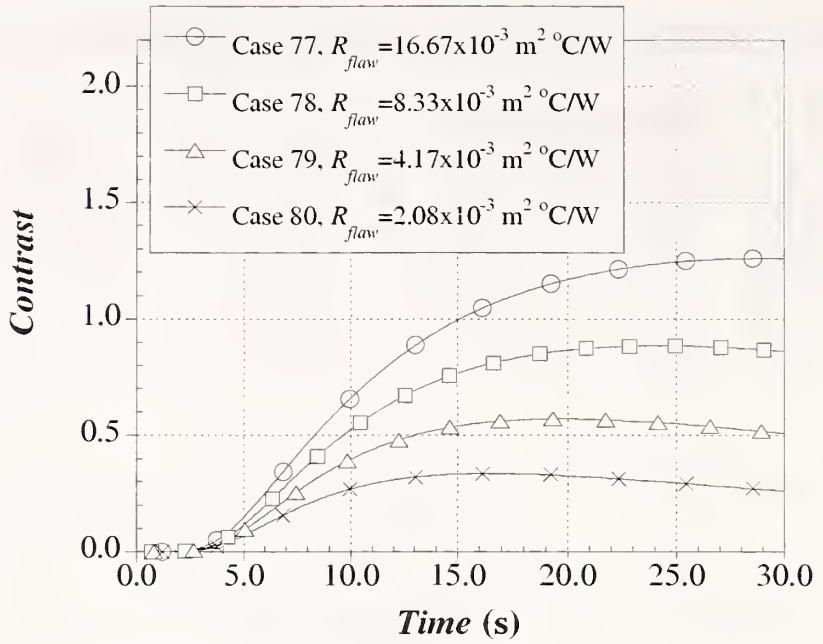

Fig. 4.86 Thermal contrast for simulations involving concrete spalls of different thickness (Cases 77 through 80)

The thermal contrast as a function of time is presented in Fig. 4.86, and it shows that the maximum contrast increases with increasing R_{flaw}. The values of maximum contrast are presented in Table 4.28. The variation in maximum contrast could be expressed as a power function of the flaw thermal resistance:

$$C_{max} = 14.4 R_{flaw}^{0.54} \tag{4.91}$$

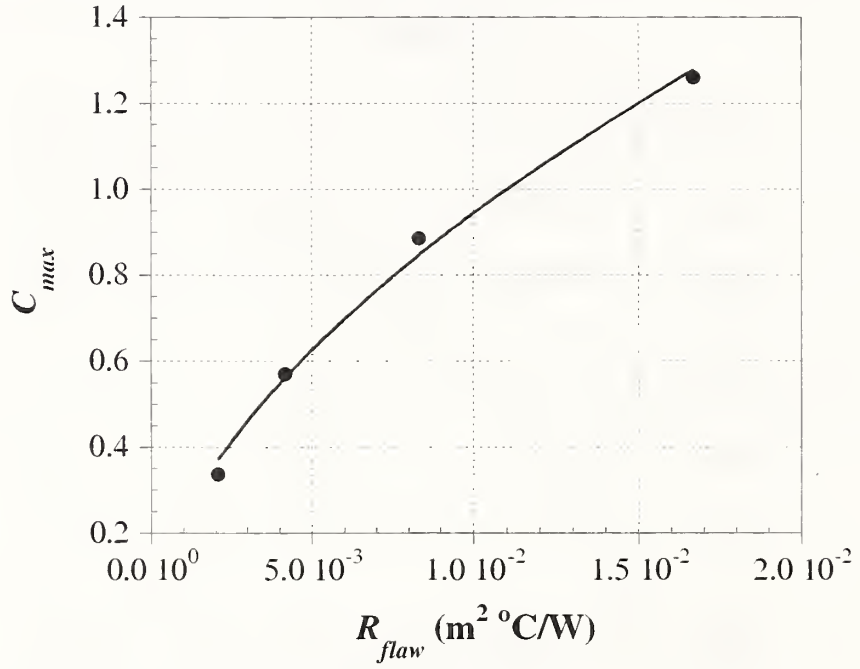

Fig. 4.87 Maximum thermal contrast as a function of thermal resistance of spalls (Cases 77 through 80)

Figure 4.87 shows the variation of the maximum thermal contrast with R_{flaw} along with the best-fit power function.

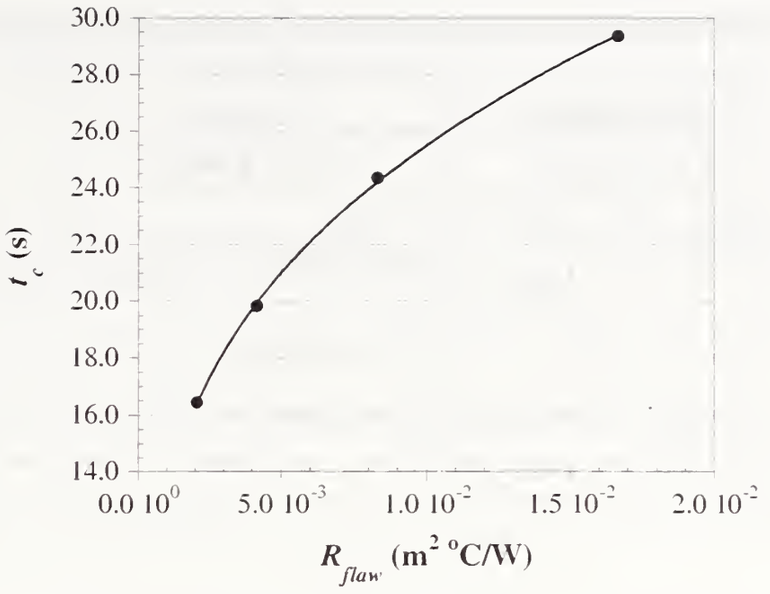

Fig. 4.88 Time for maximum contrast as a function of thermal resistance of spalls (Cases 77 through 80)

Figure 4.88 illustrates that the time for maximum contrast t_c increases with increasing flaw thermal resistance. Further analysis indicated that the change of time for maximum contrast is greater for concrete spalls than for delaminations or debonds. For example, for the case of concrete spalls, t_c increased by 12.9 s for an increase in R_{flaw} from 2.08×10^{-3} m^2·°C/W to 16.67×10^{-3} m^2·°C/W. Similar increases in R_{flaw} of delaminations only produced increases in t_c of only 3.2 s. Similar to other kind of flaws, the increase in time for maximum signal for concrete spalls could also be expressed as a power function. The power function that fits the FEM results is

$$t_c = 92.4 R_{flaw}^{0.3} \tag{4.92}$$

Figure 4.88 shows the time for maximum contrast as a function of R_{flaw} along with the best-fit power function.

4.6.4d Minimum Detectable Flaw Thickness

The minimum flaw thickness required for detection was also estimated for three different values of maximum signal: ΔT_{max} equal to 0.1 °C, 5.0 °C, and 10.0 °C. The case of a maximum signal of 0.1 °C corresponds to the thermal sensitivity expected from most IR detectors. The second and third cases were considered to compensate for the fact that the results of the FEM analysis are ideal since perfect contact was considered at the layer interface. The minimum thermal resistance of detectable flaws was computed using Eqs. 4.81, 4.85, and 4.89. The results from the calculations are presented in Table 4.32. Figure 4.89 presents the results of the minimum thickness of detectable flaws as a function of their depth. Note that a log scale is used for the flaw thickness axis.

Table 4.32 Minimum thermal resistance and thickness for detectable flaw (air void)

ΔT_{max} (°C)	**Delamination (d = 0.5 mm)**		**Debond (d = 1.5 mm)**		**Spall (d = 2.5 mm)**	
	R_{flaw} (m^2·°C/W)	Δz (mm)	R_{flaw} (m^2·°C/W)	Δz (mm)	R_{flaw} (m^2·°C/W)	Δz (mm)
0.1	1.23×10^{-6}	2.95×10^{-5}	2.08×10^{-6}	4.99×10^{-5}	5.53×10^{-6}	1.33×10^{-4}
5.0	5.55×10^{-4}	1.33×10^{-2}	6.09×10^{-3}	1.46×10^{-1}	2.73×10^{-2}	6.55×10^{-1}
10.0	1.64×10^{-3}	3.94×10^{-2}	2.50×10^{-2}	6.00×10^{-1}	1.23×10^{-1}	2.95×10^{0}

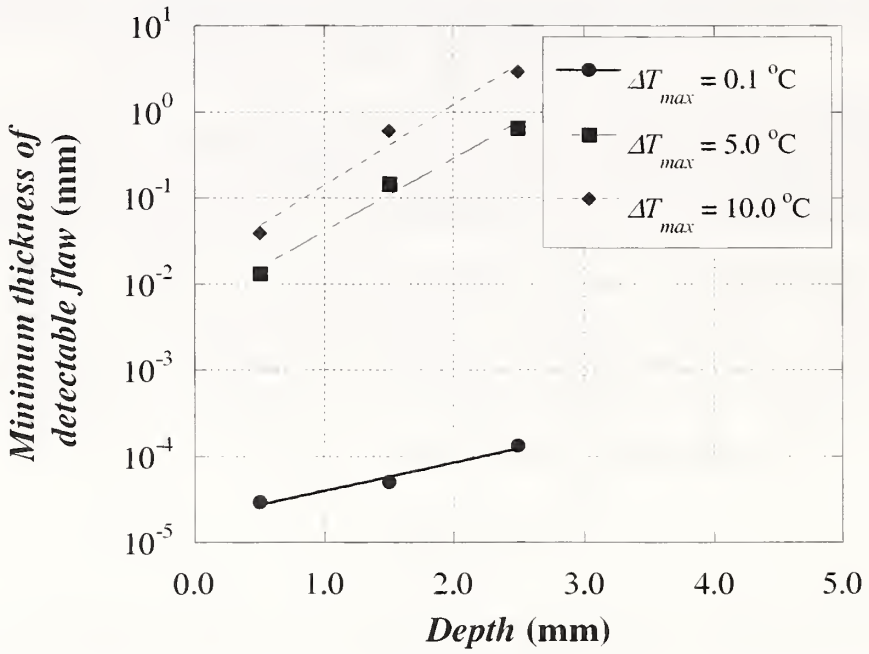

Fig. 4.89 Minimum thickness of detectable flaw as a function of flaw depth (mm)

The results presented in Figure 4.89 indicate that as the resolution of the signal increases (smaller ΔT_{max}), the minimum thickness for detectable flaws decreases. Exponential functions could be used to express the minimum thickness of detectable flaw. For the case of a thermal resolution of 0.1 °C (ΔT_{max} = 0.1 °C) the minimum thickness of detectable flaw could be expressed as

$$\Delta z_{min} = \left(1.88 \times 10^{-5}\right) e^{0.75 d_{flaw}} \tag{4.93}$$

where

Δz_{min} = minimum thickness of detectable flaws; and,
d_{flaw} = depth of the flaw.

For the case of a thermal resolution of 5.0 °C the following exponential function could be used to estimate the minimum thickness of detectable air voids:

$$\Delta z_{min} = \left(5.83 \times 10^{-3}\right) e^{1.95 d_{flaw}} \tag{4.94}$$

Finally, for the case of a maximum thermal signal of 10.0 °C the following exponential function calculates the minimum thickness of detectable air voids:

$$\Delta z_{min} = \left(1.62 \times 10^{-2}\right) e^{2.16 d_{flaw}} \tag{4.95}$$

The results indicate that the minimum thickness of detectable flaws depends on the depth of the flaw and the maximum signal required to overcome noise in the measurement process. Moreover, very thin and "zero volume flaws may be undetectable using infrared thermography.

4.6.5 Summary

Summarizing, this section of the analysis provided an understanding of the effect of flaw thickness or thermal resistance on the thermal response:

- The influence of flaw thermal resistance on the maximum surface temperature is significant in the case of delaminations but is very small for debonds and concrete spalls.
- The maximum surface temperature increases nonlinearly with increasing thermal resistance of the flaw. The variation of maximum surface temperature could be expressed as a power function of flaw thermal resistance.
- Flaws with higher thermal resistance produce higher thermal signal.
- Changes in maximum signal due to flaw thickness are more pronounced for flaws located closer to the surface.
- The time for maximum signal increases with increasing flaw thermal resistance.
- Variation in t_s with thermal resistance is greater for deeper flaws.
- An increase in flaw thermal resistance increases thermal contrast.
- Increases in maximum contrast are greater for delaminations close to the surface than for deeper flaws.
- Time for maximum contrast also increases nonlinearly with increasing flaw thermal resistance.
- The effect of flaw thermal resistance on the time for maximum contrast is greater for deep rather than shallow flaws.

- The effect of flaw thermal resistance on the different thermal parameters (T_{max}, ΔT_{max}, t_s, contrast, and t_c) can be represented as power functions.

- The minimum thickness of detectable flaws depends on flaw depth and the required thermal signal.

The next series of simulations involve the study of the effect of flaw width.

4.7 Parametric Study No. 5: Effect of Flaw Width and Estimation of Flaw Width

The size of debonds or delaminations could be the determining factor on the proper performance of FRP composites bonded to concrete. With this concern, minimum requirements on allowable flaw size have been introduced by the International Conference of Building Officials Evaluation Services (ICBO ES).

Among the conditions of acceptance, the ICBO ES states that small air voids of diameter up to 3.2 mm occur naturally in FRP systems. Flaws of this size and smaller do not require repair. Delaminations with areas of 13 cm^2 or smaller are also allowed. Flaws larger than 13 cm^2, however, should be repaired.

Based on the need to be able to measure the size of the internal flaw, the final parameter to be investigated was the width of the flaw. The fifth parametric study had the following objectives:

- Understand the effects of flaw width on the thermal response;

- Establish minimum width of detectable flaw; and

- Investigate whether flaw width can be estimated reliably from thermography testing.

Three different sets of simulations were performed which included a total of 12 finite element models.

4.7.1 Geometry of Model

The test object consisted of a 100 mm long by 20 mm thick concrete slab. Three layers of carbon FRP were bonded to the top surface of the concrete. Each layer of FRP was 0.5 mm thick. Also, each layer of composite was oriented at 90° from its adjacent ply. An internal flaw was located at the center of the cross section of the object. The thickness of the flaw was 0.1 mm. The depth of the flaw was varied to include delaminations 0.5 mm deep, debonds 1.5 mm deep, and concrete spalls 2.5 mm deep. Using symmetry about the center of the test object, flaws ranging from 3.0 mm to 25 mm wide were investigated by modeling flaws 1.5 mm to 12.5 mm wide in a half space. Figure 4.90 illustrates the geometry of the different models analyzed in this parametric study.

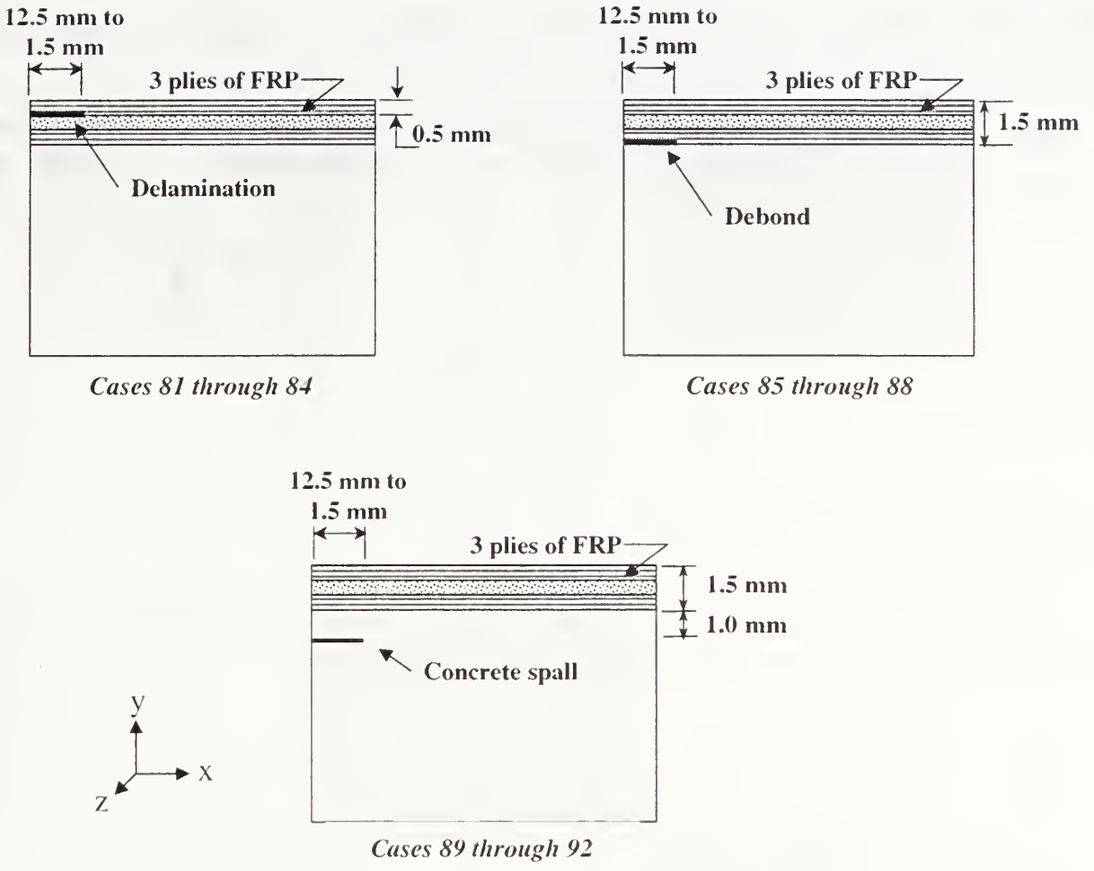

Fig. 4.90 Summary of geometry of models used in study effects of flaw width (Parametric No.5)

Plane two-dimensional modeling was again used in parametric study No.5. The model was meshed using 2-D quadrilateral thermal solid elements containing 4 nodes. Each node has one degree of freedom, temperature. The model was meshed using a global mesh size of 0.5 mm. Similar to previous simulations, the mesh was refined in the y-direction. Thinner elements were located at the FRP layers, the flaw, and the concrete close to the interface with the FRP. The thickness of the elements increased towards the bottom of the concrete slab where the effect of the thermal front tends to dissipate.

The simulations were arranged into three sets. The first set of simulations focused on the effects of width of delaminations located 0.5 mm deep. The second set involved the investigation of the effect of the width of debonds which were located at a depth of 1.5 mm. The third set involved the study of the width of concrete spalls located 2.5 mm deep. Table 4.33 summarizes the models used in Parametric No. 5.

Table 4.33 Geometry for sets of simulations to study flaw width (Parametric study No.5)

Set	Case	Flaw depth (mm)	Actual flaw width (mm)	Simulation flaw width (mm)
1	81	0.5	25.0	12.5
	82	0.5	14.0	7.0
	83	0.5	5.0	2.5
	84	0.5	3.0	1.5
2	85	1.5	25.0	12.5
	86	1.5	14.0	7.0
	87	1.5	5.0	2.5
	88	1.5	3.0	1.5
3	89	2.5	25.0	12.5
	90	2.5	14.0	7.0
	91	2.5	5.0	2.5
	92	2.5	3.0	1.5

4.7.2 Material Properties

The material properties used in the models were those of concrete for the substrate, carbon FRP for the bonded composite, and air for the internal flaw. The physical and thermal properties of these materials are presented in Table 4.1.

4.7.3 Thermal Loading and Boundary Conditions

The models were defined as transient heat transfer analyses. The models were subjected to a uniform initial temperature of 23 °C. A square pulse of magnitude 20 000 W/m^2 and duration 2 s was applied to the top surface of the model. The remaining free surfaces were subjected to adiabatic conditions ($dT/dx = 0$ and $dT/dz = 0$). The simulations were run for up to 30 s. The time stepping was the same as that used in the previous simulations.

4.7.4 Results

4.7.4a Delaminations

The first set of simulations involved the study of the effect of delamination size on the thermal response. As previously mentioned, the delamination was located 0.5 mm deep. The actual width of the flaw varied between 25.0 mm and 3.0 mm.

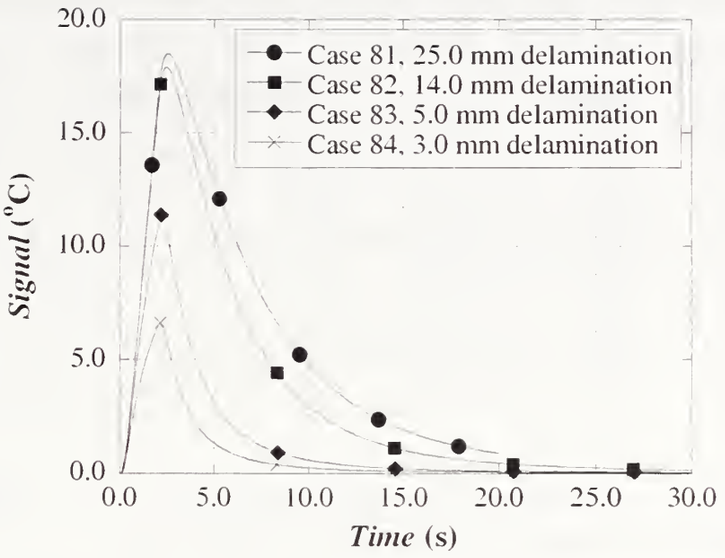

Fig. 4.91 Thermal signal for simulations involving delaminations of different widths (Cases 81 through 84)

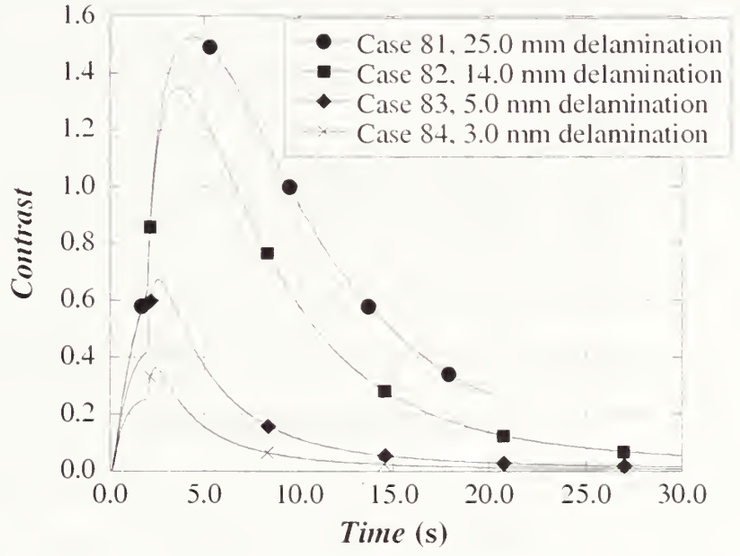

Fig. 4.92 Thermal contrast for simulations involving delaminations of different width (Cases 81 through 84)

First, the simulation output was analyzed to compute the thermal responses as a function of time. Figures 4.91 and 4.92 illustrate the thermal signal and thermal contrast as a function of time, respectively.

Table 4.34 Results of thermal responses for models involving delaminations

Case	Depth (mm)	Width (mm)	T_{max} (°C)	Maximum Signal		Maximum Contrast	
				t_s (s)	ΔT_{max} (°C)	t_c (s)	$\Delta T/\Delta T_{backgr}$
81	0.5	25.0	64.9	2.5	18.5	4.4	1.53
82	0.5	14.0	64.6	2.4	17.9	3.7	1.35
83	0.5	5.0	59.4	2.2	11.3	2.6	0.67
84	0.5	3.0	55.0	2.1	6.6	2.4	0.36

Based on these responses, the thermal response parameters T_{max}, t_s, ΔT_{max}, C_{max}, and t_c were obtained. The computed parameters are presented in Table 4.34.

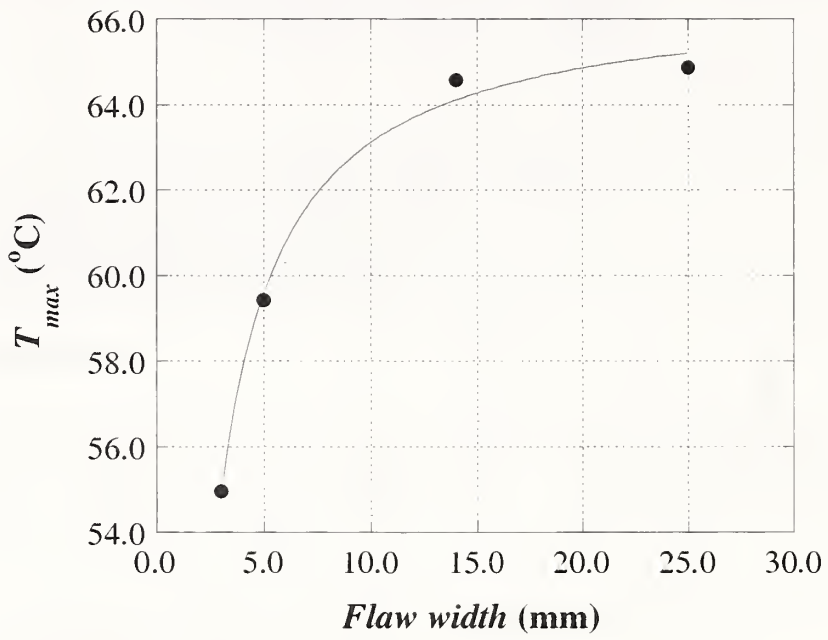

Fig. 4.93 Maximum surface temperature as a function of delamination width (Cases 81 through 84)

Figure 4.93 shows that the maximum surface temperature increases nonlinearly with increasing delamination width or size. The surface temperature, however, was asymptotic for flaws 14.0 mm or wider.

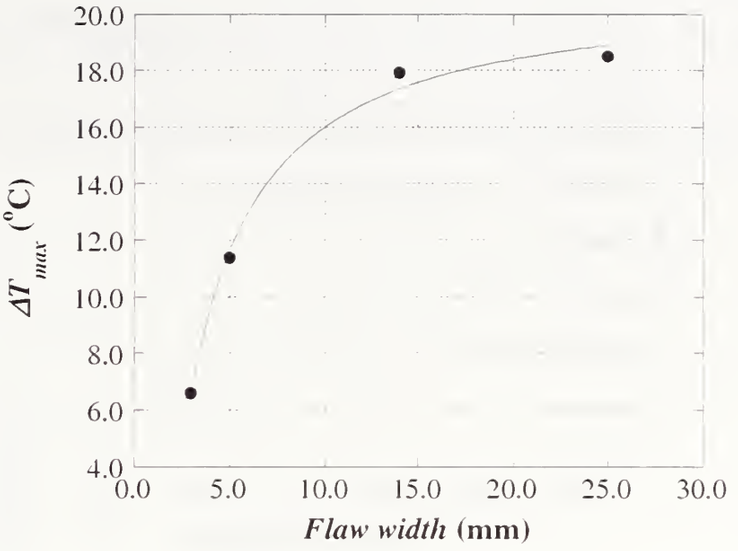

Fig. 4.94 Maximum signal as a function of delamination width
(Cases 81 through 84)

As shown in Fig. 4.94, the maximum signal increases with increasing flaw length.

The increase in maximum signal could be represented as a hyperbolic function of width as follows:

$$\Delta T_{max} = 20.948 \frac{0.397(w - 1.858)}{1 + 0.397(w - 1.858)} \tag{4.93}$$

where

w = width of the internal flaw.

The results indicate that the maximum signal increases from 6.6 °C to 18.5 °C as flaw width increases from 3.0 mm to 25.0 mm.

The time for maximum signal also increases with increasing flaw width. The change in t_s, however, is less than a second for the increase in width investigated in this study. Specifically, the time for maximum signal increased only from 2.1 s to 2.5 s. Thus, the effect of flaw width on t_s is negligible. The change in the time for maximum signal could be expressed as the following power function:

$$t_s = 1.043 + 0.922\, w^{0.151} \tag{4.94}$$

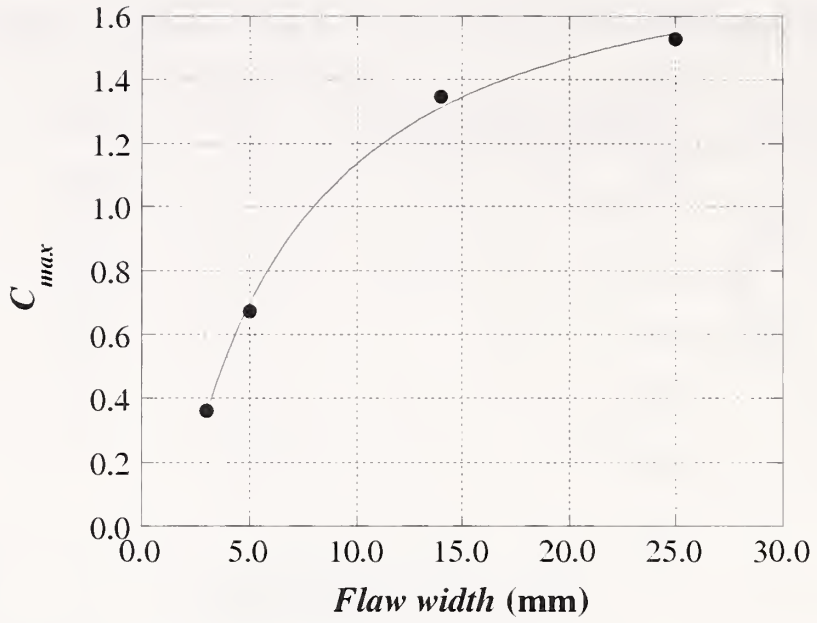

Fig. 4.95 Maximum contrast as a function of delamination width (Cases 81 through 84)

Figure 4.95 shows that the maximum thermal contrast shows the same hyperbolic trend as the maximum signal. The maximum contrast increased from 0.36 to 1.53 as flaw width increased from 3.0 mm to 25.0 mm

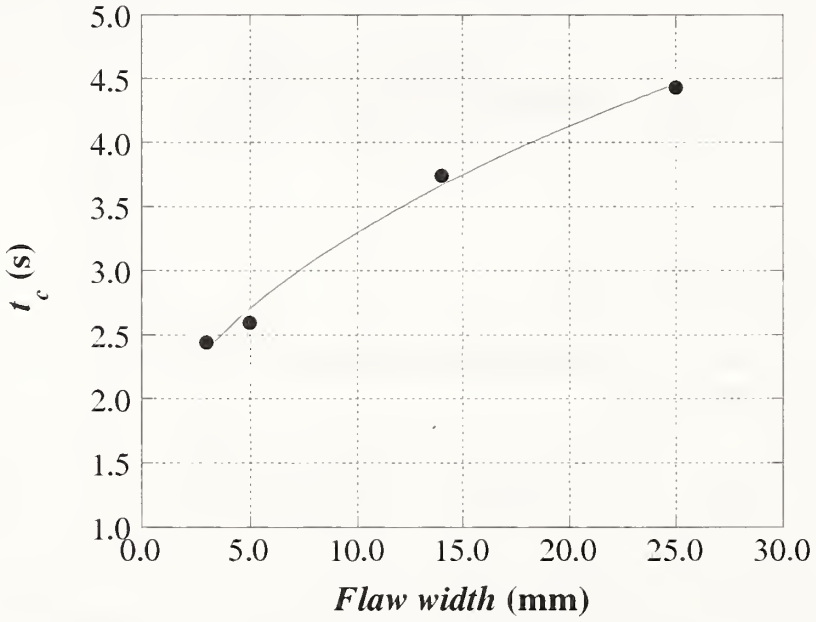

Fig. 4.96 Time for maximum contrast as a function of delamination width (Cases 81 through 84)

The increase in maximum contrast as a function of flaw width could be expressed as a hyperbolic function

$$C_{max} = 1.932 \frac{0.172(w-1.704)}{1+0.172(w-1.704)} \tag{4.95}$$

The results in Table 4.31 show that the time for maximum contrast is higher than the time for maximum signal. This behavior is also reported in previous parametric studies. As shown in

Fig. 4.96, t_c increases with increasing flaw width. The increase in t_c is 2 s when the flaw width increased from 3.0 mm to 25.0 mm.

The simulation output could be represented as the following power function:

$$t_c = 1.229 + 0.673\, w^{0.487} \tag{4.96}$$

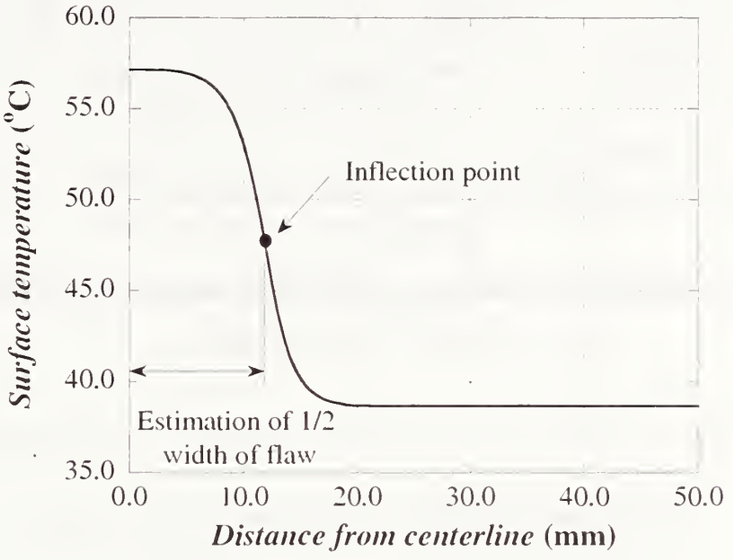

Fig. 4.97 Estimation of width of flaw

The FEM output was analyzed further to examine whether the width of the flaw could be discerned from the temperature distribution. It was found that a plot of surface temperature versus distance could be used to estimate flaw size. As can be observed on Fig. 4.97, a typical temperature-distance plot has an inflection point. The location of the inflection coincides with the location of the edge of the subsurface flaw. This observation may be limited to near surface flaws.

The location of the inflection point in the distance vs. temperature curve can be computed by setting the second derivative of the curve equal to zero

$$\frac{\partial^2 T}{\partial x^2} = 0 \quad at\ w_{estimate} \tag{4.97}$$

where

T = surface temperature;
x = distance from the center line along the x-axis; and,
$w_{estimate}$ = estimate of the distance of the edge of the flaw from the center line.

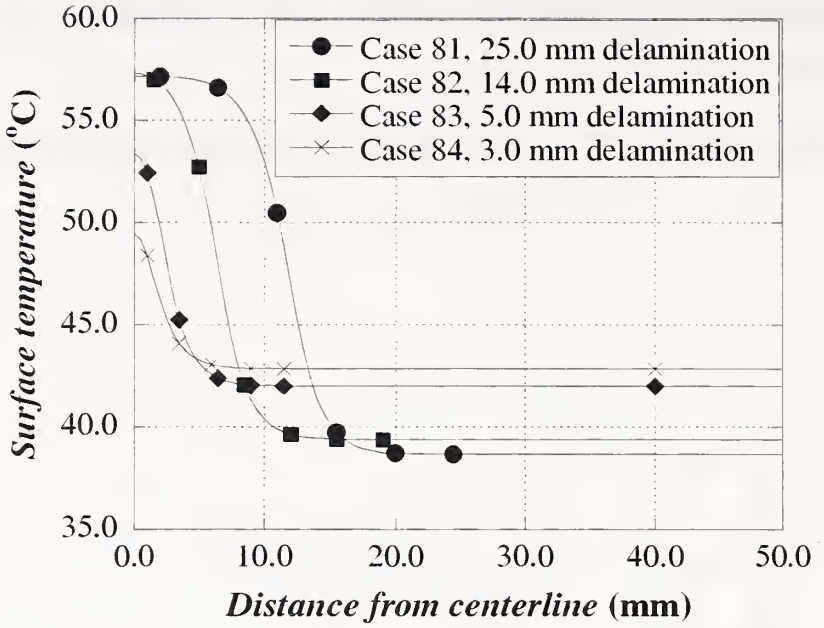

Fig. 4.98 Surface profiles for simulations involving delaminations (Cases 81 through 84)

Table 4.35 Estimated of flaw width for simulations involving delaminations

Cases	Actual flaw width (mm)	Estimated flaw width (mm)	% Error
81	25.0	24.0	4
82	14.0	13.1	6
83	5.0	4.6	8
84	3.0	3.1	-3

Surface temperature profiles are plotted for all four simulations in Fig. 4.98. The location of the inflection point from each curve was computed numerically. The results of the estimation using the location of the inflection point are presented in Table 4.32. This approach provides a good estimate of the size of the flaw.

Therefore, the analysis of the FEM output indicates that 0.5 mm deep delaminations of different widths are easily detected. Although the thermal signal decreases with decreasing width, small delaminations 5.0 mm wide produce ΔT_{max} of about 7 °C. Additionally, estimation of their size based on the surface temperature profiles results in errors smaller than 8%. The range of error appears acceptable for the purpose of the evaluation of delaminations, since the estimated widths are within a millimeter of the actual widths.

4.7.4b Debonds

The second set of simulations corresponded to test objects containing 1.5 mm deep debonds of different width. Debond width was varied between 25.0 mm and 3.0 mm.

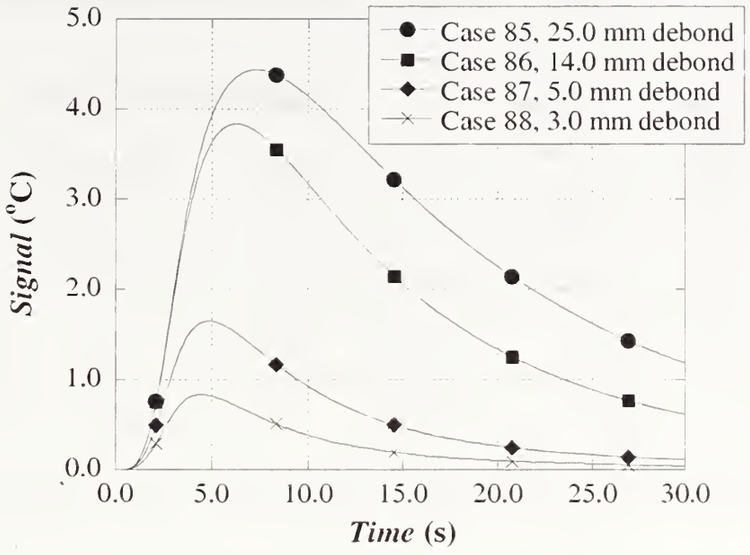

Fig. 4.99 Thermal signal for simulations involving debonds of different width (Cases 85 through 88)

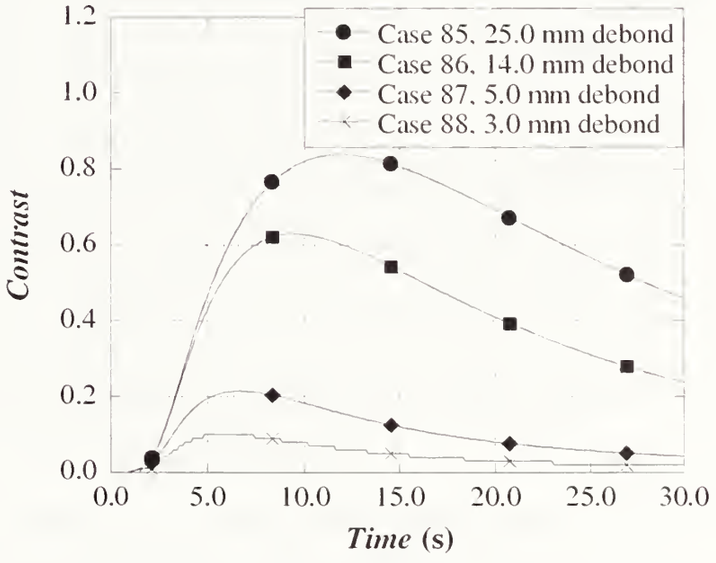

Fig. 4.100 Thermal contrast for simulations involving debonds of different width (Cases 85 through 88)

Figures 4.99 and 4.100 illustrate the time history output for the thermal signal and thermal contrast, respectively.

Table 4.33 Results of thermal responses for models involving debonds

Case	Depth (mm)	Width (mm)	T_{max} (°C)	Maximum Signal		Maximum Contrast	
				t_s (s)	ΔT_{max} (°C)	t_c (s)	$\Delta T/\Delta T_{backgr}$
85	1.5	25.0	49.1	7.3	4.4	11.8	0.84
86	1.5	14.0	49.1	6.2	3.8	9.4	0.63
87	1.5	5.0	48.9	4.8	1.6	6.6	0.22
88	1.5	3.0	48.7	4.4	0.8	5.9	0.10

Table 4.33 summarizes the thermal response parameters for the set of simulations involving debonds.

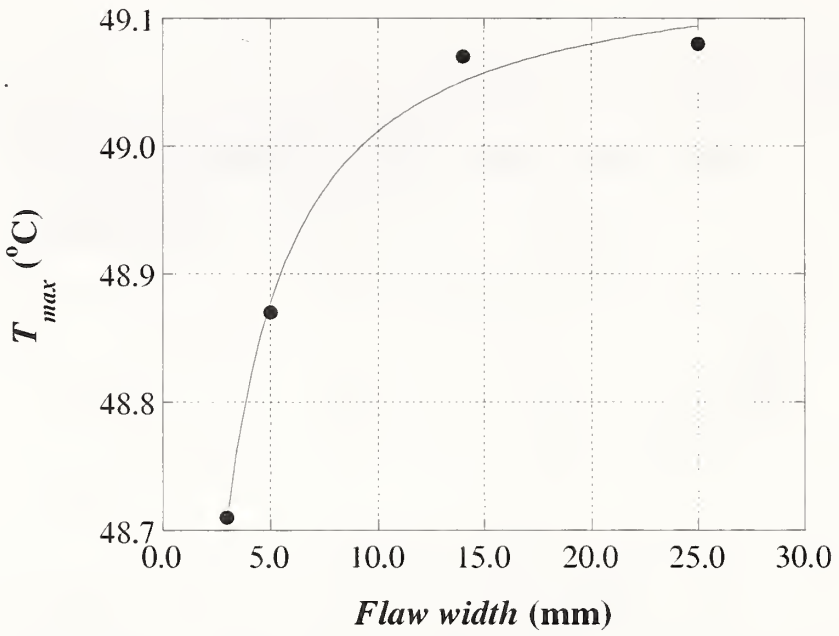

Fig. 4.101 Maximum surface temperature as a function of width of debonds (Cases 85 through 88)

Figure 4.101 shows that the maximum surface temperature increases nonlinearly with increasing width of the flaw. The value of T_{max} increases only by 0.4 °C with an increase in flaw width from 3.0 mm to 25.0 mm. The surface temperature becomes asymptotic at 49.07 °C for flaws wider than 14.0 mm.

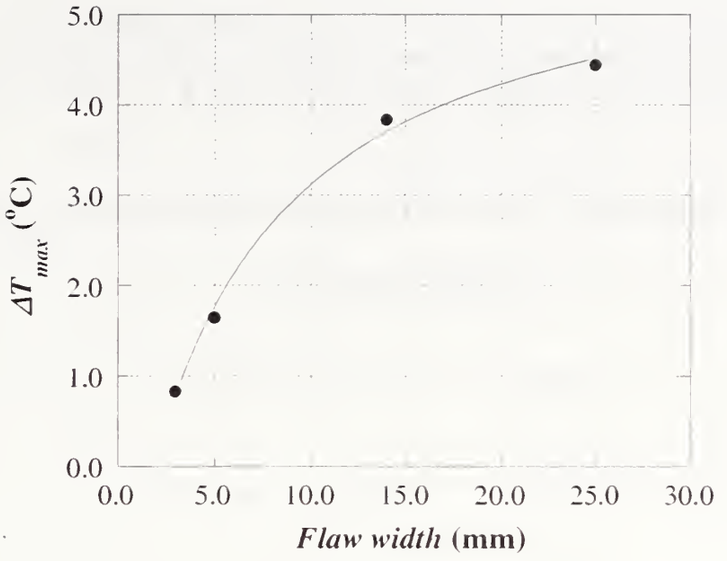

Fig. 4.102 Maximum signal as a function of debond width (Cases 85 through 88)

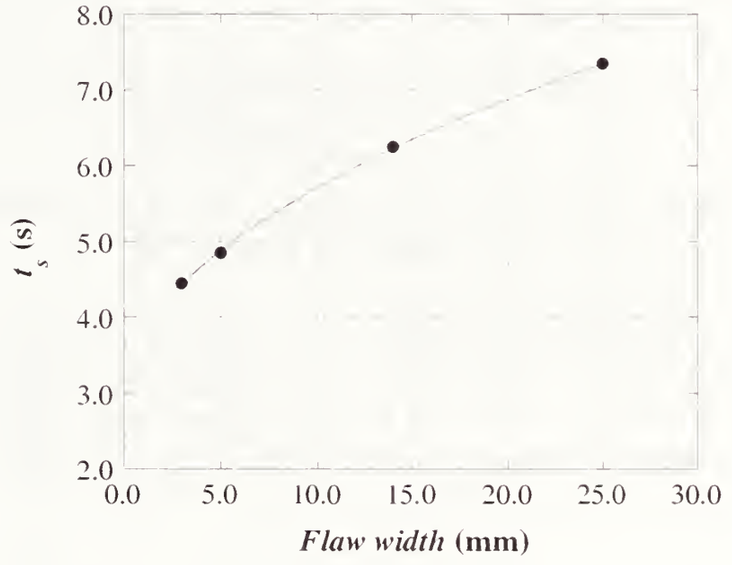

Fig. 4.103 Time for maximum signal as a function of debond width (Cases 85 through 88)

Figure 4.102 shows that the maximum thermal signal increases nonlinearly with increasing flaw width.

The variation in ΔT_{max} for debonds could be expressed as the following hyperbolic function of the width of the flaw:

$$\Delta T_{max} = 5.947 \frac{0.136\,(w - 1.897)}{1 + 0.136\,(w - 1.897)} \tag{4.98}$$

As shown in Fig. 4.103, the time to reach the maximum signal also increases with increasing flaw width. The time for maximum signal, however, increases more significantly for debonds than for delaminations. For example, t_s increases from 4.4 s to 7.3 s for debonds 3.0 mm to 25.0 mm wide.

The change in t_s as a function of flaw width could be expressed as the following power function:

$$t_s = 2.889 + 0.887\, w^{0.502} \tag{4.99}$$

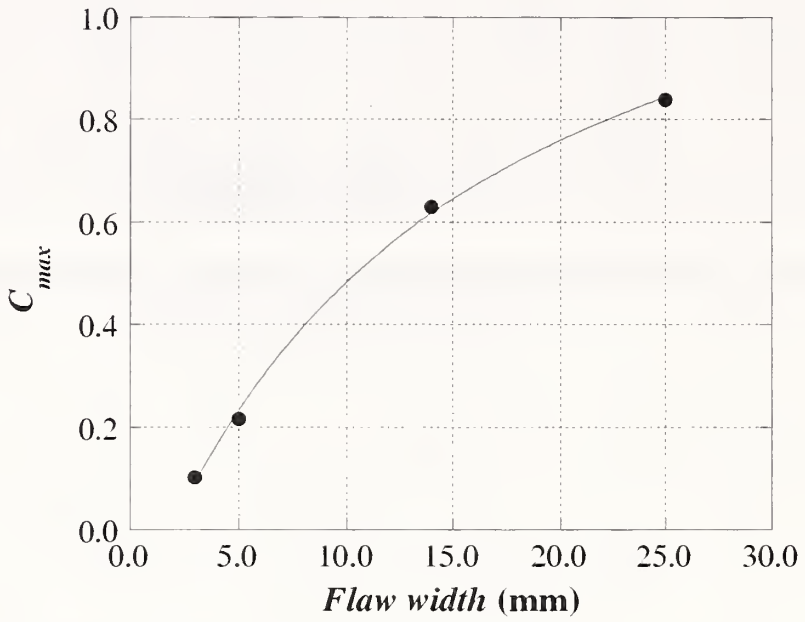

Fig. 4.104 Maximum contrast as a function of debond width
(Cases 85 through 88)

As was the case for other response parameters, the maximum thermal contrast increases with increasing flaw width. Moreover, the maximum contrast increases from 0.10 for the test object containing a 3.0 mm wide flaw to 0.84 for the test object having a flaw 25.0 mm wide. Figure 4.104 illustrates the maximum contrast as a function of debond width. The maximum contrast could be expressed as the following hyperbolic function of width:

$$C_{max} = 1.416 \frac{0.064(w - 1.932)}{1 + 0.064(w - 1.932)} \tag{4.100}$$

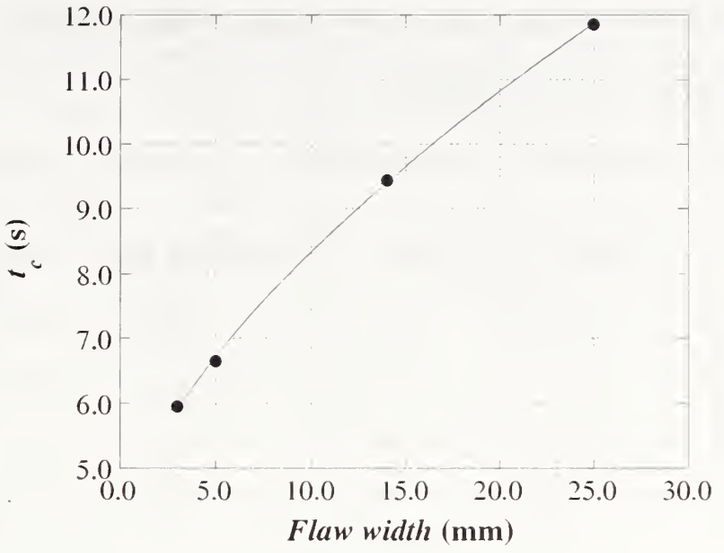

Fig. 4.105 Time for maximum contrast as a function of debond width (Cases 85 through 88)

Figure 4.105 shows that the time for maximum contrast also increases with increasing flaw width. The relationship could be expressed as the following power function:

$$t_c = 3.707 + 1.113\, w^{0.619} \tag{4.101}$$

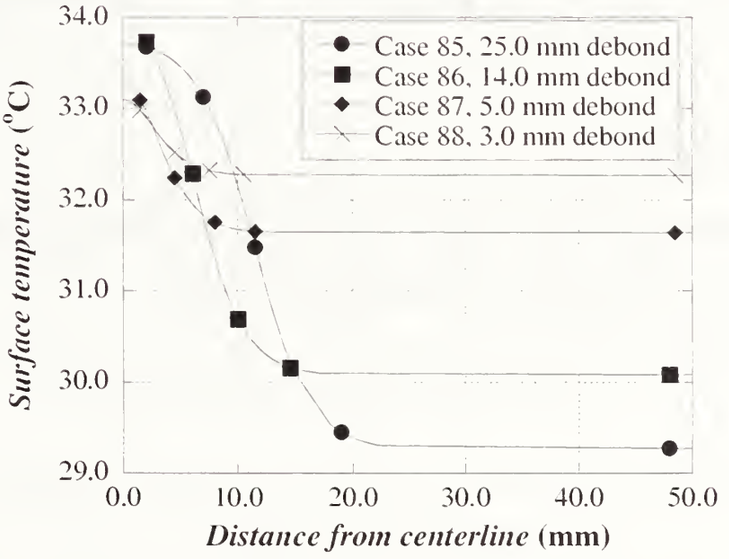

Fig. 4.106 Surface temperature profiles for simulation involving debonds (Cases 85 through 88)

Similar to the case of delaminations, the surface temperature along the x-axis is plotted in order to estimate the width of the flaw. Figure 4.106 presents the distance versus surface temperature profiles for the simulations involving debonds.

Table 4.37 Estimation of flaw width for simulations involving debonds

Case	Actual flaw width (mm)	Estimated flaw width (mm)	% Error
85	25.0	23.2	7
86	14.0	12.5	11
87	5.0	5.7	-14
88	3.0	4.9	-63

The flaw size is estimated by determining the location at which the second derivative of the surface temperature profile was equal to zero. The results of the estimation are presented in Table 4.37.

The results from the width estimation are interesting. For example, the results presented in Table 4.34 indicate that the flaw width was underestimated for the cases of flaws 25.0 mm and 14.0 mm wide. On the other hand, the width is overestimated for the smallest flaws. The over- or underestimation is only about 2.00 mm for the poorest case. This level of error could be considered negligible in the evaluation of the bond between FRP composites and concrete.

4.7.4c Concrete Spalls

The last set of simulations involved the evaluation of the effect of spall width on the thermal response. The concrete spall was located 2.5 mm from the surface of the test object, that is, 1.0 mm below the interface between the FRP and the concrete.

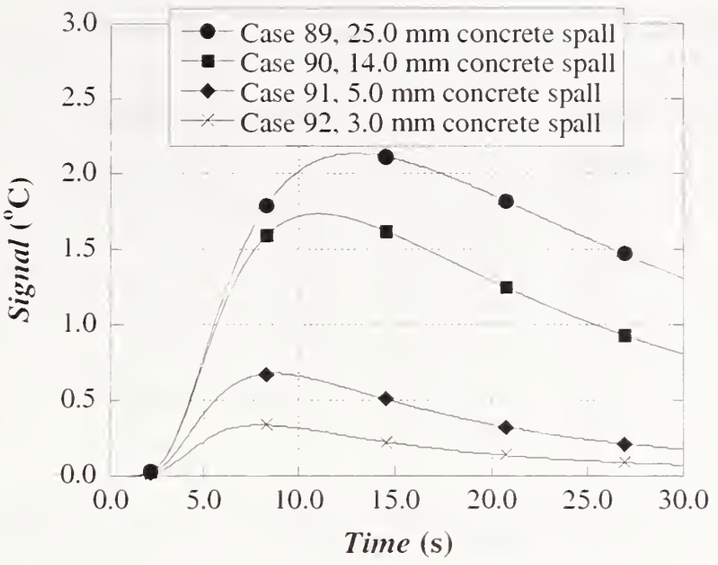

Fig. 4.107 Thermal signal for simulations involving concrete spalls of different width (Cases 89 through 92)

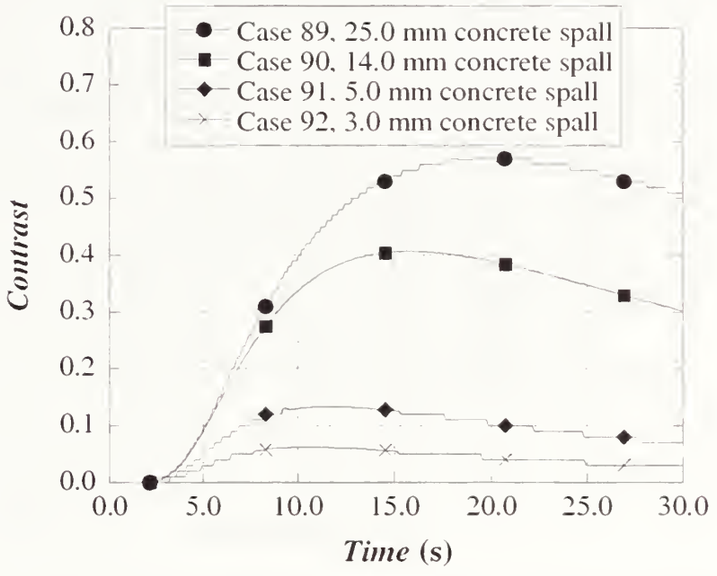

Fig. 4.108 Thermal contrast for simulations involving concrete spalls of different width (Cases 89 through 92)

The thermal signal and thermal contrast as a function of time are presented in Figs. 4.107 and 4.108.

The thermal response was analyzed to identify the response parameters: T_{max}, ΔT_{max}, t_s, C_{max}, and t_c. Table 4.38 lists the response parameters for the last set of simulations involving spalls.

Table 4.38 Results of thermal responses for models involving concrete spalls

Case	Depth (mm)	Width (mm)	T_{max} (°C)	Maximum Signal		Maximum Contrast	
				t_s (s)	ΔT_{max} (°C)	t_c (s)	$\Delta T/\Delta T_{backgr}$
89	2.5	25.0	48.5	12.9	2.1	19.6	0.57
90	2.5	14.0	48.5	11.0	1.7	15.7	0.41
91	2.5	5.0	48.5	8.7	0.6	11.6	0.13
92	2.5	3.0	48.5	7.9	0.3	10.6	0.06

As Table 4.38 indicates, the maximum surface temperature is not affected by changes in the width of the concrete spalls. The width of the flaw, however, affects the magnitude of maximum signal. It is important to note that the maximum signal only reaches a magnitude of 2.1 °C for the largest spall and 0.3 °C for the smallest flaw. This behavior suggests that small concrete spalls may be difficult to detect.

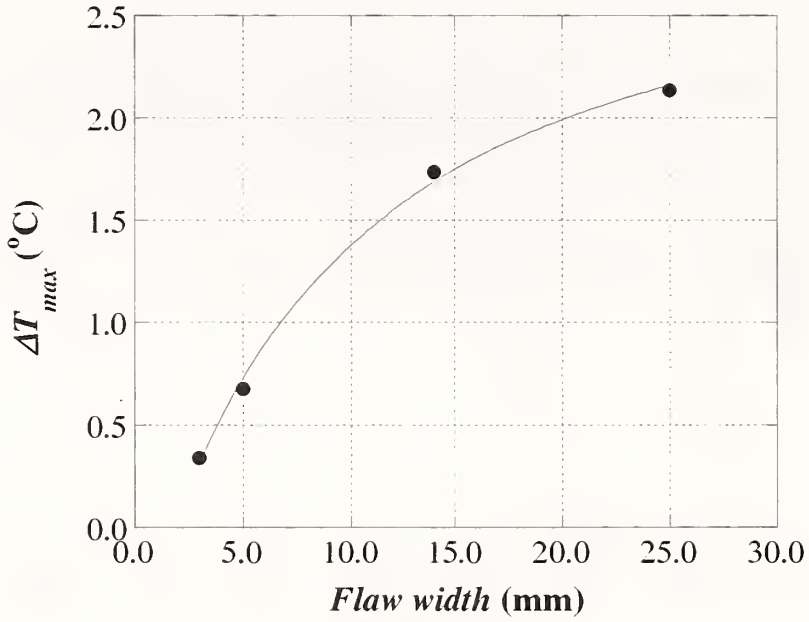

Fig. 4.109 Maximum signal as a function of spall width (Cases 89 through 92)

The maximum thermal signal as a function of the spall width is presented in Fig. 4.109. Similar to the cases of delaminations and debonds, ΔT_{max} for concrete spalls could be expressed as the following hyperbolic function:

$$\Delta T_{max} = 3.123 \frac{0.097\,(w - 1.868)}{1 + 0.097\,(w - 1.868)} \tag{4.102}$$

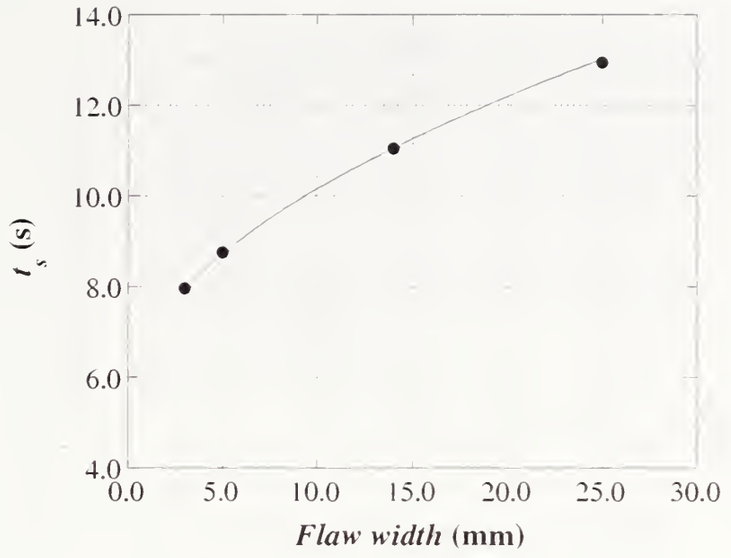

Fig. 4.110 Time for maximum signal as a function of spall width (Cases 89 through 92)

As shown in Fig. 4.110, the time to reach the maximum thermal signal increases nonlinearly with increasing flaw width.

The increase in t_s as a function of flaw width could be represented with the following power function:

$$t_s = 5.378 + 1.459\, w^{0.515} \tag{4.103}$$

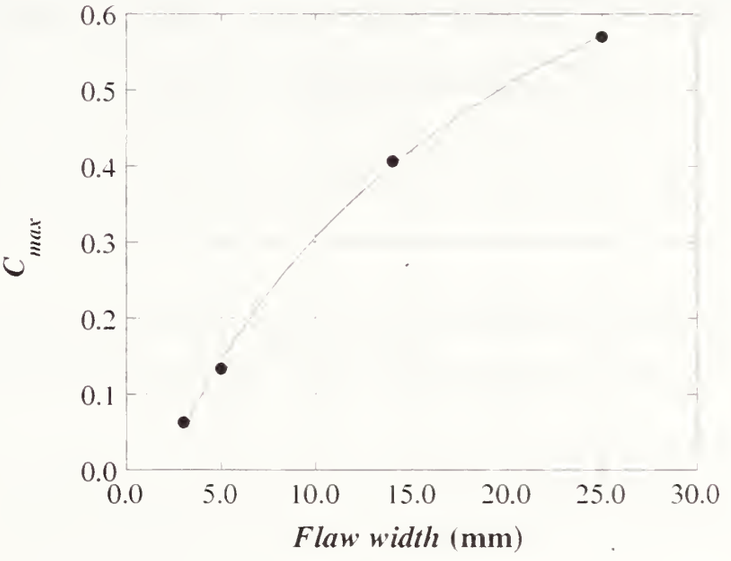

Fig. 4.111 Maximum contrast as a function of spall width (Cases 89 through 92)

As shown in Fig. 4.111, the maximum thermal contrast also increases nonlinearly with increasing width of the flaw. The variation could be expressed as the following hyperbolic function of the flaw width:

$$C_{max} = 1.084 \frac{0.048(w-1.861)}{1+0.048(w-1.861)} \tag{4.104}$$

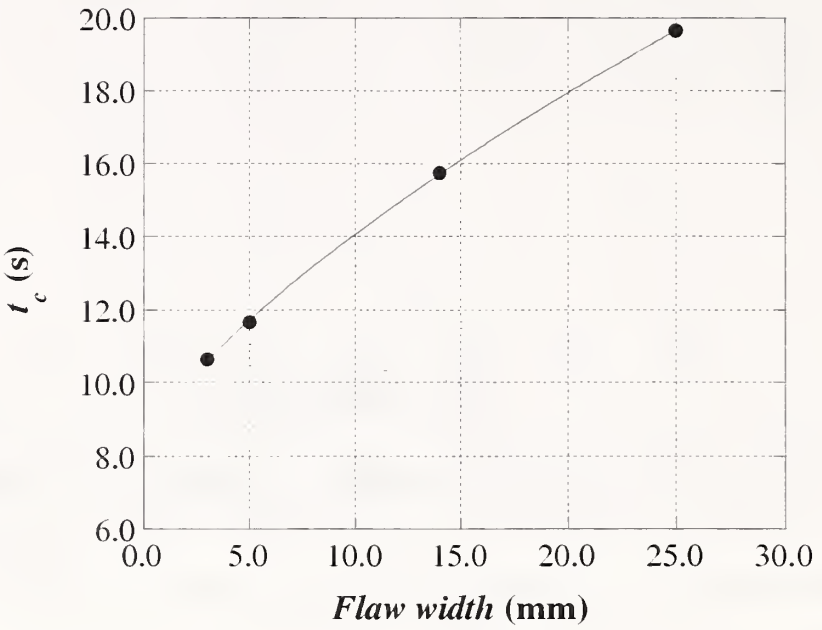

Fig. 4.112 Time for maximum contrast as a function of spall width (Cases 89 through 92)

Figure 4.112 shows the variation of the time for maximum contrast. The time rises from 10.6 s to 1.6 s as the width increases from 3.0 mm to 25.0 mm.

The variation of time for maximum contrast could be expressed by the following power function:

$$t_c = 8.100 + 1.133\, w^{0.722} \tag{4.105}$$

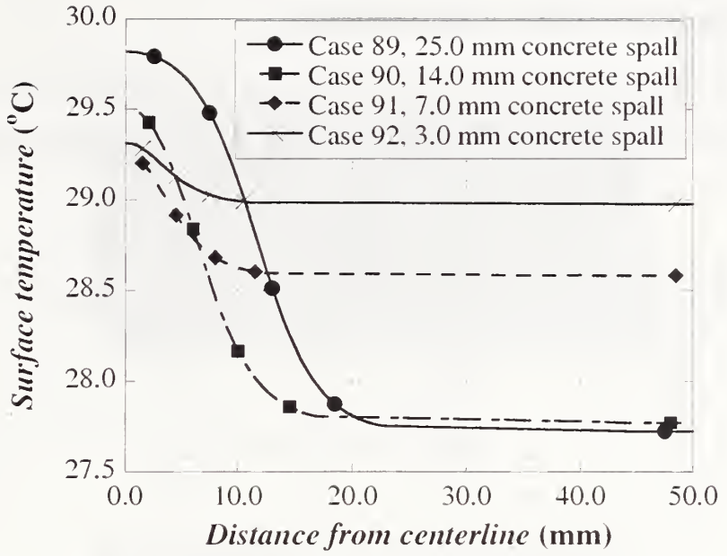

Fig. 4.113 Surface temperature profiles for simulations involving spalls (Cases 89 through 92)

To estimate spall width, the surface temperature profile is evaluated at time t_s. Figure 4.113 shows the surface temperature as a function of the distance from the centerline of the spall.

Table 4.39 Estimation of flaw width for simulations involving concrete spalls

Case	Actual flaw width (mm)	Estimated flaw width (mm)	% Error
89	25.0	23.3	7
90	14.0	12.7	9
91	5.0	6.7	-34
92	3.0	6.0	-100

The location of the inflection point on each curve provides the estimation of the half-width of the corresponding spall. The estimated flaw width and the percent error are presented in Table 4.39.

The results listed in Table 4.39 show that the width of larger concrete spalls (14.0 mm to 25.0 mm) tends to be underestimated while the width of smaller spalls (5.0 mm to 3.0 mm) tends to be overestimated. The larger percent error is observed for the smallest spall.

Large-sized flaws are the most critical for the adequate performance of FRP-strengthened structures, thus their detection and characterization is essential. The results reveal that the widths of large spalls tend to be underestimated. The error in estimation, however, is less than 10%.

For the case of small concrete spalls, the results demonstrate that their width tend to be overestimated. The result for the 3-mm wide spall (case 92) indicate an error in estimation of 100 %.

4.7.4d Comparison of width estimations

The results presented in the previous sections indicate that the width of large flaws tends to be underestimated while the width of smaller flaws tends to be overestimated.

Table 4.40 Estimation error of flaw width

Case	Depth (mm)	Actual width (mm)	Estimated width (mm)	Estimation error (mm)
81	0.5	25.0	24.0	-1.0
82	0.5	14.0	13.1	-0.9
83	0.5	5.0	4.6	-0.4
84	0.5	3.0	3.1	+0.1
85	1.5	25.0	23.2	-1.8
86	1.5	14.0	12.5	-1.5
87	1.5	5.0	5.7	+0.7
88	1.5	3.0	4.9	+1.9
89	2.5	25.0	23.3	-1.7
90	2.5	14.0	12.7	-1.3
91	2.5	5.0	6.7	+1.7
92	2.5	3.0	6.0	+3.0

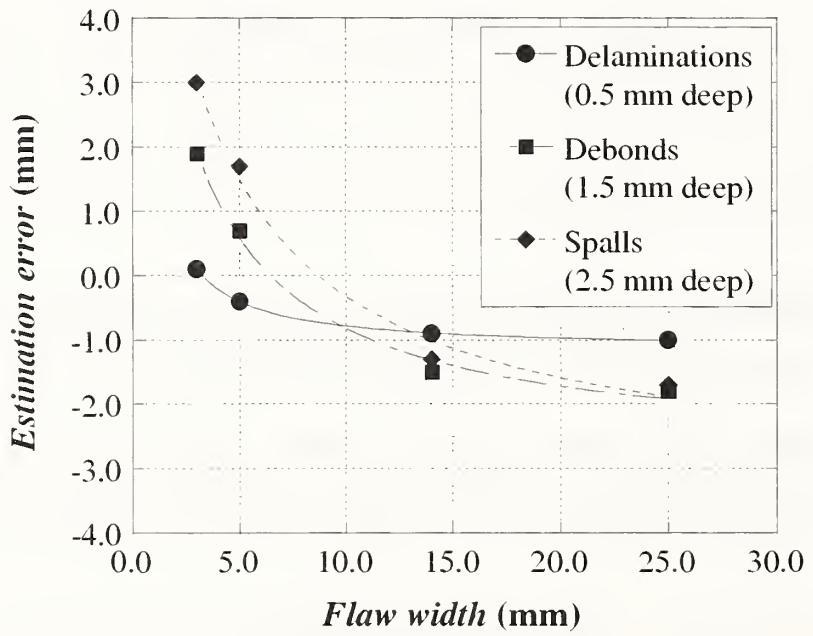

Fig. 4.114 Estimation error as a function of flaw width

The estimation error for each simulation was analyzed further. Table 4.40 presents the estimation error (difference between estimated width and actual width) for each kind of flaw. These errors are illustrated in Fig. 4.114.

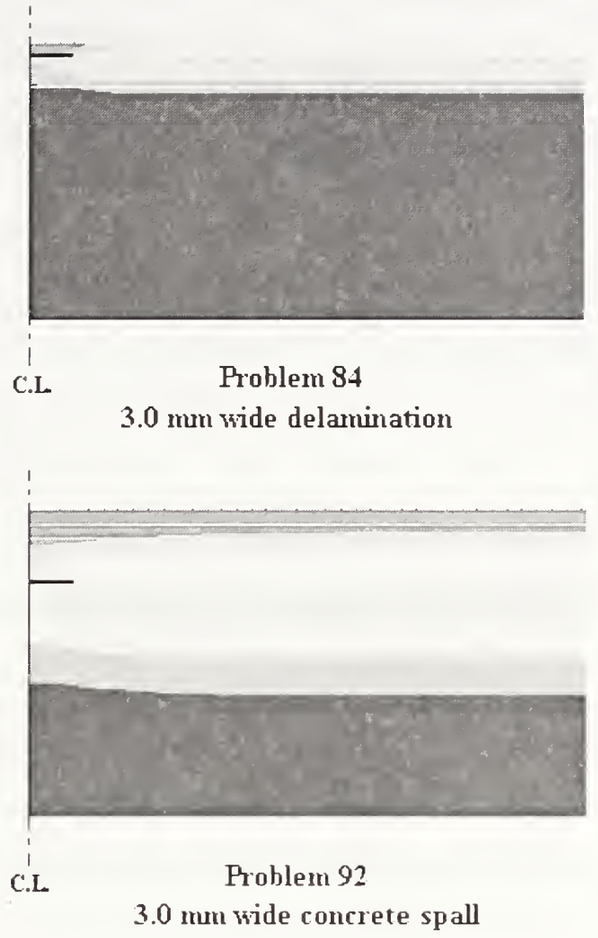

Fig. 4.115 Thermal fronts at time for maximum signal for simulations containing 3.0 mm wide delaminations and concrete spalls (Cases 84 and 92)

Plotting the errors provided some insight into the behavior. For example, the estimation error could be expressed as a hyperbolic function of the actual flaw width. The results presented in Fig. 4.114 illustrate that for the same flaw size the estimation error increases with the depth of the flaw. That is, the width estimation of a delamination is more accurate and precise than the estimation of debonds and concrete spalls. Figure 4.115 shows the temperature distributions in test objects with a delamination (top) or concrete spall (bottom).

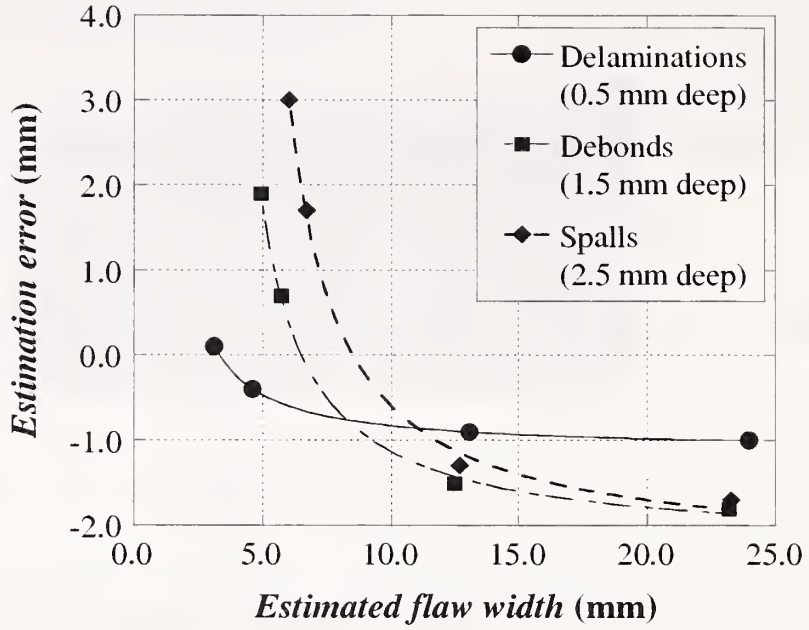

Fig. 4.116 Estimation error as a function of estimated flaw width

For the purpose of comparison, Fig. 4.116 shows the estimation error as a function of estimated flaw width for the delaminations, debonds, and concrete spalls investigated in this parametric study.

The results in Figure 4.116 could be expressed as the following hyperbolic functions:

a) for delaminations

$$Error_{delamination} = -1.11 \frac{0.43\,(w_{estimate} - 3.29)}{1 + 0.43\,(w_{estimate} - 3.29)} \tag{4.106}$$

b) for debonds

$$Error_{debonds} = -2.24 \frac{0.29\,(w_{estimate} - 6.49)}{1 + 0.29\,(w_{estimate} - 6.49)} \tag{4.107}$$

c) for concrete spalls.

$$Error_{spalls} = -2.35 \frac{0.23\,(w_{estimate} - 8.51)}{1 + 0.23\,(w_{estimate} - 8.51)} \tag{4.108}$$

These equations indicate that, for each case, there is an estimated flaw width at which the estimation error is 0 mm. The estimated flaw width at which the estimation error is zero is 3.3 mm, 6.5 mm, and 8.5 mm for delaminations, debonds, and concrete spalls, respectively. The equations could also be used to determine the estimation error for an estimated flaw width. For example, suppose that analysis of the maximum signal indicates that a debond is located at a depth of 1.5 mm (as per parametric study No. 3). Thus, Eq. 4.107 could be used to calculate the expected error in the estimated flaw. If analysis of the surface temperature data indicates that the

estimated flaw width is 12.0 mm, Eq. 4.107 predicts that the error in the width estimation is − 1.4 mm. Since error is defined as the estimated width minus the true width, the actual width of the flaw is

$$w = w_{estimate} - error \tag{4.109}$$

the actual width of the debond could be expected to be 13.4 mm.

An additional question that needs addressing is the minimum width of detectable flaws. The minimum width of detectable flaws is influenced by the thermal sensitivity of the camera and environmental noise, among others. Thus, the minimum detectable flaw width is based on the required maximum thermal signal.

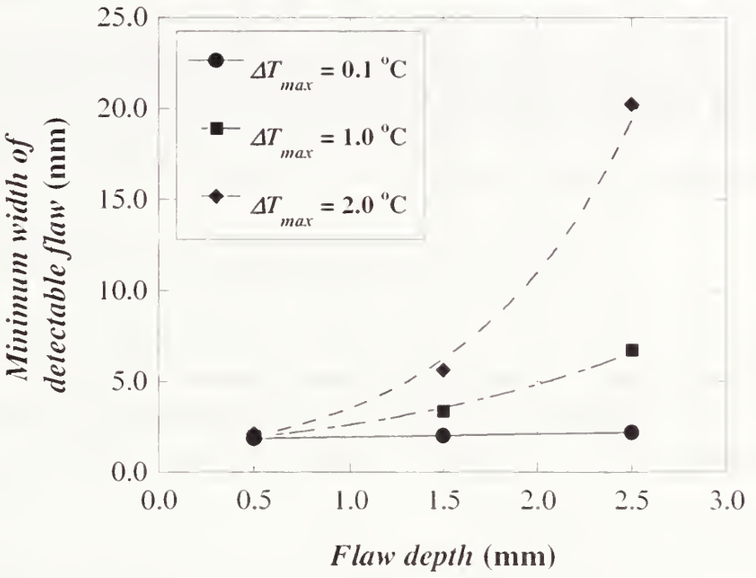

Fig. 4.117 Minimum width of detectable flaw as a function of flaw depth (mm)

The minimum detectable flaw width was estimated for three different cases: ΔT_{max} equal to 0.1 °C, 1.0 °C, and 2.0 °C. The first case, ΔT_{max} equal to 0.1 °C, corresponds to the thermal sensitivity of most IR cameras. Since, the values from the FEM analyses are ideal, that is, with perfect contact at the layer interfaces and without ambient noise, the cases with ΔT_{max} equal to 1.0 °C and 2.0 °C were also considered. The minimum width of detectable flaws could be estimated using Eqs. 4.93, 4.98, and 4.102. The results from the calculations are presented in Fig. 4.117.

The results presented in Fig. 4.117 show that as the resolution of the detectable signal increases (smaller ΔT_{max}), the minimum width of detectable flaws decreases. Power functions could be used to express the minimum width of detectable flaw. For the case of a signal resolution of 0.1 °C (ΔT_{max} = 0.1 °C), the minimum width of detectable flaw could be expressed as

$$w_{min} = 1.61 + 0.36\, d_{flaw}^{0.53} \tag{4.110}$$

where

w_{min} = minimum width of detectable flaws in millimeters; and,
d_{flaw} = depth of the flaw in millimeters.

For the case of a signal resolution of 1.0 °C, the following power function could be used to estimate the minimum width of detectable flaws:

$$w_{min} = 1.86 + 0.61 d_{flaw}^{2.27} \tag{4.111}$$

Finally, for the case of a signal resolution of 2.0 °C the following power function estimates the minimum width of detectable flaws:

$$w_{min} = 1.68 + 1.33 d_{flaw}^{2.87} \tag{4.112}$$

The results indicate that near-the-surface delaminations should be easily detected (ΔT_{max} = 2 °C) up to widths of 2 mm. The minimum width required for detection increases with increasing depth and the rate of increase related to the signal resolution of the test system. For concrete spalls 2.5 mm deep, the minimum width varies from 2 mm with ΔT_{max} = 0.1 °C to 20 mm with ΔT_{max} = 2 °C.

4.7.5 Summary

The final parametric study focused on the effect of flaw width on the thermal response and the estimation of flaw width.

The conclusions reached are as follows:

- All response parameters, T_{max}, ΔT_{max}, t_s, C_{max}, and t_c, increase nonlinearly with increasing flaw width.

- The variation in T_{max} could be expressed as an error function of the flaw width. The change in T_{max} for 2.5 mm deep concrete spalls, however, was negligible.

- The variation in ΔT_{max} as a function of flaw width could be expressed as a hyperbolic function. The effect of flaw width on the maximum signal is greater for delaminations than for deeper debonds or spalls.

- The variation in t_s as a function of the flaw could be expressed as a power function.

- Changes in t_s are negligible for shallow delaminations (less than 0.5 s for increases in w from 3 mm to 25 mm).

- The effect of flaw width on t_s is more pronounced for concrete spalls than for debonds or delaminations.

- The variation in maximum contrast could be expressed as a hyperbolic function of the flaw width.

- The variation in t_c could be expressed as a power function of the flaw width.
- The effect of the width of the flaw on t_c is greater as the depth of the flaw increases.
- The width of the flaw can be estimated by locating where $d^2T/dx^2 = 0$ from the surface temperature profile across the top of the flaw.
- The error in width estimation varies with increasing width. Moreover, the error changes signs, changing from over- to underestimations as the width of the flaw increases.
- The minimum detectable flaw width increases nonlinearly with increasing depth. The minimum width is also a function of the signal resolution, that is, the higher the signal resolution, the smaller the width of the flaw that can be detected.
- Because of their greater depth, concrete spalls are the most difficult flaws to detect and characterize. Small spalls are difficult to detect (small ΔT_{max}) and their size is difficult to estimate (large estimation error).

4.8 Summary on Single-Factor Parametric Studies

This chapter focused on the evaluation of the effect of various parameters on the thermal response of a concrete substrate covered with FRP layers. Finite element analysis was the chosen analytical tool. Five parametric studies were conducted using ANSYS 5.6. The parameters investigated were the thermal input, thermal material properties, flaw depth, flaw thickness, and flaw width.

In addition to investigating the effect of the various single-parameters on thermal response, the parametric study also aimed to:

- Optimize heating time and intensity for maximum thermal signal;
- Establish if accurate determination of material thermal properties is required for quantitative IR thermography of FRP laminates applied to concrete;
- Investigate the feasibility of estimating flaw depth from the measured thermal response;
- Establish minimum thickness of detectable flaw; and,
- Establish minimum width of detectable flaw.

It is concluded that the required thermal input is governed by the surface temperature that can be tolerated and the required input energy for the desired signal. For a given flaw geometry, the maximum signal is a linear function of the input energy E (J/m^2), and the maximum surface temperature is a function of energy as well as of the pulse duration.

The results from the second parametric study demonstrated that changes in the thermal properties of the constituent materials resulted in variations in the thermal response. The response parameters, however, were not very sensitive to these variations.

The results demonstrated that it may be possible to estimate flaw depth based on the time for maximum signal. So it is concluded that accurate knowledge of these properties is not required for successful quantitative IR inspection.

The fourth parametric study addressed the estimation of the minimum thickness of detectable flaws. The minimum flaw thickness required for detection was estimated for three values of maximum thermal signals. For each case, the minimum flaw thickness increased linearly with increasing flaw depth.

The fifth parametric study dealt with the effect of flaw width on the response parameters, and the minimum flaw width required for detection. The results indicated that the minimum flaw width required to detect a flaw increases nonlinearly with increasing depth. Similar to the case of minimum thickness, the minimum width of a detectable flaw is a function of the smallest maximum thermal signal that can be measured. This depends on the thermal resolution of the IR detector and the thermal "noise" associated with a particular testing condition. Ambient noise should also be considered since the simulations performed in this study assume perfect conditions (no convection losses, perfect material interface, etc.)

4.9 Multi-Factor Screening Study

The previous parametric studies provided information regarding the effect of single parameters on the thermal response of the FRP/concrete assembly. A ranking of the most important factors and the optional interaction among them, however, is desired. The following parametric study answers which are the most important factors, or interactions affecting three thermal response parameters: time for maximum signal t_s, magnitude of maximum signal ΔT_{max}, and maximum surface temperature. The screening study would allow the determination of what factors affect each of the thermal responses and to what degree.

4.9.1 Design of Screening FEM Experiment

The purposes of the screening FEM experiment were the following:

- Determine the statistically significant parameters and interactions affecting the thermal response; and
- Determine the ranking of parameters and interactions affecting the thermal response

The following flaw parameters and their interactions were investigated: Depth, thickness, and width. Additional factors such as thermal input and material properties of the constituents were kept fixed. The screening experiment was designed to investigate three factors with 2 levels each. An additional "center-point" simulation was added for modeling purposes. The additional

center point could provide information to model nonlinear behavior of the response. The chosen design was a full factorial experiment (2^3) with an extra center point.

In the design and planning of experiments that involve the simultaneous variation of various physical parameters or *factors*, it is customary to use the expression *Full Factorial Experimental Design* (Wu et al., 2000). Other related expressions commonly used in experimental design are also *Latin-Square Experimental Design*, *Taguchi Experimental Design*, and so forth. Each of these expressions corresponds to a particular kind of experimental design. A *full factorial experimental design* is analogous to a *full parametric analysis* in engineering science, except that it involves not only the variation of parameters affecting a given physical problem, but the specification of how the experiments ought to be carried out, and what factors need be varied. The term "full factorial design" is used in this special context in the following section.

The advantages of a full factorial design are the ability to estimate all interaction and main effects, it allows study of discrete and continuous factors, it is orthogonal in geometry, and it can generate a perfect fit model. The main disadvantage of this design is the required number of runs. In this case, nine runs were required to investigate the effect of the parameters on each thermal response.

Table 4.41 Coding of levels

Factor	**Level**		
	–	**+**	**0**
Depth of flaw, x_1	1.5 mm (debond)	0.5 mm (top delamination)	1.0 mm (bottom delamination)
Thickness of flaw, x_2	0.1 mm	0.2 mm	0.15 mm
Width of flaw, x_3	14 mm	25 mm	9.75 mm

The test object consisted of 3 layers of FRP composite bonded to a semi-infinite concrete slab. An air void was added at different depths of the FRP and at the interface with the concrete. Two levels of depth, thickness, and width were applied to the flaw. The levels of each factor were coded either – or + as shown in Table 4.41.

The full factorial design was constructed using Yates' order to guarantee orthogonal design of the experiment. Orthogonal geometry is important to ensure that the design of the experiment is balanced and fair to any single factor and interaction of factors. Orthogonal design also provides an unbiased estimate of the main effects and allows the estimation of interactions between factors. Yates order construction was also chosen because it is extensible in case additional factors need to be added to the experiment. The addition of new factors does not jeopardize the orthogonality of the design.

Table 4.42 Design of full factorial plus center-point screening study

Case	x_1 (depth of flaw)	x_2 (thickness of flaw)	x_3 (width of flaw)
1	−	−	−
2	+	−	−
3	−	+	−
4	+	+	−
5	−	−	+
6	+	−	+
7	−	+	+
8	+	+	+
9 (center point)	0	0	0

An outline of the design and factor levels is presented in Table 4.42. Randomization of the order of the runs was not necessary since these are numerical simulations rather than physical measurements.

4.9.2 Numerical Simulations

The test object consisted of a 100 mm long by 20 mm thick concrete slab with 3 layers of FRP bonded to its surface. Each layer of FRP was 0.5 mm thick. Each layer of FRP was oriented at 90 degrees with respect to the adjacent ply. The test object contained an internal flaw. The flaw (air void) was located at the center of the test object. The thickness of the flaw was either 0.2 mm or 0.1 mm. The depth of the flaw was a 0.5 mm deep delamination and a 1.5 mm deep debond. The width of the flaw was varied from 7.0 mm or 12.5 mm

Models were generated in the same manner as in previous cases.

4.9.3 Simulations Results

The simulation results for these response parameters are presented in Table 4.43. The effect on the thermal response due to each factor and their interactions was computed by subtracting the group averages as indicated in the following equation

$$\hat{\beta}_i = \bar{y}_+ - \bar{y}_- \tag{4.113}$$

where

$\hat{\beta}_i$ = measure of the effect of the factor or interaction;

$\bar{y}_+$ = average of the responses for the levels identified as "+"; and,
$\bar{y}_-$ = average of the responses for the levels identified as "−".

Table 4.43 FEM outputs for single-factor parametric study

	Factor Level			Results		
Case	x_1	x_2	x_3	t_s (s)	ΔT_{max} (°C)	T_{max} (°C)
1	−	−	−	6.25	3.83	49.1
2	+	−	−	2.44	17.9	64.6
3	−	+	−	6.85	5.12	49.3
4	+	+	−	2.54	26.1	71.7
5	−	−	+	7.35	4.44	49.1
6	+	−	+	2.53	18.5	64.9
7	−	+	+	8.55	6.10	49.3
8	+	+	+	2.73	27.2	71.2
9	0	0	0	5.14	9.1	52.3

4.9.4 Analysis of Results for t_s

The first thermal response evaluated was the time for maximum signal. The results of the computation of the effect of each factor and the interactions are presented in Table 4.44.

Table 4.44 Estimate of the effects of the factors and their interactions on the time for maximum signal

Factor or Interaction	$\bar{y}_+$ (s)	$\bar{y}_-$ (s)	$\hat{\beta}_i$ (s)
x_1 (depth)	2.5	7.3	-4.7
x_2 (thickness)	5.2	4.6	0.5
x_3 (width)	5.3	4.5	0.8
$x_1 \cdot x_2$	4.7	5.1	-0.4
$x_1 \cdot x_3$	4.6	5.2	-0.7
$x_2 \cdot x_3$	5.0	4.8	0.2
$x_1 \cdot x_2 \cdot x_3$	4.8	5.0	-0.1

The same results are presented in Fig. 4.118. Each graph plots the average of the thermal response at levels "+" and "−" for each factor and two-factor interaction. The slope of each line is an indicator of the effect of the factor on the time for maximum signal. The results indicate that factor x_1 (depth of flaw) has the greatest effect on time for maximum signal.

The first step for deciding what factors or interaction have significant effects on the response was to compare the difference of the means ($\hat{\beta}_i$) to the minimum engineering significant response. The minimum engineering significant response is a value specified a priori by the investigator and is based on instrumentation capabilities and on engineering judgment. For this particular study, the minimum engineering significant response for t_s was selected as 0.5 s. Based on this assumption and comparing with the results presented in Table 4.44, only three single factors and one interaction should be considered to have a significant effect on the response. The ranking of these factors and interactions from the highest effect to the lowest effect is as follows:

1. x_1 (depth of flaw) $\rightarrow \hat{\beta}_1 = -4.7$ s
2. x_3 (width of flaw) $\rightarrow \hat{\beta}_3 = 0.8$ s
3. x_{13} (interaction between depth and width of flaw) $\rightarrow \hat{\beta}_{13} = -0.7$ s
4. x_2 (thickness of flaw) $\rightarrow \hat{\beta}_2 = 0.5$ s

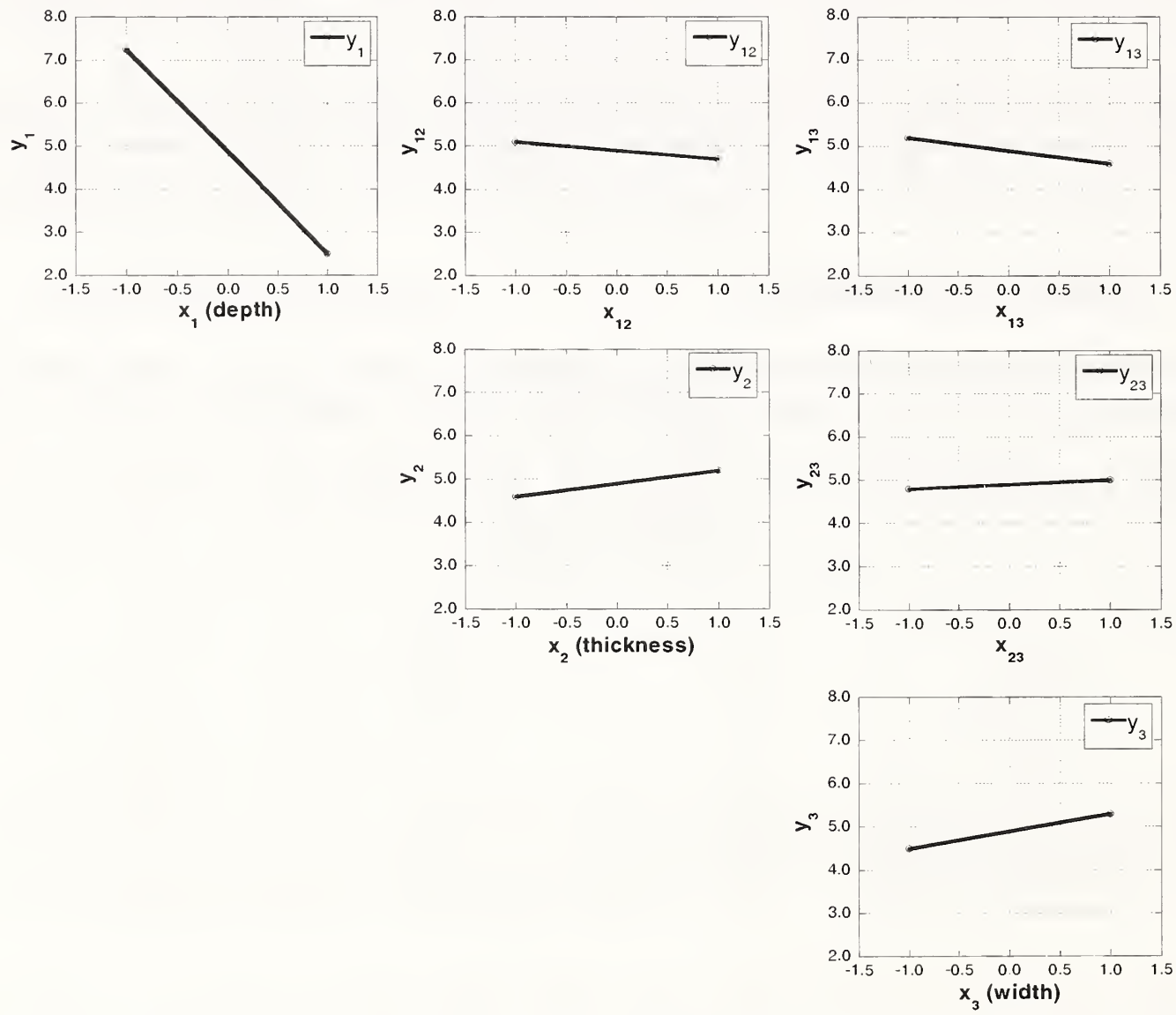

Fig. 4.118 Plots of means of factors and interactions for the time to maximum signal

The previous approach is arbitrary, and the search for the significant factors affecting a response may be further refined by using the halfnormal probability plot. Based on this plot, only the factors or interactions that deviate from the straight line fit to the points whose $\hat{\beta}_i$ are near zero have a statistically significant effect on the response. The halfnormal probability plot for the effects on t_s is presented in Fig. 4.119. The graph clearly indicates that only one factor, the depth of the flaw, has a statistically significant effect on the time for maximum signal.

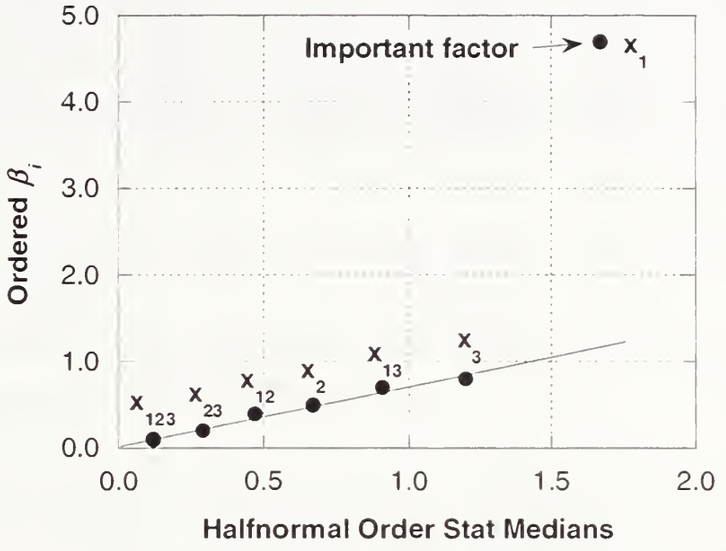

Fig. 4.119 Halfnormal probability plot for effects on time for maximum signal

4.9.5 Conclusions for t_s

The evaluation of the results from the first screening study confirms the importance of the depth of the flaw as the primary factor affecting the time for maximum signal. Even though the width and thickness of the flaw and the interaction between depth and width may have a measurable effect on the thermal response, the halfnormal probability analysis indicates clearly that the depth of the flaw is the most significant factor.

Nondestructive evaluation requires the solution to the inverse problem that is, determination of the characteristics of the flaw based on the measured thermal response. This phase of the multi-parameter study suggests that the depth of the flaw may be estimated from the time for maximum signal alone. Thus, the procedures described in Section 4.5.4d may provide an approach for estimating flaw depth.

4.9.6 Analysis of Results for ΔT_{max}

The second thermal response assessed was the magnitude of the thermal signal. The overall average value of the maximum thermal signal was 13.6 °C. The effects on ΔT_{max} due to the factors and their interactions were evaluated using Eq. 4.113. The results are presented in Table 4.45.

Table 4.45 Estimate of the effects of the factors and their interactions on the magnitude of the maximum signal

Factor or Interaction	$\bar{y}_+$ (°C)	$\bar{y}_-$ (°C)	$\hat{\beta}_i$ (°C)
x_1 (depth)	22.4	4.9	17.6
x_2 (thickness)	16.1	11.2	5.0
x_3 (width)	14.0	13.2	0.8
$x_1 \cdot x_2$	15.4	11.9	3.5
$x_1 \cdot x_3$	13.6	13.6	0
$x_2 \cdot x_3$	13.8	13.5	0.2
$x_1 \cdot x_2 \cdot x_3$	13.6	13.6	0

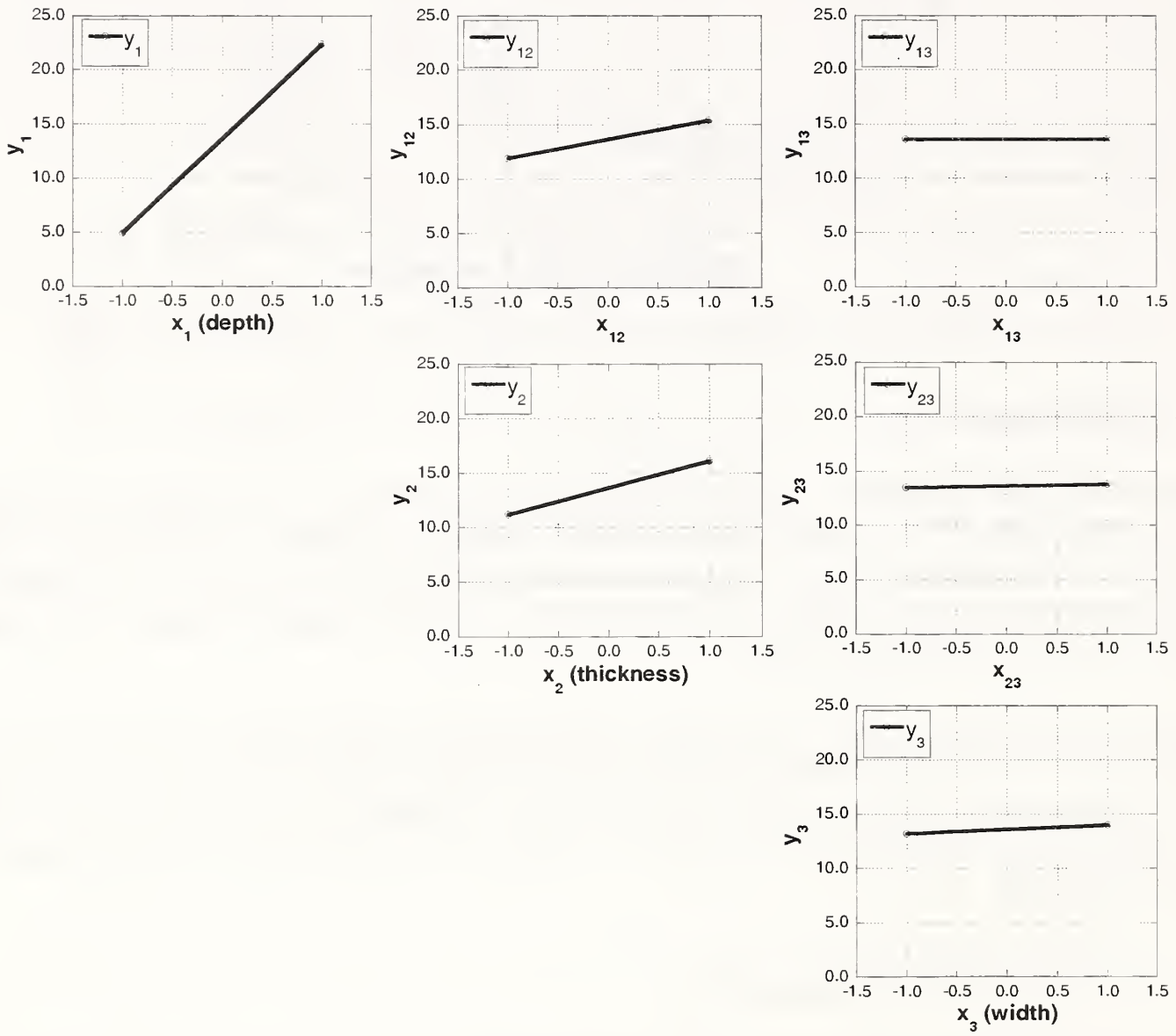

Fig. 4.120 Plot of means of factors and interactions for the maximum signal

The effects summarized in Table 4.45 are illustrated in Fig. 4.120. The slope of each line is an indicator of the degree of influence that the factor or interaction has on the maximum signal, ΔT_{max}.

The minimum engineering significant response for the magnitude of the maximum signal was assumed to be 0.2 °C, based on the thermal sensitivity of most IR cameras.

The factors were ranked based on the effect on the maximum signal and on the assumed minimum engineering significant response. The following list presents the ranking of the effects:

1. x_1 (depth of flaw) $\rightarrow \hat{\beta}_1 = 17.6$ °C
2. x_2 (thickness of flaw) $\rightarrow \hat{\beta}_2 = 5.0$ °C
3. x_{12} (interaction between depth and thickness of flaw) $\rightarrow \hat{\beta}_{12} = 3.5$ °C
4. x_3 (width of flaw) $\rightarrow \hat{\beta}_3 = 0.8$ °C
5. x_{23} (interaction between thickness and width of flaw) $\rightarrow \hat{\beta}_{23} = 0.2$ °C

Note that the last two effects could be deemed "not significant" if the minimum significant response for ΔT_{max} were assumed to be 1.0 °C.

The effects were examined further by means of the halfnormal probability plot of the results. As shown in Fig. 4.121, the factors and interactions that have statistically significant effects on the thermal response correspond to those that deviate from the best-fit straight line passing through the origin. Using this method, two factors and one interaction (flaw depth, flaw thickness, and their interaction) appear to have a statistically significant effect on the magnitude of the maximum signal.

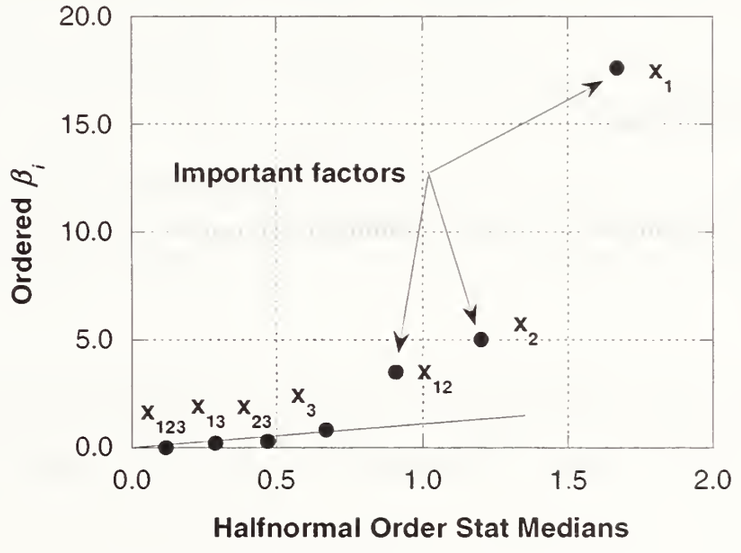

Fig. 4.121 Halfnormal probability plot for the maximum signal

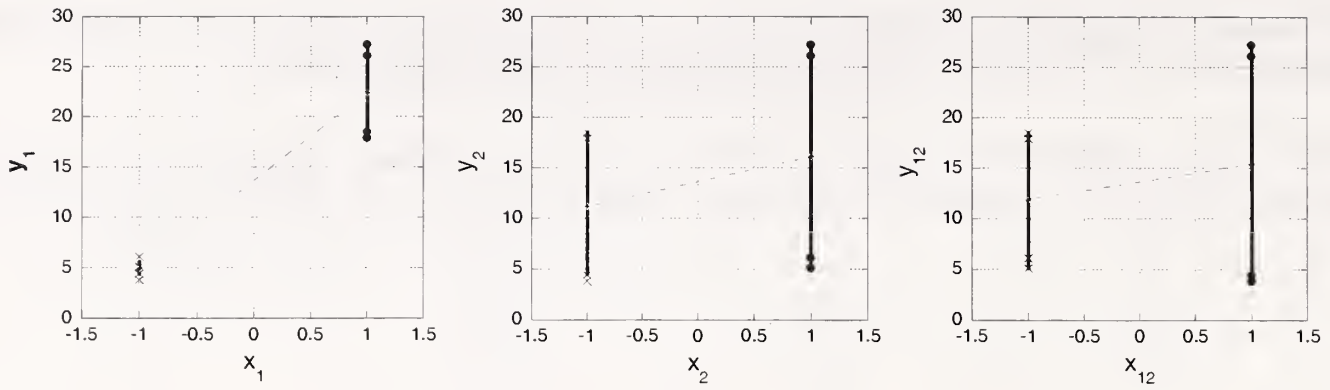

Fig. 4.122 Scatter plots of the important factors affecting ΔT_{max}

A third analysis tool was used to evaluate the results. This method involves the observation of the degree of dispersion of the thermal response when presented as scatter plots. While the plots of the means (Fig. 4.120) and the halfnormal probability plot (Fig. 4.121) explain what factors have significant effects on the thermal response, the scatter plots (Fig. 4.122) clarify the basis for the effects. Factors with more localized results around the means for the + or – levels and with larger differences in the means ($\hat{\beta}_i$) are said to be more influential on the response than factors with scattered data and smaller differences in means. The level of the factors associated with less scatter can be predicted more reliably from the response than the level of factors associated with large scatter.

Figure 4.122 illustrates that of the 2 factors and one interaction that have significant effects on ΔT_{max}, only flaw depth (x_1) results in low scatter about the + and – levels. Flaw thickness and the interaction between both factors result in large scatter about the means. This scatter would impede any attempt to estimate flaw thickness based on the maximum signal, and this approach is not recommended.

4.9.7 Conclusions for ΔT_{max}

The evaluation of the results from the second screening study confirms the importance of the depth of the flaw as the primary factor affecting the magnitude of the maximum signal. In this case, however, flaw thickness and the interaction between flaw depth and thickness also affect the maximum signal.

The scatter plots illustrated the high dispersion of ΔT_{max} as a function of the thickness of the flaw and the interaction between flaw depth and thickness. The evaluation of the scatter plots indicates that flaw thickness cannot be estimated reliably on the bases of measured maximum thermal signal.

4.9.8 Analysis of Results for T_{max}

The final thermal response examined was the maximum surface temperature. The overall average value of the maximum surface temperature for the simulation was 58.7 °C. The effect of

each factor and the interactions on the maximum surface temperature were evaluated using Eq. 4.113. The results are presented in Table 4.46.

Table 4.46 Estimate of the effects of the factors and their interactions on the magnitude of the maximum surface temperature

Factor or Interaction	$\bar{y}_+$ (°C)	$\bar{y}_-$ (°C)	$\hat{\beta}_i$ (°C)
x_1 (depth)	68.1	49.2	18.9
x_2 (thickness)	60.4	56.9	3.5
x_3 (width)	58.7	58.7	0
$x_1 \cdot x_2$	60.3	57.0	3.3
$x_1 \cdot x_3$	58.7	58.7	0
$x_2 \cdot x_3$	58.6	58.8	-0.2
$x_1 \cdot x_2 \cdot x_3$	58.6	58.8	-0.2

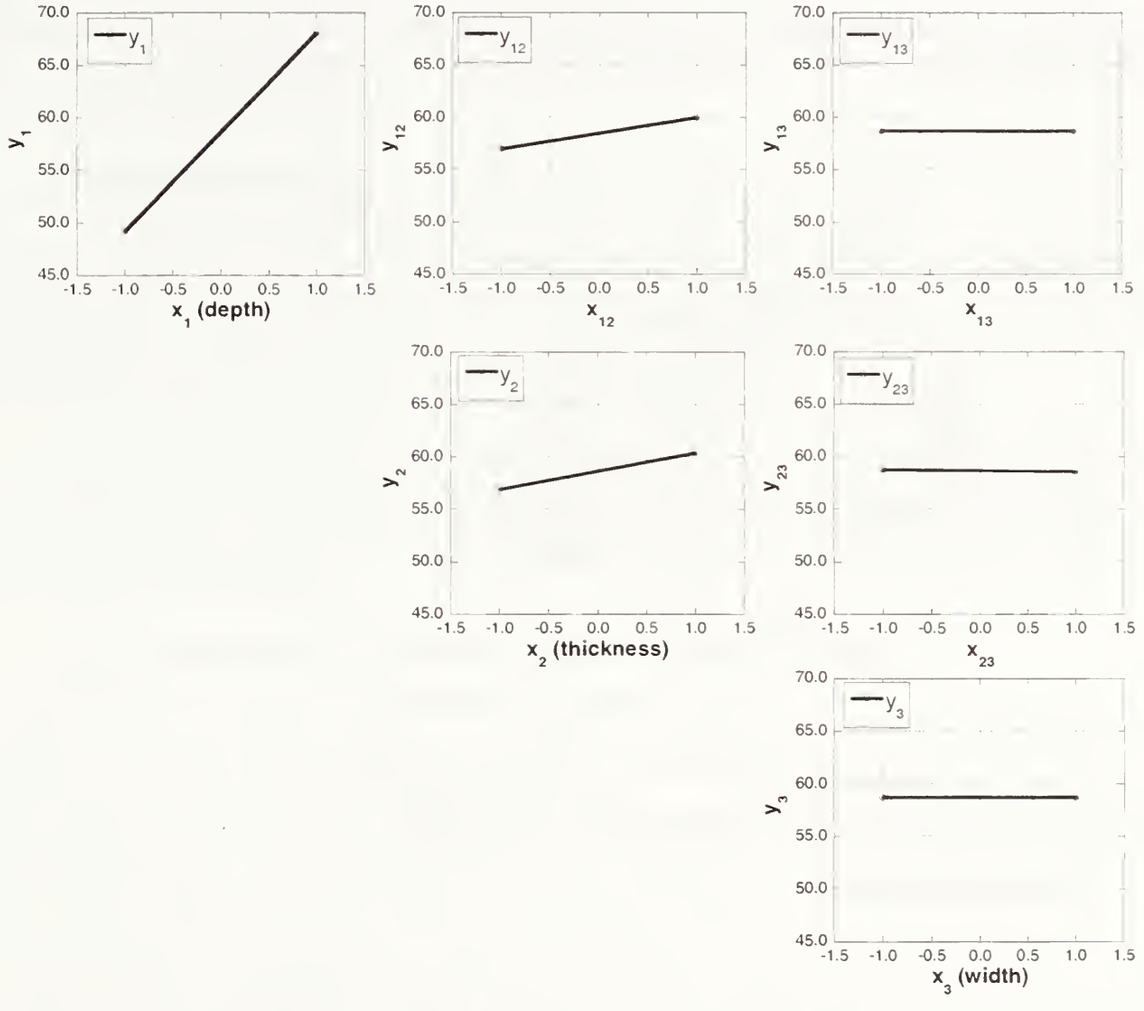

Fig. 4.123 Plot of means of factors and interactions for the maximum surface temperature

The effects of the factors are also illustrated in Fig. 4.123. The slope of each line denotes the magnitude of the effect of the factor or interaction on the maximum surface temperature. The

minimum engineering significant response for T_{max} was assumed to be 0.2 °C, which corresponds to the thermal sensitivity of most infrared detectors.

Based on the assumed minimum engineering significant response, the factors and their interactions were ranked in decreasing order as follows:

1. x_1 (depth of flaw) $\rightarrow \hat{\beta}_1 = 18.8$ °C
2. x_2 (thickness of flaw) $\rightarrow \hat{\beta}_2 = 3.5$ °C
3. x_{12} (interaction between depth and thickness of flaw) $\rightarrow \hat{\beta}_{12} = 3.3$ °C
4. x_{23} (interaction between thickness and width of flaw) $\rightarrow \hat{\beta}_{23} = -0.2$ °C
5. x_{123} (interaction between depth, thickness, and width of flaw) $\rightarrow \hat{\beta}_{123} = -0.2$ °C

Next, the halfnormal probability of the $\hat{\beta}_i$s was plotted as shown Fig. 4.124. Using this analytical tool, significant effects were due to two factors (depth and thickness) and their interaction.

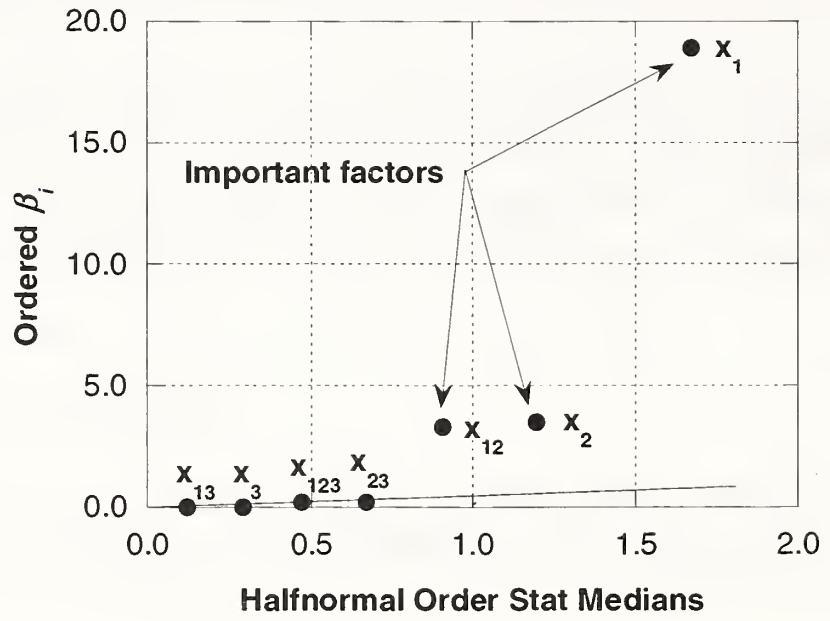

Fig. 4.124 Halfnormal probability plot for the maximum surface temperature

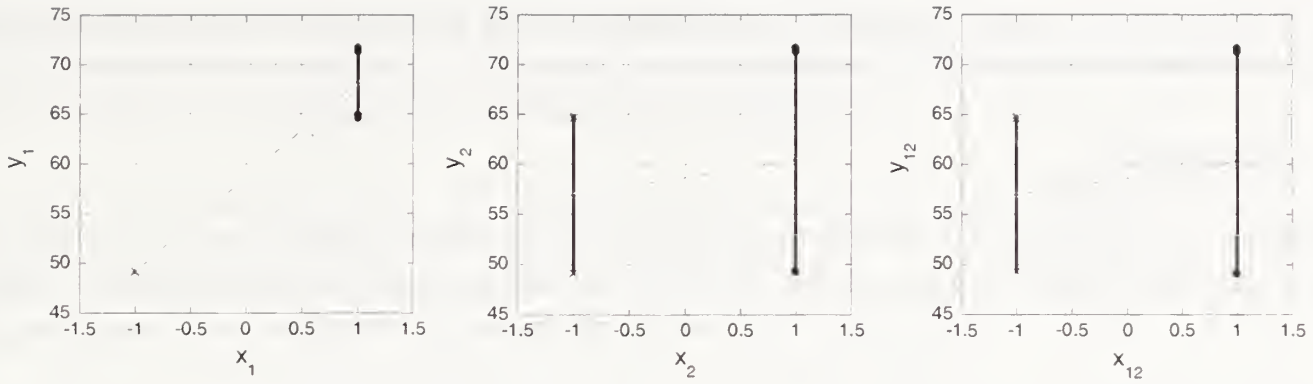

Fig. 4.125 Scatter plots of the important factors affecting T_{max}

Next, the maximum surface temperatures were plotted using scatter plots, as shown in Fig. 4.125. The results are similar to those for the magnitude of the maximum signal. The plots indicated that the only factor resulting in low scatter is the depth of the flaw. When the results are plotted in terms of flaw thickness, there is large scatter.

The determination of an adequate model to estimate the maximum surface temperature from the significant factors is improbable due to the high dispersion of the output values for the flaw thickness and the interaction factor.

4.9.9 Conclusions for T_{max}

The evaluation of the results from the final screening study confirms the significance of the depth of the flaw as the primary factor affecting the maximum surface temperature. The thickness of the flaw and the interaction between flaw depth and thickness also affect parameters influencing the magnitude of the maximum surface temperature.

The analysis also showed large scatter when the maximum surface temperature was plotted as a function of the thickness of the flaw and the interaction between flaw depth and thickness. This indicates that it may not be possible to estimate flaw thickness based solely on the measured maximum surface temperature.

4.9.10 Conclusions for the Multi-Factor Parametric Study

A multi-parameter screening study was conducted to determine the flaw geometry factors that have significant effects on the thermal responses. A full factorial design was used to investigate the effect of the factors and their interactions. The factors investigated were the depth, thickness, and width of the flaw. The screening study was conducted for three thermal responses: time to maximum signal, magnitude of maximum signal, and maximum surface temperature.

The screening study showed that the depth of the flaw is the only factor that has a significant effect on the time to maximum signal. Thus the study confirmed that it should be possible to estimate the depth of the flaw using the time for maximum signal.

The analyses also established that the magnitude of the maximum signal and the maximum surface temperatures are affected by the depth of the flaw, the thickness of the flaw, and their interaction. The large scatter of the maximum signal or the maximum surface temperatures

when plotted as a function of the thickness indicated that it would be difficult to estimate flaw thickness based on these measured responses.

4.10 Summary

Finite-element modeling was used as the analytical tool to investigate the effect of various parameters on the thermal response of FRP bonded to concrete and containing flaws. The study focused on the evaluation of the various parameters that influence thermal evolution (the spatial and temporal variations of surface temperature). The investigation was subdivided into a series of single-factor parametric studies and a multi-factor parametric study.

The first series of parametric studies involved "one-at-a time" evaluations of the parameters that affect the thermal response. The objectives for the single-factor parametric studies were the following:

- Understand the effects of the thermal input;
- Optimize heating time and intensity for maximum image contrast while controlling the maximum surface temperature;
- Determine the effects of material properties on the thermal response;
- Investigate the effect of flaw depth;
- Investigate the estimation of flaw depth;
- Examine the effect of type of flaw (delamination versus debond versus concrete spall);
- Study the effect of flaw thickness and flaw width;
- Investigate the estimation of flaw width;
- Determine minimum detectable flaw size.

It was found that for a given flaw geometry, the maximum thermal signal is a linear function of the input energy (expressed in J/m^2). Thus, a maximum value of input energy can be established for a given minimum signal. The maximum surface temperature is also a linear function of the input energy, but it also depends on the pulse duration. The selection of the pulse duration to produce the minimum input energy is governed by the maximum surface temperature that can be tolerated. These results have led to a simple approach for selecting the thermal input so as to obtain a desired thermal signal while limiting the surface temperature due to heating. The investigation also concluded that, based on the thermal input, variations in the pulse duration affect both the magnitude of the signal and the time to maximum signal, while variations in the magnitude of the heat flux only affect the magnitude of the signal.

The results from the study of the effect of material thermal properties indicated that, while variations in the thermal properties of the FRP and concrete resulted in systematic variations in thermal response, none of the response parameters were very sensitive to changes in material properties. Thus, the success of infrared thermography testing will not depend strongly on the specific values of the thermal properties of the FRP or concrete substrate.

The study of the effect of the flaw depth demonstrated that the thermal responses are a function of the flaw depth and the number of FRP plies bonded to the concrete. Estimation of the depth of the flaw was demonstrated using the time to maximum signal.

It was shown that the influence of flaw thickness on the thermal responses is significant in the case of delaminations near the surface but is very small on debonds and concrete spalls. No simple procedure was indicated for estimating flaw thickness.

The results also indicated that the width of the flaw could be estimated from the second derivative of the surface temperature profile. The investigation of the minimum detectable flaw width demonstrated that the smallest detectable flaw is a function of the depth of the flaw and the maximum signal required to overcome noise in the measuring process.

The multi-factor parametric study confirmed which factors have the most significant effect on the thermal responses. The investigation concluded that the depth of the flaw is the only factor that has a significant effect on the time to maximum signal. Thus the results confirmed that the depth of the flaw could be estimated using the time for maximum signal. On the other hand, the large scatter of the thermal responses as a function of the thickness indicated that this factor would be difficult to characterize accurately.

Chapter 5

Laboratory Studies

5.1 Introduction

The second component of the project focused on a series of laboratory studies aimed to define good testing and analysis procedures for IR thermography testing of FRP composites bonded to concrete. In addition, experimental measurements were used to verify the FEM simulations was. Specifically, the objectives of the experimental program were the following:

- Determination of emissivity values of pultruded FRP laminates and wet lay-up FRP laminates;
- Comparison of FEM simulation with results from actual infrared testing;
- Confirm the potential of flaw width estimation based on surface temperature profiles;
- Verification of the importance of key flaw parameters such as, depth thickness, and width, on thermal responses;
- Verification of approach to estimate flaw depth based on time of maximum signal;
- Evaluation of test repeatability; and
- Determination of an adequate sampling rate.

The objectives were carried out by:

- Selection of adequate heating devices;
- Measurement of heat flux input;
- Construction of an experimental setup to permit repeatable thermal pulses; and
- Conducting controlled-flaw experiments.

5.2 Design of Experiments

The experimental program was subdivided into 5 parts, each involving one experiment:

- The first part of the experimental study was qualitative in nature, and its focus was to evaluate the suitability of different materials for creating simulated flaws in controlled-flaw specimens. A specimen having two bonded pultruded CFRP laminates and containing eight simulated debonds was used for this experiment.

- The second test focused on comparison of infrared thermography results to the results of FEM simulations. An air void contained in the specimen from the first experiment (pultruded CFRP bonded to concrete slab) was used as the test case.

- The purpose of the third experiment was to verify the procedure for estimation of the flaw width based on surface temperature profiles. For this purpose, the size of the air void in the specimen fabricated with pultruded CFRP was measured.

- The fourth experiment was a screening study to confirm the results of the analytical screening study. Three flaw parameters were investigated: depth, thickness, and width. To investigate these three parameters, a full factorial experimental design was planned. Factors such as thermal input, and material properties were kept fixed in the experimental design. The full factorial screening experiment was designed to investigate three factors with 2 levels each. Two additional "center-points" were added for modeling purposes. The additional center points could provide the data needed to model nonlinear behavior of the response.

Table 5.1 Coding of levels for screening experiment

Factor	**Level**	
	–	+
Depth of flaw, x_1	1.5 mm (debond)	0.5 (top delamination)
Thickness of flaw, x_2	0.1 mm	0.2 mm
Width of flaw, x_3	7 mm	12.5 mm

The test object for the study consisted of 3 layers of FRP wet lay-up composite bonded to a concrete slab. Simulated flaws were included at different depths in the FRP layers and at the interface with the concrete. Flaws had two different depths, thicknesses, and widths. The levels of each factor were coded "–" or "+" as shown in Table 5.1.

The full factorial design was constructed using Yates' order as discussed in Chapter 4.

Table 5.2 Design of full factorial plus center-points screening study

Case	x_1 (depth of flaw)	x_2 (thickness of flaw)	x_3 (width of flaw)	Run Sequence
1	−	−	−	6
2	+	−	−	4
3	−	+	−	2
4	+	+	−	1
5	−	−	+	9
6	+	−	+	10
7	−	+	+	5
8	+	+	+	7
9 "center" point	0	−	0	8
10 "center" point	0	+	0	3

Run randomization was used in selecting the order in which the flaws were investigated. Randomization was introduced to ensure that uncontrolled variables did not bias the results. The design and run sequence of this experiment are presented in Table 5.2. Code levels "0" represents levels of flaw depth and width that are intermediate to the levels shown in Table 5.1.

The construction of the specimen and testing procedures for are explained in the subsequent sections.

- The final part of the experimental study focused on the investigation of test repeatability and the effect of sampling rate.

5.3 Testing Configurations

Depending on the objective of the experiments, two different configurations were used for thermography testing. The first set of tests involved qualitative assessment of the presence of debonds in a controlled-flaw specimen. The remaining experiments involved quantitative evaluation of several subsurface flaws. The test configuration for quantitative testing was more elaborate than that for qualitative testing.

Detection and quantitative characterization of subsurface flaws require an external heat source to produce the desired transient heat transfer conditions. Moreover, a short-duration, high-intensity thermal pulse is ideal for producing highly transient behavior. As discussed in the previous

chapter and in Starnes et al. (2002), selection of the thermal input requires achieving a balance between the desired thermal signal (surface temperature differential between flawed and sound material) and the maximum allowable surface temperature. This balance is achieved by selecting appropriate values of the heat flux intensity and the heating period. The inspector may choose a short-duration heating period with high-intensity heat flux, or vice versa. The parametric studies described in the previous chapter also indicate that for civil engineering applications, lower intensity heat flux with a longer heating period (for example, seconds instead of microseconds) provides the balance needed to obtain a desired thermal signal and limit the maximum surface temperature.

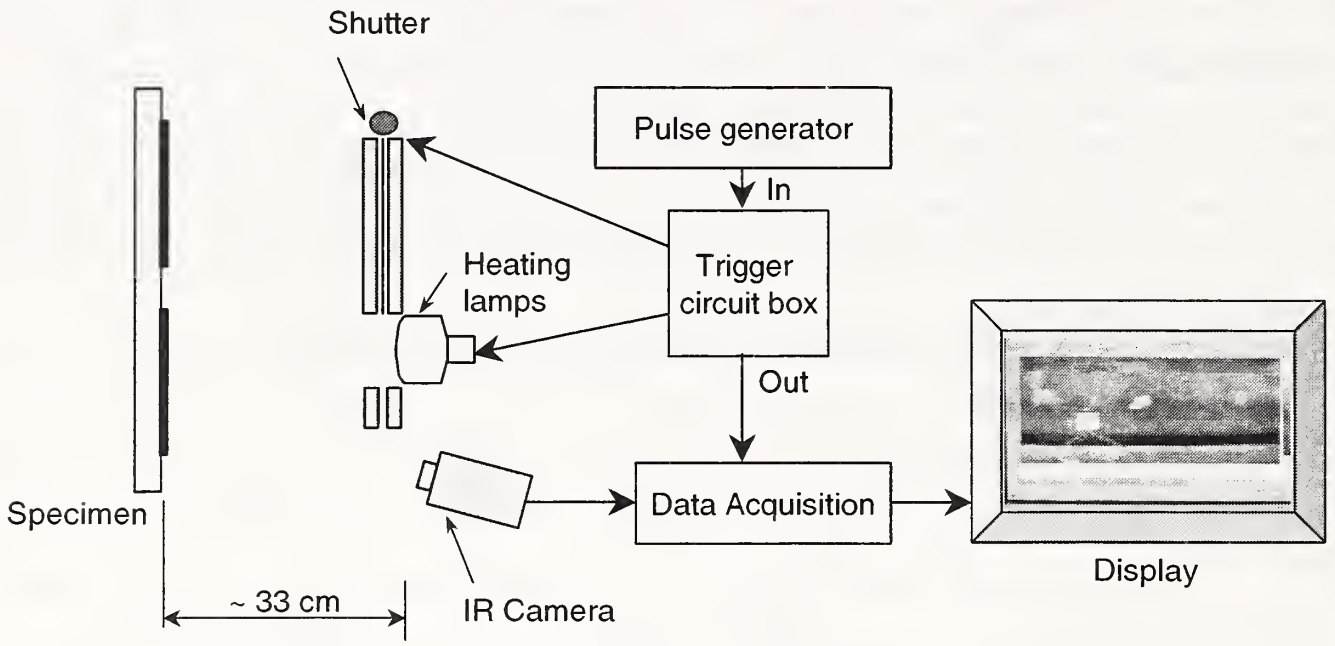

Fig. 5.1 Test configuration for quantitative infrared thermography

Qualitative and quantitative thermographic testing techniques require an IR camera and a data acquisition system that allows viewing of the thermograms. Quantitative testing, however, requires the capability of recording and measuring the thermal response as a function of time. To fulfill this requirement a more involved testing setup was constructed. Additionally, the experimental setup included shutters for the heating system, external triggers to synchronize data acquisition with the start of the thermal pulse, and data analysis software. A schematic of the test configuration for quantitative testing is presented in Fig. 5.1.

The following subsections describe the qualitative and quantitative test configurations in greater detail.

5.3.1 Qualitative Test

The purpose of qualitative testing is to detect the presence of subsurface anomalies. Qualitative testing does not require accurate control of the input thermal pulse nor does it require detailed analyses of the temperature history. The qualitative test involved the use of one 250 W infrared lamp. Heating was done by sweeping the infrared heat lamp over the surface of the FRP at a

distance of 50 mm and at a speed of approximately 0.15 m/s. This technique is similar to the method used in practice (Hawkins et al., 1999).

The time history of the thermal response was not subjected to detailed analysis. The surface temperatures recorded by the infrared camera were logged with the aid of the data acquisition system. Subsurface flaws were identified visually through the thermograms recorded by the data acquisition system. The specifications for the IR camera and the data acquisition software are described further in the next section.

5.3.2 Quantitative Tests

The overall purpose of these studies is to provide the basis for quantitative infrared thermography in which not only the presence but also characteristics of a flaw can be established. The experimental configuration for quantitative testing included a heating module, IR cameras, and data acquisition and analysis software capable of recording and analyzing thermal behavior as a function of time.

5.3.2a Heat Sources

A heating module was fabricated to provide the controlled heat flux pulse required for quantitative testing. Two 250 W infrared heating lamps mounted at 200 mm on center were used as the heat source. An aluminum frame was made to hold the heating lamps and an aluminum shutter. The shutter was necessary to block radiation from the lamps after they were turned off. This was required so that the heat pulse would be similar to the rectangular pulse used in the FEM simulations. The shutter was kept open during heating using an electromagnet. A photograph of the heating configuration is presented in Fig. 5.2.

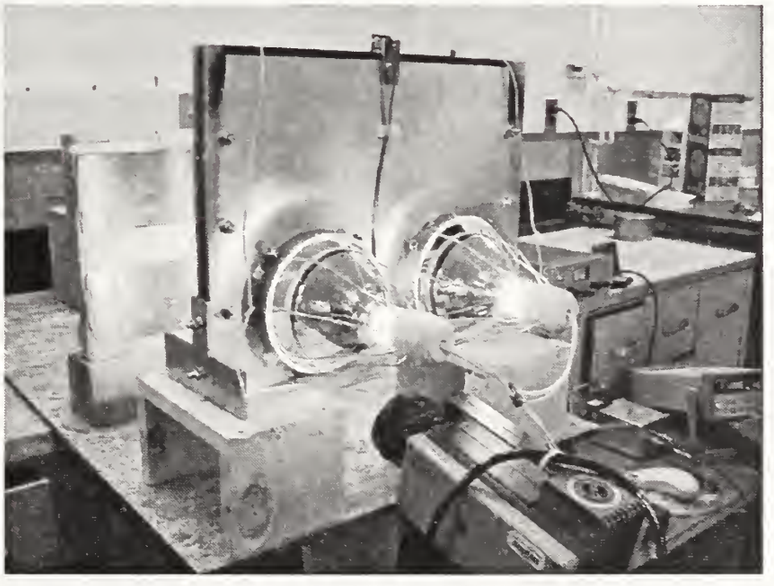

Fig. 5.2 Configuration of heating module for quantitative testing

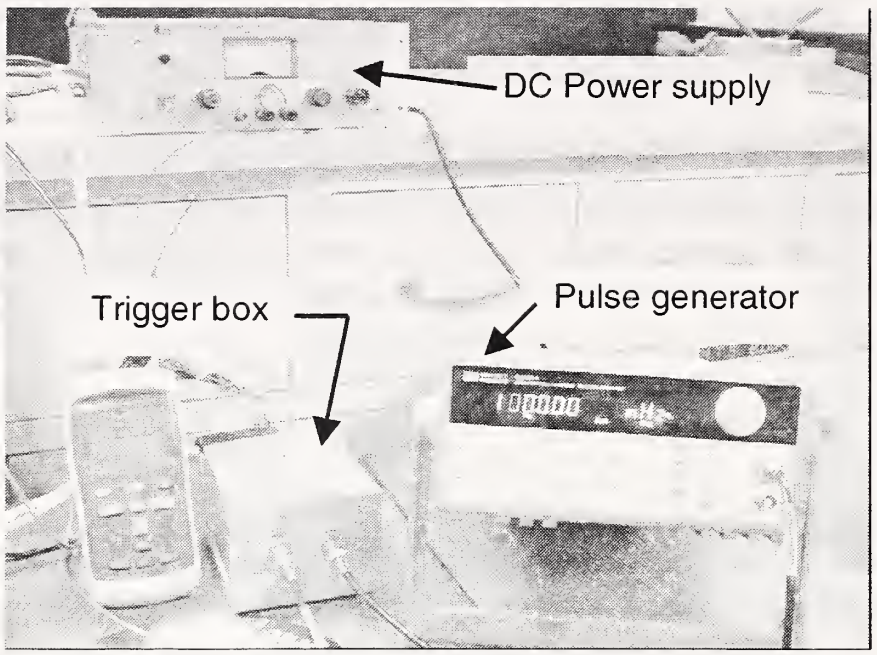

Fig. 5.3 Pulse generator, trigger box, and power supply

A DC power supply, a pulse generator, and a trigger circuit were also needed for producing a "square" heat pulse. A waveform generator was connected to the trigger circuit. At the end of the pulse, the trigger turned off the lamps and the current supplied to the electromagnet, and the shutter fell in front of the lamps. An additional function of the trigger was to externally trigger the data acquisition system at the beginning of the heat pulse. Figure 5.3 shows the pulse generator, DC power supply and trigger box used in the experiments.

5.3.2b Infrared Cameras

Two different infrared cameras were used during the project. The initial experiments, those involving pultruded CFRP composites, were performed using an infrared camera with a nitrogen-cooled detector. An uncooled microbolometer was used for the final set of experiments.

Infrared Camera with Nitrogen-Cooled Detector

The infrared camera used in the first three sets of experiments was an AGEMA Thermovision 900. The infrared camera has a mercury-cadmium-telluride (HgCdTe or MCT) detector. The scanner operates in the long-wave infrared region with a spectral response between 8 μm and 12 μm. The detector has a sensitivity of 0.08 °C at 30 °C and a measurement accuracy of ± 1 °C. As mentioned, this detector requires continuous cooling with liquid nitrogen. The scanner was able to record data at a maximum sampling rate of 15 Hz.

Infrared Camera with an Uncooled Detector

The experiments involving wet lay-up composites were carried out using a FLIR ThermaCAM SC2000†. This infrared camera has a focal plane array (FPA) uncooled microbolometer detector with 320 pixels × 240 pixels. The camera operated in the long wavelength infrared spectral band (7.5 μm and 13 μm), thus minimizing atmospheric attenuation of the received radiation. The camera has an atmospheric filter with cut-on at 7.5 μm. The thermal sensitivity of the detector is 0.08 °C at 30 °C with a measurement accuracy of ±2 °C. The infrared camera allowed recording of thermograms at a rate of 60 Hz.

5.3.2c Data Acquisition and Analysis Software

The data acquisition and analysis software for infrared measurements was Researcher High Speed from FLIR Systems†. This software provides up to 60 Hz digital video and data acquisition and retrieval. For quantitative testing, an external trigger was connected to the data acquisition system. Data acquisition was triggered at the time the heating lamps were turned on.

For heat flux measurement, a DataShuttle† data acquisition system and QuickLog† software from Omega were used to measure the output of the heat flux sensor.

5.3.3 Specimens

Three different specimens were constructed for the experimental studies. The first specimen was constructed using pultruded CFRP laminates (Carbodur® from Sika)†. The remaining two specimens were fabricated using wet lay-up CFRP fabric (M-Brace from Master Builders)†.

5.3.3a Specimen Fabricated with Pultruded CFRP Laminates

The controlled-flaw specimen was constructed by using a 610 mm × 250 mm × 45 mm precast concrete slab as the substrate. Two pultruded carbon FRP (CFRP) laminates were bonded to the substrate, as shown in Fig. 5.4. The laminates are available commercially and contained unidirectional carbon fibers. Each laminate had the following dimensions: 609 mm × 102 mm × 1.3 mm. The surface of the concrete slab was cleaned to remove any existing dust. The composite laminates were precut to the appropriate length and cleaned with acetone. The bonding epoxy (SikaDur®)† was applied over the concrete surface to a thickness of about 1.6 mm using a spatula. Application of epoxy was avoided at the location at which the artificial flaws were going to be placed. Eight "flaws" were created by placing different materials at the interface between the concrete substrate and the FRP. Each flaw was approximately 25 mm × 25 mm in plan. The materials used to simulate flaws and their approximate thickness are summarized in Table 5.3. One of the objectives of the experiment was to see whether there is a material that would produce results similar to an air void (flaw #6). The laminate was placed on the epoxy and pressed down using a rubber roller. The specimen was kept undisturbed for one day to allow curing of the epoxy.

Table 5.3 Summary of simulated flaws

Flaw #	Material	Placement/construction	Approximate thickness (mm)
1	Air & plastic	Air-filled plastic	0.4
2	Air & wax	Lost wax process	0.6
3	Styrofoam®		0.5
4	Masking tape		0.3
5	Low *k* fabric & plastic	Fabric wrapped in plastic	0.8
6	Air	Air void created with wire dam	0.6
7	Parafilm®		0.1
8	Vitreous aluminosilicate fiber insulation & plastic	Insulation wrapped in plastic	0.8

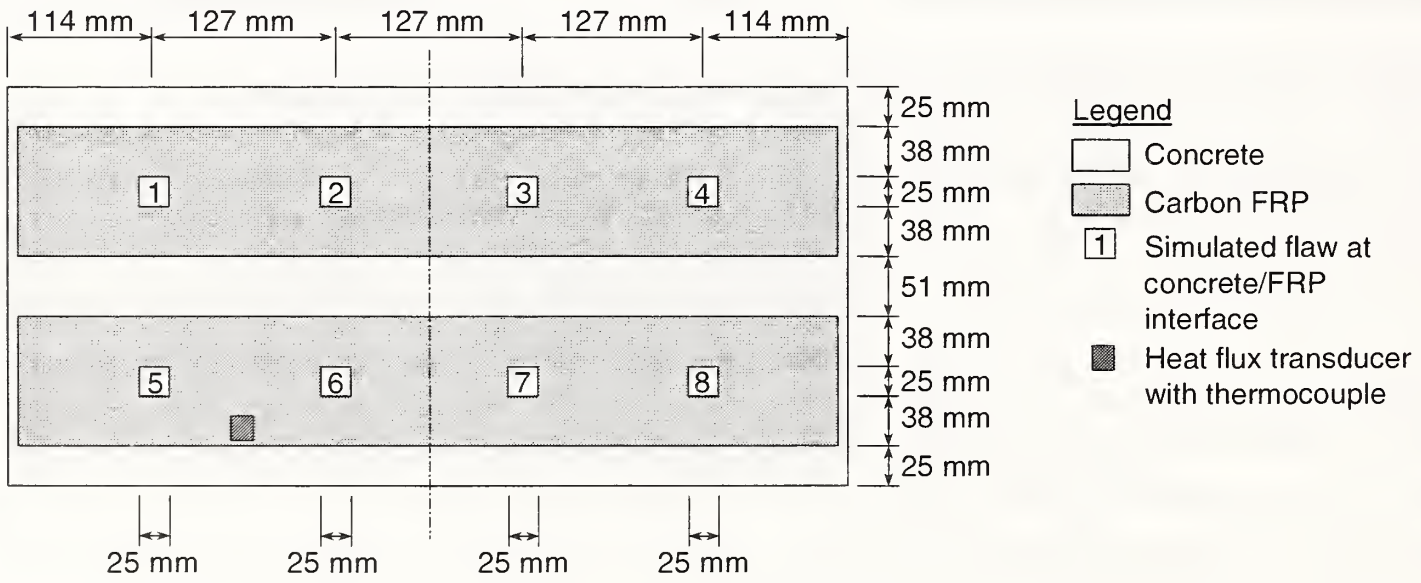

Fig. 5.4 Controlled-flaw test specimen

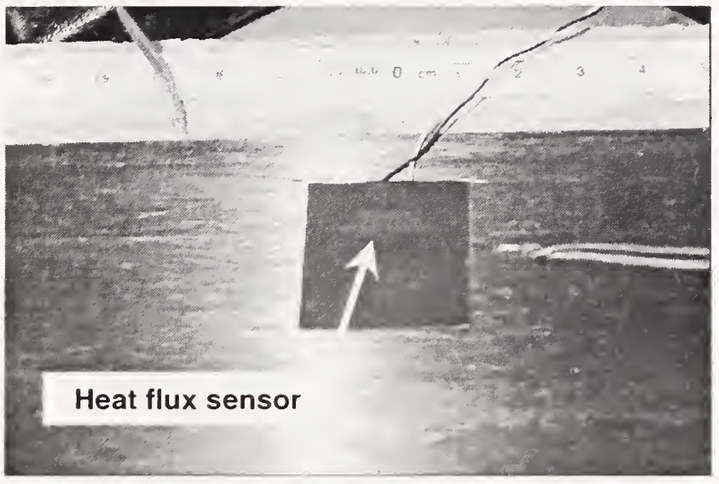

Fig. 5.5 Heat flux sensor bonded to FRP laminate

Additionally, a self-sticking heat flux transducer with an internal thermocouple was placed on the surface of the FRP. The thermocouples and the heat flux transducer were linked to a data acquisition system.

The heat flux sensor bonded to the surface of the specimen was an Episensor B04 from Vatell Corporation†. Episensor is an inexpensive and flexible transducer. The sensor is 24.5 mm × 24.5 mm in area and contains 1600 thermocouples per square centimeter. It operates to a maximum temperature of 150 °C. The sensor has a self-sticking adhesive backing. Figure 5.5 illustrates the heat flux sensor bonded to the surface of the CFRP laminate.

5.3.3b Specimens Fabricated with Wet-Lay Up CFRP Laminates

The second set of specimens involved wet lay-up CFRP composites bonded to concrete. The substrates were 610 mm × 250 mm × 45 mm precast concrete slabs. Two specimens were constructed by bonding three layers of MBrace™ carbon fiber sheets from Master Builders† to the concrete slab. Two materials were used to simulate internal flaws. One specimen contained flaws constructed with low k fabric (Nomex® III-Defender†, material used for firefighter clothing). The second specimen had flaws created using Parafilm®. Parafilm® is a flexible film that consists primarily of polyolefins and paraffin waxes. Figure 5.6 shows the materials used as flaws in this set of experiments.

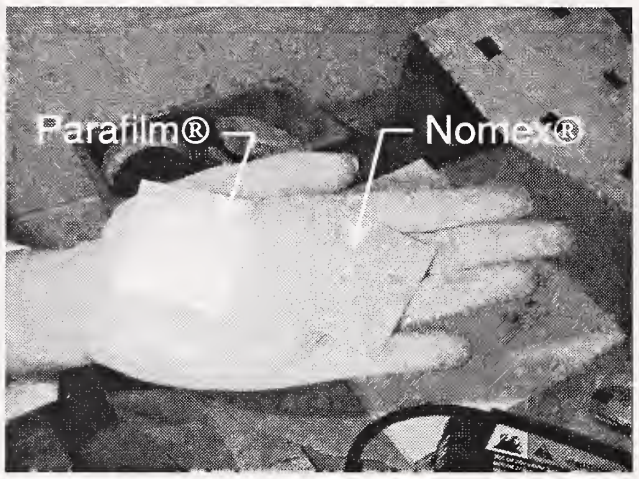

Fig. 5.6 Materials used as flaws in wet lay-up specimens

Both specimens were constructed following the same layout. Each specimen included all the flaws specified in the design of the experiments summarized in Tables 5.1 and 5.2. A plan view of the location of the flaws for both specimens is presented in Fig. 5.7. The numbers on the simulated flaws correspond the cases shown in Table 5.2.

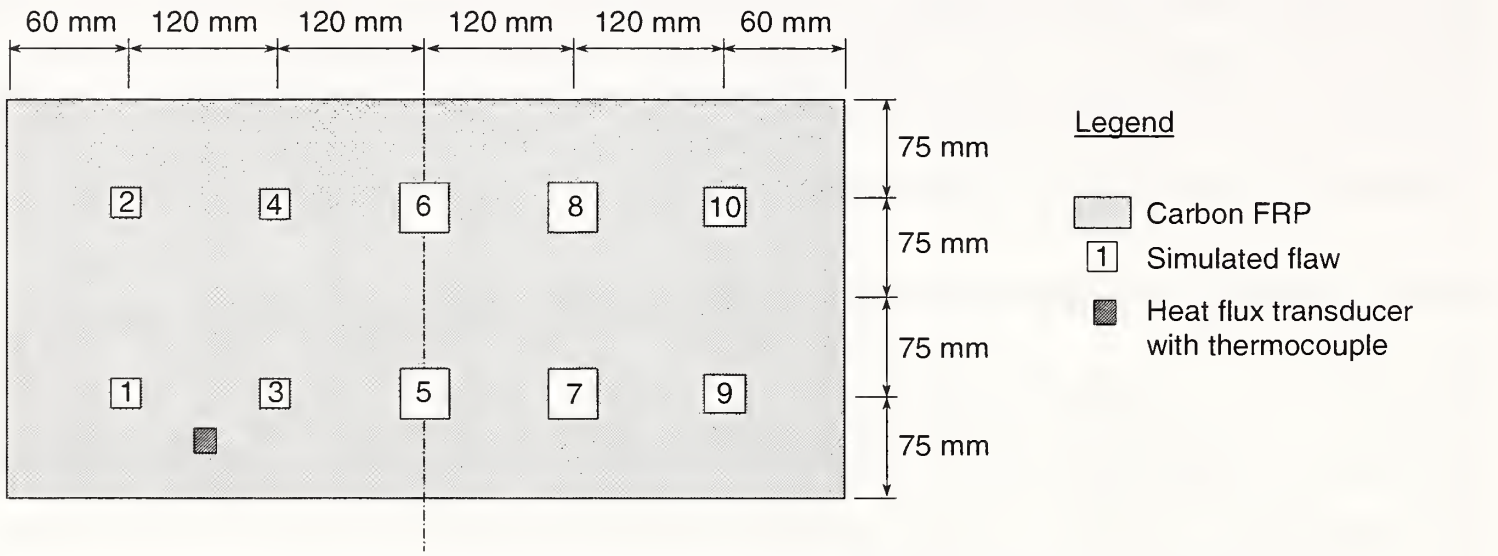

Fig. 5.7 Configuration of specimens constructed with wet lay-up FRP

The FRP reinforcement was bonded to the concrete slab using the procedures specified by the manufacturer of the composite system.

- First, the concrete substrate was prepared by cleaning the surface and applying a thin layer of MBrace putty using a trowel (Fig. 5.8).

Fig. 5.8 Application of MBrace putty

The putty is a thick, paste-like epoxy used to fill holes and surface defects. The putty was allowed to cure before proceeding to the following step.

- A coat of MBrace saturant was applied over the puttied surface. The saturant or resin is formulated to impregnate the fibers and hold the tow sheet in place until it cures. Application of saturant was avoided at the location were the first set of flaws (debonds) were going to be located (Fig. 5.9). The thickness of the resin layer was 0.4 mm approximately.

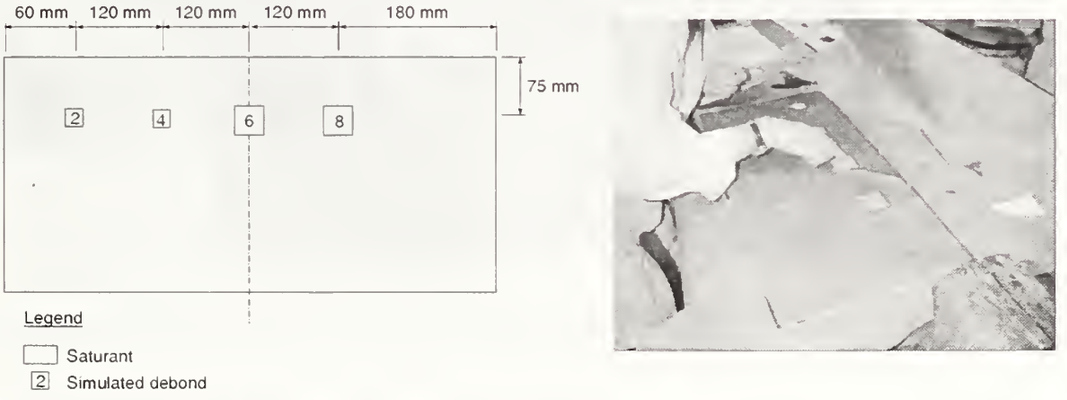

Fig. 5.9 Location (plan view) and placement of debonds

The first fiber sheet was cut to the proper size prior to placement. The sheet was placed on top of the resin. The direction of the fiber was along the longitudinal direction of the concrete slab. A trowel was pressed over the paper backing of the fiber sheet in order to remove air bubbles. The paper backing was removed to allow pressing of the fiber sheet into the resin with a ribbed roller. Rolling over the sheet in the direction of the fiber allowed resin impregnation of the fibers. A second coat of resin was applied and allowed

to cure partially before application of the following layer. Figure 5.10 illustrates some of the procedures described in this paragraph.

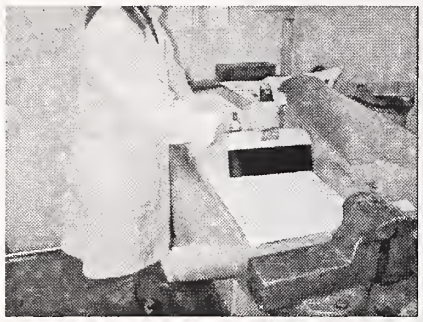

FRP sheet being pressed with trowel

FRP sheet being pressed with roller

Application of resin

Fig. 5.10 Application of first layer of FRP

- After 30 minutes, another coat of resin was applied. Again, care was taken to avoid placement of resin on the areas where the next set of flaws were to be located. Two bottom delaminations were located at this interface as illustrated in Fig. 5.11.

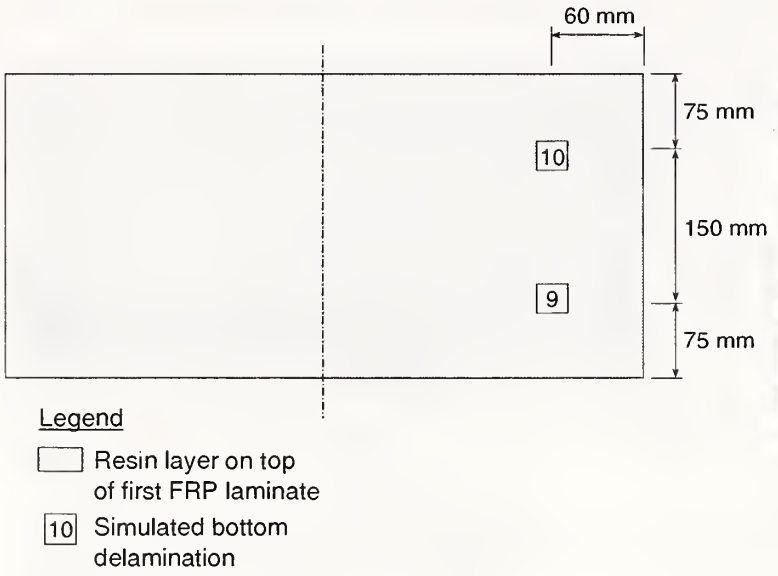

Fig. 5.11 Location (plan view) and placement of bottom delaminations

The second sheet of fiber was applied on top of the resin. In this case, the fibers were running at 90° relative to the fiber sheet located below. The fiber sheet was again pressed with a trowel and a ribbed roller in the direction of the fibers. A coat of resin was applied on top of the fiber sheet and was allowed to cure for 30 min.

- After 30 min, another coat of saturant was applied. Again, care was taken to avoid placement of resin on the areas where top delaminations were to be located. The location and actual placement of the top delaminations are presented in Fig. 5.12. A sheet of carbon fiber was placed on top of the resin (Fig. 5.13). In this case, the fiber ran in the

longitudinal direction of the specimen. The final coat of resin was applied. The specimen was allowed to cure overnight.

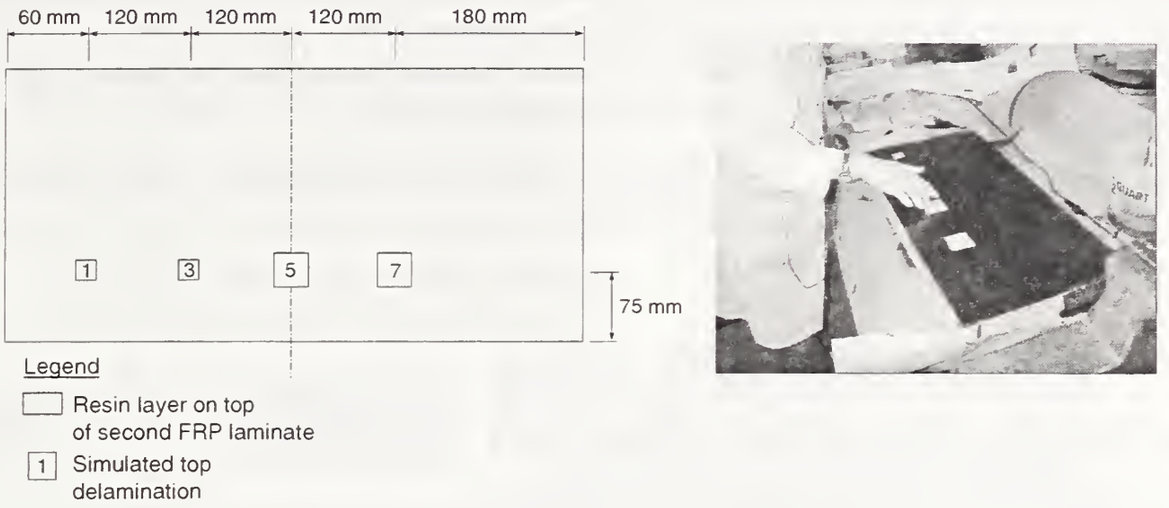

Fig. 5.12 Location (plan view) and placement of top delaminations

Fig. 5.13 Placement of last fiber sheet

Specimen Containing Flaws Created with Low *k* Fabric

One of the specimens was constructed using a low *k* fabric (Nomex®) for the simulated flaws. The material had a thickness of 0.6 mm. The layout of the specimen followed the outline specified in Table 5.2 and in Fig. 5.7. In accordance with the design of the experiment summarized in Table 5.2, the following levels were assigned to the parameters under study:

- Depth of flaw, $x_1 \rightarrow$ (−) indicates a top delamination with a depth of 0.5 mm approximately;
  (+) indicates a debond with a depth of 1.5 mm approximately; and,

(0) indicates a bottom delamination at a depth of 1.0 mm approximately.

- Thickness of flaw, $x_2 \rightarrow$ (−) indicates a thin flaw with a thickness of 0.6 mm approximately;
  (+) indicates a thick flaw with a thickness of 1.2 mm approximately; and,

  Using this material, no center point (0) was assigned to this parameter.
- Width of flaw, $x_3 \rightarrow$ (−) indicates a small with a width of 25 mm;
  (+) indicates a large flaw with a width of 40 mm; and,
  (0) indicates a flaw that is 32.5 mm wide.

Specimen Containing Flaws Created with Thin Film

The second specimen was constructed using a thin film (Parafilm®) for the simulated flaws. The material has a thickness of 0.13 mm. The layout of the specimen conformed to the outline specified in Table 5.2 and in Fig. 5.7. The following levels were assigned to the parameters under study:

- Depth of flaw, $x_1 \rightarrow$ (−) indicates a top delamination with a depth of 0.5 mm approximately;
  (+) indicates a debond with a depth of 1.5 mm approximately; and,
  (0) indicates a bottom delamination at a depth of 1.0 mm approximately.
- Thickness of flaw, $x_2 \rightarrow$ (−) indicates a thin flaw with a thickness of 0.13 mm approximately;
  (+) indicates a thick flaw with a thickness of 0.38 mm approximately; and,
  (0) indicates a flaw that is 0.25 mm thick.
- Width of flaw, $x_3 \rightarrow$ (−) indicates a small with a width of 25 mm;
  (+) indicates a large flaw with a width of 40 mm; and,
  (0) indicates a flaw that is 32.5 mm wide.

5.4 Experiment #1: Qualitative Test

The first part of the experimental study was qualitative in nature, and was intended to evaluate the potential detection of each simulated flaw embedded in the test object. For this purpose, the entire surface of the specimen was heated and the surface temperature was recorded using the infrared camera and associated software. The qualitative nature of the test did not require measurement of applied heat flux. Heating, in this case, was done by sweeping an infrared heat lamp along the length of the FRP at a distance of 50 mm from the surface and at a speed of

approximately 0.15 m/s. Observation of the thermogram shown in Fig. 5.14 reveals that all eight flaws were detectable. The thermogram was recorded approximately 5 s after the heat was applied. The most visible flaws were numbers 5, 6 and 8, which corresponded to low-conductivity fabric, air, and vitreous aluminosilicate fiber insulation, respectively (see Fig. 5.4). Flaw number 4 (masking tape) and flaw number 7 (Parafilm®) produced the smallest signals. The thermogram clearly indicates the location of the subsurface flaws and the sensors bonded to the surface of the specimen (i.e., heat flux sensor and thermocouple wires).

In practice, this quick technique could be used to easily detect subsurface flaws. Actual characterization of the flaw, however, requires additional analysis of surface temperatures as a function of time.

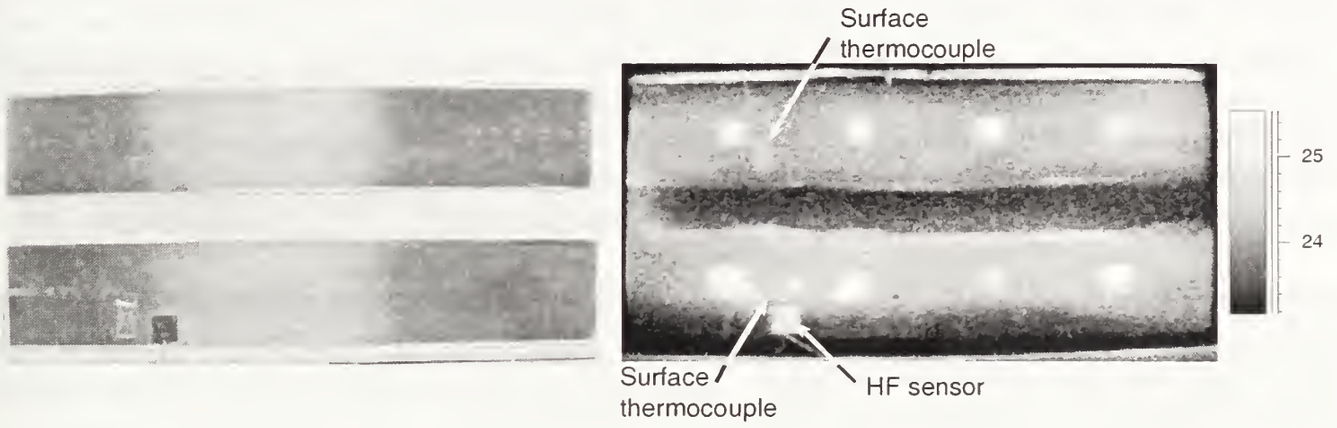

Fig. 5.14 Visual image and thermogram of test object fabricated with pultruded FRP during qualitative detection of internal flaws created artificially with different materials

5.5 Experiment #2: Comparison of IR Thermography and FEM Simulations

Experiment #2 concentrated on quantitative testing and comparison of the results with FEM simulations. For the case of comparison of test results with numerical simulations, the air-void flaw (flaw number 6) was selected for further study. The reason for the choice was twofold:

- The air void provided a significant thermal signal; and,
- The thermal material properties of air are known, thus reducing uncertainty in the numerical modeling.

During the qualitative test, it was observed that the apparent shape of air void was not square as intended. This meant that epoxy had flooded over the "wire dam" that was used to try to create a square-shaped void. Thus it was recognized that the thickness as well as the area of the flaw was different from intended. To estimate the actual thickness of the air void, seven measurements of the height of the FRP laminate were taken using a caliper. From the known laminate thickness, the mean value of the epoxy thickness was 0.9 mm and the standard deviation was 0.2 mm. The thickness of air void was thus assumed to be 0.9 mm.

5.5.1 Determination of Surface Emissivity for Pultruded FRP

Accurate determination of surface emissivity, and compensation for it, is key for correct measurement of surface temperatures by using an infrared camera. The Stefan-Boltzmann principle (Eq. 2.1) relates the surface temperature of an object to the radiation emitted by it. This relationship, however, is affected by the characteristics of the surface of the material. The emissivity measures the relative capability of a material to emit radiation. In particular, emissivity is the ratio of the radiance of a body at a given temperature to the radiance of a black body at the same temperature (ASTM E 1316).

Standard methodology for determining emissivity is described in ASTM E 1933. First, the contact thermometer method described in the standard was used in this experimental study. Surface temperatures of the FRP laminate were measured using a copper/constantan thermocouple (ANSI Type T, special limits, 0.010 mm in diameter). Each thermocouple was embedded in the FRP so that half of the perimeter of the wire was in contact with the composite and the other half of the wire was in contact with air. A small notch was cut into the laminate and epoxy adhesive was used to hold the thermocouple in place.

In accordance with ASTM E 1933, the test specimen was heated so the surface reached at least 10 °C above ambient temperature. To avoid rapid cooling of the surface, the specimen was heated in an oven to a temperature of 45 °C. As a result, surface cooling of the surface was slow enough to allow for estimation of the emissivity of the surface.

The data acquisition and analysis software calculates surface temperatures based on the following equation (Rinaldi, 2002):

$$W = \varepsilon \sigma T^4 + (1 - \varepsilon) \sigma T_{amb}^4 \tag{5.1}$$

where W is the radiation emitted by the specimen, ε is the emissivity of the material being tested, σ is the Stefan-Boltzmann constant, and T_{amb} is the ambient temperature. Equation 5.1 allows accurate measurement of the surface temperature by compensating for the atmospheric radiation emitted by the surroundings and recorded by the infrared detector. The "ambient temperature" should not be confused with the "atmospheric temperature." The atmospheric temperature is the actual temperature of the air in the surroundings of the test. Ambient temperature, however, corresponds to the temperature equivalent to the radiation emitted by the surroundings (objects and atmosphere) and reflected by the surface of the specimen under test (Rinaldi, 2002). To measure it, the infrared camera is placed next to the test object and facing away from the surface being tested using infrared thermography. The emissivity for the IR image is set to 1.0 and the average temperature of the image is measured. The recorded average temperature is the "ambient temperature" required to calibrate the thermograms for quantitative testing.

For the experimental configuration described in this section, the value of T_{amb} was 24 °C.

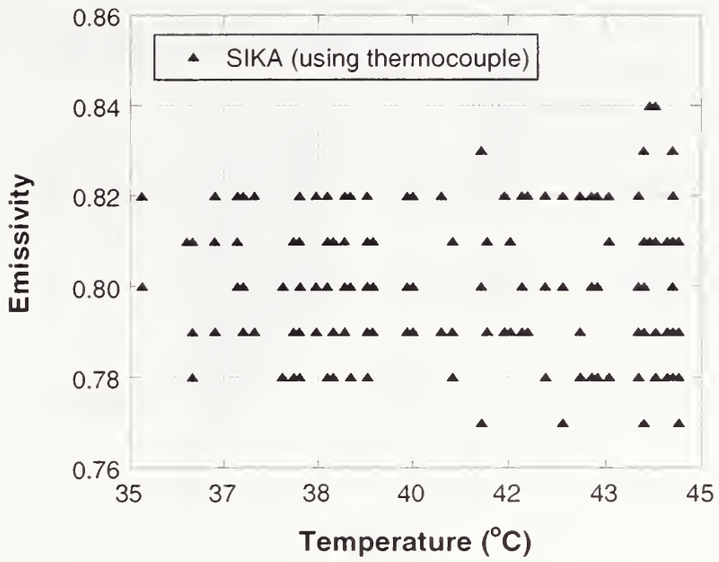

Fig. 5.15 Emissivity measurements for pultruded CFRP laminate using thermocouples

To measure the emissivity of the laminate, the test specimen was located 0.55 m from the infrared camera and aligned perpendicular to the line of view of the camera. The perpendicular placement of the test object with respect to the camera's line of view is an important consideration since emissivity varies with the angle of view. Surface temperatures next to the location of a thermocouple were taken with the infrared camera using spot meters, which are measurement tools used by the analysis software to determine the temperature at a point. Specifically, the spot meter averages the temperature of the pixels around the chosen point. Surface temperatures were measured at 3 points next to a thermocouple using 3 spot meters. The emissivity at each point was varied in order to match the temperature indicated by the camera with the temperature measured with the thermocouple. The measurements were repeated 55 times, for a total of 165 individual determinations that ranged from 0.77 to 0.84 (Fig. 5.15), the average emissivity of the FRP laminate was 0.80, with a standard deviation of 0.016. Thus the expanded uncertainty interval is 0.80 ± 0.03, for a coverage coefficient of k=2.

The *noncontact thermometer method* specified in ASTM E1933 was also used to determine the emissivity of the pultruded composite laminate. For this measurement, a small piece of electrical tape was applied to the surface of the specimen. Electrical tape has a typical value of emissivity equal to 0.95 (Mikron, 2002 and Rinaldi, 2002). Additionally, the ambient temperature of the room was calculated. The ambient temperature was 24 °C. The specimen was heated in an oven to a temperature of 43 °C. The specimen was removed from the oven to make the emissivity determinations. Since the electrical tape was bonded to the surface of the specimen, both the FRP and the tape had the same temperature. Two "area" measurement functions were used to measure the average temperature of the tape and the FRP adjacent to the tape. The temperature of the tape was measured using an emissivity equal to 0.95. The emissivity of the "area" used to measure the FRP temperature was adjusted to match the temperature of the tape. This computation is done automatically by the analysis software using an *Emissivity Calculation* tool.

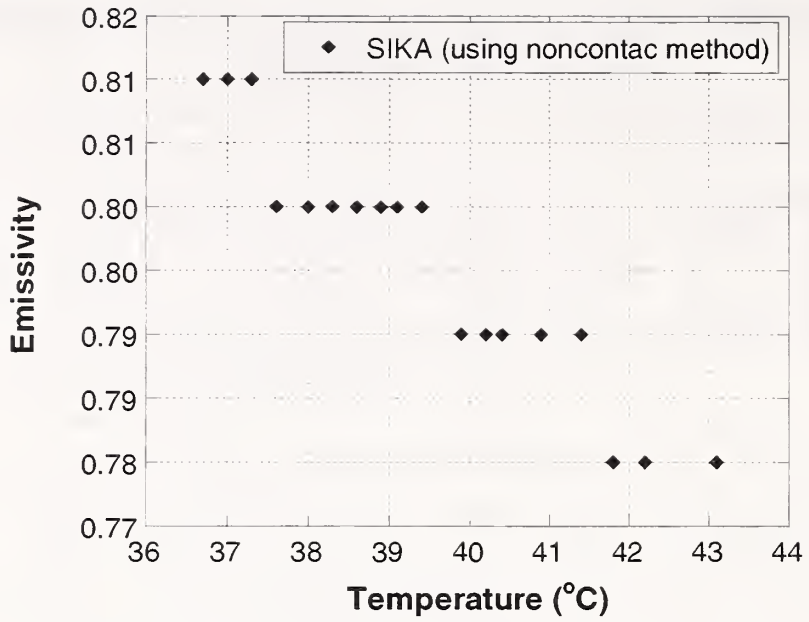

Fig. 5.16 Emissivity measurements for pultruded CFRP laminate using noncontact method

A total of 18 measurements were recorded. The values ranged from 0.78 to 0.81 (Fig. 5.16). The average emissivity of the FRP laminate was 0.80, with a standard deviation of 0.01. Thus the expanded uncertainty interval based on the noncontact thermometer method is 0.80 ± 0.02.

5.5.2 Determination of Heat Flux

Two sets of measurements were performed to determine the heat flux incident onto the surface of the test object. First, the heat flux distribution was measured along the surface of the specimen to determine the homogeneity of the heat flux produced by the heating module. The second set of tests involved measurement of the heat flux pulse as a function of time.

5.5.2a Homogeneity of Heat Flux

The quantitative thermography method investigated in this research involves application of uniform heat flux over the surface of the object being tested. The heat flux produced by the two-lamp heating module was measured to ensure this homogeneity.

The heating module was placed 0.33 m from the surface of the specimen and aligned so the lamps were parallel to the specimen. The heat flux sensor was placed on the surface of the specimen at the same height as the center of the heating lamps. The heat flux at the surface of the specimen was measured at intervals of 20 mm along a line parallel to the 2 lamps. The configuration of the test is presented in Fig. 5.17.

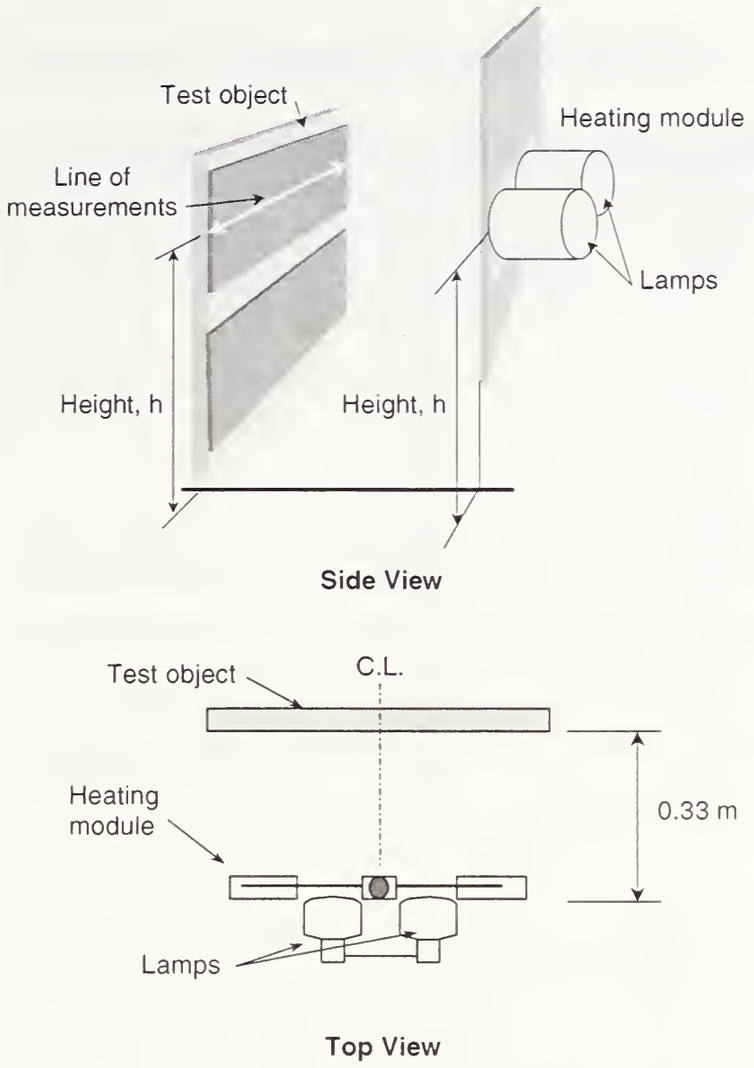

Fig. 5.17 Experimental setup for measurement of homogeneity of incident heat flux

Heat flux measurements were recorded at 16 different locations along the line of measurement thus covering a length of 0.3 m along the surface of the test object. For each measurement, the heat lamps were activated for 10 s. After 10 s, the lamps were turned off and the shutter fell in front of the lamps to shield any additional radiation. The measured heat flux at 10 s was used as the value of heat flux at the specific location along the line of measurement.

The values of the recorded heat flux are presented in Table 5.4. The relevant location to evaluate heat flux homogeneity was between the two lamps, since this is the region where a potential flaw would be located and measured. The results summarized in Table 5.4 and illustrated in Fig. 5.18 show some undulation of the heat flux between the two lamps suggesting a small heterogeneity of the incident heat flux. Also, the highest heat fluxes were not located at the center of the lamps, as expected. These aspects could be due to the irregularity of the electrical filaments inside the lamps. The average measured heat flux between the two lamps (measurements between 80 mm and 280 mm) was 1650 W/m^2 and the standard deviation was 80 W/m^2.

Table 5.4 Heat flux distribution along line of measurement

Distance, mm	Heat flux, q (W/m^2)	Comments
0	1210	
20	1160	
40	1440	
60	1470	
80	1530	C.L. of lamp
100	1760	
120	1730	
140	1660	
160	1620	
180	1600	C.L. of module
200	1570	
220	1770	
240	1640	
260	1590	
280	1650	C.L. of lamp
300	1580	

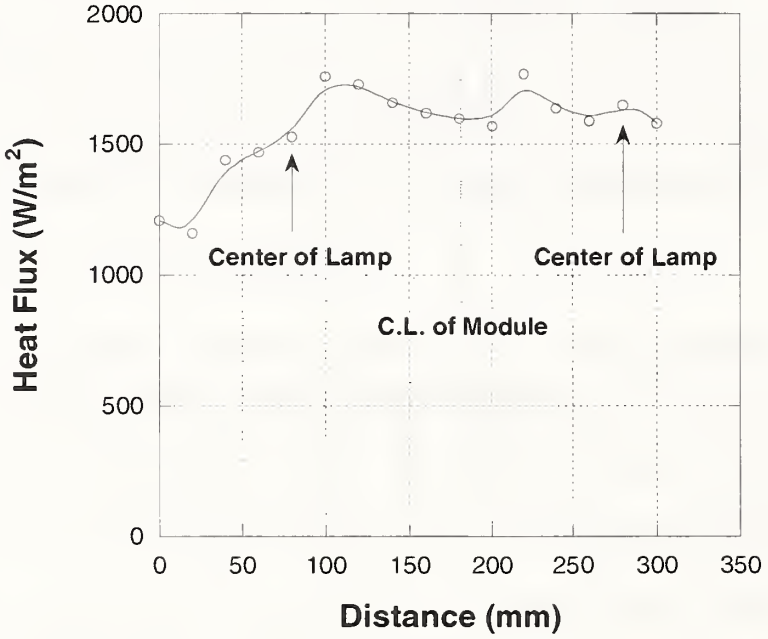

Fig. 5.18 Results of heat flux distribution measurements

The results show that the heat flux in the area located between the two lamps of the heating module is sufficiently uniform.

5.5.2b Heat Flux Pulse as a Function of Time

As previously stated, the surface temperature of the FRP laminate and thermal signal due to subsurface flaws depend on the input thermal pulse. The input thermal pulse has two parameters that may be varied: the duration of the pulse and the magnitude of the heat flux. The pulse duration is easily controlled. For this particular experiment the pulse duration was adjusted to 10 s using a pulse generator, an external trigger, and the shutter system.

In this study, 250 W heating lamps were used as the heat source, and the magnitude of the thermal pulse depends on the distance from the lamps to the test object.

The incident heat flux was measured using a heat flux sensor placed on the surface of the FRP laminate. The sensor also included a thermocouple. Heat flux and temperature measurements from the sensor were recorded using a data acquisition system. The measurements were made with the heating lamps located 0.33 m from the surface of the FRP laminate. In order to record the heat flux that the specimen would be subjected to during thermography testing, the heat flux sensor was placed at the same position with respect to the heating lamps that the flawed specimen would be during thermography testing. For convenience, this position will be referred to as location A.

Table 5.5 Heat flux measurements

Time (s)	Incident heat flux, $q_{incident}$ (W/m^2)		
	Test 1	Test 2	Test 3
0	0	0	0
1	1360	1400	1420
2	1480	1500	1570
3	1600	1610	1610
4	1640	1640	1650
5	1680	1680	1670
6	1690	1690	1690
7	1710	1710	1710
8	1720	1720	1730
9	1740	1740	1730
10	1750	1740	1740
11	350	340	310
12	250	240	220
13	160	160	150
14	120	140	130

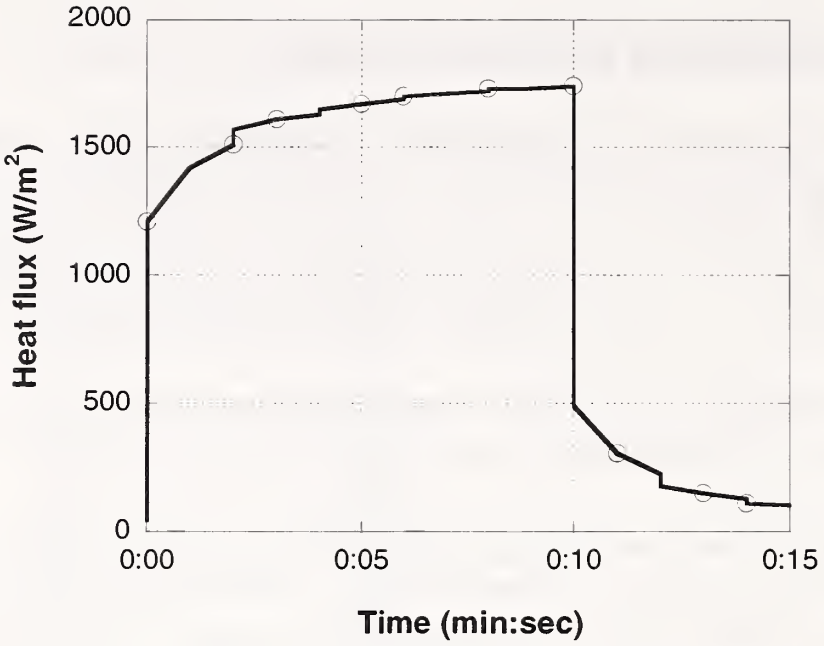

Fig. 5.19 Measured heat flux pulse (replicate test #3)

Three heat flux measurements were obtained. As shown in Table 5.5, the heat flux measurements were repeatable. Table 5.5 summarizes the input heat flux data and Fig. 5.19 shows the shape of one of the heat pulses. The maximum magnitude of the heat flux was 1750 W/m^2 measured at 10 s.

An important consideration with respect to numerical simulations is that the heat flux sensor measures the incident heat flux, $q_{incident}$. This heat flux, however, needs to be adjusted to determine the amount absorbed by the FRP. The fraction of the incident heat flux absorbed by the surface of a material is referred to as absorptivity. Kirchhoff's law relates the absorptivity of a surface to its emissivity as follows (Özişik, 1985):

$$\varepsilon_\lambda(T) = \alpha_\lambda(T) \tag{5.2}$$

where $\varepsilon_\lambda(T)$ is the spectral emissivity for the emission of radiation at temperature T and $\alpha_\lambda(T)$ is the spectral absorptivity for radiation coming from a blackbody at temperature T. With a gray-body assumption (ε, α independent of λ), the absorbed radiation can be expressed as

$$q_{absorbed} = \varepsilon\, q_{incident} \tag{5.3}$$

Since the emissivity of the FRP laminate was measured to be 0.80, the heat flux absorbed by the FRP was 80 % of the incident heat flux measured by the sensor.

5.5.3 IR Thermography Test Procedure and Analysis

For quantitative thermographic testing, the heating lamps were located 0.33 m from the surface of the specimen. The specimen was placed so the air void was positioned at the same location relative to the heating lamps as was the heat flux sensor during heat flux measurement (position A as mentioned in the previous section). The duration of the thermal pulse was set to 10 s. Thermogram data were recorded at 15 Hz for a period of 60 s from the start of heating.

Two procedures were investigated for determining the signal due to the air void. The first procedure involved two tests. In the first test, the air void was at location A. In the second test, an unflawed region of the specimen was placed at location A. Temperature data were analyzed at the same location using the same spot meter. The signal as a function of time was obtained by subtracting the temperature data of the second measurement ($T_{background}$) from the temperature data from the first measurement (T_{defect}). This setup may seem unnecessary, but it ensured that both $T_{background}$ and T_{defect} were measured for the same heat flux input. This detail was important for comparison with analytical results. Additionally, it provided for comparison with the second to be described.

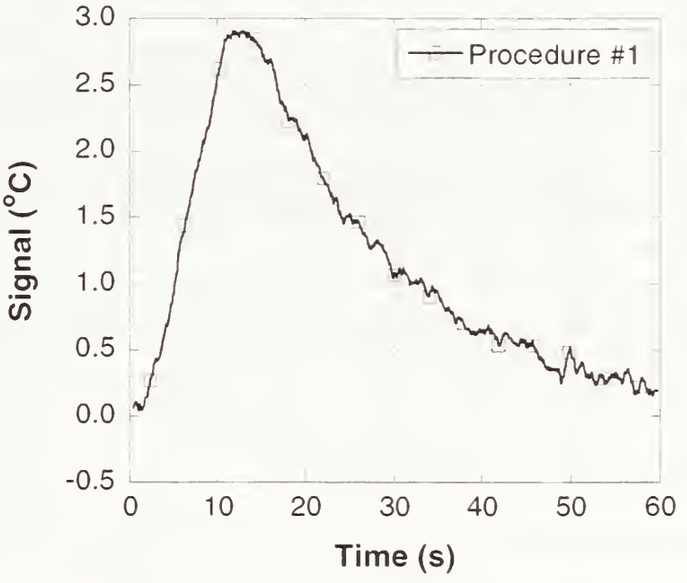

Fig. 5.20 Smoothed thermal response due to air void for testing procedure #1

A 10-point averaging filter that computes a moving average of the temperature data was used to smooth the signal. The smoothed signal from the first procedure is presented in Fig. 5.20. The maximum signal was 2.9 °C, and it occurred 12 s after the start of the test. A maximum surface temperature of 28.7 °C was measured at the location of the flaw.

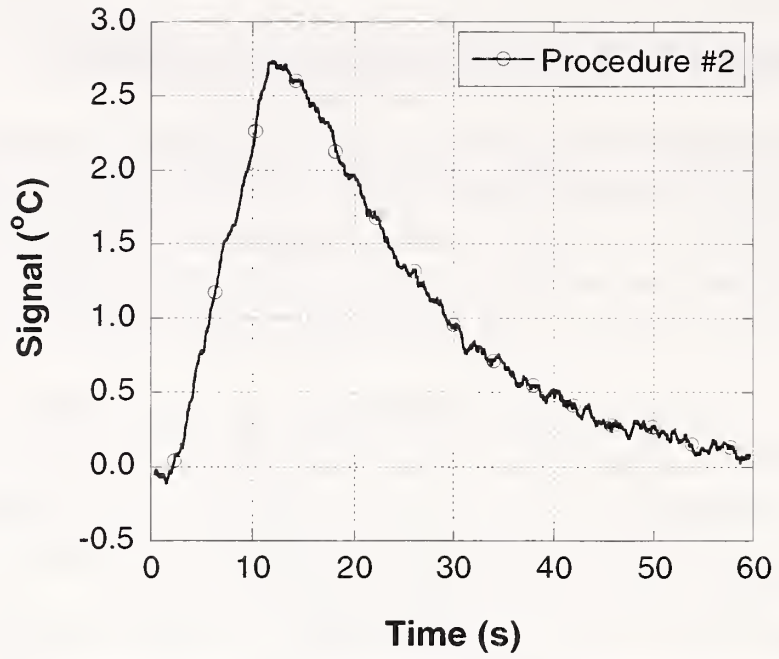

Fig. 5.21 Smoothed thermal response due to air void for testing procedure #2

The second procedure involved one test, which would be similar to actual field-testing. The specimen was positioned so that the air void was at location A. The recorded data were analyzed by using two spot meters: one was placed above the center of the flaw to measure T_{defect}, the other was placed 15 mm from the apparent boundary of the air void (over an unflawed region) to measure $T_{background}$. The smoothed signal as a function of time is presented in Fig. 5.21. In this case, the maximum signal was 2.7 °C, and it also occurred 12 s after the start of heating. The maximum surface temperature was 28.4 °C.

The two tests gave essentially the same results. This provides some assurance that the signals shown in Figs. 5.20 and 5.21 are valid.

5.5.4 Verification of FEM Simulations

5.5.4a Simulation Models

The results discussed in 5.5.3 were compared with the results of numerical simulations to verify the suitability of the analytical models. The numerical simulations were performed using ANSYS 5.6. To reduce computation time, a two-dimensional model was used. The simulation object consisted of a 127 mm long by 20 mm thick concrete slab covered with one laminate of carbon FRP (CFRP). The CFRP laminate was 1.33 mm thick. A 0.9 mm thick by 25.4 mm long air void was introduced at the center of the specimen between the concrete substrate and the composite laminate. The bonding layer was modeled as a 0.9 mm thick layer of epoxy. The complete model is shown on the left side of Fig. 5.22. Since the air void was located at the centerline of the model, the simulation was simplified by using plane symmetry. Thus only one-half of the object was analyzed, as shown on the right side of Fig. 5.22.

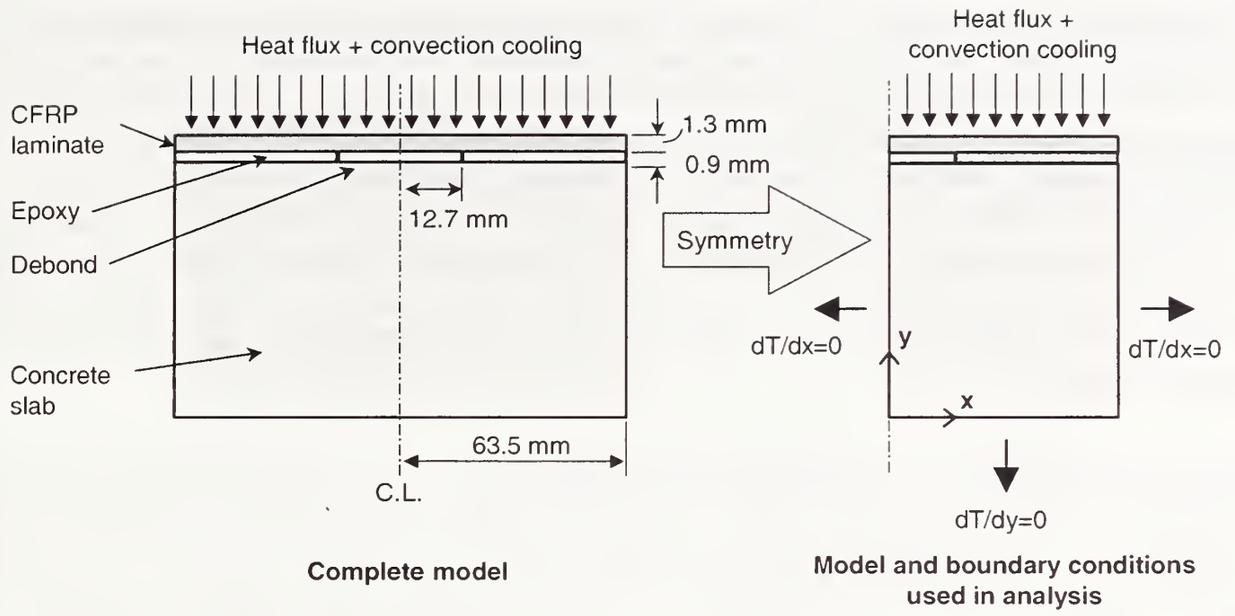

Fig. 5.22 Test object used in finite-element simulations for comparison with measurement

Table 5.6 Material properties used in numerical simulations

Material	Density, ρ (kg/m^3)	Thermal conductivity, k (W/m·K)			Specific heat, c (J/kg·K)
		k_x	k_y	k_z	
Concrete	2400	1.5	1.5	1.5	800
FRP	1760	8.9	2.9	2.9	800
Air	1.2	0.024	0.024	0.024	700
Epoxy	1960	0.19	0.19	0.19	1700

The material properties used in the model were those of concrete for the substrate, air for the defect, CFRP for the bonded composite, and epoxy for the bonding agent. The CFRP laminate had the fibers running in the longitudinal direction (x-direction). The material properties of air and concrete were gathered from the literature, and those of the FRP and epoxy were estimated from data provided by manufacturers. The thermal properties of carbon FRP varies significantly among products. The differences are due to the volumetric fraction of fibers used (which is usually greater than 68 %), and due to the material properties of the constituents (the fibers and the bonding agent). In addition, thermal properties of carbon fiber may vary widely. For example, a commercially available high-strength fiber is reported to have a thermal conductivity of 9.38 W/m·K while its high-modulus counterpart is reported to have a thermal conductivity of 68.7 W/m·K. Since the material properties of the FRP composite used in this study were unknown, their values were estimated from available information. The material properties used in the finite-element simulations are listed in Table 5.6.

The model was meshed using eight-noded, 2-D, quadrilateral elements. For the simulation of convective cooling, 2-D plane surface elements with two nodes were used. An extra node was

added and linked to the surface elements to provide the input for ambient temperature. Each node in the model had one degree of freedom, temperature. Mapped meshing was used to allow direct control of the element size. The global element size was set to 0.1 mm. Mesh refinement was applied to the thin composite layers and at the FRP/concrete interface. The thickness of the composite laminate was subdivided into 4 elements while the thickness of the flaw was subdivided into 3 elements. The rest of the concrete substrate was meshed using a graded mesh with a finer mesh at the top and a coarser mesh at the bottom of the specimen. The average element size in the y-direction for the concrete was 0.00263 mm with a "spacing ratio" of 20. The spacing ratio is the ratio of the dimension of the largest element to the dimension of the smallest element.

The analysis was defined as a transient heat transfer problem. The applied heat pulse was based on the measured pulse shown in Fig. 5.19 as modified by Eq. (5.3). Uniform heating of the top surface was assumed. Convection cooling was applied to the top surface for the second and third simulations, and the convection coefficients were 10 W/(m^2·K) and 25 W/(m^2·K), respectively. Adiabatic conditions ($dT/dx = 0$ and $dT/dy = 0$) were assumed for the additional surfaces. This assumption was realistic since the thermal pulse did not reach the bottom of the concrete during the duration of testing. In addition, the width of the flaw was small enough so that it did not affect heat flow at the vertical boundary of the model. The initial temperature for all the simulations was 22.8 °C, which represented the initial temperature of the specimen measured during testing. Perfect contact between the materials was assumed. Automatic time stepping with a minimum of 0.008 s and a maximum of 0.1 s was set for the analyses.

5.5.4b Results

Comparison of experimental measurements with analytical results was done by comparing three thermal response parameters: maximum surface temperature (T_{max}), maximum thermal signal (ΔT_{max}) and time for maximum signal (t_s).

For numerical simulations, the maximum surface temperature was affected slightly by convection cooling, and varied from 29.1 °C for no-convection to 28.7 °C for a convection coefficient of 25 W/m^2·K. The maximum surface temperatures measured in the two experiments were 28.7 °C and 28.4 °C.

The maximum thermal signal for the simulations ranged from 2.9 °C to 2.5 °C, depending on the convection coefficients while the experimental values were 2.9 °C and 2.7 °C.

Table 5.7 Summary of thermal response parameters for experiments and simulations

	IR measurements		FEM results		
	Test #1	**Test #2**	**h = 0 W/(m^2·K)**	**h = 10 W/(m^2·K)**	**h = 25 W/(m^2·K)**
T_{max} (°C)	28.7	28.4	29.1	28.9	28.7
ΔT_{max} (°C)	2.9	2.7	2.9	2.7	2.5
t_s (s)	12.0	12.1	12.5	12.0	11.7

The time for maximum signal was 12 s for both experimental tests. For simulations, the time for maximum signal was 12.5 s, 12 s and 11.7 s for simulations with convection coefficients of 0 W/(m^2·K), 10 W/(m^2·K) and 25 W/(m^2·K), respectively. Table 5.7 summarizes the experimental and analytical response parameters. Overall, the thermal responses from the simulations compared favorably with measurements.

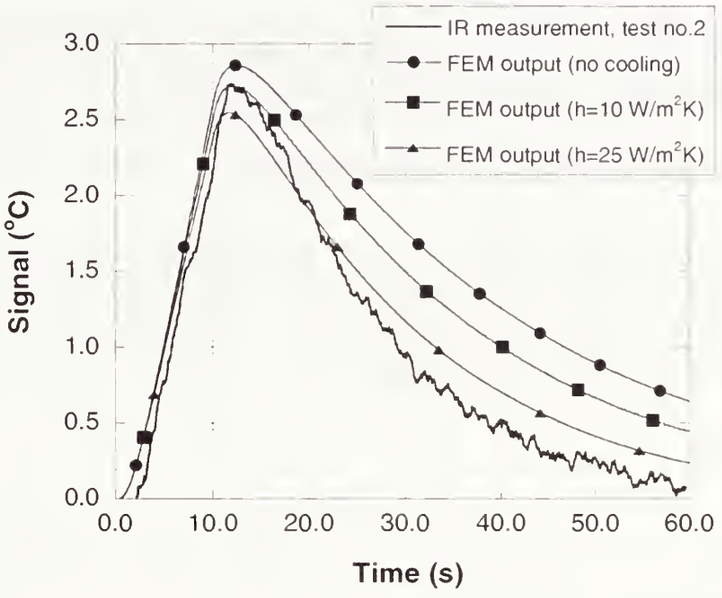

Fig. 5.23 Comparison of thermal signals for IR test #2 and FEM simulations

Comparison of the thermal signals as a function of time, however, showed a systematic difference between the measured and computed results. As shown in Fig. 5.23, the experimental thermal signal decayed at a faster rate than the analytical results. This mismatch may be the result of assumptions of the model. The model was assumed to be 2-dimensional and uniformly heated, which means no heat flow in the z-direction (normal to the cross-section shown in Fig. 5.22). In reality, this would not be the case and the rate of temperature drop would be expected to be higher.

For the purpose of quantitative thermographic testing, however, the primary thermal response parameters are T_{max}, ΔT_{max}, and t_s. The analytical and experimental results were in good agreement, and provided reassurance that the analytical model is valid.

5.5.5 Conclusions of the Comparison of IR Thermography and FEM Simulation

Experiment #2 involved experimental measurements and numerical simulations of infrared thermography testing of pultruded FRP laminates applied to concrete.

Infrared thermography testing was performed on an air void contained at the interface between a pultruded FRP laminate and the concrete substrate. In addition to thermography measurements, the experimental study involved the determination of surface emissivity using the contact and noncontact methods described in ASTM E 1933, and heat flux measurements. This was necessary to allow comparison of measured thermal response parameters with those computed using numerical models.

Numerical simulations were performed using 2-D models of the controlled-flaw specimen. Three cases were simulated to represent different levels of convective cooling of the surface. The measured thermal responses associated with the air void were compared with the analytical results. It was found that the amount of convective cooling had minor effects on the maximum signal and the time to maximum signal. The good agreement between the experimental and analytical results provided assurance that numerical simulations could be used to study the effects of different test parameters (as were reported in Chapter 4).

5.6 Experiment #3: Estimation of Flaw Width

During the qualitative test (see Section 5.3.1), it was observed that the air-filled flaw (#6) was not square as intended. The bonding epoxy apparently flooded over the "wire dam" that was used to exclude epoxy and create the intended flaw. Thus the air-void was chosen for verification of the procedure for width determination.

5.6.1 Test Procedure

The specimen was tested using the experimental configuration described in Fig. 5.1. The specimen was located at 0.33 m from the camera lens. The specimen was placed so that the air-filled flaw was positioned at the centerline between the two heating lamps. The duration of the thermal pulse was set to 10 s, and thermogram data were recorded at 15 Hz for a period of 60 s.

The surface temperatures above the flaw (T_{defect}) and above the bonded laminate near the flaw ($T_{background}$) were obtained as a function of time. The maximum signal was 2.7 °C, which occurred at 12 s after the beginning of the test. The measured maximum surface temperature was 28.4 °C.

5.6.2 Data Analysis

To estimate the width of the air-filled flaw, the thermogram corresponding to the time of maximum signal was analyzed. The surface temperatures of the region surrounding the flaw were retrieved using an *area*-measuring tool. The retrieved *area* had dimensions of 35 pixels × 28 pixels. Since the analysis software provides surface temperatures at each pixel, a conversion between pixel size and actual physical size was required. The conversion was done

using the known dimensions of a heat flux sensor and a piece of tape located on the surface of the specimen as reference. The heat flux sensor and the tape had actual widths of 25.4 mm and 18.7 mm, respectively, and in thermogram image the corresponding dimensions were 23 pixels and 17 pixels. Thus, each pixel corresponded to a 1.1 mm square, and the analyzed region surrounding the flaw was 38.5 mm × 30.8 mm. This area box (AR01) is shown in Fig. 5.24.

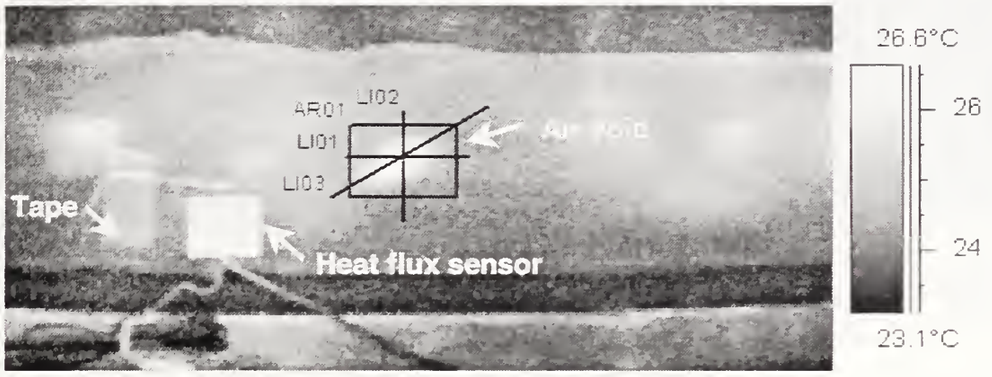

Fig. 5.24 Thermogram of air void at time of maximum signal

The plan dimensions of the flaw were estimated by analyzing the surface temperatures along three lines, as shown in Fig. 5.24. Unlike the FEM output, the surface temperature data along each line did not vary smoothly, and a 5-point moving average was computed to smooth the data. This smoothing was also applied to the second derivative of the temperature profile.

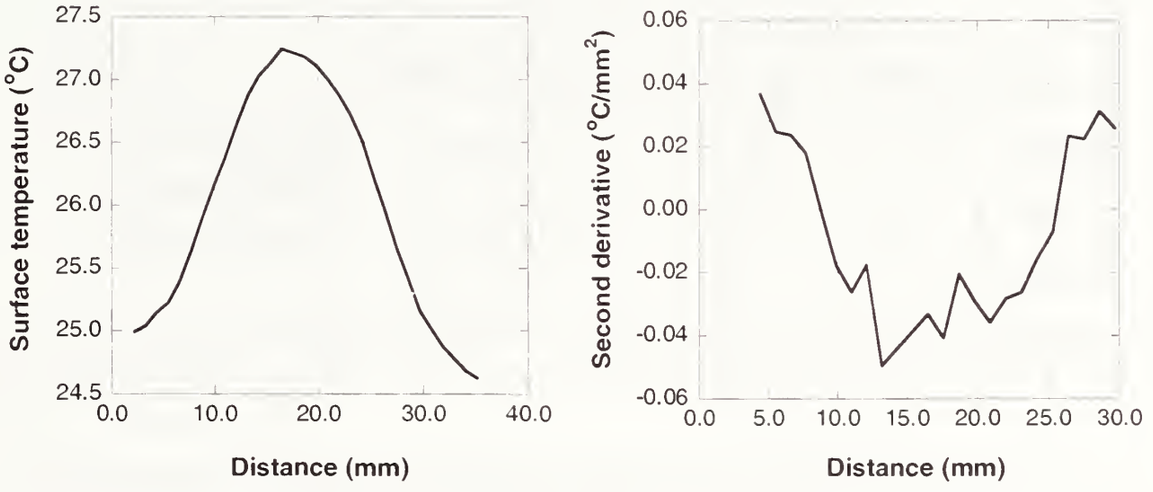

Fig. 5.25 Smoothed surface temperature profile and second derivative with respect to distance along horizontal line (LI01)

The smoothed surface temperature and the smoothed second derivative along the horizontal line (LI01) are presented in Fig. 5.25. The roots of the second derivative ($d^2T/dx^2=0$) were located at 8.8 mm and 25.6 mm from the origin. Thus the estimated width of the flaw along the horizontal line is 16.8 mm.

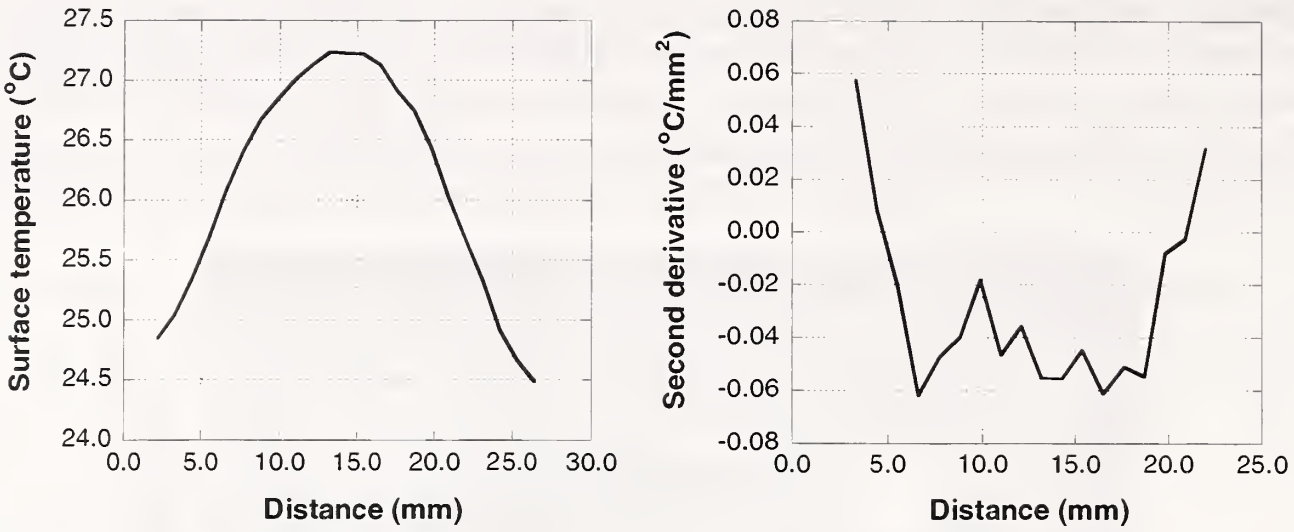

Fig. 5.26 Smoothed surface temperature profile and second derivative with respect to distance along vertical line (LI02)

A similar procedure was used for the vertical line (LI02). In this case, the surface temperature profile and the second derivative curve were smoothed using the moving average of 5 points and 3 points, respectively. The resulting smoothed plots are shown in Fig. 5.26. The roots of the second derivative were located at 4.7 mm and 21.0 mm from the origin of the line. Thus the estimated width of the flaw along the vertical line is 16.3 mm.

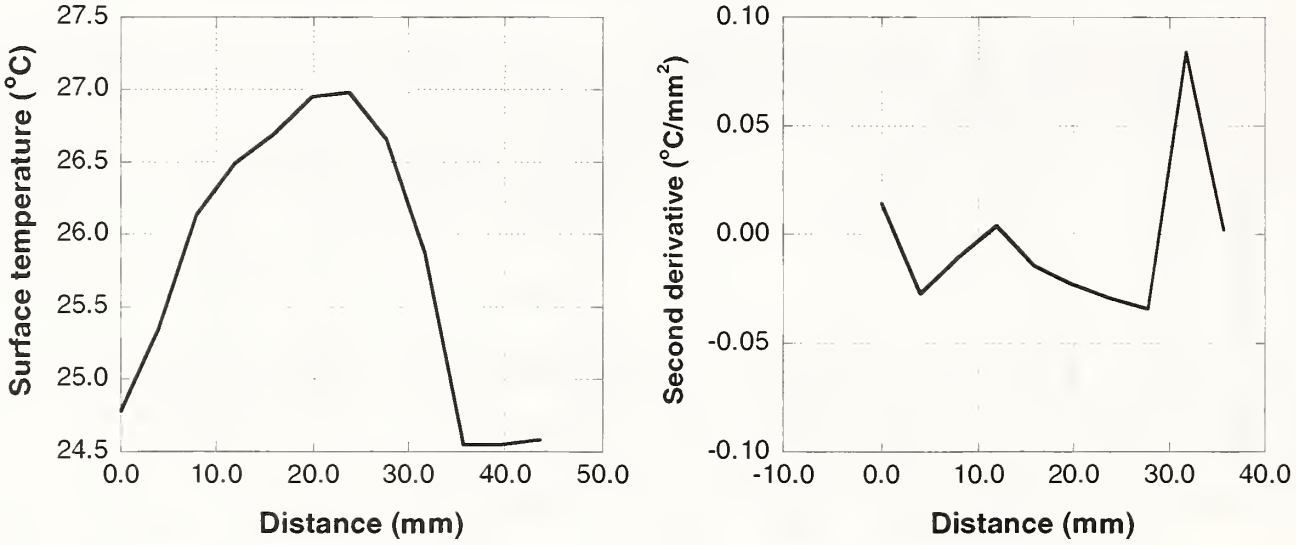

Fig. 5.27 Surface temperature profile and second derivative with respect to distance along diagonal line (LI03)

Finally, the diagonal dimension was estimated. For this case, temperatures along the diagonal of the surface temperature matrix were used. The surface temperature was extracted every 3.97 mm along the diagonal. No smoothing of the temperature profiles and second derivative was required in this case. The temperature profile and its second derivative are presented in Fig. 5.27. The second derivative provided four roots. Based on observation of the surface temperature profile, the outer roots were used for estimation of the width. The outer roots of the second derivative were 1.4 mm and 29 mm, and the estimated diagonal width of the air void is 27.6 mm.

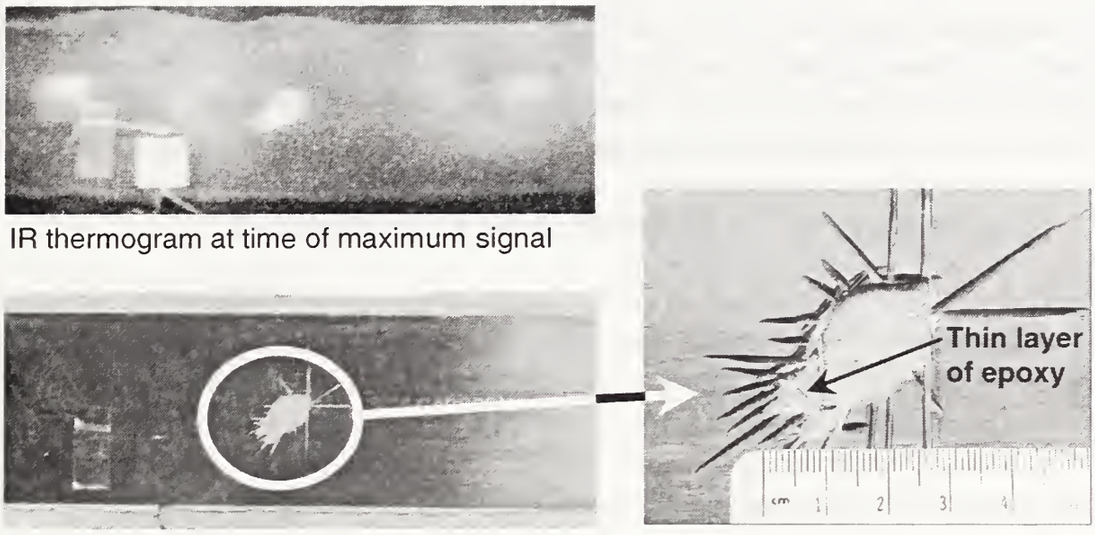

Fig. 5.28 Thermogram and visual images of air void

To verify the estimated dimensions, the portion of FRP laminate above the air flaw was removed carefully by using a miniature high-speed cut-off wheel. This procedure revealed the true shape of the air void. A visual image of the exposed air void is presented in Fig. 5.28 and compared with its image during thermographic testing.

Table 5.8 Estimated and actual widths of air void

	Estimated width (mm)	**Actual width (mm)**
Horizontal line	17	17
Vertical line	16	17
Diagonal line	28	31

The dimensions of the exposed air void were measured as close along the same lines used to analyze the thermogram. Table 5.8 summarizes the estimated and actual widths of the air void. The agreement is good.

The maximum estimation error was in the diagonal dimension, where the width was underestimated by 3 mm. Observation of the flawed region revealed that in the lower left corner of the flaw there was an unbonded area with a thin layer of epoxy on the concrete (see Fig. 5.28). Thus, the thickness of the air void was reduced in this region. The estimated diagonal width matched the distance between the upper right corner of the flaw and the edge of the thin layer of epoxy. The thinner air gap at the lower-left corner produced a lower signal than the rest of the flaw where there was no epoxy between the FRP and the concrete. It is possible that the error in width estimation could have been reduced by placing the camera closer to the specimen so that more pixels covered the flaw area

The results show that curve smoothing using a moving average filter is an effective means for dealing with noisy signals. The number of points used in the smoothing may depend on the

surface temperature profile. The goal is to easily identify the roots of the second derivative curve while minimizing the distortion of the original data. Thus, the number of points used to smooth the curves should be kept as small as possible. Additional studies on estimating flaw size should lead to guidelines for proper smoothing of temperature profile data.

5.6.3 Conclusions of the Estimation of Flaw Width

The experiment involved estimation of the width of an air void located at the interface between the concrete and the pultruded FRP laminate. The width of the flaw was assessed by estimating the location of the second derivative of the surface temperature profile at the time of maximum signal. A smoothing procedure using a moving average algorithm proved to be an effective means for dealing with noisy signals and second derivatives. The agreement between the estimated and actual flaw dimensions was good. This confirmed the procedure suggested by the results of the numerical simulations.

5.7 Experiment #4: Screening Experiment

The next set of tests involved a screening experiment. The aim of this experiment was to verify the results from the analytical multi-factor parametric study described in section 4.9.

The details of the experiment design and specimen fabrication were presented in sections 5.2 and 5.3.3b, respectively.

5.7.1 Determination of Surface Emissivity of Wet Lay-Up FRP

The surface emissivity of the wet lay-up carbon FRP was determined using the procedures described in ASTM E 1993. The two controlled-flaw specimens were used to measure the emissivity of the wet lay-up composite. One specimen was built with the normal amount of topcoat resin. This specimen was tested using the contact method, which involved the use of surface thermocouples, and the noncontact method using a reference tape. The other specimen was constructed with a smaller amount of topcoat resin than that recommended by the manufacturer and was used to determine the emissivity by the noncontact method only.

The procedures for measuring the surface emissivity were the same as those explained in section 5.5.1.

The ambient temperature of the room was measured as discussed in Section 5.5.1, and its value was 24 °C. The specimen under testing was placed at a distance of 0.55 m from the infrared camera and perpendicular to the line of view of the camera.

The first method used to estimate the surface emissivity was the contact method using thermocouples. Surface temperatures of the FRP laminate were measured using a copper/constantan thermocouple (ANSI Type T, special limits, 0.010 mm in diameter). The thermocouple was bonded to the surface of the test object so half of the perimeter of the wire was embedded in the FRP material and half of the perimeter was in contact with the air. A 20 mm long notch was cut into the composite and epoxy adhesive was used to hold the thermocouple in place.

The test specimen was heated in an oven set at 60 °C. This procedure ensured that the test object was thoroughly heated to avoid rapid transient cooling. Once out of the oven, cooling of the specimen occurred slowly thus allowing emissivity measurement. Measurements were recorded for temperatures ranging from 32 °C to 10 °C above room temperature.

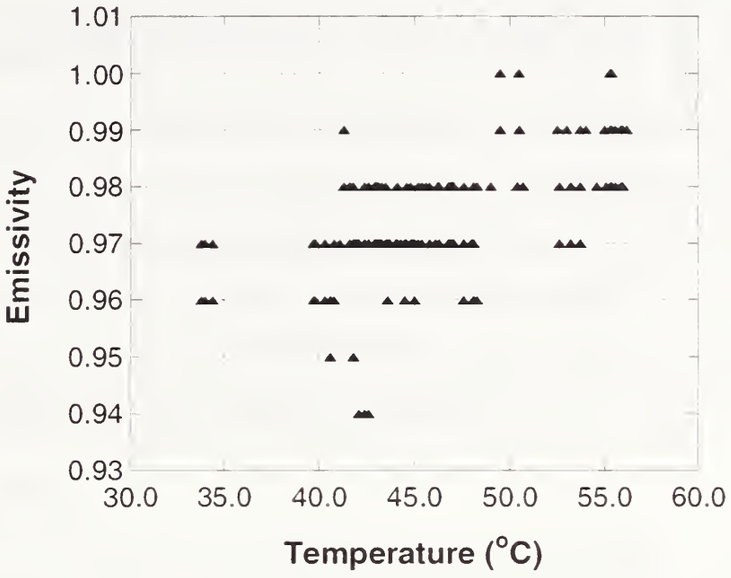

Fig. 5.29 Emissivity measurements using thermocouples for wet lay-up carbon FRP

Surface temperatures were measured with the infrared camera at 3 points next to a thermocouple using 3 spot meters. The emissivity associated with each spot meter was varied in order to match the temperature measured with the thermocouple and the temperature indicated by the camera. The measurements were repeated 231 times. The measured emissivity ranged from 0.94 to 1.0 (Fig. 5.29), the average emissivity of the FRP laminate was 0.98, with a standard deviation of 0.01. Thus the expanded uncertainty interval is 0.98 ± 0.02 for a coverage factor $k = 2$. It is important to note that a large number of measurements had to be disregarded because they had values of emissivity above 1.0, which are not theoretically possible. This indicates a possible limitation of the contact method procedure for materials with high emissivity. This issue should be investigated further in the future.

The second method used to determine the emissivity of the wet lay-up composite was the noncontact thermometer method specified in ASTM E 1933. For this measurement, a small piece of electrical tape with an emissivity of 0.95 (Mikron, 2002 and Rinaldi, 2002) was applied to the surface of the specimen. The specimen was heated in an oven to a temperature of 89 °C. The specimen was removed from the oven to take the emissivity measurements. An "area" measurement function was used to measure the average temperature of the tape. The temperature of the FRP adjacent to the tape was measured using 3 spot meters. The temperature of the tape ($\varepsilon = 0.95$) was measured with the infrared camera. The emissivity of the "spot" measuring the FRP temperature was adjusted to match the temperature of the tape. The computation of the emissivity at the location of the spot meters was done automatically by the analysis software using an *Emissivity Calculation* tool. Emissivity measurements were recorded for surface temperatures ranging from 60 °C to 37 °C above room temperature.

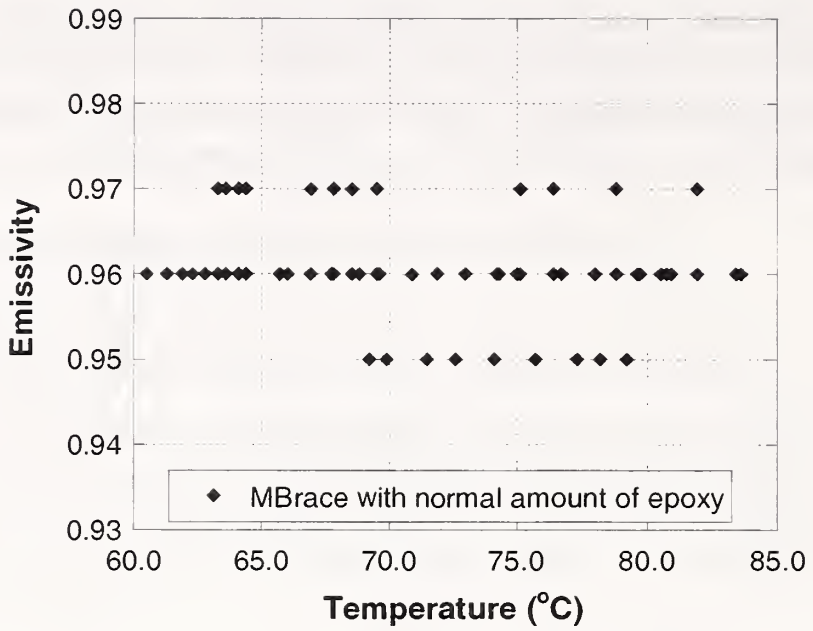

Fig. 5.30 Emissivity measurements using noncontact method for wet lay-up carbon FRP with normal amount of resin

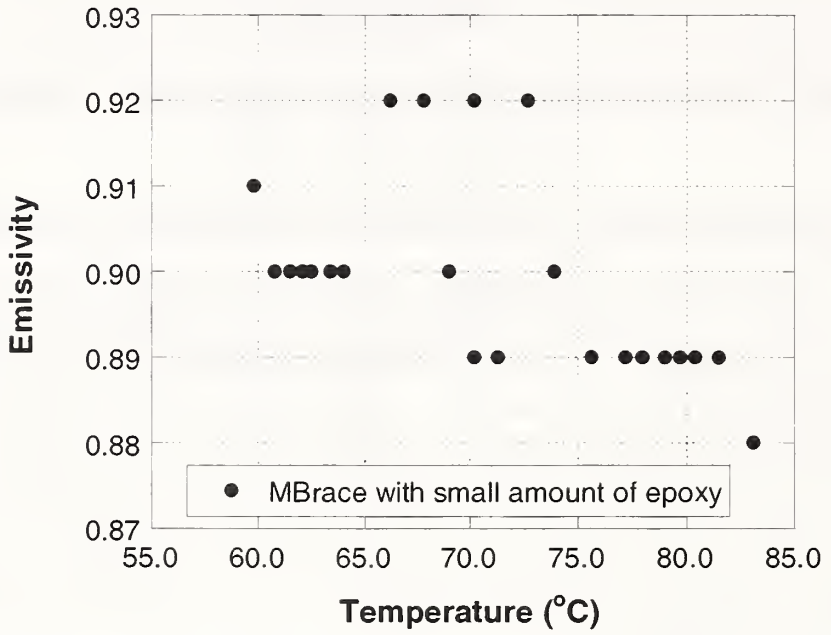

Fig. 5.31 Emissivity measurements using noncontact method for wet lay-up carbon FRP with small amount of resin

A total of 81 measurements were recorded. The values of emissivity ranged from 0.95 to 0.97 (Fig. 5.30). The average emissivity of the wet lay-up FRP with normal amount of epoxy was 0.96, with a standard deviation of 0.005. Thus the expanded uncertainty interval is 0.96 ± 0.01.

The same noncontact procedure was used to measure the emissivity of the wet lay-up FRP composite fabricated with a small amount of topcoat resin. As previously stated, the specimen was heated in an oven to a temperature of 89 °C. The specimen was removed from the oven to take the emissivity measurements. Emissivity measurements were recorded for surface temperatures ranging from 60 °C to 37 °C above room temperature. Room temperature was 23 °C and ambient temperature was 24 °C (see 5.5.1).

A total of 23 emissivity measurements were taken. The recorded values, which are shown in Fig. 5.31, ranged from 0.88 to 0.92. The average emissivity of the wet lay-up FRP with small amount of topcoat resin was 0.90, with a standard deviation of 0.01. Thus the expanded uncertainty interval is 0.90 ± 0.02.

The results indicate a significant difference between the emissivity of wet lay-up carbon FRP containing different amounts of topcoat resin.

It is important to remember that emissivity values depend on temperature, angle of observation, and spectral wavelength at which they are measured. Temperature has to vary by several hundreds of degrees in order to have a significant effect in the emissivity of a material. The effect of angle of observation was not evaluated in this project. For this project, the angles of observation during thermography testing were smaller than 10° from the perpendicular to the surface of the test object. The emissivity values reported in this chapter apply to measurements taken in the 8 μm to 12 μm spectral wavelength, at angles near the 90° with respect to the surface of the FRP, and for temperatures near room temperature.

5.7.2 Test Procedure

First, a qualitative test was performed to determine the potential detection of all the flaws in each of the two specimens fabricated for this experiment. The qualitative test followed the procedure explained in 5.3.1. The qualitative test showed that all the low-*k* fabric (Nomex®) flaws were detectable. On the other hand, most of the thin film (Parafilm®) flaws were not detectable. Thus subsequent quantitative measurements were performed only on the specimen containing flaws made from Nomex®.

Before starting the test, the ambient temperature was measured following the procedure described in Sec. 5.5.1. The infrared camera was placed against the surface of the test object and facing away from its surface. The emissivity of the IR image was set to 1.0 and the average temperature of the image was measured. This average temperature corresponded to the ambient temperature and had a value of 24 °C.

Each subsurface flaw was tested separately. The flaws were tested according to the random sequence indicated in Table 5.2.

The experimental configuration was as illustrated in Fig. 5.1, except that the specimen was located at 0.37 m from the heating lamps and the IR camera. The specimen was placed so that the flaw under study was positioned at the centerline between the two heating lamps. The duration of the thermal pulse was set to 10 s, and the thermogram data were recorded at 15 Hz for a period of 60 s following the start of heating.

The surface temperatures above the flaw (T_{defect}) and above the bonded laminate near the flaw ($T_{background}$) were obtained as a function of time for each test. These temperature were used to compute the thermal signal and contrast as a function of time.

5.7.3 Data Analysis

5.7.3a Analysis of Individual Tests

As in previous tests, the thermal responses as a function of time were noisy and had to be filtered to aid in interpretation. Smoothing of the data was accomplished using a moving average filter. An example of the measured signal and the smoothed signal (using a 25-point moving average) is presented in Fig. 5.32.

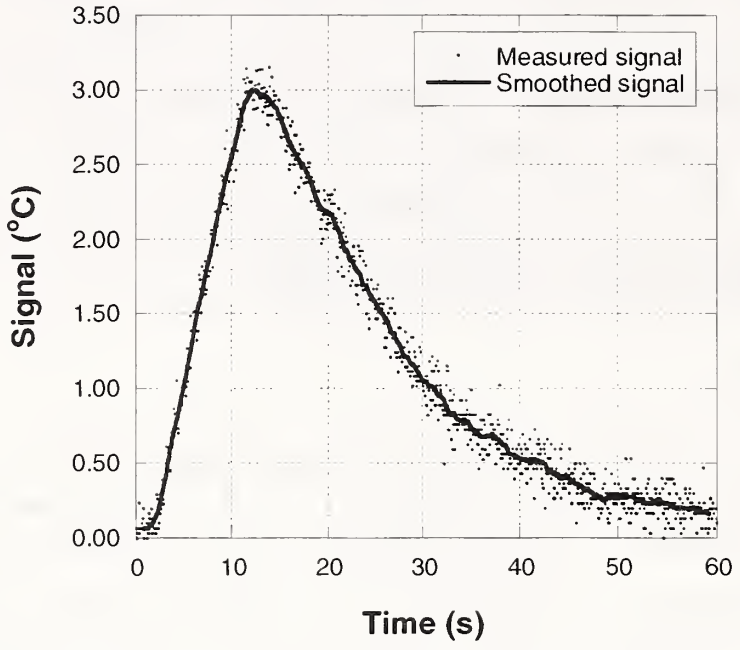

Fig. 5.32 Example of signal smoothing (run #3 corresponding to flaw #10)

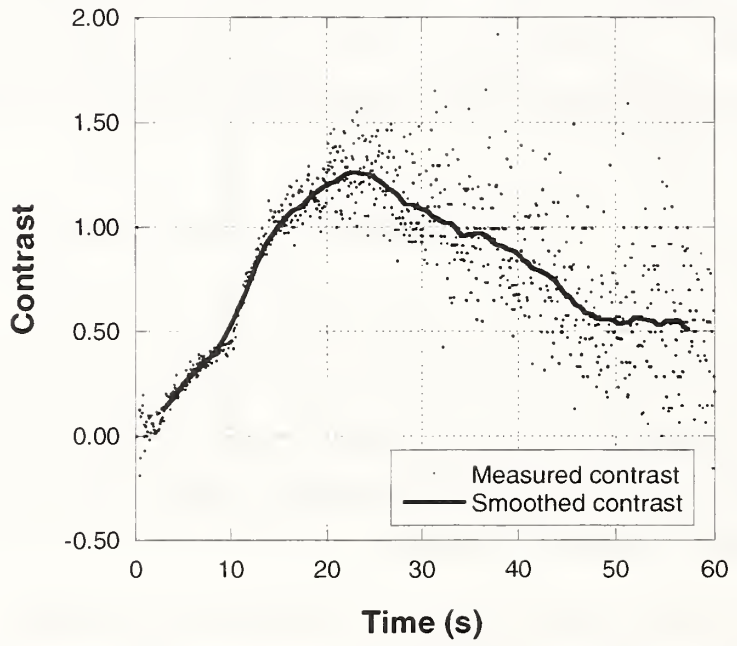

Fig. 5.33 Example of contrast smoothing (run #3 corresponding to flaw #10)

The contrast was computed using Eq. 4.8. Figure 5.33 is an example of measured contrast. It is seen that the contrast tended to have a small amount of noise at the beginning of the test until the maximum signal was obtained at about 12 s. The contrast, however, becomes increasingly noisier after the end of the heat pulse as illustrated in the example in Fig. 5.33.

In an attempt to obtain meaningful values of maximum contrast and time to maximum contrast, a moving-average smoothing procedure was used. First, the temperature in the background $T_{background}$ and the signal ΔT were smoothed. Typically, 9 data points were used for the moving average of these two thermal responses. The contrast was computed using these two smoothed values and the initial temperature of the background at $t = 0$ s. After smoothing, the contrast still showed high noise, thus preventing the determination of the maximum contrast and the time to maximum contrast. The contrast as a function of time was smoothed a second time using 75-points for the calculation of the moving average. The smoothed contrast curve is presented in Fig. 5.33 in addition to the measured (unsmoothed) contrast data. The need for such data manipulation casts doubt on the usefulness of contrast as a practical response parameter.

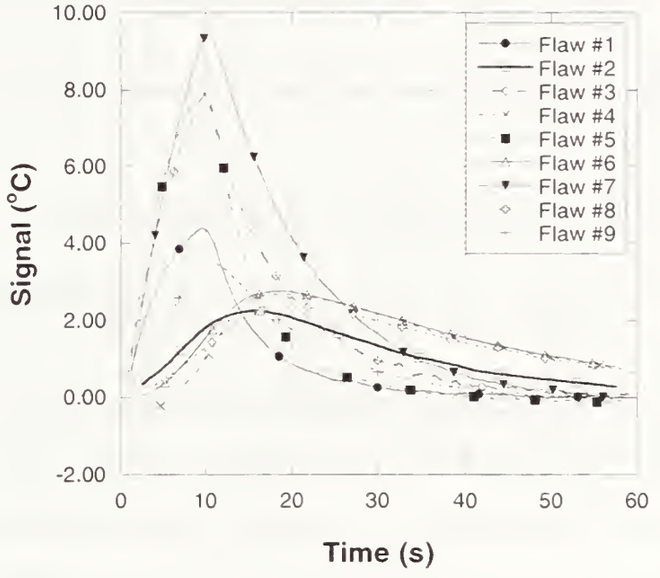

Fig. 5.34 Smoothed signals for flaws #1 through #9

The same smoothing procedures were applied to the data from each test. The results of the smoothed signals for flaws #1 though #9 are presented in Fig. 5.34.

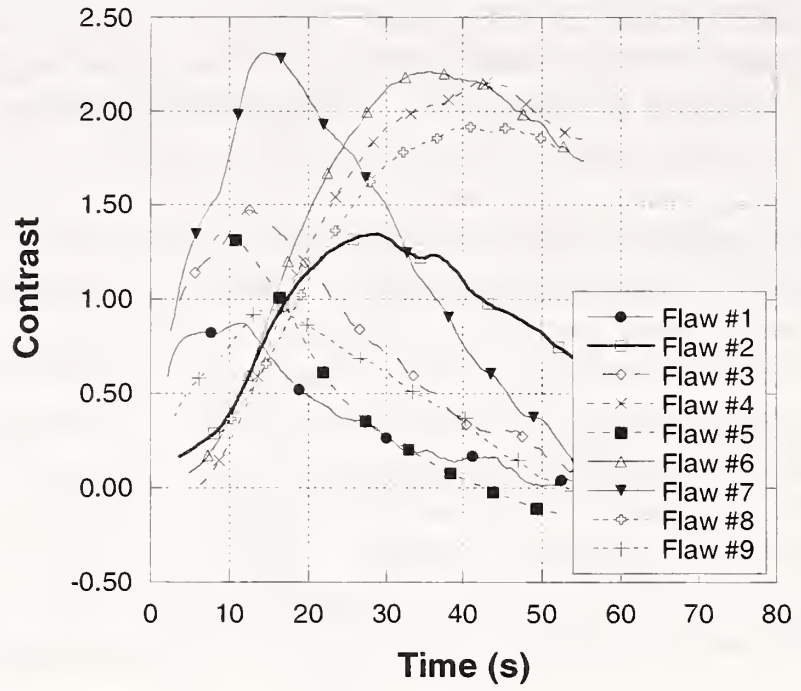

Fig. 5.35 Smoothed contrast for flaws #1 through #9

The results of the smoothed contrast curves for flaws #1 through #9 are presented in Fig. 5.35.

5.7.3b Analysis of Full Factorial Screening Experiment

The results of the screening experiment were evaluated for five different thermal responses: t_s, ΔT_{max}, C_{max}, t_c, and T_{max}. A summary of the resulting thermal responses is presented in Table 5.9.

The results of the analytical multifactor parametric study described in Chapter 4 indicated that the only thermal response that has the potential to characterize a flaw is the time to maximum signal t_s. The maximum signal ΔT_{max} and the maximum temperature T_{max} provided data that were too scattered to be used in an effective model to characterize the subsurface flaw. These results were confirmed by the experimental data. Of the five responses summarized in Table 5.9, only the results for the time to maximum signal and the time to maximum contrast are summarized in the following sections.

Table 5.9 Results from experimental screening study

		Factor level			Results				
Flaw #	**Run Sequence**	x_1	x_2	x_3	t_s (s)	ΔT_{max} (°C)	T_{max} (°C)	C_{max}	t_c (s)
1	6	−	−	−	10.2	4.6	33.5	0.87	11.5
2	4	+	−	−	15.5	2.3	30.6	1.35	28.9
3	2	−	+	−	10.0	8.1	37.9	1.47	12.4
4	1	+	+	−	17.9	2.9	32.0	2.16	42.7
5	9	−	−	+	10.0	8.1	38.2	1.51	10.6
6	10	+	−	+	19.0	2.8	31.8	2.21	34.4
7	5	−	+	+	10.4	9.4	40.3	2.31	14.4
8	7	+	+	+	19.9	2.4	31.8	1.92	40.9
9	8	0	+	0	10.8	3.5	33.1	0.94	15.2
10	3	0	−	0	12.3	3.0	32.6	1.26	23.0

5.7.3c Analysis of Results for t_s

The effect due to each factor on the thermal response was computed by subtracting the group averages, as indicated in Eq. 4.113. The results of the calculation of the effect of each factor and their interactions on the time to maximum signal are presented in Table 5.10.

Table 5.10 Estimate of the effects of the factors and their interactions on the time to maximum signal

Factor or Interaction	$\bar{y}_+$ (s)	$\bar{y}_-$ (s)	$\hat{\beta}_i$ (s)
x_1	18.1	10.2	7.9
x_2	14.6	13.7	0.9
x_3	14.8	13.4	1.4
$x_1 \cdot x_2$	14.5	13.7	0.8
$x_1 \cdot x_3$	14.8	13.5	1.3
$x_2 \cdot x_3$	14.0	14.2	-0.2
$x_1 \cdot x_2 \cdot x_3$	13.8	14.4	-0.5

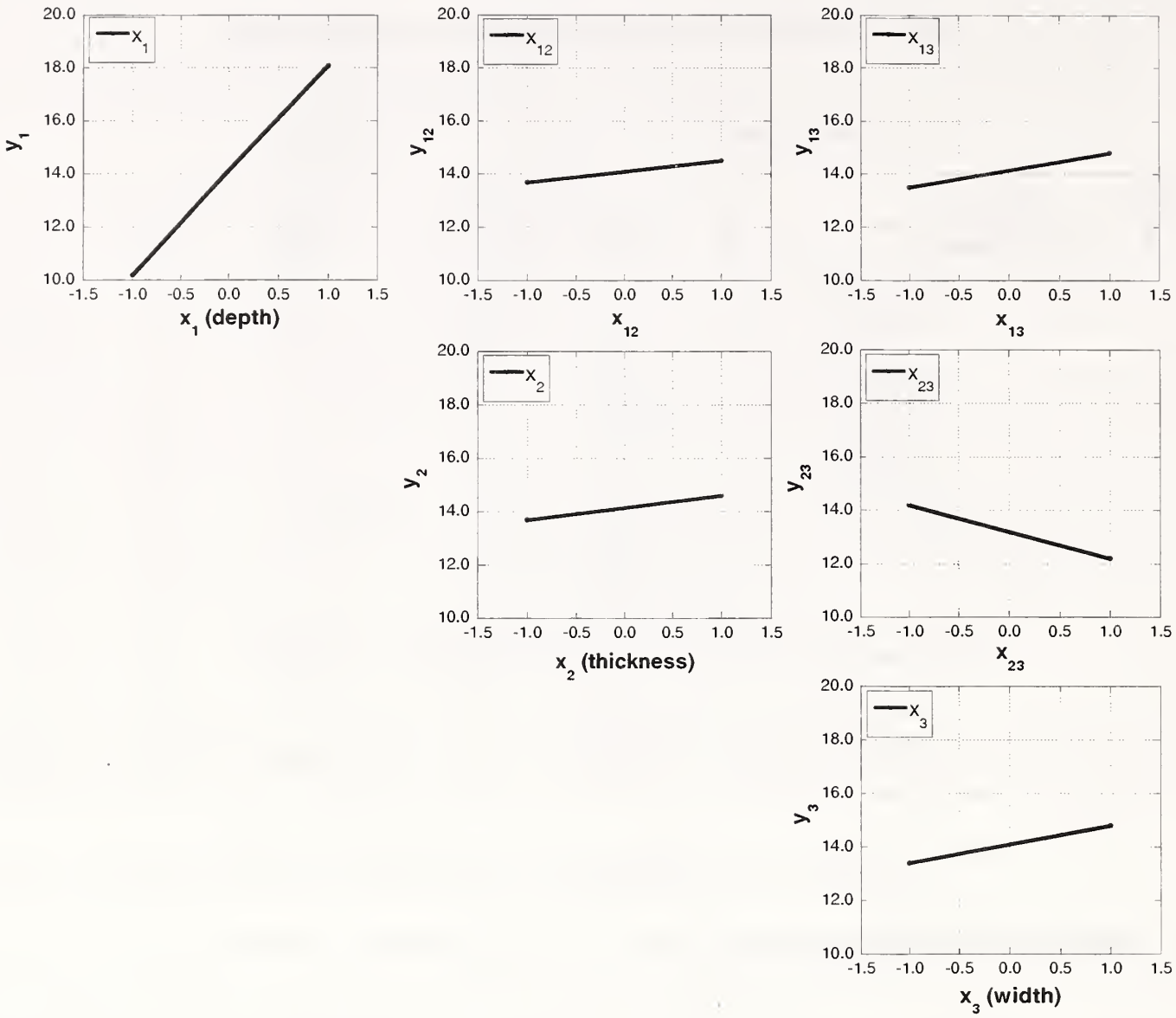

Fig. 5.36 Plots of means of factors and interactions for the time to maximum signal

Figure 5.36 illustrates the results summarized in Table 5.10. As explained in section 4.9, each plot presents the average of the thermal response at levels "+" and "−" for each factor or interaction. The slope of each line is an indicator of the effect of the factor on the time for maximum signal. The plots with greater slopes correspond to the factor or interaction with greater effect on the response. The results indicate that the depth of the flaw (factor x_1) had the greatest effect on the time to maximum signal the most.

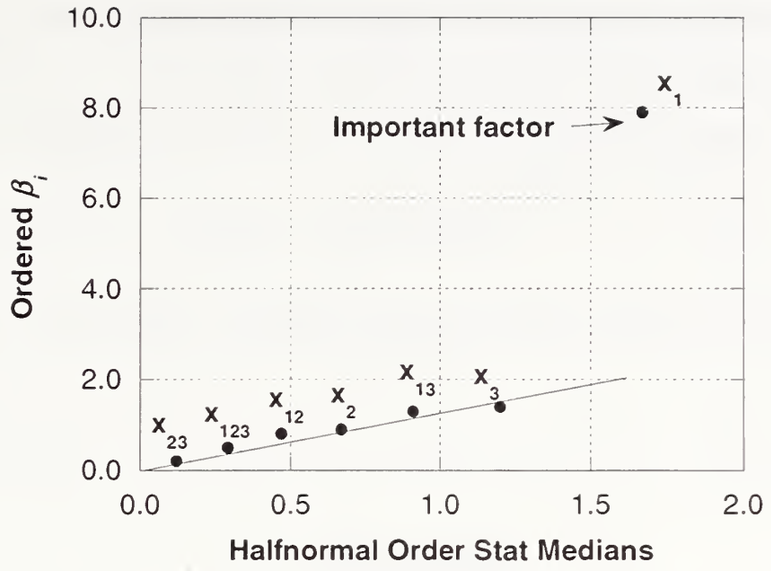

Fig. 5.37 Halfnormal probability plot for the time to maximum signal

The halfnormal probability plot of the effects listed in Table 5.11 was used to determine which factors or interactions have significant effects on t_s. Refer to Section 4.9.4 for discussion of the halfnormal probability plot. Figure 5.37 presents the halfnormal probability plot and it confirms that only the depth of the flaw has a statistically significant effect on the time to maximum signal. Therefore, the results of this screening test are in agreement with the results presented for the simulations in Sec. 4.9.4.

The analytical study indicated that time to maximum signal had potential for use to estimate flaw depth. The experimental data were used to verify this. The time to maximum signal was plotted as a function of the depth from the results of the full factorial experiment and including the two center data points.

Figure 5.38 displays the time to maximum signal at each of the coded depths, -1, 0, and +1 (see data in Table 5.9). The graph illustrates that the time to maximum signal for flaws located near the surface is similar regardless of the width and the thickness of the flaw. All the flaws at a coded depth of −1 generated times to maximum signal between 10.0 s and 10.4 s. The time to maximum signal results spread as the depth of the subsurface flaw increases. Thus at large depths, the remaining factors, flaw width and thickness, have more effect on the response than at small depths. A potential approach to estimate the depth involves the development of an envelope with an upper and a lower bound of the t_s as a function of the actual depth of the subsurface flaw, as illustrated in Fig. 5.38. A function using the averages at each depth is also plotted.

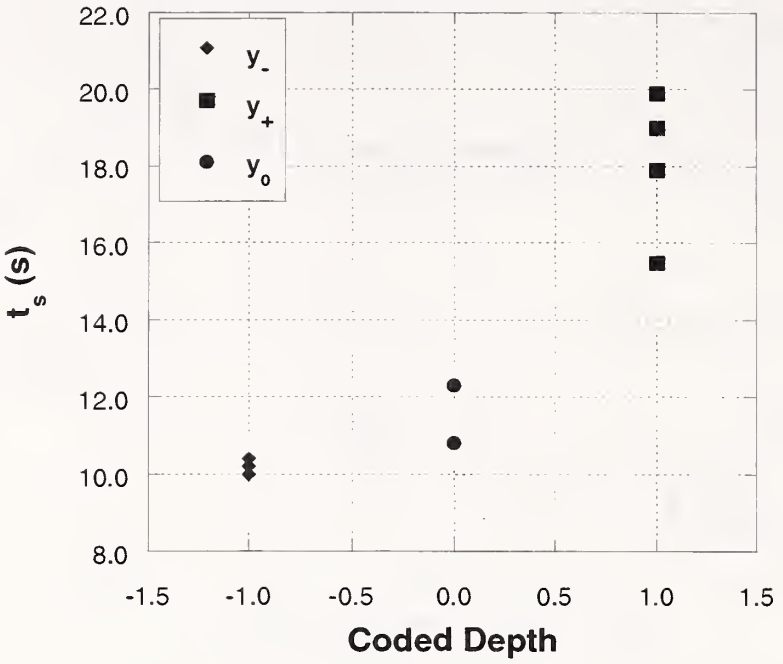

Fig. 5.38 Time to maximum signal data as a function of the coded depth (-1,0,+1)

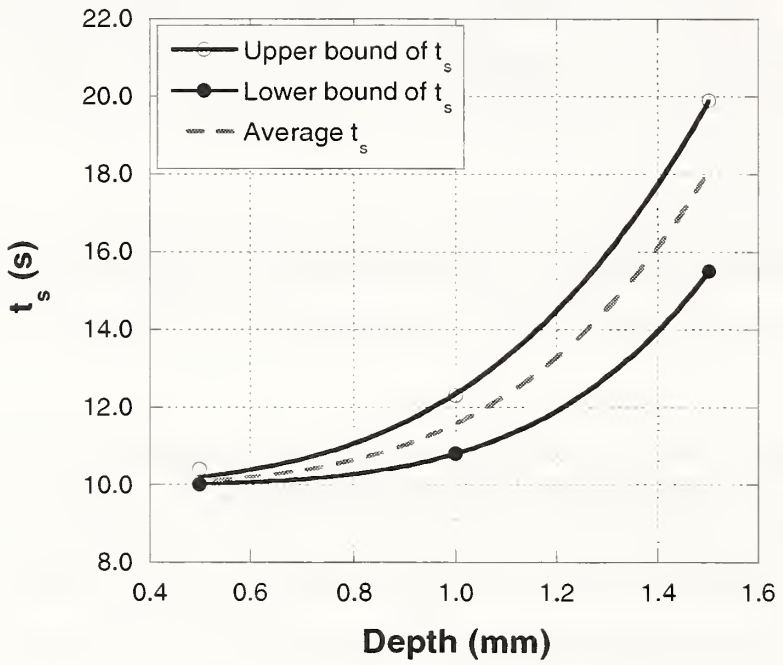

Fig. 5.39 Time to maximum signal data as a function of the actual depth

The functions that define the upper and lower bounds of the envelope are the following:

- for the upper bound,

$$t_s\big|_{upper} = 10 + 2.35 d_{flaw}^{3.55} \tag{5.4}$$

where $t_s|_{upper}$ is the time to maximum signal for the upper bound, and d_{flaw} is the depth of the flaw; and

- for the lower bound,

$$t_s|_{lower} = 10 + 0.80 d_{flaw}^{4.76} \tag{5.5}$$

where $t_s|_{lower}$ is the time to maximum signal for the upper bound, and d_{flaw} is the depth of the flaw.

The function defining the average time to maximum signal as a function of the depth is the following:

$$t_s|_{avg} = 10 + 1.57 d_{flaw}^{4.05} \tag{5.6}$$

where, $t_s|_{avg}$ is the average time to maximum signal and d_{flaw} is the depth of the flaw.

Once a graph such as Fig. 5.39 has been developed, the depth of a flaw could be estimated using the average time to maximum signal. For example, if the time to maximum signal is 13 s, the estimated depth of the flaw would be 1.2 mm, approximately. On the other hand, the depth using the upper bound of the envelope estimates a depth of 1.1 mm, while the lower bound envelopes estimates a value of 1.3 mm, approximately. The estimation of the depth using $t_s|_{avg}$ differs only by ±0.1 mm from the values of the depth corresponding to the upper and lower bounds. Thus the potential error in the estimation of the flaw using the average t_s is smaller than the thickness of one layer of FRP, which is usually on the order of 0.5 mm.

5.7.5 Conclusions for the Screening Experiment

The screening experiments provided several conclusions. The first phase of the experiment focused primarily measuring the thermal responses such as T_{max}, ΔT_{max}, t_s, C_{max}, and t_c. The exercise provided some insight to the procedures necessary to treat actual measurement data and interpret the results. The following are some of the conclusions from this phase of the experiment:

- The thermal signal as a function of time may be smoothed using a moving average filter without compromising the results.

- The thermal contrast as a function of time may also be smoothed using a moving average. The contrast data, however, are very noisy. The moving average filter requires a large number of data points to smooth the contrast function sufficiently to obtain meaningful values of maximum contrast and t_c .

The second phase of the experiment was the analysis of the results of the full factorial screening study. The analyses demonstrated that the depth of the flaw is the principal factor affecting every thermal response. It was concluded that the best thermal responses to estimate the depth of the flaw are the time to maximum signal t_s and the time to maximum contrast t_c. Thus only the results of t_s and t_c were summarized in this section.

The analytical studies suggested that flaw depth could be estimated from the time to maximum signal. The results of the screening study confirmed that the time to maximum signal can be used to estimate the depth of the flaw. The flaw depth estimation function is based on a power function fitted through the average $\hat{\beta}_i$ values as a function of flaw depth.

Thus evaluation of the results indicates the following:

- The depth of the flaw should be estimated using the time to maximum signal t_s; and
- A power function fitted though the average t_s at each depth provides the tool to estimate the depth of the flaw.

5.8 Experiment #5: Investigation of Test Repeatability and Effect of Sampling Rate

The final set of experiments involved the study of the repeatability of the infrared thermography measurements and the effect of sampling rate on the data analysis results. In order for any test method to have credibility it must be repeatable. That is, the results obtained by different sets of measurements under similar conditions should be similar. For the study of repeatability, three sets of measurements of thermal signal were compared. It was desired to determine how much the measured thermal signal was affected by the chosen locations of the spot meters and by the data set (thermogram) used. The comparison was done for the following:

- Same data sets using different locations of spot meters for measuring T_{flaw} and $T_{background}$;
- Different data sets using the same location of spot meters for measuring T_{flaw} and $T_{background}$; and,
- Different data sets and different location of spot meters for measuring T_{flaw} and $T_{background}$.

The second component of this experiment involved the study of the effect of the data sampling rate on the measured response parameters. The data acquisition system that was used allows sampling rates either at the highest possible speed for the infrared camera or at hour-minute-second intervals (no fractions of seconds are allowed). For the uncooled infrared camera, the highest possible sampling rate is 60 Hz. Thus the fastest sampling rates allowed by the system is 60 Hz, followed by 1 Hz. Sampling at 60 Hz permits recording thermal responses at video speed, which a priori may seem desirable. It is, however, computationally intensive and it requires large data storage. Tests recorded at 60 Hz for a duration of 60 s require at least 500 Mbytes of data storage. On the other hand, tests recorded at 1 Hz for a duration of 60 s require only 9 Mbytes of data storage.

This part of the investigation tried to answer if a 60 Hz sampling rate is necessary or if a 1 Hz sampling rate would be sufficient for the evaluation of FRP composites bonded to concrete. To answer this question, the results of eight tests performed using a 60 Hz sampling rate were compared to six tests performed using a 1 Hz sampling rate.

5.8.1 Test Procedure

To investigate the repeatability of the thermal response parameter measured by infrared thermography testing and the effect of sampling rate, a series of measurements were performed on the same flaw. The tests were carried out on the specimen fabricated with wet lay-up CFRP and containing Nomex® flaws. The selected flaw for the study was flaw #3, which corresponded to the last run of the previous set of experiments (screening experiment). This flaw was chosen simply for convenience, since the test configuration did not require any changes.

First, the ambient temperature was measured following the procedure described in Sec. 5.5.1. The measured ambient temperature was 24 °C.

Fifteen different infrared thermography tests were performed to determine the repeatability of the thermal response for flaw #3. The specimen was tested using the experimental configuration illustrated in Fig. 5.1. The specimen was located 0.37 m from the heating lamps and the IR camera. The specimen was placed so that the subsurface flaw under study was positioned at the centerline between the two heating lamps. The duration of the thermal pulse was set to 10 s. Data were recorded for 60 s for each test. For nine of the measurement the sampling rate was 60 Hz. The remaining six tests were recorded at a sampling rate of 1 Hz.

The surface temperature above the flaw (T_{defect}) and above the bonded laminate near the flaw ($T_{background}$) were recorded as a function of time for each test.

5.8.2 Data Analysis

As mentioned in the previous section, fifteen infrared thermography measurements were performed. The objective of the repeatability study was to examine the effects of using replicate thermograms and of the placement of the spot meters. The set of tests were organized into three categories as follows:

- Same thermogram – different locations of spot meters to measure T_{flaw} and $T_{background}$ (analysis set #1);
- Different thermograms – same location of spot meters to measure T_{flaw} and $T_{background}$ (analysis set #2); and,
- Different thermograms – different location of spot meters to measure T_{flaw} and $T_{background}$ (analysis set #3).

Three replicate determinations were performed for analysis set #1. The infrared thermography test was performed once, thus there was one thermogram. The temperature of the surface above the flaw T_{flaw} and the temperature in the background $T_{background}$ were measured three times using different spot meters at various locations. The locations, however, were positioned within the region above the flaw or background; that is the location of the spot meters was varied only by a couple of millimeters in different directions. Thus three sets of measurements were compared.

For analysis set #2 five replicate infrared thermography tests were carried out. Thus five thermograms were analyzed. The locations of the spot meters to measure surface temperatures were fixed at the same points for the analysis of the thermograms. Thus the only variant in each analysis was the thermogram that was analyzed.

Table 5.11 Summary of analysis categories for the study of test repeatability
(data recorded at 60 Hz)

		Tests or thermograms	
		Same	**Different**
Location of spot meters to measure T_{flaw} and $T_{background}$	**Same**	N/A	Set #2: 5 analyses
	Different	Set #1: 3 analyses	Set #3: 3 analyses

For analysis set #3, three replicate infrared thermography tests were analyzed using different spot meter locations to measure T_{flaw} and $T_{background}$. For each analysis, the spot meters were moved only by a few millimeters. A schematic of the analysis categories for this experiment is presented in Table 5.11.

For each analysis, the magnitude of the maximum signal and the time to maximum signal were determined for comparison.

The second component of the investigation focused on the effect of sampling rate. For this comparison, six tests were recorded at a sampling rate of 1 Hz. For analysis set #4, three infrared thermography measurements were done. The location of the spot meters was kept constant for the analysis of the three thermograms. For analyses set #5, three new thermograms were recorded. The spot meters were place at different locations.

Table 5.12 Summary of analysis categories for the study of test repeatability
(data recorded at 1 Hz)

		Tests or thermograms	
		Same	**Different**
Location of spot meters to measure T_{flaw} and $T_{background}$	**Same**		Set #4: 3 analyses
	Different		Set #5: 3 analyses

To evaluate the effect of the sampling rate, the results for set #2 were compared with set #4 and the results of set #3 were compared was compared with set #5. A summary of the analysis categories for this component of the study is presented in Table 5.12.

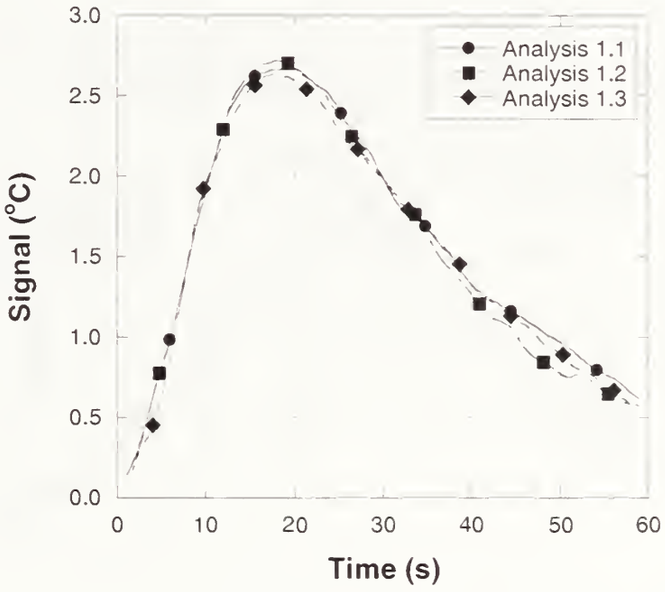

Fig. 5.40 Smoothed thermal signal as a function of time
for analysis set #1

The thermal signal as a function of time was computed based on the recorded data for each test. As in previous tests, the thermal signal as a function of time was smoothed to eliminate noise. Smoothing of the data was required to be able to determine the maximum signal ΔT_{max} and the time to maximum signal t_s. Smoothing of the data was accomplished using a moving average filter. The thermal signal of analysis set #1 was smoothed using 135 points in the moving average. This high number of points was necessary since the data, recorded at 60 Hz, was very noisy. The resultant thermal signals for analysis set #1 are presented in Fig. 5.40.

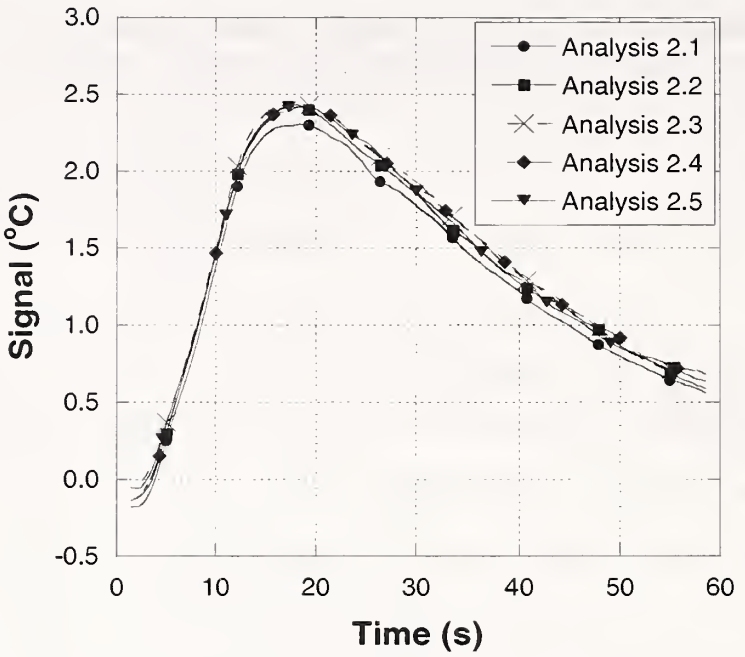

Fig. 5.41 Smoothed thermal signal as a function of time for analysis set #2

The measured signals for analyses set #2 were smoothed using 175 points for the moving average. The resulting smoothed signals are presented in Fig. 5.41.

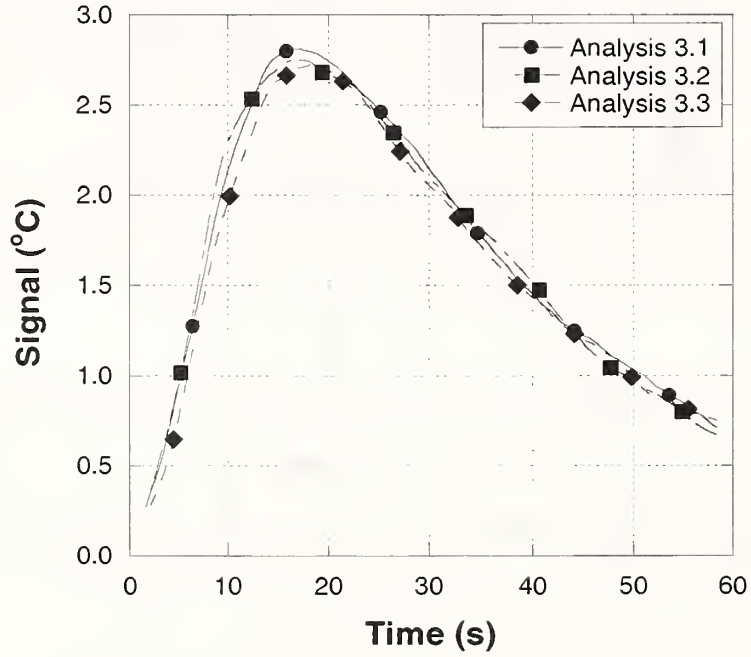

Fig. 5.42 Smoothed thermal signal as a function of time for analysis set #3

The measured signals for analysis set #3 were smoothed using 250 points for the running average. The resulting smoothed signals are presented in Fig. 5.42.

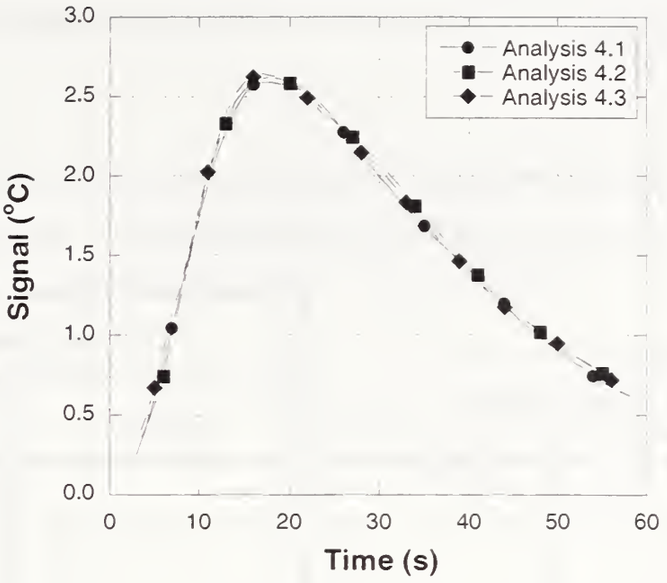

Fig. 5.43 Smoothed thermal signal as a function of time for analysis set #4

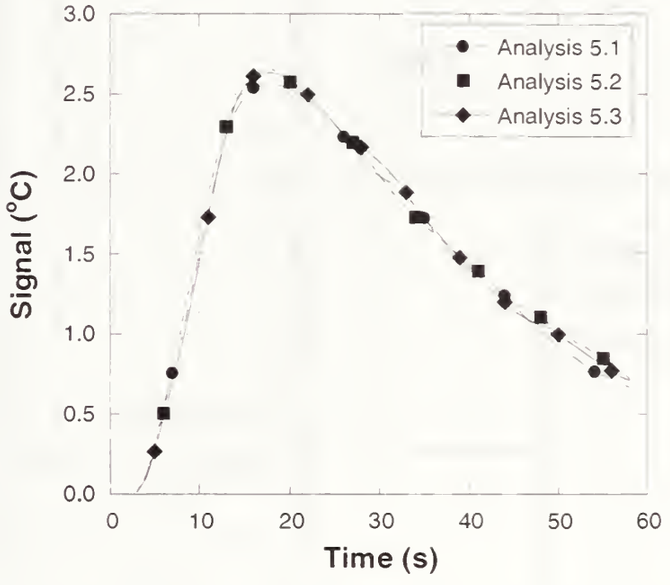

Fig. 5.44 Smoothed thermal signal as a function of time for analysis set #5

The data for analysis set #4 and analysis set #5 required only 5 points in the moving average for smoothing. The smoothed signals for analysis set #4 and analysis set #5 are presented in Figs. 5.43 and 5.44 respectively.

The results of ΔT_{max} and t_s for the analyses involving sampling rates of 60 Hz are presented in Table 5.13. Similarly, the results of the analyses involving sampling rates of 1 Hz are summarized in Table 5.14. Finally, Tables 5.15 and 5.16 summarize the averages and the

standard deviations of the thermal responses for the measurements involving sampling rates of 60 Hz and 1 Hz, respectively.

Table 5.13 Results of individual analyses for the study of test repeatability (data recorded at 60 Hz)

		Tests or thermograms	
		Same	**Different**
Location of spot meters to measure T_{flaw} and $T_{background}$	**Same**		Analysis 2.1: ΔT_{max} = 2.3 °C, t_s = 17.1 s
			Analysis 2.2: ΔT_{max} = 2.4 °C, t_s = 18.1 s
			Analysis 2.3: ΔT_{max} = 2.4 °C, t_s = 17.5 s
			Analysis 2.4: ΔT_{max} = 2.4 °C, t_s = 18.6 s
			Analysis 2.5: ΔT_{max} = 2.4 °C, t_s = 18.4 s
	Different	Analysis 1.1: ΔT_{max} = 2.7 °C, t_s = 20.1 s	Analysis 3.1: ΔT_{max} = 2.8 °C, t_s = 16.6 s
		Analysis 1.2: ΔT_{max} = 2.7 °C, t_s = 19.2 s	Analysis 3.2: ΔT_{max} = 2.7 °C, t_s = 17.4 s
		Analysis 1.3: ΔT_{max} = 2.6 °C, t_s = 18.8 s	Analysis 3.3: ΔT_{max} = 2.7 °C, t_s = 18.5 s

Table 5.14 Summary of individual results of analyses for the study of test repeatability (data recorded at 1 Hz)

		Tests or thermograms	
		Same	**Different**
Location of spot meters to measure T_{flaw} and $T_{background}$	**Same**		Analysis 4.1: ΔT_{max} = 2.6 °C, t_s = 18 s
			Analysis 4.2: ΔT_{max} = 2.7 °C, t_s = 18 s
			Analysis 4.3: ΔT_{max} = 2.6 °C, t_s = 18 s
	Different		Analysis 5.1: ΔT_{max} = 2.6 °C, t_s = 17.5 s
			Analysis 5.2: ΔT_{max} = 2.6 °C, t_s = 18 s
			Analysis 5.3: ΔT_{max} = 2.6 °C, t_s = 17 s

Table 5.15 Summary of averages and standard deviations for the study of test repeatability (data recorded at 60 Hz)

		Tests or thermograms	
		Same	**Different**
Location of spot meters to measure T_{flaw} and $T_{background}$	**Same**	ΔT_{max} Average = 2.4 °C Standard deviation = 0.05 °C t_s Average = 17.9 s Standard deviation = 0.6 s	
	Different	ΔT_{max} Average = 2.7 °C Standard deviation = 0.06 °C t_s Average = 19.4 s Standard deviation = 0.7 s	ΔT_{max} Average = 2.7 °C Standard deviation = 0.06 °C t_s Average = 17.5 s Standard deviation = 1.0 s

Table 5.16 Summary of averages and standard deviations for the study of test repeatability (data recorded at 1 Hz)

		Tests or thermograms	
		Same	**Different**
Location of spot meters to measure T_{flaw} and $T_{background}$	**Same**		ΔT_{max} Average = 2.6 °C Standard deviation = 0.06 °C t_s Average = 18.0 s Standard deviation = 0.0 s
	Different		ΔT_{max} Average = 2.6 °C Standard deviation = 0.0 °C t_s Average = 17.5 s Standard deviation = 0.5 s

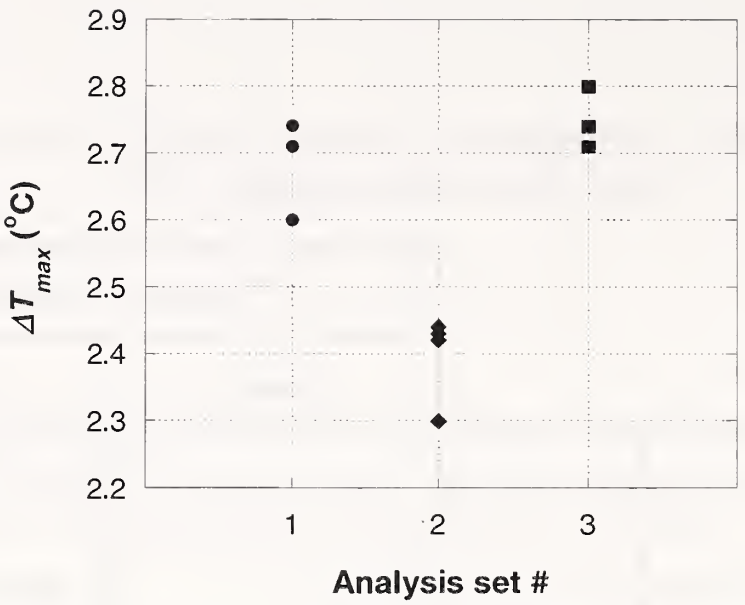

Fig. 5.45 Individual results for maximum signal (sampling at 60 Hz)

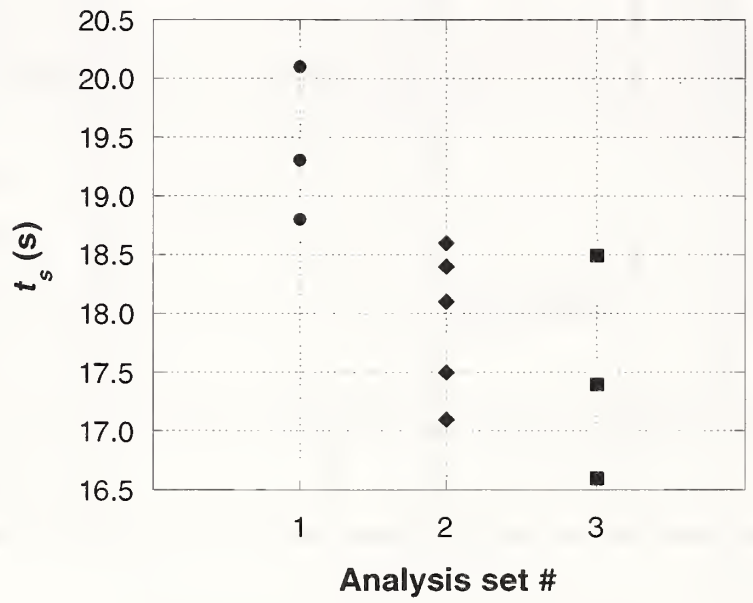

Fig. 5.46 Individual results for time to maximum signal (sampling at 60 Hz)

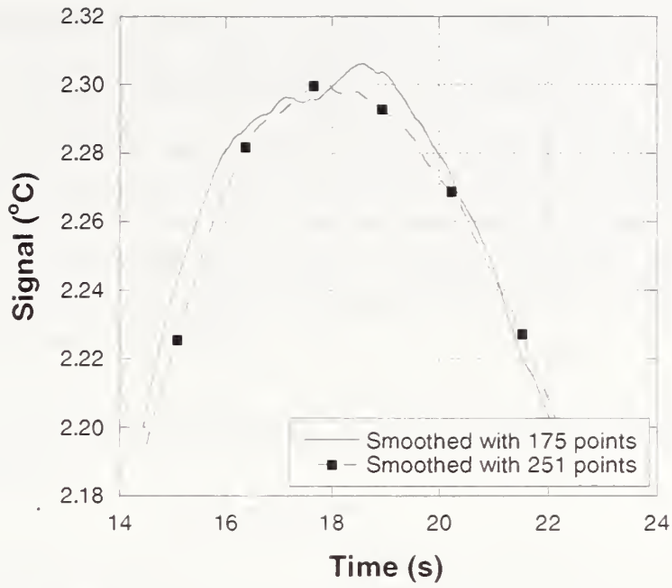

Fig. 5.47 Detail of thermal signal for two different cases of smoothing for Analysis 2.5

The repeatability of the measured thermal responses was evaluated using the results obtained from data recorded at 60 Hz. Figures 5.45 and 5.46 show the individual values of the maximum signal and time to maximum signal for analysis sets #1, #2, and #3. It is seen that the average maximum signal for analysis set #2 was lower than for the other sets. For the time to the maximum signal, the average value was longer for analysis set #1. Analysis of variance confirmed that these differences were statistically significant at the 5% confidence level. Visual examination of Figs. 5.45 and 5.46, indicates that the scatter of the individual determination was not affected by the method of data analysis. The scatter was small, with coefficients of variation of 5% or less. Thus it is concluded that the procedure used in this project results in reliable values of measured thermal response parameters. It is recommended that replicate thermograms be used to increase the reliability of results from quantitative thermographic testing.

Data analysis of measurements taken at a sampling rate of 60 Hz is computationally intensive and requires a large number of points to smooth the signal response as a function of time. Additionally, analysis of the data indicated that smoothing with a large number of points does not always guarantee that a single time to maximum signal would be found, thus requiring several iterations of smoothing until a single t_s is found. The time to maximum signal seemed to be sensitive to the amount of smoothing of the signal. An example of this behavior is illustrated in Fig. 5.47, which shows a detail of the thermal signal at the location of ΔT_{max} for two different cases of smoothing.

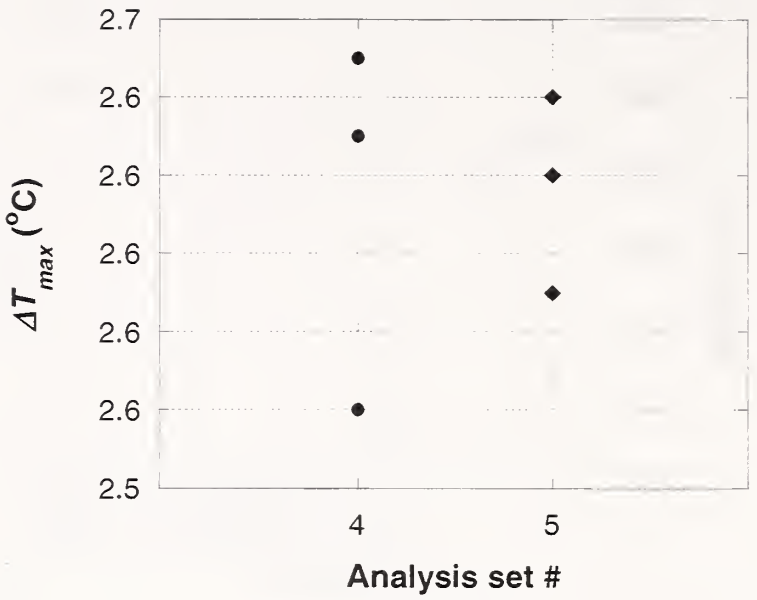

Fig. 5.48 Individual results for maximum signal (sampling at 1 Hz)

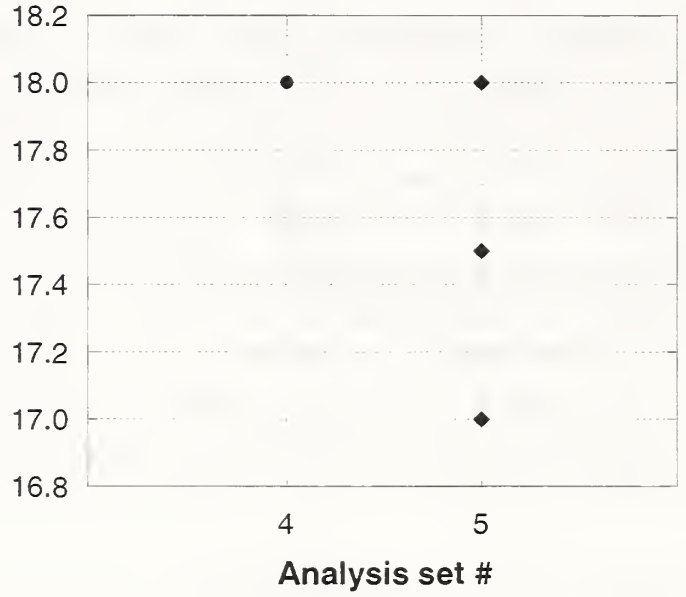

Fig. 5.49 Individual results for time to maximum signal (sampling at 1 Hz)

The results obtained from the analyses of data recorded at 1 Hz were similar to the results obtained from analyses of data recorded at 60 Hz. Figure 5.48 shows the individual results for maximum signal obtained from the five sets of analysis. The results for analysis sets #4 and #5 (based on 1 Hz data) are consistent with the results obtained from the 60 Hz data. Figure 5.49 shows the individual results for time to maximum signal. It is seen that the results based on the 1 Hz data are comparable to those based on the 60 Hz data.

Comparison of the results suggests that a 1 Hz sampling rate could be adequate for quantitative infrared thermography testing using the configuration presented in this project. Analysis of variance confirmed that differences in results for analysis sets #4 and #5 are not statistically significant at the 5% confidence level. Additionally, test data recorded at 1 Hz require less computer storage and data processing effort than test data recorded at 60 Hz.

The results of this investigation showed that the replication method (replicate measurements using the same thermogram versus using replicate thermograms) might affect the measured thermal response. For quantitative thermographic inspection, it is recommended that replicate thermograms should be recorded. The number of replicates will depend on the repeatability of the results. For the laboratory measurement obtained in this project, the repeatability was good, with confidence of variation less than 5 % for the maximum signal and the time to maximum signal. Thus at least two replicate thermograms should be used. In practice, the amount of replication will be dictated by the specific objective of the thermographic inspection and the degree of uncertainty that can be tolerated.

5.8.3 Conclusions of the Investigation of Test Repeatability and Effect of Sampling Rate

The closing set of experiments included a study of the repeatability of the infrared thermography measurements and the effect of sampling rate on the data analysis results. Five sets of analyses were performed for the investigation.

The results of the investigation indicated that for tests recorded at 60 Hz, the resulting thermal signal as a function of time was noisy, requiring several iterations of smoothing to discern values for ΔT_{max} and t_s.

The results for data recorded at 1 Hz indicated that average values of the thermal responses were similar to those from data recorded at 60 Hz. Additionally, analysis of data recorded at 1 Hz required less computational effort and data storage than data recorded at 60 Hz.

Therefore, it appears that a 1 Hz sampling rate may be adequate for quantitative infrared thermography testing of FRP composites bonded to concrete using the configuration presented in this project.

As for any other experimental measurement, replicate measurements, that is, thermograms, should be used for added reliability in the results of quantitative thermographic inspection.

5.9 Conclusions of Laboratory Studies

The experimental program was divided into 5 different studies. Following are the descriptions of the studies:

- The first part of the experimental study was qualitative in nature. The focus of the qualitative experiment was to evaluate the potential detection of simulated flaws embedded in the test object. The specimen had a single layer of pultruded CFRP laminates and contained eight simulated debonds made of different materials.

- The second experiment was quantitative and focused on the comparison of infrared thermography results with the results from FEM simulations. The air void contained in the specimen fabricated with pultruded CFRP bonded to concrete slab was used for comparing the experimental and analytical results.

- The third experiment involved the verification of the procedure for estimating flaw width based on analysis of surface temperature profiles.

- The fourth experiment involved a screening parametric investigation. The effect of three flaw parameters were investigated: flaw depth, flaw thickness, and flaw width. A full factorial experimental design with 2 "center" points was used. The purpose of the screening experiment was to verify the conclusions of the companion analytical screening study , and to verify the approach for estimating flaw depth on the basis of the time to maximum signal.

- The final study focused on the repeatability of thermal response parameters obtained from infrared thermography testing and the effect of the sampling rate.

The series of laboratory studies provided some interesting conclusions regarding infrared thermography testing. The following is a summary of the conclusions:

- Low-k materials can be used to simulate flaws that behave similar to air voids.

- Characterization of the flaw requires precise measurement of thermal signals as a function of time.

- Knowledge of the surface emissivity is not required for flaw characterization using infrared thermography. Knowledge of the emissivity is required only for precise measurement of surface temperatures. Measurement of the thermal signal, however, is independent of the value of the surface emissivity because ΔT is a differential between two temperatures measured using the same emissivity ($\Delta T = T_{defect} - T_{background}$). Thus, if the test object has uniform surface emissivity, the results for the maximum thermal signal and the time to maximum signal are the same regardless of the value of emissivity used to compute the surface temperatures.

- Using the contact method, the average emissivity of the CFRP laminate was 0.80, with a standard deviation of 0.016. Thus the expanded uncertainty interval is 0.80 ± 0.03, for a coverage factor $k = 2$. Using the noncontact method, the average emissivity of the pultruded laminate was 0.80 with a standard deviation of 0.01. Thus the two methods gave comparable results for this composite.

- For the wet lay-up composite, measurements using the contact method proved unreliable. Emissivity values greater than 1.0 were obtained using this technique. Thus the contact method may be unreliable for materials with high emissivity. The noncontact method, however, provided consistent results: the average surface emissivity of the wet lay-up composite was 0.98, with a standard deviation of 0.01. Thus the expanded uncertainty interval is 0.98 ± 0.02, for a coverage factor of $k = 2$.

- The heating module used for the experiments produced a relatively uniform heat flux at the surface of the test object and the shape of the heat flux pulse was repeatable.

- Agreement between the experimental data and the FEM simulations for the response of the air void provided reassurance that the conclusions derived from the simulations are valid.

- It was confirmed that the width of the flaw may be estimated by determining the location of the roots of the second derivative of the surface temperature profile at the time of maximum signal.

- A smoothing procedure using a moving average filter proved to be an effective means for dealing with noisy data. Thermal contrast is noisier and requires more smoothing than the thermal signal.

- It was confirmed that flaw depth is the major factor affecting the time to maximum signal. Thus, the time to maximum signal is the best thermal response parameter to estimate the depth of the flaw. A procedure for estimating the depth of the flaw from the time to maximum signal was presented.

- The investigation indicated that the procedures used in this project resulted in good test repeatability of measured thermal response parameters. It is recommended that replicate thermograms should be used to increase the reliability of quantitative thermographic testing.

- A sampling rate of 1 Hz is sufficient for quantitative testing of FRP bonded to concrete. The thermal responses based on data recorded at 1 Hz had similar average values to those based on data recorded at 60 Hz. The 60 Hz sampling rates resulted in noisier data and required more computational effort to produce clear measures of thermal response.

Chapter 6

Discussion

6.1 Summary

6.1.1 Introduction

Fiber reinforced polymer (FRP) composites, in the form of pultruded laminates or wet lay-up woven fabrics, are being used to rehabilitate existing concrete and masonry structures. The success of these materials in performing their intended functions depends, to a large extent, on how well they are bonded to themselves and to the substrate. Thus, there is a need for an efficient and reliable method to detect and characterize defects at the substrate interface and within multi-ply systems.

Quality control of the final product is a requirement for the reliable performance of any new material in structural engineering systems. Presently, there are no standard quality control procedures to assess the integrity of bonded FRP composite systems used in civil engineering applications. The best NDE technique needed to detect and characterize subsurface defects in any material depends on the critical size of the defect, the size of the structure being tested, and the environment in which the inspection is carried out. Moreover, the ideal NDE method in civil engineering applications should be accurate, reproducible, reliable, robust, and economical; able to inspect large areas as well as localized areas; able to detect critical defect sizes; and non-obtrusive to the surrounding environment, portable, and convenient to the users and evaluator of the structure.

Nondestructive testing of thin FRP laminates bonded to concrete or masonry presents a variety of difficulties in the use of the traditional methods developed for inspection of metals due to the anisotropy, variable and non-homogenous composition, non-magnetic properties, and high ultrasonic attenuation of FRP materials. Among the various available techniques, however, infrared thermography offers the greatest potential as a global NDE method.

Current inspection techniques using infrared thermography provide only qualitative assessments of the state of the structure, but give no quantitative information on existing defects. That is, they establish whether a subsurface flaw exists within the FRP-substrate system, but not the depth of the defect or its approximate volume. This qualitative nature of the results derives from the

complex relationships among the variables affecting the thermal response of the bonded laminates.

6.1.2 Research Objective

In order to allow widespread use of infrared thermography for quantitative assessment of FRP applied to concrete, a standard test method is needed. To develop such a standard, it is necessary to develop a greater understanding of the factors affecting the thermal response of FRP composites bonded to composites.

The purpose of this report was to develop the technical bases for quantitative infrared thermography testing of FRP bonded to concrete. Specifically, the report focused on a preliminary assessment of testing and analytical procedures that will aid the development of a standard method for NDE of FRP bonded to concrete using infrared thermography.

6.1.3 Approach

The objective of the report was achieved by a series of numerical and laboratory studies that investigated the effect of testing parameters and different types of defects.

The report was divided into three components: dimensional analysis, parametric studies, and laboratory studies.

First, a dimensional analysis of a simplified one-dimensional heat transfer model was performed to determine the parameters that needed to be investigated in the parametric studies.

The second component involved parametric studies performed using finite element analysis. The parametric studies were subdivided into investigations involving single factors and investigations involving multiple factors. Two-dimensional planar models were used to simulate infrared thermography testing of a semi-infinite concrete slab strengthened with FRP laminates.

The single-factor parametric study aimed to determine the effect of the following individual factors on the thermal response:

- Thermal input;
- Material thermal properties;
- Flaw depth;
- Flaw thickness; and,
- Flaw width.

The second set of parametric studies involved a screening numerical experiment focused on the determination of the important factors and interactions affecting the response. The purpose of the screening experiment was to determine which factors have the most significant effect on the thermal responses, thus enabling the solution of the inverse problem.

The final phase focused on a series of laboratory studies aimed to confirm the potential of using infrared thermography for quantitative testing and to verify the results achieved in the numerical parametric studies. The experiments were conducted on controlled-flaw specimens fabricated

with pultruded FRP laminates and wet lay-up fabric. An infrared thermography test configuration was designed and constructed to perform quantitative measurements of the time dependent thermal behavior. The laboratory studies involved five experiments:

- Qualitative testing;
- Comparison of infrared thermography and finite-element simulations;
- Estimation of flaw width;
- Screening experiment; and,
- Investigation of test repeatability and effect of sampling rate.

The laboratory studies also involved measurements of the input heat flux and emissivity of both kinds of FRP composites used in the research.

6.2 Conclusions

6.2.1 Dimensional Analysis

A dimensional analysis of a semi-infinite half space solid was performed and is described in Chapter 3. The analysis demonstrated that for the case of a semi-infinite half space subjected to a heat flux, the physical quantities that influence the thermal evolution (the spatial and temporal variations of temperature) are the depth z, time t, thermal conductivity of the material k, thermal diffusivity of the material α, and the input heat flux q. In the case of a solid containing a subsurface flaw, additional physical quantities such as the thermal resistance of the flaw should be taken into consideration. The results from the dimensional analysis identified the parameters that had to be investigated in the numerical parametric study.

6.2.2 Parametric Studies

The investigation described in Chapter 4 focused on the effect that various parameters have on the thermal response. The key thermal response parameters are the maximum surface temperature, the maximum signal (surface temperature difference) and the time to maximum signal. The investigation was subdivided into a single-factor parametric study and a multi-factor parametric study.

The first single-factor study involved the effect of the thermal input. The magnitude and duration of the input heat flux were varied to evaluate the variation in the thermal response parameters. The results showed that selection of the thermal pulse is governed by the desired maximum signal and by the maximum surface temperature that can be tolerated by the material. The findings indicated that for a given flaw geometry, the maximum signal is a linear function of the input energy (product of pulse amplitude and pulse duration). Therefore, a maximum value of input energy can be selected for a desired minimum signal. The maximum surface temperature is also a linear function of the input energy, but it depends also on the pulse duration. The selection of the pulse duration to produce the minimum input energy is governed by the maximum surface temperature that the FRP composite can tolerate. These results led to a simple approach for selecting the thermal input for a specific test object so as to obtain a desired thermal signal while limiting the surface temperature. An additional important conclusion from

the study was that only the duration of the heat pulse affects the time to maximum signal; the magnitude of the input heat flux does not affect this thermal response parameter.

The second study involved the effect of thermal material properties on the thermal response of the test object. The thermal conductivity and specific heat of the FRP composite and the concrete substrate were varied. The investigation concluded that, while variations in the thermal properties of the FRP and concrete resulted in systematic variations in thermal response, none of the thermal response parameters were very sensitive to these variations. Thus it is concluded that the success of infrared thermography testing will not depend strongly on the specific values of the thermal properties of the FRP or concrete substrate.

The third parametric study involved the effect of the depth of the flaw on the thermal response. For this purpose, delaminations, debonds, and concrete spalls at various depths were modeled. Additionally, the number of laminates bonded to the concrete substrate was varied. The results indicated that the thermal responses are a function of both the depth of the flaw and the number of FRP. The time to maximum signal was, however, affected little by the number of FRP layers. A possible procedure for estimation of flaw depth was demonstrated using the time to maximum signal.

The fourth parametric study focused on the effect of the thickness of the subsurface flaw. Again, delaminations, debonds and concrete spalls were studied. This parametric study showed that the flaw thickness has a significant effect on the thermal responses in the case of delaminations near the surface, but the effect is minor for debonds and concrete spalls. Very thin delaminations are difficult to detect because their thermal resistance is negligible.

The last single-factor investigation involved the effect of the width of the flaw and it aimed to determine whether a suitable procedure could be developed to estimate the flaw width. The results indicated that the width of the flaw could be estimated from the second derivative of the surface temperature profile at the time of maximum signal. Additionally, the investigation demonstrated that the smallest detectable flaw is a function of the depth of the flaw and the maximum signal required to overcome noise in the measuring process. The width of the smallest detectable flaw varied as a power function of the depth of the flaw. Thus as flaw depth increases, the minimum flaw width that can be detected also increases.

Finally, a multi-factor parametric study was performed to determine which factors and interactions have statistically significant effects on the response parameters. Three parameters were investigated simultaneously: depth, thickness, and width of the flaw. A full-factorial experiment design was simulated using the three factors, each containing two levels. The screening study proved that flaw depth is the only factor that has a statistically significant effect on the time to maximum signal. Thus it should be possible to estimate using the time for maximum signal alone. On the other hand, the large scatter of the thermal responses T_{max}, ΔT_{max}, and t_s as a function of the thickness indicated that the thickness of the flaw would be difficult to characterize accurately.

6.2.3 Laboratory Studies

The laboratory studies demonstrated that quantitative testing of FRP bonded to concrete is possible.

The qualitative infrared thermography experiment confirmed that detection of subsurface flaws is achieved easily by sweeping an infrared heat lamp over the surface of the FRP at a distance of 50 mm and at a speed of approximately 0.15 m/s. This quick technique could be used to easily detect subsurface flaws. Characterization of the flaw requires, however, accurate measurement of surface temperatures as a function of time.

In the case of the simulations reported in Chapter 4, the calculated time dependent temperature data allow easy determination of the response parameters. In the case of experimental data, however, a smoothing procedure is required in order to determine the basic response parameters T_{max}, ΔT_{max} and, most importantly, t_s. Using a moving average filter proved to be an effective means for dealing with noisy data.

As part of the laboratory studies, the results of FEM simulations were compared to experimental data. Agreement between the experimental data and the FEM simulations provided assurance that the analytical model and thus the results from Chapter 4 are valid.

The experimental investigation confirmed that the width of the flaw may be estimated by determining the location of the roots of the second derivative of the surface temperature profile at the time of maximum signal. As was the case for the temperature profile, the second derivatives of the profile must be smoothed in order to determine where the second derivative equals zero. A moving average filter proved effective for this purpose.

Similar to the screening simulation study described in Chapter 4, the screening laboratory experiment involving the depth, thickness, and width of the flaw established that flaw depth is the most significant factor affecting the time to maximum signal. This conclusion confirmed that the time to maximum signal is the most appropriate thermal response parameter to estimate the depth of the flaw. It was shown that flaw depth can be estimated by using a pre-established relationship between the average time to maximum signal and the flaw depth The details of how this relationship should be established requires further research.

The investigation indicated that test repeatability could be an issue depending on the location of the measuring spot meters and the run. Replicate tests revealed that the response parameters are highly repeatable (low standard deviation) under laboratory conditions.

The study also indicated that sampling rates of 1 Hz are sufficient for quantitative testing of FRP bonded to concrete. Higher sampling rates (i.e., 60 Hz) are noisier, computationally intensive, and require large amounts of data storage.

The investigation also concluded that the use of thermal signal is a more reliable response parameter than the use of thermal contrast. In principle, contrast has the advantage of not requiring knowledge of the input heat flux. Thus, a priori, it may seem preferable to use the thermal contrast data instead of the thermal signal. The laboratory studies, however, indicated

that the thermal contrast is much noisier that the thermal signal making it difficult to determine the time to maximum contrast.

6.2.4 Summary

In summary, the objectives of the project were achieved through numerical and experimental studies. The investigation confirmed that qualitative testing, as already performed by some inspectors, is an efficient and simple way to detect the presence of subsurface air voids embedded in either FRP composites or in the concrete substrate. Characterization of the flaws, however, requires quantitative testing procedures.

The study concluded that both flaw depth and flaw width (or area) may be estimated easily. The flaw depth could be estimated by measuring the time to maximum signal. The flaw width could be estimated by locating the roots of the second derivative of the surface temperature profile at the time of maximum signal. Thus, for quantitative assessment of the depth and the width of the flaw only the thermal signal history of the test object is needed.

The magnitude of heat flux applied to the surface does not need to be measured. The first parametric study indicated that the time to maximum signal does not vary with the magnitude of the applied heat pulse, only with its duration. Additionally, knowledge of the surface emissivity of the test object is not required to determine the time to maximum signal and the roots of the second derivative of the surface temperature profile. These two findings will simplify the development of a standard test procedure.

It was also concluded that determination of the thickness of the flaw is not possible using the thermal response parameters considered in this study.

6.2.5 Research Limitations

The research conducted proved that quantitative nondestructive evaluation of FRP composites bonded to concrete is possible.

Some limitations, however, were identified in this research. For example, emissivity measurements using the contact method (involving thermocouples) proved unreliable. Emissivity values greater than 1.0, which are not possible, were measured using this technique. This fact indicated a possible limitation of the contact method procedure for materials with high emissivity. This issue will have to be investigated further.

A procedure for estimating the depth of the flaw from the time to maximum signal was demonstrated. The predictive model, however, was simple since it was developed using only a few flaw depths. Regression experiments with additional flaw depths and other relevant factors should allow the definition of a better model in the future. Development of graphs (or models) such as those illustrated in Fig. 5.46 and 5.47 is needed for typical air voids encountered in FRP composites bonded to concrete.

An additional limitation of this research is that testing was conducted under laboratory

conditions. *In situ* testing would have been more realistic of actual testing for civil engineering applications. Forced convection due to high wind speed and atmospheric attenuation may have an important effect on the thermal response of the test object and on the temperature measurement recorded by the infrared detector. Future research should focus on the implementation of the testing procedures for *in situ* evaluation. Experimental testing and numerical simulations similar to those carried out in this investigation should overcome this limitation.

6.3 Future Implications

The photonics industry is quickly developing more accurate and reliable infrared detectors at a lower price, and the use of infrared thermography for routine evaluation of civil engineering structures is growing. Additionally, widespread use of FRP composites in civil engineering infrastructure will depend on the development of a standard methodology to test the quality of the bond between the fiber composites and the substrate. There is a danger, however, of generalized used of infrared thermography testing without full understanding of the thermal response of these materials and components

The conclusions from this report demonstrate that quantitative infrared thermography testing of FRP composites bonded to concrete has the potential to estimate the depth and width of subsurface voids. Further research, however, is needed to develop a standard test for quantitative infrared thermography testing. The research should focus on optimization of the testing configuration and on dealing with uncontrolled atmospheric variables (wind speed, air temperature, and solar radiation). The ultimate goal is to use infrared thermography to test structures in the field. Thus a field demonstration project should be carried out to verify that this test method can accurately evaluate the state of the FRP composite, the concrete substrate, and their bond.

A second field of study needed for the success of infrared thermography is the development of specialized software to allow automation of the data analysis process. Current data analysis software for infrared thermography testing provides only some of the tools needed for quantitative assessment. From the quantitative testing perspective, it would be beneficial to have data analysis software able to filter the raw data and compute and record thermal signals in real time. Then, based on the measured time to maximum signal, the flaw depth could be estimated. Algorithms using neural networks, for example, have the potential to answer this need. By automating the calculation of the second derivatives of surface temperature profiles, the size (area) of the subsurface flaw could be estimated quickly.

More research is needed on thermography of testing curved surfaces. Many civil structures retrofitted with FRP composites, such as columns, have curved surfaces. It is expected that the curved surface would produced a visually distorted image of the surface temperatures of the test object. Thus, quantitative infrared thermograph testing of these structural components would require different considerations because of their particular shape.

Bibliography

Allport, J.; McHugh, J. (1988) "Quantitative Evaluation of Transient Video Thermography." Review of Progress in Quantitative non Destructive Evaluation, Vol.7a, pp.253-262.

Almond, D.P.; Lau, S.K. (1994) "Defect Sizing by Transient Thermography I: An Analytical Treatment." Journal of Physics D: Applied Physics, Vol.27, pp.1063-1069.

ANSYS. (2000) ANSYS Heat Transfer Training Manual for Release 5.6.

Balageas, D.L.; Krapez, J.C.; Cielo, P. (1986) "Pulsed Photothermal Modeling of Layered Materials." Journal of Applied Physics, Vol.59, No.2, pp.348-357.

Ball, R.J.; Almond, D.P. (1998) "The Detection and Measurement of Impact Damage in Thick Carbon Fibre Reinforced Laminates by Transient Thermography." NDT & E International, Vol. 31, No. 3, p 165-173.

Bar-Cohen, Y. (1986) "NDE of Fiber-Reinforced Composite Materials-A Review." Materials Evaluation, Vol.44, pp. 446-453.

Bendada, A.; Maillet, D.; Degiovanni, A. (1992) "Nondestructive Transient Thermal Evaluation of Laminated Composites: Discrimination Between Delaminations, Thickness Variations, and Multidelaminations." Eurotherm Seminar 27, Quantitative Infrared Thermography QIRT'92, pp.218-223.

Bonacci, J.F.; Maalej, M. (2000) "Externally Bonded FRP for Service-Life Extension of RC Infrastructure." Journal of Infrastructure Systems, Vol.6, No.1, pp.41-51.

Büyüköztürk, Oral. (1998) "Imaging of Concrete Structures." NDT & E International, Vol. 31, No. 4, pp. 233-243.

Cielo, P.; Maldague, X.; Déom, A.A.; Lewak, R. (1987) "Thermographic Nondestructive Evaluation of Industrial Materials and Structures." Materials Evaluation, Vol.45, No.6, pp.452-460.

CNDE (1999) "Tap Test Improved by Instrumentation Development." Center for NDE News. Vol. 10, Issue 2.

Connolly, M.P. (1992) "The Measurement of Porosity in Composite Materials Using Infrared Thermography." Journal of Reinforced Plastics and Composites, Vol.11, No.2, pp.1367-1375.

Connolly, M.P. (1991) "A Review of Factors Influencing Defect Detection in Infrared Thermography: Applications to Coated Materials." Journal of Nondestructive Evaluation, Vol. 10, No. 3, pp.89-96.

Connolly, M and Copley, D. (1990) " Thermographic Inspection of Composite Materials." Materials Evaluation, December, pp.1461-1463.

Cowell, S.D.; Burleigh, D.D. (1991) "Numerical Modeling of Thermographic Nondestructive Testing for Epoxy Laminates." Thermosense XII. Proceedings of SPIE, Vol.1313, pp.143-150.

Cramer, K.E.; Winfree, W.P. (1992) "Thermographic Imaging of Cracks in Thin Metal Sheets." Thermosense XIV. Proceedings of SPIE, Vol.1682, pp.162-170.

Dattoma, V.; Marcuccio, R.; Pappalettere, C.; and Smith, G.M. (2001) "Thermographic Investigation of Sandwich Structure Made of Composite Material." NDT &E International. Vol. 34, pp. 515-520

Delpech, Ph.M.; Boscher, D.M.; Lepoutre, F.; Déom, A.A.; Balagueas, D.L. (1993) "Quantitative Nondestructive Evaluation of Carbon-Carbon Composites by Pulsed Infrared Thermography." Review of Progress in Quantitative Nondestructive Evaluation, Vol.12, pp.1297-1304.

Ede, A.J. (1967) *An Introduction to Heat Transfer Principles and Calculations.* Oxford: Pergamon Press Ltd.

Ford, P. and Lovejoy, D. (2001) "Meeting the Challenge of Training for NDT of Advanced Composite Materials and Structures." Insight: Non-Destructive Testing and Condition, Vol. 43, No. 12, pp. 794-796.

Galmiche, F.; Maldague, X.P. (1999) " Active Infrared Thermography for Land Mine Detection." Proceedings of SPIE: Conference on Diagnostic Imaging Technologies and Industrial Applications, Vol. 3827, pp.146-154.

Ghiringhelli, G.L. (1997) "On the Thermal Problem for Composite Beams Using a Finite Element Semi-Discretisation." Composites, Part B: Engineering, Vol.28, No.5/6, pp.483-495.

Giorleo, G.; Meola, C. (1998) "Location and Geometry of Defects in Composite Laminates from Infrared Images." Journal of Materials Engineering and Performance, Vol. 7, No. 3, pp. 367-374.

Grinzato, E.; Bison, P.; Marinetti, S.; Vavilov, V. (1994) "Nondestructive Evaluation of Delaminations in Fresco Plaster Using Transient Infrared Thermography." Research in Nondestructive Evaluation, Vol.5, pp.257-274.

Grinzato, E.; Vavilov, V.; Kuppinen, T. (1998) " Quantitative Infrared Thermography in Buildings." Energy and Buildings, Vol.29, pp.1-9.

Hartikainen, J.; Jaarinen, J.; Luukkala, M. (1989) "Delamination and Crack Detection by the Synchronous Heating Method: Theoretical Aspects." Review of Progress in Quantitative Nondestructive Evaluation, Vol.8B, 1989, pp.1321-1328.

Hawkins, G.F.; Johnson, E; Nokes, J. (1999) "Typical Manufacturing Flaws in FRP Retrofit Applications." NISTIR 6288. Proceedings from NIST Workshop on Standards Development for the Use of Fiber Reinforced Polymers for the Rehabilitation of Concrete and Masonry Structures. January 7-8. Tucson, Arizona.

Hawkins, G.F.; Johnson, E.C.; Nokes, J.P. (1999) "Detecting Manufacturing Flaws in Composite Retrofits." SPIE, vol. 3587, pp.97-104.

der Hovanesian, J., Hung, Y.Y. (1995) "Shearography for Discontinuity Detection." Materials Evaluation, Vol.53, No.6, pp.725-729.

Hamzah, A.R.; Delpech, P.; Saintey, M.B.; Almond, D.P. (1996) "An Experimental Investigation of Defect by Transient Thermography." Insight, Vol.38, No.3, pp.167-173.

Howell, P.A.; Winfree, W.P.; Crews, B.S. (1991) "Numerical Simulations of Thermal Detection of Disbonds in Lap Joints." Review of Progress in Quantitative Nondestructive Evaluation, Vol.10B, pp.1367-1374.

Hung, Y.Y.; Luo, W.D.; Lin, L.; and Shang, H.M. (2000) "Evaluating the Soundness of Bonding Using Shearography." Composite Structures, Vol.50, No. 4, pp.353-362.

Kaminski, M.; Hien, T.D. (1999) "Stochastic Finite Element Analysis of Transient Heat Transfer in Composite Materials with Interface Defects." Archives of Mechanics, Vol.51, No.3/4, pp.399-418.

Jahnke, D.A.; Sandor, B.I. (1997) "Forced Diffusion Thermography for Nondestructive Evaluation of Microstructures." TMS Annual Meeting: Design Reliability of Solders and Solder Interconnections, 1997, pp.43-47.

Karbhari,V.M.; Seible, F. (1998) "Design Considerations for the Use of Fiber Reinforced Polymeric Composites in the Rehabilitation of Concrete Structures." NISTIR 6288. Proceedings from NIST Workshop on Standards Development for the Use of Fiber Reinforced Polymers for the Rehabilitation of Concrete and Masonry Structures. January 7-8, 1998. Tucson, Arizona.

Kleinfeld, Jack M. (1999) "Finite Element Analysis as a Tool for Thermography." Thermosense XXI. Proceeding of SPIE, Vol.3700, April 1999, pp.6 –13.

Lankford, Bill. (2000) "Infrared Imaging." Photonics Spectra. p. 115.

Lehtiniemi, R.; Rantala, J.; Hartikainen, J. (1995) "A Photothermal Line-Scanning System for NDT of Plasma-Sprayed Coatings of Nuclear Power Plant Component." Research in Nondestructive Evaluation, Vol.6, No.2, 1995, pp.99-123.

Lienhard, J.H. (1981) *A Heat Transfer Textbook*. Englewood Cliffs, New Jersey: Prentice-Hall, Inc.

Lulay, K.E.; Safai, M. (1994) "Optimization of Thermographic NDT Using Finite Element Analysis." Thermosense XVI. Proceedings of SPIE, Vol.2245, 1994, pp.106-110.

Lüthi T.; Meier H.; Primas R.; Zogmal O. (1995) "Infrared Inspection of External Bonded CFRP-Sheets." International Symposium Non-Destructive Testing in Civil Engineering, Berlin, Germany. Lectures Volume 1, pp. 689-696.

Maji, A.K. and Satpathi, D. (1997) "Electronic Shearography for Detecting Disbonds in Lattice/Skin Structures." Research in Nondestructive Evaluation, Vol.9, No.1, pp. 1-11.

Maldague, Xavier. (1993) *Nondestructive Evaluation of Materials by Infrared Thermography*. New York: Springer-Verlag.

Malhotra, V.M.; Carino, N.J. (1991) *Handbook on Nondestructive Testing of Concrete*. Boca Raton, Florida: CRC Press.

Marinetti, Sergio; Muscio, Alberto; Bison Paolo G.; and Grinzato, Ermanno.(2000) " Modeling of Thermal Non-Destructive Evaluation Techniques for Composite Materials." Thermosense XXII. Proceedings of SPIE, Vol.4020, pp.164-173.

Maser, K.R.; Roddis, W.M.K. (1990) "Principles of Thermography and Radar for Bridge Deck Assessment." Journal of Transportation Engineering, Vol.116, No.5, Sept-Oct 1990, pp.583-601.

MatWeb, "Material Property Data." http://www.matweb.com/

Mikron Instrument Company, "Table of Emissivity of Various Surfaces." http://www.transmetra.ch/pdf/publikatinen/emissivity.pdf

Morton, S. (2001) "Externally Bonded Composites for Strengthening Concrete Bridges." Proceedings of the 33rd International SAMPE Technical Conference. Vol. 33, pp. 808-820

Muscio, A.; Corticelli, M.A.; Tartarini, P.(2000) "Theoretical, Numerical, and Experimental Investigation of a One-Side Measurement Technique for Thermal Diffusivity." Thermosense XXII. Proceedings of SPIE, Vol.4020, pp.143-151.

Newnham, P. and Abrate, S. (1993) " Finite Element Analysis of Heat Transfer in Anisotropic Solids: Application to Manufacturing Problems." Journal of Reinforced Plastics and Composites, Vol. 12, August 1993, pp.854-864.

Özişik, M.N. (1985). *Heat Transfer: A Basic Approach.* New York: McGraw-Hill Book Company.

Plattner, L. (1999) "In-Situ Measurement of Chip Temperature During Soft Solder Die Bonding Using Integrated Microsensors." International Symposium on Microelectronics. Proceedings of SPIE, Vol.3906, pp.213-220.

Rantala, J.; Hartikainen, J. (1991) "Numerical Estimation of the Spatial Resolution of Thermal NDT Techniques Based on Flash Heating." Research in Nondestructive Evaluation, Vol.3, 1991, pp.125-139.

Rantala, J.; Jaarinen, J.; Kuo, P.K. (1992) "The Effects of Experimental Parameters in the Thermal Diffusivity Measurements of Oriented Polymer Films Using Mirage Effect: Computer Simulation." Applied Physics A: Solids and Surfaces, Vol.55, 1992, pp.586-595.

Rens, K.L.; Wipf, T.J. Klaiber, F.W. (1997) "Review of Nondestructive Evaluation Techniques of Civil Infrastructure." Journal of Performance Constructed Facilities. Vol.11, No.4, pp.152-160.

Rinaldi, Roberto, (2002) "Emissivity: The Common Problem for All Thermographers." Inframation Newsletter, Volume 3, Issue 4.

Sainley, M.B.; Almond, D.P. (1995) "Defect Sizing by Transient Thermography II: A Numerical Treatment." Journal of Physics D: Applied Physics, Vol.28, 1995, pp.2539-2546.

Satonaka, Shinobu; Ohba, Hiroyasu; Shinozaki, Kenya. (1995) "Nondestructive Evaluation of Weld Defects by Infrared Thermography." Proceedings of the International Conference on Offshore Mechanics and Arctic Engineering, Vol.3, 1995, pp.305-312.

Sayers, C.M. (1984) "Detectability of Defects by Thermal Non-Destructive Testing." British Journal of Non-Destructive Testing, Vol.26, No.1, pp.28-33.

Shuler, S.F., Advani, S.G. Kaliakin, Victor N. (1999) " Transient Analysis and Measurement of Anisotropic Heat Conduction in Transversely Isotropic Composite Materials." Journal of Composite Materials, Vol.33, No.7, pp.594-613.

Sjökvist, S.; Georgson, M.; and Ringberg, S.; Uppsäll, M.; and Loyd, D. (1998) "Thermal Effects on Solar Radiated Sand Surfaces Containing Landmines-a Heat Transfer Analysis." Proceedings of the International Conference on Advanced Computational Methods in Heat Transfer, pp.177-187.

Snell, John R. Jr. (1995) "Problems Inherent to Quantitative Thermographic Electrical Inspections." Proceedings of SPIE Thermosense XVII An international Conference on Thermal Sensing and Diagnostic Applications, Vol. 2473, pages 75-81.

Valerand, S.; Maldague, X. (2000) "Defect Characterization in Pulsed Thermography: a Statistical Method Compared with Kohonen and Perceptron Neural Networks." NDT&E International, Vol.33, pp.307-315.

Varis, J; Rantala, J.; Hartikainen, J. (1996) "An Infrared Line Scanning Technique for Detecting Delaminations in Carbon Fiber Tubes." NDT & E International, Vol.29, No.6, pp.371-377.

Varis, J.; Rantala, J.; Hartikainen, J. (1995) "Numerical Study on the Effects of Line Heating in Layered Anisotropic Carbon Fiber Composites." Research in Nondestructive Evaluation, Vol.6, No.2, 1995, pp.69-83.

Varis, J.; Lehtiniemi, R.; Hartikainen, J.; Rantala, J. (1995) "Transportable Infrared Line Scanner Based Equipment for Thermal Nondestructive Testing." Research in Nondestructive Evaluation, Vol.6, 1995, pp.85-97.

Vavilov, V.; Maldague, X.; Dufort, B.; Robitaille, F.; and Picard, J. (1993) "Thermal Nondestructive Testing of Carbon Epoxy Composites: Detailed Analysis and Data Processing." NDT & E International, Vol. 26, No. 2, pp. 85-95.

Vavilov, V.; Kauppinen, T.; Grinzato, E. (1997) "Thermal Characterization of Defects in Building Envelopes Using Long Square Pulse and Slow Thermal Wave Techniques." Research on Nondestructive Evaluation, Vol.9, pp.181-200.

Vavilov, V. (2000) "Three-Dimensional Analysis of Transient Thermal NDT Problems by Data Simulation and Processing." Thermosense XXII. Proceedings of SPIE, Vol.4020, pp.152-163.

Wiecek B.; De Baetselier, E.; De Mey, G. (1998) "Active Thermography Application for Solder Thickness Measurement in Surface Mounted Device Technology." Microelectronics Journal, Vol.29, No.4-5, pp.223-228.

Wu, C.F; Hamada, M. (2000) *Experiments: Planning, Analysis, and Parameter Design Optimization*. New York: J. Wiley.

Zalameda, J.N. (1999) "Measured Through-the-Thickness Thermal Diffusivity of Carbon Fiber Reinforced Composite Materials." Journal of Composites Technology & Research, JCTRER, Vol.21, No.2, pp.98-102.